A Changepoint-Based Framework for Climate–Hydrology Teleconnection Analysis

By

Carlos Rosas Cabello

Thesis submitted to the University of Ottawa

In Partial Fulfillment of the Requirements for degree of

Doctor of Philosophy in Civil Engineering

Department of Civil Engineering

Faculty of Engineering

University of Ottawa

© Carlos Rosas Cabello, Ottawa, Canada, 2025

Laudato si', mi' Signore, per sor'aqua,
la quale è multo utile et humile et
pretiosa et casta.

Francesco d'Assisi

Acknowledgements

To God, the Creator who sustains me at all times.

I am deeply grateful to my supervisor, Dr. Ousmane Seidou, for his confidence in my abilities, his invaluable guidance, insightful suggestions, and humility in generously sharing his knowledge and experience throughout the development of this work. I am also grateful to the University of Ottawa for providing me with the opportunity to grow both academically and professionally. I would like to extend my sincere appreciation to Professors Majid Mohammadian, Hossein Bonakdari, and Sara Magdouli for their valuable contributions and service as members of my examination committee. I would also like to extend my gratitude to Dr. Salah-Eddine El Adlouni for serving as external examiner, and to Dr. Mohammad Alobaidi and Dr. Fateh Chebana for their contributions to scientific publications.

I owe a special debt of gratitude to my family for their unconditional support. In particular, I would like to thank my parents, Elsa and Carlos, for their sacrifices, dedication, and guidance; my sisters, Astrid and Ingrid; and my second mother, María de la Luz, whose encouragement and companionship have sustained me, especially during difficult times, despite the distance. I would also like to acknowledge my close friends and extended colleagues in Mexico and Canada- especially Emmanuel, Javier, Mohammad, Abdurrahman, Amirmohammad, Sadah, Amirreza, Elsayed, Amir Noori, Sina, Mohammad Salimi, Ahmad Nasser, and Tram- for their friendship, support, and encouragement throughout this journey.

Finally, I would like to express my heartfelt appreciation to the people of Mexico, through CONAHCYT, for the generous support that enabled me to complete my studies and contribute to society.

Abstract

Accurate prediction of hydroclimatic extremes, such as droughts, floods, and water availability, hinges on understanding how remote oceanic forcings modulate continental precipitation. Conventional teleconnection analyses face two critical limitations: (i) their reliance on linear, stationary assumptions, which conceal regime shifts and erode predictive skill, and (ii) their vulnerability to short or fragmented records, which amplifies uncertainty. Although traditional methods can estimate degrees of ocean–land influence, a clear need remains for approaches that link both processes under nonlinear, nonstationary conditions while retaining strong physical interpretability for forecasting and decision-making.

This dissertation advances teleconnection and hydroclimate analysis by: (a) formulating the Point–Slope (PS) similarity metric, which blends Bayesian changepoint detection with segment-specific trend estimation to capture evolving, potentially nonlinear ocean–land connections; (b) generating station-specific Oceanic Regions of Influence (ROIs) that locate where low-frequency climate modes exert maximal control on local rainfall; (c) designing a geographically flexible PS-driven clustering framework that produces hydrologically homogeneous, physically interpretable regions; (d) benchmarking PS against Spearman correlation and Empirical Orthogonal Functions (EOFs) to quantify improvements in signal detection, spatial coherence, and resilience to missing data; and (e) testing PS sensitivity to confirm computational efficiency and methodological stability.

The findings demonstrate that PS (i) uncovers dynamic teleconnections overlooked by conventional metrics; (ii) scales linearly with record length, yielding 0–1 values that directly represent the joint probability of synchronized changepoints and aligned trends; (iii) generates ROI maps that expose fine-scale oceanic zones governing variability at individual rain gauges; (iv)

forms clusters with markedly greater monthly-precipitation homogeneity than those produced with Spearman correlation, especially for key modes such as Niño-3.4; and (v) simultaneously delineates oceanic regions of influence across the full predictor field, and their corresponding terrestrial clusters, more accurately than traditional EOF analysis. Together, these advances provide a scalable, reproducible, and transparent framework for incorporating teleconnection insights into regional water-management planning and next-generation predictive systems under a changing climate.

Looking ahead, the PS framework is not intended to replace established methodologies but rather to complement and enhance them. Its probabilistic and segment-based structure provides a foundation that can be readily combined with emerging technologies such as artificial intelligence, machine learning, and high-performance computing. Such integration can improve both the detection and interpretation of teleconnections, enabling hybrid approaches that fuse statistical rigor with computational adaptability. This opens promising avenues for advancing predictive accuracy, refining early-warning systems, and strengthening the scientific basis of climate-informed water-management strategies.

Table of Contents

List of Figures

List of Tables

List of Abbreviations

Abbreviation	**Definition**
AMM	Atlantic Meridional Mode
AMO	Atlantic Multi-decadal Oscillation
AMOC	At Most One Change
AO	Arctic Oscillation
CCA	Canonical Correlation Analysis
COI	Cone of Influence
CP	Changepoint
CUSUM	Cumulative Sum
CWT	Continuous Wavelet Transform
DANA	*Depresión Aislada en Niveles Altos*
DJF	December-January-February
DOISST	Daily Optimum Interpolation Sea Surface Temperature
DTW	Dynamic Time Warping
EA	Eastern Atlantic
EMD	Empirical Mode Decomposition
ENSO	El Niño-Southern Oscillation
EOF	Empirical Orthogonal Function
ERSST	Extended Reconstructed Sea Surface Temperature
HadISST	Hadley Centre's Sea Ice and Sea Surface Temperature
IOD	Indian Ocean Dipole
IPCC	Intergovernmental Panel on Climate Change
IPO	Interdecadal Pacific Oscillation
JJA	June-July- August
JSD	Jensen-Shannon Distance
LPS	Linear Partial Spearman
MAM	March-April-May
MCMC	Markov Chain Monte Carlo
MJO	Madden-Julian Oscillation
MW	Meridional Winds
NAO	North Atlantic Oscillation
NCEI	National Centers for Environmental Information
NESDIS	National Environmental Satellite, Data, and Information Service
NL	Nonlinearity
NLPCA	Nonlinear Principal Component Analysis
NPS	Nonlinear Point-Slope Similarity Measure
NOAA	National Oceanic and Atmospheric Administration
NS	Nonstationarity
OISST	Optimum Interpolation Sea Surface Temperature
PC	Principal Component
PCA	Principal Component Analysis

Abbreviation	**Definition**
PDO	Pacific Decadal Oscillation
PELT	Pruned Exact Linear Time
PMM	Pacific Meridional Mode
PNA	Pacific North Atlantic Oscillation
PS	Point-Slope Similarity Measure
PWC	Phase Wavelet Coherence
PWR	Wheelabrator Saugus Power Station
QBO	Quasi-biennial Oscillation
ROI	Region of Influence
RPCA	Rotated Principal Component Analysis
SAT	Surface Air Temperature
SAM	Southern Annular Mode
SIOD	Subtropical Indian Ocean Dipole
SLP	Sea Level Pressure
SON	September-October-November
SST	Sea Surface Temperature
SSTA	Sea Surface Temperature Anomaly
UNDRR	United Nations Office for Disaster Risk Reduction
WA	Western Atlantic
WA	Wavelet Analysis
WMO	World Meteorological Organization
WP	Western Pacific
WRCC	Western Regional Climate Centers
WTC	Wavelet Transform Coherence
XWT	Cross Wavelet Transform
ZW	Zonal Wind

Chapter 1 Introduction

1.1. Research background

Extreme hydroclimatic phenomena, like floods, droughts, and wildfires, have been increasing in magnitude and frequency, revealing a fundamental vulnerability within contemporary socioeconomic systems (IPCC, 2021; Blöschl et al., 2019). The damage caused by these events requires an assessment of impacts beyond direct physical losses, as indirect effects on public health and the economy, can equal or exceed the initial damage (Hsiang et al., 2017). This problem cannot be solved by halting natural processes, but rather by understanding precisely *where*, *how*, and *when* these phenomena will manifest, thereby enabling strategic reductions in vulnerability for both critical infrastructure and populations.

From an analytical perspective, the assumption of hydrologic stationarity, where past observations predict future conditions due to their behavioural performance, has been proposed as invalid (Milly et al., 2008; Serinaldi and Kilsby, 2015). Such nonstationarity (NS) arises from the direct influence of climate change on hydrological variables, compounded by anthropogenic modifications of watersheds through urbanization and alterations to natural environments (Philip et al., 2022). These drivers are not independent; they interact in a loop inherently variable in climate and rainfall patterns (AghaKouchak et al., 2020).

In this context, growing evidence demonstrates that remote climate forcings called teleconnections govern much of the timing, location, and intensity of hydroclimatic extremes. However, analyzing teleconnections is statistically challenging because the processes are simultaneously nonlinear (NL) and nonstationary (NS). Traditional methodologies such as Empirical Orthogonal Functions (EOFs) and Principal Component Analysis (PCA) extract linear, variance-maximizing modes

(Wallace and Gutzler, 1981; Jolliffe and Cadima, 2016), but can hide rare events and structural shifts (Ouarda et al., 2019). Wavelet Analysis (WA) captures efficiently the multiple timescales (Torrence and Compo, 1998). Nevertheless, its output is sensitive to the chosen mother wavelet and might be affected by edge effects (Cazelles et al., 2008). On the other hand, deep learning models improve prediction skill (Ham et al., 2019; Barnes et al., 2022) but sometimes operate as black boxes, making it impossible to extract the internal process and the adjacent analysis (Reichstein et al., 2019).

1.2. What are Teleconnections?

A teleconnection is a statistically significant, physical climate linkage between geographically distant regions (Walker and Bliss, 1932; Nigam, 2003). These links can be understood through planetary-wave propagation, ocean–atmosphere coupling, and jet-stream modulation. When a sudden perturbation occurs in one sector of the globe, typically in the sea, it can reorganize temperature, pressure, and moisture fields perceptibly far inland. One of the most common teleconnections is the El Niño–Southern Oscillation (ENSO), documented for its global effects. In this case, the sea surface temperature changes along the equatorial Pacific produce disruptions in rainfall patterns in distant areas with heterogeneous impacts. The most important characteristic of this phenomenon is its oscillatory process with periodicity, location, and spatio-temporal variation. Given these factors, its study inherently involves complexity of understanding.

1.3. Impacts of Teleconnections on Hydrological Extremes

Low flows induced by dry atmospheric conditions and flash floods caused by intense, short-duration rainfall are often triggered, amplified, or suppressed by large-scale teleconnections. For example, strong El Niño winters shift the Pacific jet southward, facilitating atmospheric rivers towards coastal and southern California, producing devastating floods (Dettinger, 2011; 2013). In contrast, during the same austral summer, the identical ENSO phase can increase dry air over tropical South America, leading to rainfall deficits and contributing to multi-year drought in northeast Brazil (Marengo et al., 2011). This dual behaviour underscores the nonlinearity inherent in ocean–land relations, where identical ocean-atmosphere signals may yield opposite hydrological outcomes depending on regional circulation. While monotonic metrics, such as Spearman correlation, can detect recurrent linear signals, they falter when the forcing is intermittent, the response is episodic, or both exhibit structural breaks in magnitude and frequency (Destouches et al., 2025). Brazilian droughts, for instance, do not recur annually with uniform severity; their timing aligns with specific ENSO phase combinations and interactions with other teleconnections.

Optimal teleconnection analyses must capture intermittency, which demands tools that relax stationary assumptions. Adopting a multi-axis perspective, considering *space*, *mechanism*, and *temporality*, is crucial for generating explainable and operationally useful results in hydroclimatic risk management based on teleconnections under nonstationary (NS) conditions (Slater et al., 2021; Volpi et al., 2024). However, most current frameworks are limited by their linear, variance-centred, or parameter-sensitive nature. This leaves important questions about *how* and *when* remote climate forcings modulate hydrological extremes unanswered.

1.4. Knowledge Gaps

Current teleconnection methodologies struggle to meet the practical requirements for water-resource management. This section outlines the knowledge gaps motivating this study, identified through a comprehensive literature review in Chapter 2.

1. Orthogonal decompositions (PCA/EOF) maximize linear variance, blurring synchronous breaks and nonlinear dependencies. As a result, they miss the structural evolution, activation and decay phases of ocean–land teleconnections.
2. Wavelet coherence depends strongly on the selected mother wavelet, interpreting the output demands expert judgement and seldom yields physically explicit, management-ready metrics.
3. Neither PCA/EOF nor WA provides a built-in mechanism for propagating the teleconnection signal into predictive models under NL, NS conditions, significantly reducing their practical forecast utility. Both techniques assume data completeness. Even modest gaps destabilize covariance matrices and inflate edge effects.
4. Existing tools isolate oceanic and continental modes separately. They cannot produce a single, cohesive map that links forcing regions at sea with impacted terrestrial stations, an operational requirement for regional water planning.
5. Current frameworks do not quantify NL and nonstationarity via structural features such as synchronous changepoints and aligned trends. This gap prevents robust answers to the essential questions of *where*, *how*, and *when* oceanic forcings modulate continental precipitation.

1.5. Research Objectives

To address these identified gaps and analyze teleconnections under explicitly nonlinear, nonstationary conditions, this dissertation aims to create a robust method that quantifies relationships between climatic forcings and hydrological responses across geographically distant regions without sacrificing physical interpretability. To achieve this, the following specific objectives will be pursued:

1. Develop a similarity measure (PS) that captures structural alignments by changepoint detection with segment-specific trend estimation, thereby identifying synchronous breaks and trends between oceanic and terrestrial time series.
2. Identify precise marine Regions of Influence (ROIs) at the station level by pinpointing the marine grid points where low-frequency climate modes exert maximal control on individual rainfall gauges and defining each ocean–gauge pair with a PS similarity value.
3. Group rain-gauge stations into hydrologically homogeneous regions by applying the new similarity metric to cluster stations in a manner that preserves spatial coherence and physical interpretability.
4. Benchmark the proposed metric against conventional approaches by quantitatively comparing it with Spearman correlation and EOF/PCA in terms of signal detection, spatial consistency, and resilience to missing data.
5. Demonstrate the predictive utility of the framework by showing how ROI maps and cluster assignments can inform regional water management and lay the groundwork for future forecasting applications.

To meet the research objectives, this dissertation analyzes two complementary observational datasets: rainfall time series from gauges distributed across California and global sea-surface-temperature anomaly fields derived from satellite observations. We employed a Bayesian changepoint-detection framework, detailed in Chapter 3, to quantify synchronous breaks and trend alignments, thereby revealing robust ocean-land teleconnection patterns under explicitly non-stationary, non-linear conditions. California serves as a test example because its intricate topography and sharp hydroclimatic gradients pose a stringent challenge and hold high societal relevance; however, the methodology itself is fully transferable to other regions facing similar data limitations and teleconnection complexities.

1.6. Novelty

This study introduces a series of novel methodologies designed to enhance the detection, measurement, and interpretation of teleconnections with enhanced accuracy:

- *Where:* Spatial Influence

  Existing research has not produced interpretable maps that directly link specific oceanic grid cells to individual rain-gauge stations, enabling multiscale visualization of teleconnection patterns and their continental impacts. The PS workflow yields an intuitive 0–1 similarity score and ROI maps, avoiding the interpretative burden of rotated EOFs or multi-scale wavelet plots and facilitating adoption by water resource practitioners.

- *How:* Physical Mechanism

  No previous studies have proposed a new structure-aware similarity measure that quantifies the joint probability of synchronous breaks and aligned trends, thus capturing nonlinear, nonstationary links between remote climatic forcings and local hydrological responses.

- *When:* Temporal Activation

  This study pioneers the application of Bayesian changepoint detection coupled with segment-specific slope estimation to teleconnections. The approach reveals coupling episodes that elude standard correlation metrics, uncovering hidden, nonstationary relationships without altering the original data.

1.7. Dissertation Layout

This dissertation consists of seven chapters, with Chapters 4 through 6 formatted as standalone technical papers. Figure 1.1 outlines schematically the contents of this work and describes its material as follows:

Chapter 1 introduces the reader to Teleconnections and the importance of their study. The gaps and Objectives for the present dissertation. **Chapter 2** surveys the state of knowledge on climate teleconnections, describing their main types, characteristic periodicities, and the atmospheric–oceanic variables through which they operate. It also critiques the analytical techniques currently used to study teleconnections, establishing why a method that can accommodate their intrinsic nonlinearity and nonstationarity is required.

Chapter 3 introduces the study's methodological framework. It first situates changepoint detection within a Bayesian setting, outlining the advantages and practical scope of this approach. Building on these concepts, it presents the Point–Slope (PS) similarity metric, which integrates information from both changepoints and trends to quantify teleconnection strength.

Presented in article format, **Chapter 4** employs the PS metric to delineate Regions of Influence (ROIs) for hydrological stations across California. The resulting maps identify six climatic stations that exhibit distinctive oceanic forcing patterns. The manuscript has been submitted to the Journal of Hydrology. Also structured as an article, **Chapter 5** proposes a homogeneous regionalization of California based on the Niño-3.4 climate index. It offers an alternative means of assessing how sea-surface temperature anomalies (SSTAs) affect precipitation stations throughout the state.

Chapter 6 establishes a new regionalization paradigm that uses a 1.5° gridded PS metric spanning the entire Pacific Ocean. This paper provides a robust climate–hydrology teleconnection framework that moves beyond single indices, comparing the gridded PS results with modes extracted via Empirical Orthogonal Functions (EOFs).

The final **Chapter 7** outlines promising avenues for extending PS-based analyses to other teleconnection problems, highlighting both the metric's strengths and its current limitations. It concludes the dissertation by summarising the main findings, emphasizing the advantages of the PS approach, and suggesting pathways for further refinement and application.

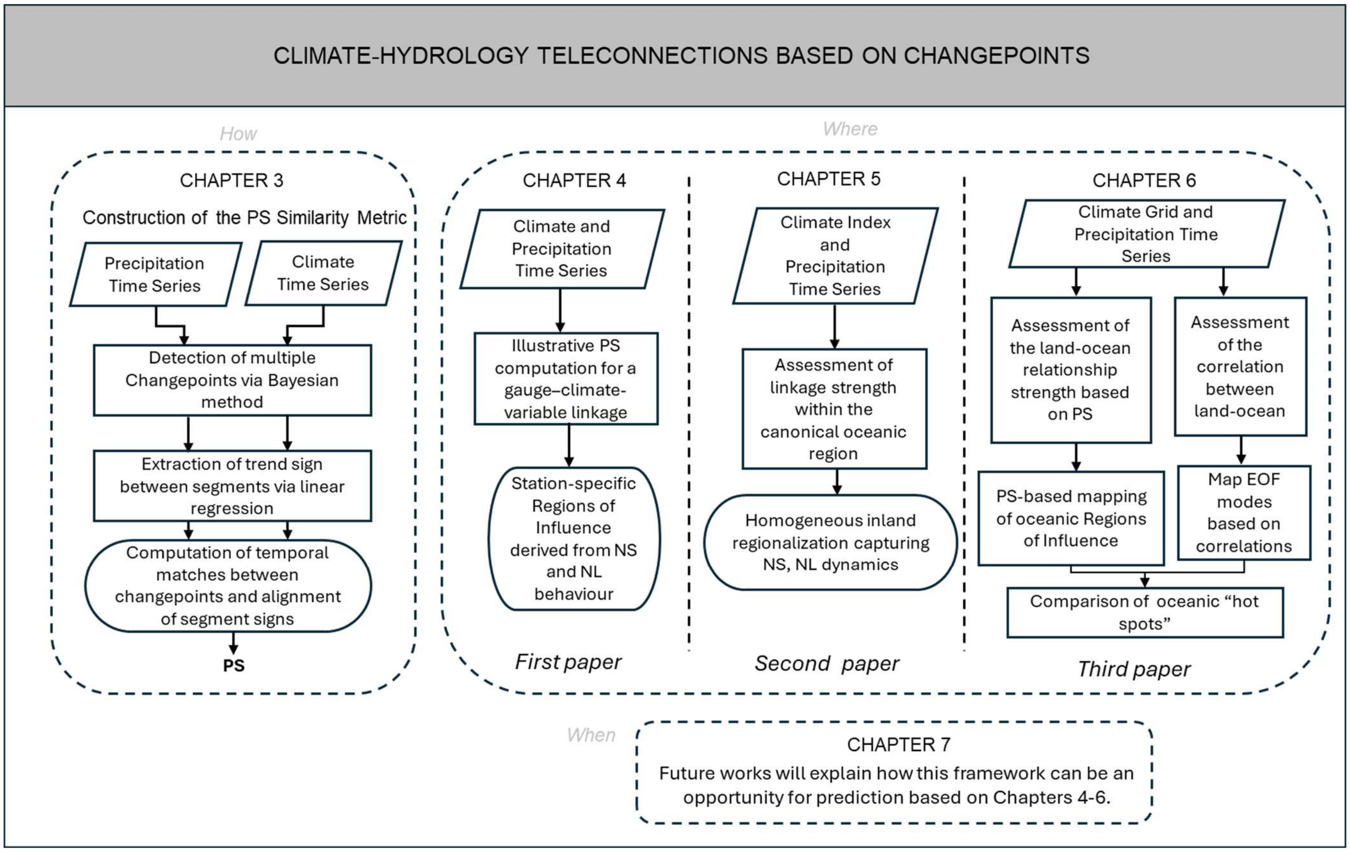

Figure 1.1 Thesis Organization

Chapter 2 Literature Review

Climate-hydrology interactions have been studied intensively due to the effects of climate instability. Despite this, oscillatory processes that link shifts in climate variables with rainfall and temperature patterns have been documented since the late 19th century (Hildebrandsson, 1897; Walker and Bliss, 1932). The recent acceleration of climate change has amplified its complexity and regional consequences. Although the spatial signatures of teleconnections are well-documented (Nigam and Baxter, 2015), key knowledge gaps persist. This chapter reviews the state of knowledge on teleconnection patterns, the climatic variables and analytical methods used to study them. These include the nonlinear physical mechanisms driving these interactions and their evolving behaviour under anthropogenic modifications. Furthermore, methodological limitations are discussed exist in quantifying their hydrological impacts, particularly in topographically complex regions.

2.1. Introduction to Teleconnections

As stated in Chapter 1, teleconnections are defined as a statistical correlation between temporal variability in hydroclimate parameters at different points on Earth (Wallace and Gutzler, 1981). Kwon et al. (2009) further conceptualized teleconnections as a physical linkage of slow-evolving climate processes impacting hydrological extremes. Therefore, teleconnections can be sketched as a bridge facilitating communication between the atmosphere and various parts of the ocean. They also enable the ocean to act as a tunnel, linking distant atmospheric regions (Liu et al., 2007).

This ocean-atmosphere communication primarily occurs through two mechanisms. First, the atmosphere and ocean organize into coherent circulations across various space-time scales, such as monsoons or sea and mountain breezes.

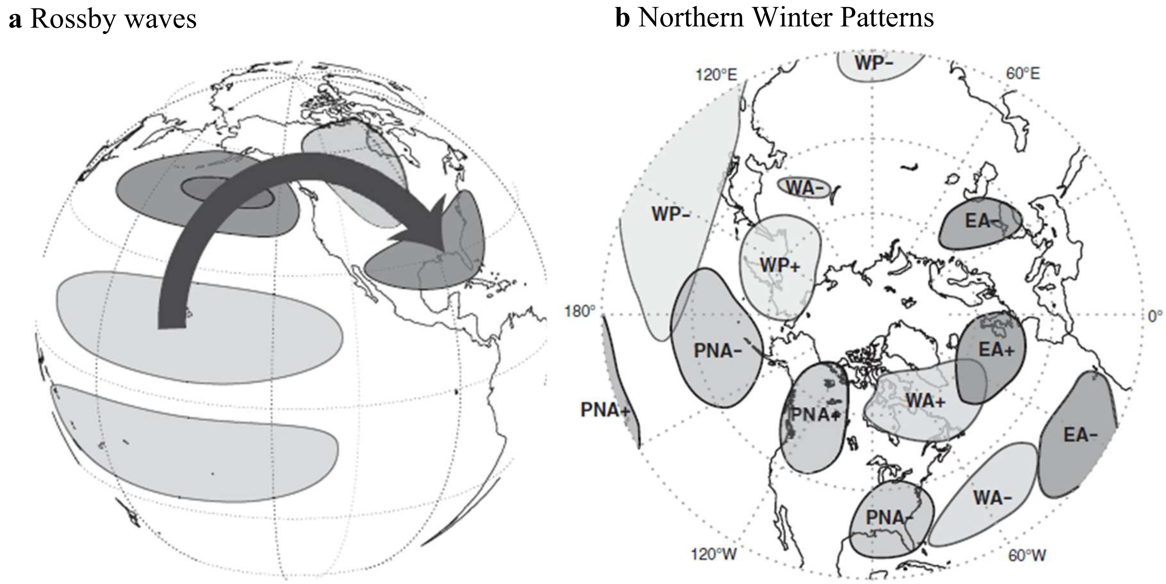

Figure 2.1 Schematic representation of teleconnection patterns around the globe. (a) Rossby waves transfer the anomalies in the ocean to remote areas. (b) Northern Winter Patterns (An et al., 2020).

A sudden shift in the location or intensity of these circulations can be perceptible over a wide area (Chase et al., 2006). Secondly, internal disturbances can trigger atmospheric or oceanic waves, such as Rossby or Kelvin waves, that propagate far beyond the reach of the original circulation. Because these waves often arise from abrupt or subtle shifts in a nonlinear climate system, they can generate regional-to-global climate anomalies far from their source, ultimately altering hydrological variables.

Figure 2.1a shows a scheme of Rossby waves circulating from the central Pacific toward the northeast, illustrating how a sea-surface-temperature anomaly can be transmitted to North America. Figure 2.1b shows the Northern-Hemisphere winter modes conveyed by these waves, the Pacific–North American (PNA), Western Pacific (WP), Western Atlantic (WA) and Eastern Atlantic (EA) patterns (An et al., 2020). These conditions redirect storm tracks, alter moisture transport and modify downstream river flows.

2.2. Patterns and principal modes

Given this framework, many teleconnection studies identify large-scale atmospheric patterns as key predictors for rainfall-forecast models. The literature recognizes a spectrum of phenomena, such as El Niño-Southern Oscillation (ENSO), Pacific Decadal Oscillation (PDO), Atlantic Multi-decadal Oscillation (AMO), North Atlantic Oscillation (NAO), and Indian Ocean Dipole (IOD), among others, each with distinct periodicity, spatial reach, and climatic footprint. For example, the AMO (Hu and Feng, 2012) behaves over multidecadal scales, typically between 60 and 80 years, while the NAO (Hurrell and Deser, 2010) fluctuates with a periodicity of 1 to 2 years. However, ENSO remains the most studied teleconnection due to its complexity and global impact. Still, the spatial heterogeneity of ENSO's teleconnections suggests that regional responses require more nuanced approaches.

2.2.1. Climate Variables

Teleconnection patterns manifest through specific climate variables that capture their influence on global atmospheric circulation and regional climate. Table 2.1 summarizes the key diagnostics, sea-surface temperature (SST), sea-level pressure (SLP), surface-air temperature (SAT), atmospheric winds, and shows how each variable relates to the principal modes of variability. These climate variables operate on different time scales, capturing the unique periodicity of teleconnection phenomena.

2.2.1.1. Sea-Surface Temperature (SST)

Sea-Surface Temperature is a significant physical characteristic of the oceans taken from the water near the surface. The SST varies depending on latitude, where the warmest waters being found close to the equator and the coldest waters found in the Arctic and Antarctic. It rises as the seas absorb more heat, and the patterns of ocean circulation carry warm and cold water across the global interchange (Hurrell and Trenberth, 1999). Multiple approaches exist for how variations in sea surface temperature might impact marine ecosystems. For instance, changes in ocean temperature can modify the ecosystem of plants, animals, and bacteria that live in a particular area. However, SST has a decisive impact on the global climate since the seas and atmosphere are constantly in contact with one another (Ropelewski and Halpert, 1987). The amount of atmospheric water vapour over the seas has increased as a result of increases in sea surface temperature. This water vapour can be reflected by meteorological systems that bring about precipitation, raising the probability of heavy rainfall events. Changes in sea surface temperature can alter the paths of storms, which is a factor in droughts in certain regions.

Owing to the temperature in the sea having a variation in location and time period, with respect to the average value, it is known as an oscillatory anomaly. This can be seen in the phases of specific phenomena such as El Niño, which is the dominant mechanism and pattern of interannual variability in the climate system. Large stretches of the equatorial Pacific alternate between surface waters that are warmer and colder than usual known as El Niño/La Niña phenomena (McPhaden et al., 2020).

2.2.1.2. Sea-Surface- Level Pressure (SLP)

Sea surface level pressure is the atmospheric pressure at a given location. This variable is linked to SST in such a way that the pressure gradient affects sea surface temperatures and vice versa. It is understood that when there is a sudden drop in atmospheric pressure, it allows the circulation of air masses transporting clouds and favoring precipitation. For example, a decrease in pressure off the coast of Australia and an increase in pressure in French Polynesia, promote an east-west air circulation, drawing warm surface water to the west leading to precipitation in Australia.

Table 2.1 Teleconnection variables.

Teleconnection	Temporal Resolution	Spatial Scale	Periodicity	Variable	Significative Studies
ENSO	Monthly	Global	2- 7 yrs	SST/SLP	Wallace and Gutzler, 1981
AMO	Monthly	Global	60 – 80 yrs	SST	Hu and Feng, 2012
PDO	Monthly	Global	20 – 30 yrs	SST	McAfee, 2014; Newman et al., 2016
QBO	Monthly	Global	2 – 3 yrs	ZW	Lindzen and Holton, 1968
IOD	Monthly	Regional	2 – 3 yrs	SST	Zhang et al., 2024
NPO	Monthly	Regional	1 – 10 yrs	SLP	Li et al., 2024
EPO	Daily	Regional	1 – 2 yrs	SLP	Dai and Tan, 2019a
WP	Daily	Regional	1 – 2 yrs	SLP	Choi and Moon, 2012
NAO	Daily	Regional	1 – 2 yrs	SLP	Hurrell and Deser, 2010
PNA	Daily	Regional	1 – 2 yrs	SLP	Wallace and Gutzler, 1981

However, the character of this variable is global, understood as a pressure variation in the Northern and Southern hemispheres. Likewise, since SLP is dependent on SST, the changes will be dominated by the aforementioned atmospheric circulation anomalies. For such a reason, teleconnections can be presented in a range of cardinal direction linked with the place is calculated. For example, North Pacific Oscillation (NPO) refers to teleconnection analyzed from the coast along North Pacific Ocean.

2.2.1.3. Surface Air Temperature (SAT)

One of the most observational indicators and contributors to climate change are the surface air temperatures (SAT) specifically those measured in the Artic. They are collected 1.5 to 2 metres above the surface of the land, ocean, or ice cover. Several studies have revealed that there has been a noticeable positive warming trend of over 3°C above the average SAT across the Arctic lands.

Air temperature rises have been linked to changes in the frequency, severity, and duration of hydrometeorological extremes. This variable is mostly used for boreal teleconnection studies (Shi et al., 2019).

2.2.1.4. Zonal and Meridional winds (ZW, MW)

Two different measures of winds can be taken: Zonal and Meridional Winds (ZW, MW). The atmosphere is thermalized longitudinally in the west-to-east direction by zonal flow, which moves along latitude parallel to the equator. In contrast, meridional flow follows a pattern along the Earth's longitude lines, that goes from north to south or from south to north. When ENSO occurs, zonal wind changes mostly in the western equatorial Pacific, impacting Sea Surface Temperatures. Changes in the mean winds are generated by imposing heat flux forcing in two confined regions at a sufficient distance north and south of the equator (Fedorov and Zhao, 2021). Strengthening of either wind component (zonal or meridional) decreases ENSO amplitude, notably in the eastern Pacific SST variability, and prevents meridian swings in the zone known as the Intertropical Convergence Zone.

2.2.2. El Niño-Southern Oscillation (ENSO)

The El Niño-Southern Oscillation (ENSO) is a phenomenon that has been perceptible around the globe. It results from abnormal temperature differences across the equatorial Pacific, connecting sea-surface temperature (SST) and sea-level pressure (SLP) anomalies through ocean–atmosphere feedback. The warm (El Niño) and cool (La Niña) phases take place every 2–7 years, with intensities ranging from mild to severe events. During El Niño, positive SST anomalies in the central–eastern Pacific (5° S–5° N, 170° W–90° W) reduce regional SLP. This process shifts rainfall patterns toward normally dry areas such as the Peruvian coast, while causing droughts over parts of Southeast Asia and Australia. As can be seen in Figure 2.2a, these conditions are typically perceptible from January to May in Peru but from July to January in Australia. In North America, El Niño winters are typically wetter and cooler across the southwestern United States and the Gulf Coast, whereas Alaska and western Canada tend to be warmer (Ropelewski and Halpert, 1986). Conversely, La Niña (see Figure 2.2b) brings warm, dry winters to much of the western U.S. and Canada (Cayan et al., 1999). Additionally, ENSO influences the North American monsoon, with El Niño strengthening it and La Niña reducing summer rainfall over northwestern Mexico and the southwestern U.S. (Higgins et al., 1999). South American teleconnections related to ENSO are similarly asymmetric. El Niño reduces rainfall across northern Amazonia and northeastern Brazil (Chiang et al., 2002; Nobre and Shukla, 1996; Canchala et al., 2020). At the same time, La Niña-induced warming in the tropical South Atlantic shifts the Intertropical Convergence Zone southward, resulting in wet anomalies in those regions.

a El Niño **b** La Niña

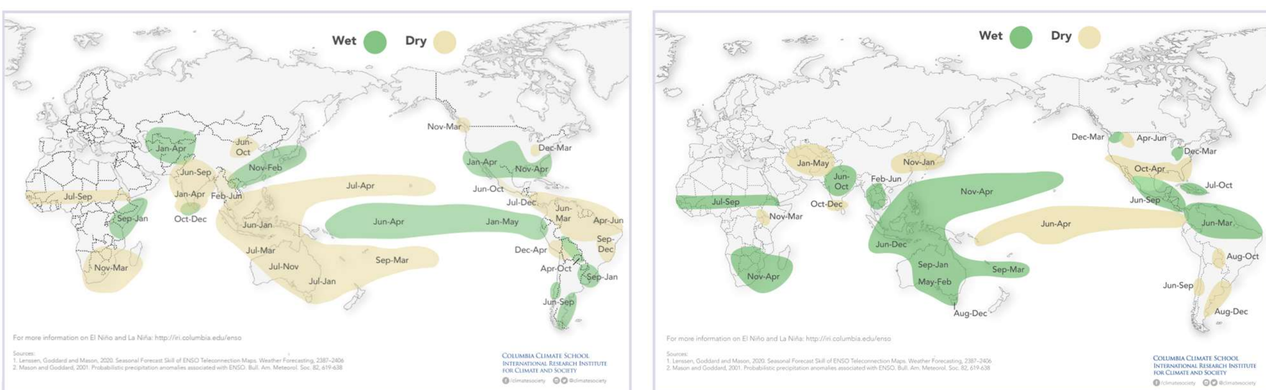

Figure 2.2 Expected changes in precipitation regionally during an (a) El Niño event, (b) La Niña event (IRI-Columbia, 2023).

In Europe, the influence of ENSO phases is relatively weak. However, El Niño winters (January–March) have been linked to increased rainfall across central and western Europe and the Mediterranean. This connection involves a key atmospheric pressure system near Iceland that influences regional weather patterns (Mariotti et al., 2002; Brönnimann, 2007). In East Africa, El Niño enhances precipitation during March–May but suppresses it toward the end of the season. During October–November, a period of rain combined with ENSO and Indian Ocean Dipole (IOD) produces notable wet anomalies (Nicholson and Kim, 1997; Zhang et al., 2024). Instead, Southern Africa experiences drought during El Niño from December to March, while West Africa and the Sahel become drier in boreal summer, coinciding with the peak of the West African monsoon. Across Southeast Asia, El Niño, especially Central-Pacific, Modoki events increase drought risk, with this effect intensified by positive IOD phases (Ashok et al., 2004). Nevertheless, Australia's response is distinctly nonlinear, as it has been described in the rest of the locations. La Niña brings more rainfall depending on the intensity of the phenomenon, but it has drier conditions than El Niño.

2.2.1.1. Nonlinearity and Nonstationarity behaviour

Detecting teleconnections between large-scale climate factors and regional hydroclimatic variables requires methods that can model their behaviour and capture both spatial and temporal complexity. As described in previous sections, this is challenging because teleconnections often exhibit nonstationarity. Their spatial patterns and intensities evolve over time rather than remaining constant around a mean state. Many of these relationships are also nonlinear, meaning the hydroclimatic response to a climate factor is not proportional across the full range of variability (Slater et al., 2021).

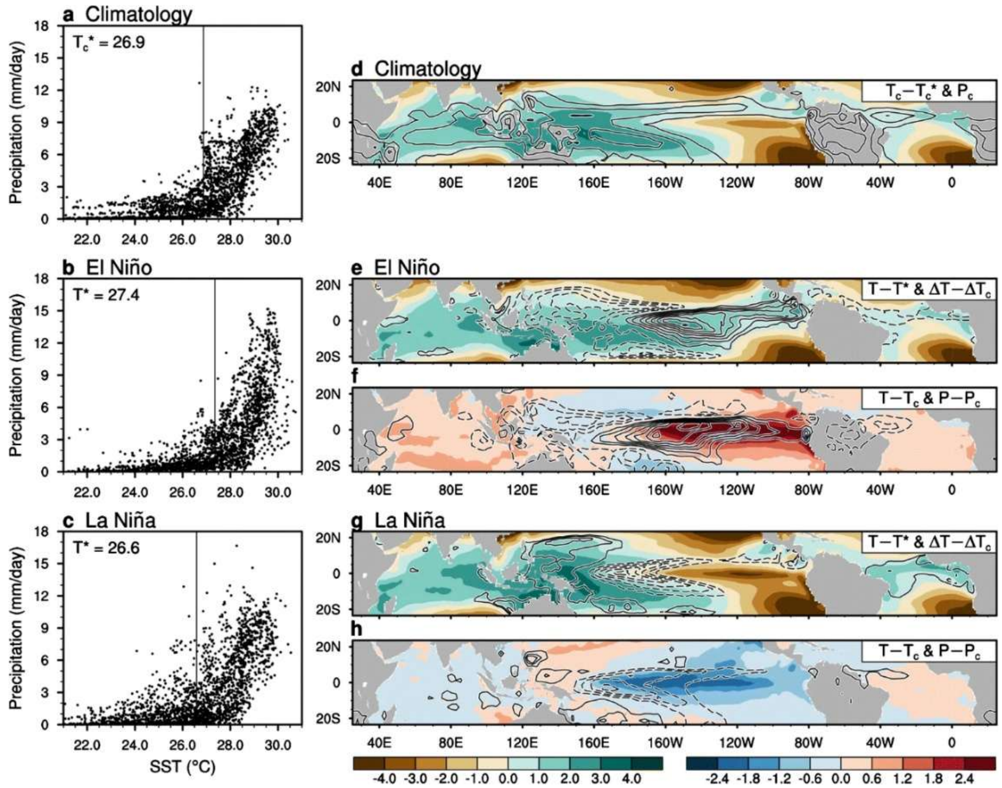

Figure 2.3 Relationship between sea surface temperature (SST) and daily precipitation during (a) climatology, (b) El Niño, and (c) La Niña conditions during December–February of 1982–2018. (d-h) Maps of SST deviations and precipitation (Okumura, 2019).

This nonlinearity is evident in Figure 2.3. A change in SST can produce impacts of varying magnitude; for example, extreme ENSO phases may trigger disproportionate precipitation anomalies. Panels a–c show the relationship between sea surface temperature (SST) and daily precipitation for the climatology, El Niño, and La Niña phases. In all cases, precipitation remains relatively low until a critical SST threshold (T*) is reached, beyond which it increases sharply, indicating a nonlinear response. This threshold shifts depending on the ENSO phase, being higher during El Niño (27.4 °C) and lower during La Niña (26.6 °C), with different maximum precipitation values. Panels d–h map the spatial anomalies in SST and precipitation relative to the climatology, showing that the regions of strongest teleconnection change in both magnitude and location between ENSO phases. This illustrates a form of nonstationarity, not as a temporal shift in the mean, but as a conditional change in spatial patterns and intensities depending on the climate state. In some cases, the sign and magnitude of the response shift beyond certain thresholds. Such behaviours cannot be fully explained by simple linear dependence measures, which assume a constant and proportional relationship between variables (Hlinka et al., 2012; Okumura, 2019).

2.2.1.2. ENSO-Related Climate Indices

A critical aspect of ENSO teleconnections is their nonstationarity, as their regional influence is modulated by other large-scale climate patterns, such as the Pacific Decadal Oscillation (PDO) and the Interdecadal Pacific Oscillation (IPO), which can either amplify or dampen their effects (Power et al., 1999; Wang et al., 2014). In that sense, a way to characterize this complex behaviour is by employing several SST-based indices. These include the Niño regions (Niño 1+2, 3, 3.4, and 4), which track sea surface temperatures across different sectors of the equatorial Pacific. Table 2.2 summarizes the regions where changes in SST have been detected, their associated impacts, and key relevant studies. It is important to note that Niño 3.4 exhibits the most widespread global influence compared to the other regions. Another option is the Oceanic Niño Index (ONI), taken from a three-month running mean of the Niño 3.4 index and the Southern Oscillation Index (SOI), which provides further insights into the spatial and atmospheric response based on different variables (see Table 2.1).

Although the physical aspect of ENSO is a crucial factor for hydrological impacts, the intensity of these events is important. Patricola et al. (2019), for example, provided a useful classification from strong to weak El Niño winters based on the Niño 3.4 index, offering an objective framework to distinguish between significant and minor climate forcings (See Table 2.3).

Table 2.2 Niño Regions and their impacts by Teleconnection Areas.

Niño Region	Coordinates	Teleconnection Areas	Impacts	Key Reference
Niño 1+2	0°–10° S, 90°–80° W	West coast of South America (Ecuador, Peru, and Chile), tropical Atlantic.	Intense rainfall and floods along Peruvian and Ecuadorian coasts; drought in Brazil.	Takahashi and Martínez (2019). Extreme coastal rainfall and flooding.
Niño 3	5° N–5° S, 150°–90° W	Tropical South America, tropical Africa.	Amazon drought; rainfall anomalies in Sahel and Horn of Africa.	Nicholson and Kim (1997). ENSO influence on East African rainfall.
Niño 3.4	5° N–5° S, 170°–120° W	North America, Pacific Islands, global teleconnection hotspot.	Wet winters in SW USA; warm winters in W Canada; drought in SE Asia and Australia.	Ropelewski and Halpert (1987). Global precipitation patterns associated with ENSO
Niño 4	5° N–5° S, 160° E–150° W	Western Pacific, Southeast Asia, Australia.	Drought in Indonesia and Philippines; changes in cyclone genesis in the W Pacific.	Ashok et al. (2007), L'Heureux et al. (2013). El Niño Modoki and its teleconnection patterns.

This classification highlights the complex evolution and behaviour of ENSO events. For instance, the Niño 3.4 index can change dramatically from year to year. As seen in the 2016 event, it was categorized as strong with temperatures above 1.5°C, despite being considered weak the previous year. Similarly, the 2010 strong El Niño event transitioned into a moderate La Niña in 2011 and a weak La Niña in 2012. This example demonstrates that oceanic variability is not only abrupt. The shifts underscore the nonstationarity of ENSO, where a seemingly similar phase can have a different hydrological impact. This will depend on its magnitude and position within a longer-term oscillation.

Table 2.3 List of ENSO events during 1895–2016 according to the DJF average in Niño 3.4 (Adapted Patricola et al., 2019)

Phase	Strong	Moderate	Weak
	(Niño 3.4 ≥ 1.5°C)	(1 °C ≤ Niño3.4 < 1.5°C)	(0.5°C ≤ Niño3.4 < 1°C)
El Niño	**2016**,1941,1998,1983, 1958,1973,1919,1992, 1897,1903,**2010**,1931	1900,1926,1915,1966,1912, 1987,1914,1942,1969,1964, 1905,1920	1995,1924,1906,2003,1940, 1988,**2015**,1954,1959,2007, 1977,1978,1948,2005,1930, 1896,1952,1901
	(Niño3.4 ≤ -1.5°C)	(-1.5°C < Niño3.4 ≤ -1°C)	(-1°C < Niño3.4 ≤ -0.5°C)
La Niña	1950,2008,2000,1976, 1943,1989,1974,1917	1956,1911,1934,1939,**2011**, 1925,1971,1909,1904,1999, 1910	1932,1975,1933,1927,1921, 1984,1965,1923,1918,1968, 1916, **2012**,2009,2001,1972, 1899,1955,1907,2006,1996, 1951,1985

2.2.1.3. ENSO in future scenarios

Another important dimension of teleconnections, particularly ENSO, is their response to climate change. There is growing evidence that a warmer climate may increase the frequency of extreme ENSO events (Cai et al., 2014; Wang et al., 2019). Recent research by Shin et al. (2022) indicates that greenhouse warming is likely to amplify ENSO variability, enhancing both the frequency and intensity of El Niño and La Niña events.

Using CMIP6 simulations, Shin et al. (2022) demonstrated that climate warming is expected to increase the occurrence of both El Niño and La Niña events. Figure 2.4 presents projected changes in the proportion of moderate, strong, and extreme ENSO events for the Niño 3 and Niño 4 regions between the 20th and 21st centuries. Over South Asia, the projected impact on extreme conditions is not expected to change drastically (Figure 2.4e). In contrast, the Eastern Pacific, whose teleconnections strongly influence North America, South America, and Africa, is projected to experience stronger El Niño events (Figure 2.4b). For La Niña, the authors found that Central

Pacific events are likely to have greater future impacts compared to their Eastern Pacific counterparts.

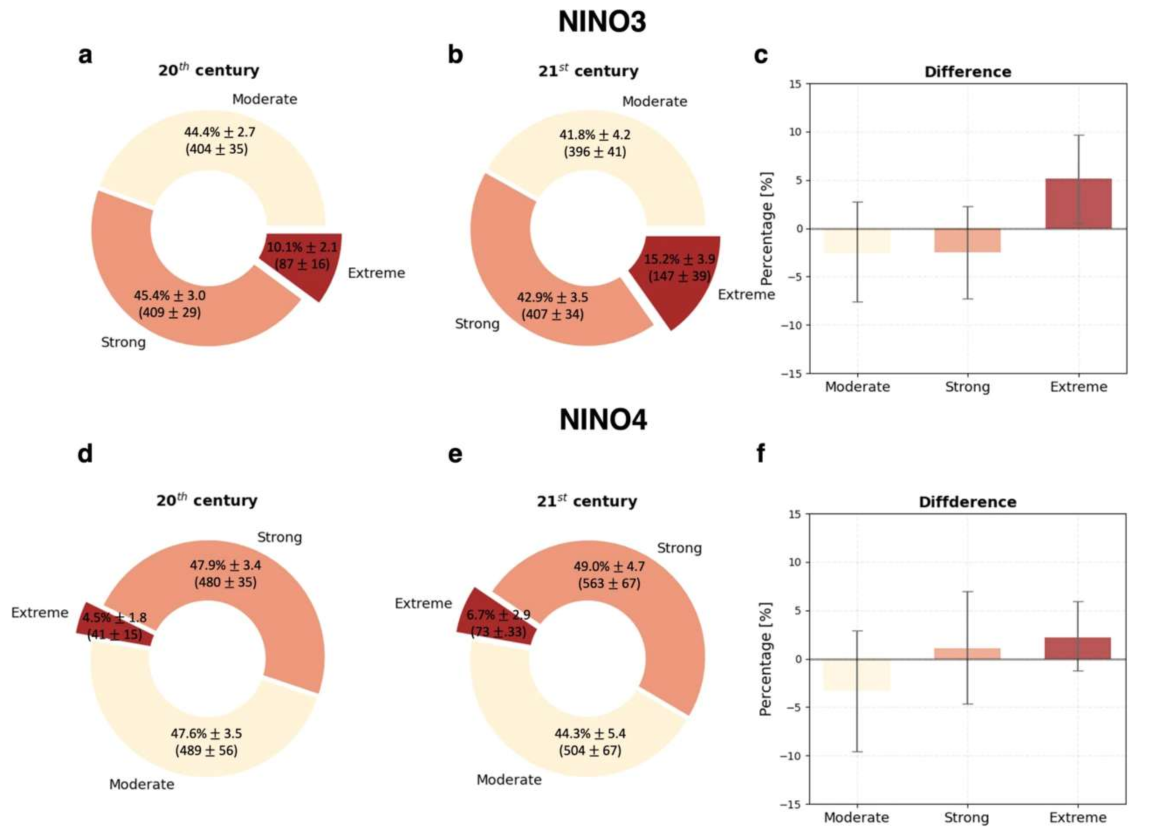

Figure 2.4 Projected changes in the frequency of moderate, strong, and extreme ENSO events for Niño 3 (a–c) and Niño 4 (d–f) regions between the 20th and 21st centuries (Shin, 2022).

The differences in impacts between the 20th and 21st centuries (Figure 2.4c–f) indicate that ENSO events are projected to become more extreme, underscoring the importance of analyzing this phenomenon when assessing future risks. Section 2.3 will discuss the potential impacts of such extreme events across different sectors.

2.3. Hydrological and economic impacts of teleconnections

By altering cyclone tracks, extending droughts, or intensifying storms, teleconnections convert ocean-atmosphere thermodynamic perturbations into socioeconomic impacts. The WMO Atlas of Mortality and Economic Losses (1970–2019) recorded more than 11,000 hydrometeorological disasters, two million deaths and US$3.6 billion in direct damages. Seventy-four percent of those losses and half of the fatalities stem from floods, storms, droughts, and wildfires. However, the most harmful, according to the report (see Figure 2.5), are floods and storms, events strongly modulated by modes such as the El Niño–Southern Oscillation (ENSO) and the North Atlantic Oscillation (NAO) (WMO, 2021; UNDRR 2019).

For example, during the 2017 Atlantic hurricane season, Hurricanes Harvey, Maria, and Irma together accounted for 35% of the total losses recorded in the ten costliest U.S. disasters to date (WMO, 2021). Their intensification coincided with a weak La Niña phase of ENSO, intermittent negative phases of the NAO that steered the storms westward, and an exceptionally warm tropical Atlantic linked to the Atlantic Meridional Mode (AMM). That combination of anomalies in the sea surface temperature and the hurricane season maximized the available energy for cyclones (NOAA, 2017; Lim et al., 2018; Klotzbach et al., 2018).

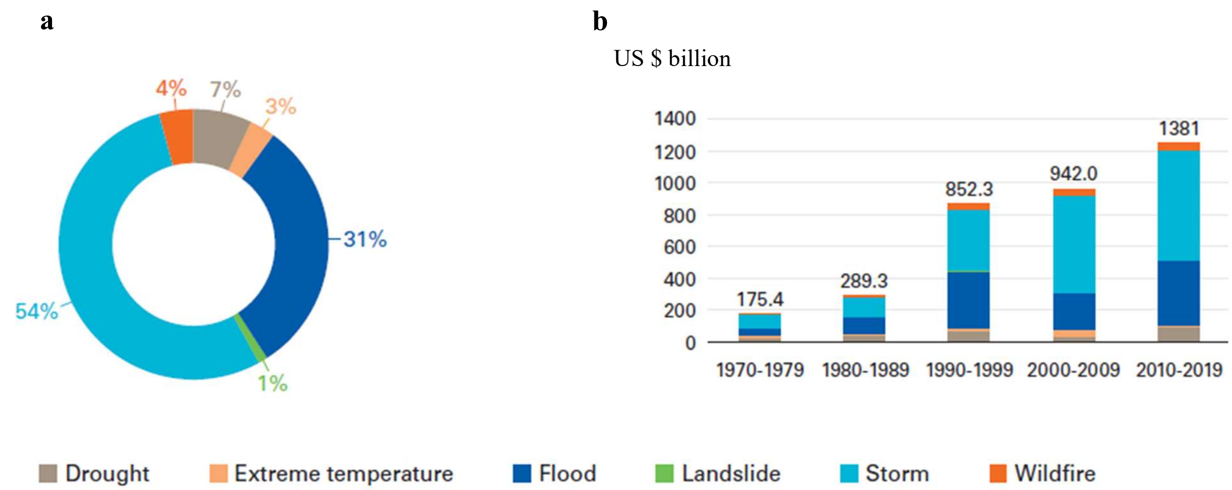

Figure 2.5 Distribution of economic losses by hazard type by decade globally (a) Percentage of Losses depending on extreme event (b) Economic losses per year depending on each extreme event (WMO, 2021).

In that sense, North America, Central America and the Caribbean have demonstrated the highest losses during 1970 – 2019 due to cyclones (Table 2.4). However, Asia tops in the number of deaths and disasters. For Europe, the statistics show the lowest rate of deaths and extreme events compared to other regions. Nevertheless, more events have arisen in the last two decades. Recently, on 29 October 2024, a cut-off low (in spanish: *Depresión Aislada en Niveles Altos*, DANA) over Valencia, Spain, caused 231 fatalities and 2.6 billion euros in damages (El País, 2025). DANAs have become increasingly potent triggers of flash floods, with their frequency rising since the 1960s (Muñoz et al., 2020). Although historically only about one-third of Spain's most significant floods have been linked to these systems (Llasat et al., 2007). The unprecedented damage from the 2024 event ranks it among the most severe hydrometeorological disasters on the Iberian Peninsula, driven by a combination of climate-mode influences that have yet to be fully identified (Nieto et al., 2021; Fuenzalida et al., 2005; Favre et al., 2012; Muñoz et al., 2020; Castro-Melgar et al., 2025).

Table 2.4 Distribution of number of disasters, number of deaths and economic losses attributed to tropical cyclones globally (WMO, 2021).

Region	Number of disasters	Number of deaths	Economic losses in US $billion
Africa	135	5,419	11.4
Asia	**732**	**682,646**	364.66
South America	18	691	2.66
North America, Central America and the Caribbean	543	45,300	**977.48**
South-West Pacific	502	45,181	60.91
Europe	15	87	3.3

In contrast to the excesses of storms and floods, teleconnections can also manifest as seasons of dryness and extreme heat. Because these modes redistribute energy and moisture globally, intense rainfall in one region is often mirrored by drought in a remote location. According to the Atlas of Mortality and Economic Losses (WMO, 2021), droughts, together with extreme heat and wildfires, account for only 14% of the total meteorological hazards recorded. Nevertheless, their deferred effects on food security, health, and infrastructure are frequently more severe. The El Niño events of 1982-1983 and 1997-1998 reduced global income by US$4.1 billion and US$5.7 billion, respectively, demonstrating that economic repercussions can far exceed immediate physical damage. Projections indicate that a warming-amplified ENSO could inflict cumulative losses of up to US$84 trillion over the twenty-first century (UNDRR, 2023; Schaeffer et al., 2025). Losses are unevenly distributed: along South America's west coast, the 1982-1983 El Niño caused 1,656 deaths and US$3.6 billion in direct damage.

Water-related sectors are especially sensitive. River discharge, groundwater levels, and snow storage respond directly to climate-mode variability (Dettinger and Díaz, 2000; Chiew and McMahon, 2002). Nearly half of the gauging stations analyzed by Ward et al. (2014) show significant shifts in flood probability during El Niño or La Niña years, while Van Loon and Laaha (2015) link multi-year drought severity to combined ENSO–PDO phases and regional atmospheric blocking. In snow-dominated basins, large-scale modes control accumulation and melt timing, altering the reliability of spring water supply (Mote et al., 2005).

Thus, in July–August 2022, China's Yangtze River Valley endured an unprecedented compound heat-wave–drought. Maximum temperatures exceeded the 1981–2010 mean by more than 3 °C for 24 consecutive days, while basin-wide rainfall dropped to its lowest level since 1961 (Hu et al., 2024). Satellite gravimetry revealed a surface-water storage deficit of 158 km^3, among the most significant regional losses ever recorded (Duan et al., 2024). Consequences were immediate: in Sichuan, where hydropower supplies typically over 80 % of electricity, reduced inflow halved generation, triggering rolling blackouts and factory closures (Reuters, 2022). Extreme dryness also sparked at least 19 off-season wildfires between 14 and 23 August in Sichuan and Chongqing, forcing evacuations (Reuters, 2022). Agriculture was hit hard; crop failures in rice, maize, and rapeseed were reported alongside widespread ecological stress in lakes and wetlands (Ma et al., 2022; Hao et al., 2023; Zhang et al., 2024).

These cases highlight why analyzing climate-hydrology teleconnections and their interaction with long-term climate change is essential. The IPCC synthesis (2021) goes beyond water-sector impacts across three dimensions: physical, human, and ecosystem. The physical dimension tracks changes in hydrological variables themselves: flood magnitude, drought frequency, groundwater decline, while the human dimension evaluates disruptions to water supply for agriculture, cities, and sanitation. The ecosystem dimension reports stress on wetlands, rivers, and biodiversity. For every variable, the assessment indicates whether the observed trend is an apparent increase, a clear decrease, or mixed when no single trajectory dominates.

This categorical approach highlights where the signal of climate variability and change is unambiguous and where uncertainties remain, providing a vital framework for linking teleconnections to water-management decisions. The cells are shaded from low confidence to high confidence (light colour to dark colour), signalling the level of certainty.

Heavy precipitation and pluvial flooding stand out: every continent shows an increase, with Europe displaying the strongest, most confident rise. Drought, by contrast, registers its most apparent upward trend in Africa. At the same time, the signal remains mixed elsewhere, a finding consistent with the contrasting wet-dry anomalies illustrated by our Yangtze and DANA cases. Also, for groundwater, there is a decline across all regions, compounding stress on both agriculture and urban supply. The ecosystems and municipal water services are flagged as negative in almost every region, and agriculture is already suffering adverse effects in Africa and Asia while facing mixed outcomes on the other continents. Notably, the table contains no cells suggesting improvement for any sector or variable: even where the trend is mixed, there is no robust evidence of positive change.

Table 2.5 Regional synthesis of assessed changes in water and consequent impacts (IPCC,2021).

Variables affected by Climate Change	Africa	Asia	Austral-Asia	Central and South America	Europe	North America	**Global**
Heavy Precipitation and pluvial flood	Increase	Increase	Increase	Increase	Increase	Increase	Increase
Runoff and streamflow	Mixed	Mixed	Mixed	Mixed	Mixed	Mixed	Mixed
River flood	Mixed	Mixed	Mixed	Mixed	Mixed	Mixed	Mixed
Drought	Increase	Mixed	Mixed	Mixed	Mixed	Mixed	Mixed
Groundwater	Decrease	Decrease	Decrease	Decrease	Decrease	Decrease	Decrease
Agriculture	Negative	Negative	Negative	Mixed	Mixed	Mixed	Mixed
Water, sanitation, hygiene	Negative	Negative					Negative
Urban and Municipal sector	Negative	Negative	Negative	Negative	Negative	Negative	Negative
Ecosystems	Negative		Negative		Negative	Negative	Negative

The Climate Change Report (IPCC, 2021) indicates that the effects summarized in Table 2.5 are expected to intensify. In other words, climate warming will drive extreme hydrometeorological events to occur more often and with greater severity. However, this increment will not happen smoothly; it will be modulated by large-scale ocean–atmosphere linkages. Teleconnections, therefore, become a critical aspect through which to interpret future risk. Tracing how their strength, timing and spatial reach evolve under greenhouse forcing is essential if we are to anticipate where, when and how climate change will most disrupt water resources.

2.4. Analytical Approaches to Detect Teleconnections

While teleconnection analysis is widely used in climate–hydrology interaction analysis, there is no single explicit protocol. The operational complexity, involving choices of variables, metrics, analytical frameworks, and the handling of nonstationary and nonlinear behaviour, demands a structured workflow. Based on the approach of Magnini et al. (2024), a typical teleconnection approach can be broken down into the following steps:

(i) Definition: Define the variables, indices, metrics, and temporal windows for both climate drivers (e.g., Niño 3.4/ONI) and hydrologic targets (e.g., streamflow, precipitation, soil moisture). In this step, the spatial domain or region of analysis is typically established based on prior literature or research objectives. However, this definition should remain flexible, as the spatial extent may need to be redefined if subsequent analyses reveal new teleconnection patterns or if the study scope changes.

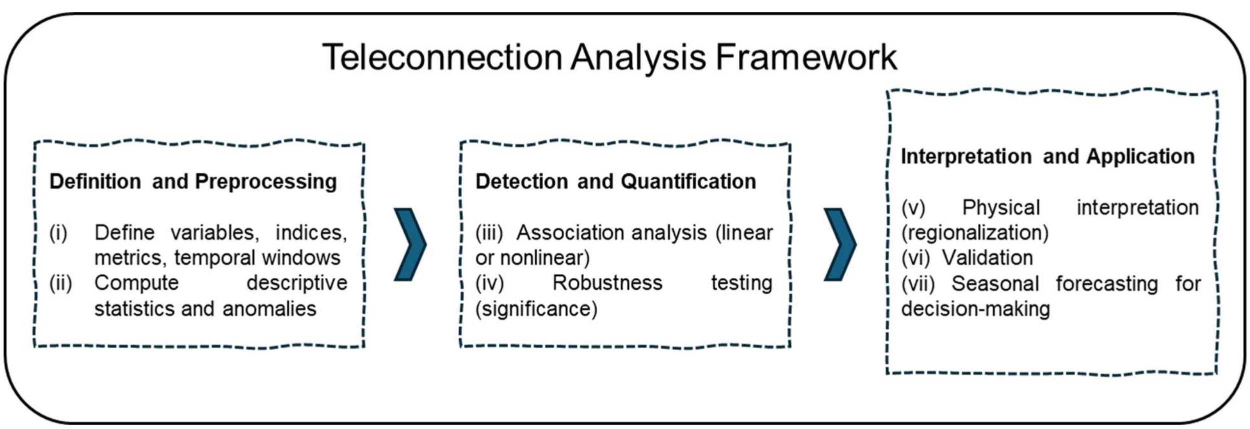

Figure 2.6 General Teleconnection Analysis Framework.

(ii) Computation: Compute basic descriptive statistics and create anomaly frameworks to isolate relevant signals. Develop frameworks by removing seasonal cycles or long-term means to isolate signals of interest from background noise. This step ensures that the extracted variability reflects clear climate–hydrology interactions rather than spurious seasonality.

(iii) Exploratory Analysis: Conduct an exploratory analysis to identify suitable linear or nonlinear methods for detecting associations. This involves statistical examination of the data to spot relevant signals, trends, changepoints, or spatial and temporal variations that may inform the choice of analytical method. It also includes assessing the consistency of associations across different periods and scales, as well as identifying the presence of nonlinear or nonstationary behaviours that could impact subsequent interpretation. This stage aims to establish a solid foundation for the formal analysis, ensuring that the selected techniques align with the nature and complexity of the teleconnections under study.

(iv) Robustness Testing: Assess the stability of the results by varying window sensitivity, using different metrics, and evaluating field significance. This involves changing temporal windows, adjusting spatial boundaries, and applying alternative formulations to ensure that the observed patterns are independent and not modes of another pattern. It also includes measuring the consistency of results across various sampling periods and datasets and confirming their statistical robustness through field significance tests. This stage ensures that the identified relationships hold under different analytical conditions, enhancing confidence that the detected teleconnections are real climatic–hydrological linkages rather than coincidental correlations.

(v) Physical Interpretation: Analyze the results physically at regional scales, ensuring consistency with known mechanisms. Convert the statistical findings into physically meaningful insights at these scales. This involves connecting the identified teleconnection patterns to established circulation dynamics, ensuring that the relationships are physically coherent and aligned with known climate–hydrology interactions. At this stage, initial tangible results often appear, such as spatial maps of correlation, regions of influence in the ocean or inland and plots of temporal evolution that match specific climatic phases. These early outputs act as a link between statistical detection and process-based understanding, laying the groundwork for more focused hydrological assessments or predictive applications.

(vi) Validation: Validate the findings with independent data to ensure reliability.

(vii) Seasonal Forecasting: Build probabilistic forecasts by driving hydrological models with climate predictions. This final step leverages established (e.g. ENSO) forecast skill to translate teleconnections into actionable water-management guidance.

In this section, we describe established linear and nonlinear methods for detecting and quantifying climate–hydrology associations. We also outline their respective advantages and limitations, emphasizing how these approaches can be applied to real-world hydroclimatic contexts to improve understanding and predictive capabilities. Due to the nonlinear and nonstationary nature of teleconnections, the choice of analytical method is critical for accurately capturing their dynamics. Some approaches are designed to detect proportional relationships, while others focus on changes in intensity, spatial extent, or even the sign of the relationship over time. The linear and nonlinear approaches commonly used in teleconnection studies are described below (see Figure 2.7).

Many analytical methods used to study teleconnections share a common theoretical basis in multivariate projection techniques. Methods such as Principal Component Analysis/Empirical Orthogonal Functions (PCA/EOF), Canonical Correlation Analysis (CCA), Rotated Principal Component Analysis (RPCA), and Nonlinear Principal Component Analysis (NLPCA) all work by transforming a set of correlated variables into a smaller, more manageable set of components. This process allows them to extract the dominant spatial and temporal patterns from the data, with each method offering specific modifications to enhance flexibility or capture nonlinear structures.

Similarly, methods based on wavelet analysis, like Cross Wavelet Transform (XWT) and Wavelet Coherence (WTC), are grounded in a shared framework. They decompose time series into time–frequency space to identify co-variability between them. Their primary differences lie in how they normalize the data, their interpretive focus (common power versus coherence), and their robustness in assessing the strength and phase of the relationships.

2.4.1. Linear Approaches

Linear approaches form the foundation of many teleconnection analyses, primarily because of their simplicity, interpretability, and long-standing use in climate and hydrological research. These methods assume that the relationship between variables remains proportional and temporally consistent, allowing changes in one variable to be explained by constant coefficients in another. While this assumption often overlooks the nonlinear and nonstationary behaviours described in Section 2.4, linear techniques remain valuable for identifying first-order associations, screening potential predictors, and establishing a baseline for comparison with more complex methods.

2.4.1.1. Simple Correlation

Correlation analysis is a straightforward statistical tool for identifying teleconnections, as it quantifies the strength and direction of the linear association between two variables. In climate–

hydrology studies, it is frequently used to assess the joint variability between large-scale climate indices and hydrological variables such as precipitation. Despite its simplicity and ease of interpretation, correlation analysis has notable limitations. A significant drawback is its inability to distinguish direct from indirect relationships, primarily when spatial autocorrelation or overlapping climate influences exist. Nigam and Baxter (2015) showed that relying solely on correlation failed to capture the full extent of ENSO's influence on extratropical teleconnection patterns due to confounding variability from other climate drivers.

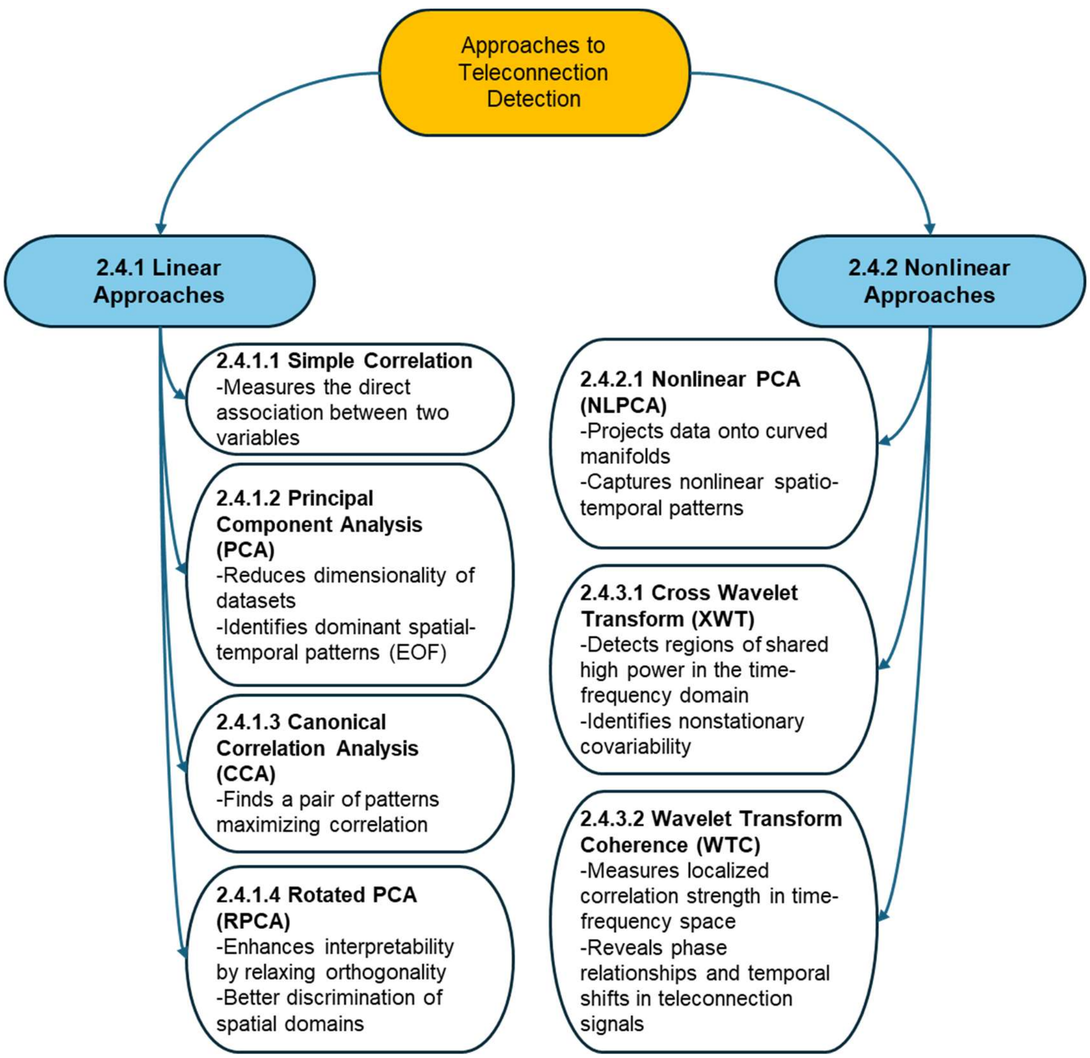

Figure 2.7 Analytical Approaches to Detect Teleconnections.

Furthermore, correlation assumes stationarity, which can misrepresent relationships that vary in strength or sign over time.

Nevertheless, correlation analysis remains a valuable first step in teleconnection studies, particularly for the preliminary screening of potential predictors before applying more sophisticated approaches. Typically, correlation analysis in teleconnection studies employs either the Pearson or Spearman coefficient, with some variations, such as partial correlation, in which time is treated as a controlling variable to account for the influence of long-term trends or shared temporal variability between the series. For instance, Djibo et al. (2015) successfully used simple correlation to identify candidate climate predictors for rainfall variability in the Sahel. Similarly, Jong et al. (2016) examined the relationship between the Niño 3.4 index and California precipitation using seasonal correlations.

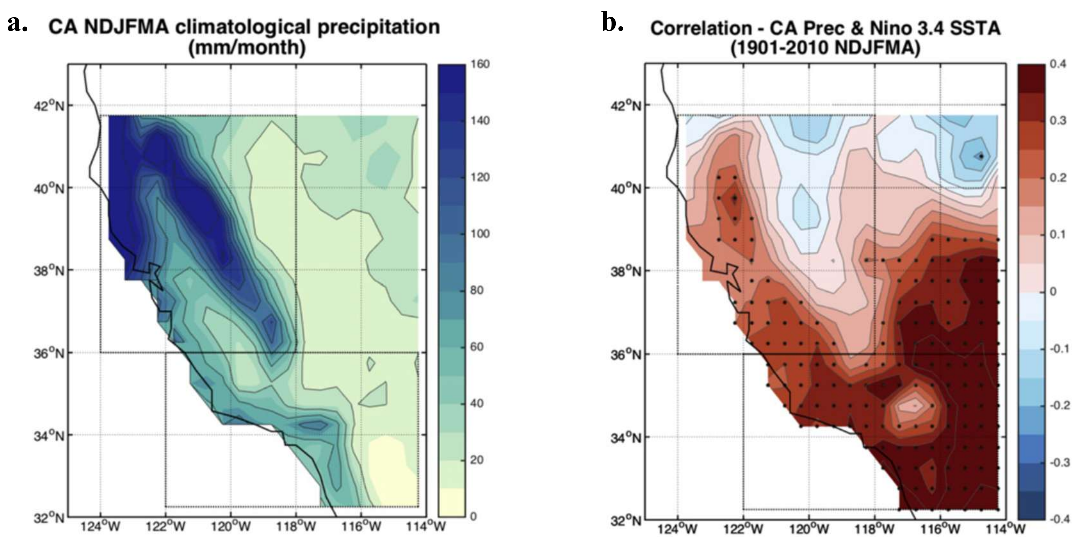

Figure 2.8 California linear regionalization based on Niño 3.4, (a) Precipitation distribution for November-December-January-February-March-April, (b) Correlation between Precipitation and Niño3.4 for those months (Jong et al., 2016).

Their analysis revealed strong, statistically significant correlations in southern California during intense El Niño winters, while northern California showed weaker or even opposite-signed correlations. A limitation of their spatial correlation maps, however, was the division of California into two main latitudinal zones (north and south of about 36° N), which did not capture more detailed intra-regional variability (see Figure 2.8). This indicates that although simple correlation can identify broad-scale patterns, it may miss finer-scale heterogeneity that is important for hydrological applications and physical understanding, like forecasting.

2.4.1.2. Principal Component Analysis (PCA)

Principal Component Analysis (PCA) is frequently used in hydroclimatic studies due to its ability to reduce dimensionality and reveal dominant patterns of variability (Jackson, 2005). This method transforms correlated variables into a new set of orthogonal components that concentrate most of the variance in the first few axes. PCA produces spatial patterns (eigenvectors or loading patterns) and associated time series that describe how variability is distributed across space and how it evolves over time. Although these patterns are mathematically orthogonal, this does not imply physical independence between the underlying processes.

In this context, PCA requires the preprocessing of climate and hydrological datasets. Once the data are preprocessed, a covariance or correlation matrix is constructed to obtain either absolute variability or standardized anomalies. The choice depends on the scope of the analysis: the covariance matrix measures the linear relationship between two variables in their original magnitudes, whereas the correlation matrix measures the linear relationship after normalizing the data, enabling comparisons without scale effects. A key limitation of this methodology is that it cannot be applied with missing data, since the computation of the covariance or correlation matrix requires complete datasets. Incomplete records, common in most hydrological variables, must be excluded, reducing spatial coverage and potentially biasing the results. This introduces assumptions that can affect the physical meaning of the derived EOF patterns.

The method decomposes the matrix into its eigenvalues and eigenvectors. The eigenvalues represent the fraction of the total variance explained by each principal component, while the eigenvectors provide spatial loading patterns that indicate the contribution of each location or variable to a mode of variability. The temporal evolution of each mode is captured by the associated principal component score, describing how the spatial pattern fluctuates over time. In teleconnection studies, these PC time series are often compared with known climate indices to evaluate statistical relationships and identify climate-driven modes of hydrological variability.

For example, Lana et al. (1995) applied PCA to data from 99 rain gauges in Catalonia, Spain, to identify patterns of rainfall variability. Another example was presented by El Alaoui El Fels et al. (2020), who used precipitation data from the Tensift Basin, Morocco, to delineate three homogeneous regions. Figure 2.9 shows a schematic output from their PCA analysis. Panel (a) depicts the correlation circle for the variables, where each arrow represents a monthly precipitation variable and geographic descriptor (longitude, latitude, altitude). The orientation of the arrows reflects the direction of maximum correlation with the principal components, while their length indicates the strength of the relationship. Panel (b) displays the projection of individual precipitation stations onto the same component space, where stations cluster according to similarities in their precipitation regimes and geographic attributes. Although the results reveal consistent clustering among the three regions, this analysis was conducted solely between stations and precipitation variability over time, rather than in relation to climate forcings.

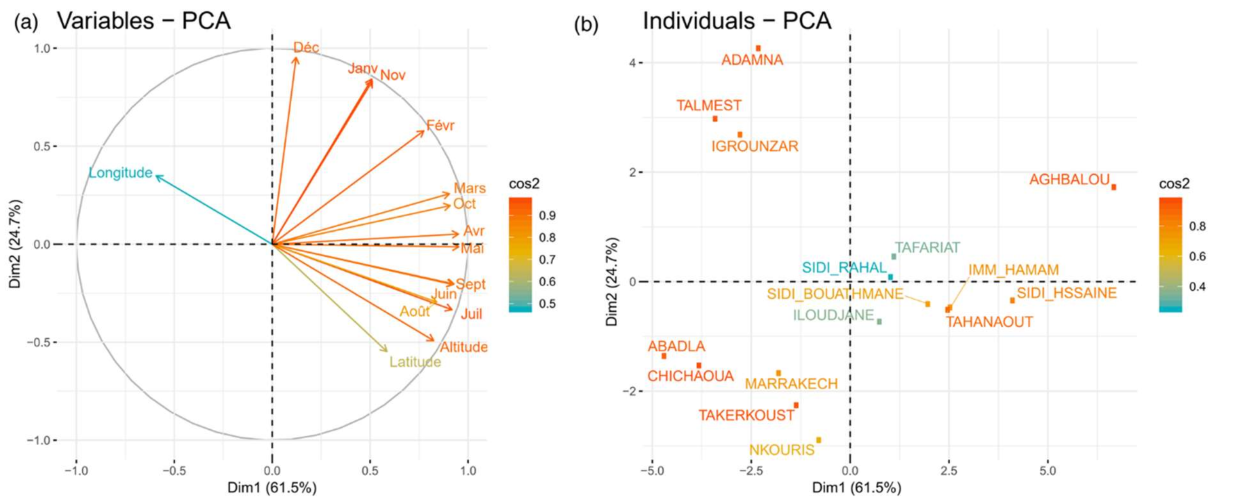

Figure 2.9 Principal component analysis of (a) variables during the year and (b) station-based rainfall time series (El Adloui El Fels et al., 2020).

On the other hand, L'Heureux et al. (2013) applied PCA to decompose monthly sea surface temperature (SST) variability in the tropical Pacific during 1950–2010, using three datasets (HadISST1, ERSST.v3b, and OISST.v2) to ensure robustness. This decomposition allowed them to isolate dominant spatial patterns and their associated time series, identifying the primary modes of variability and assessing the role of long-term linear trends in shaping these modes.

The results showed that a significant portion of the multidecadal trends was concentrated in the first two principal components. The first mode (PC1) represented the canonical El Niño–Southern Oscillation (ENSO) pattern, while the second mode (PC2) contained a mixture of ENSO-related variability and a long-term trend signal. Figure 2.10 illustrates these first three modes, with PC1 capturing the canonical ENSO, PC2 reflecting trend–ENSO mixed variability, and PC3 associated with the ENSO Modoki pattern. Without detrending the data, PC3 exhibits a temporal behaviour that closely follows the variance structure influenced by the underlying trend, suggesting that its detection depends heavily on the inclusion of trend-related variance. This demonstrates that detrending is not a neutral step, removing trends can substantially alter the detection and physical interpretation of climate modes. While PCA is effective at extracting dominant linear patterns, it can mix signals of different physical origins if preprocessing decisions, such as detrending, are not carefully considered.

2.4.1.3. Canonical Correlation Analysis (CCA)

Principal Component Analysis (PCA) works by identifying linear combinations of variables that maximize variance within a dataset. The aim is to reduce the number of variables by combining them into new variables (principal components) that retain as much of the original variability as possible, thereby summarizing a large set of variables into a smaller set. In contrast, Canonical Correlation Analysis (CCA) focuses on two distinct datasets, seeking linear combinations that maximize their mutual correlation. CCA operates with two separate datasets measured over the same observations.

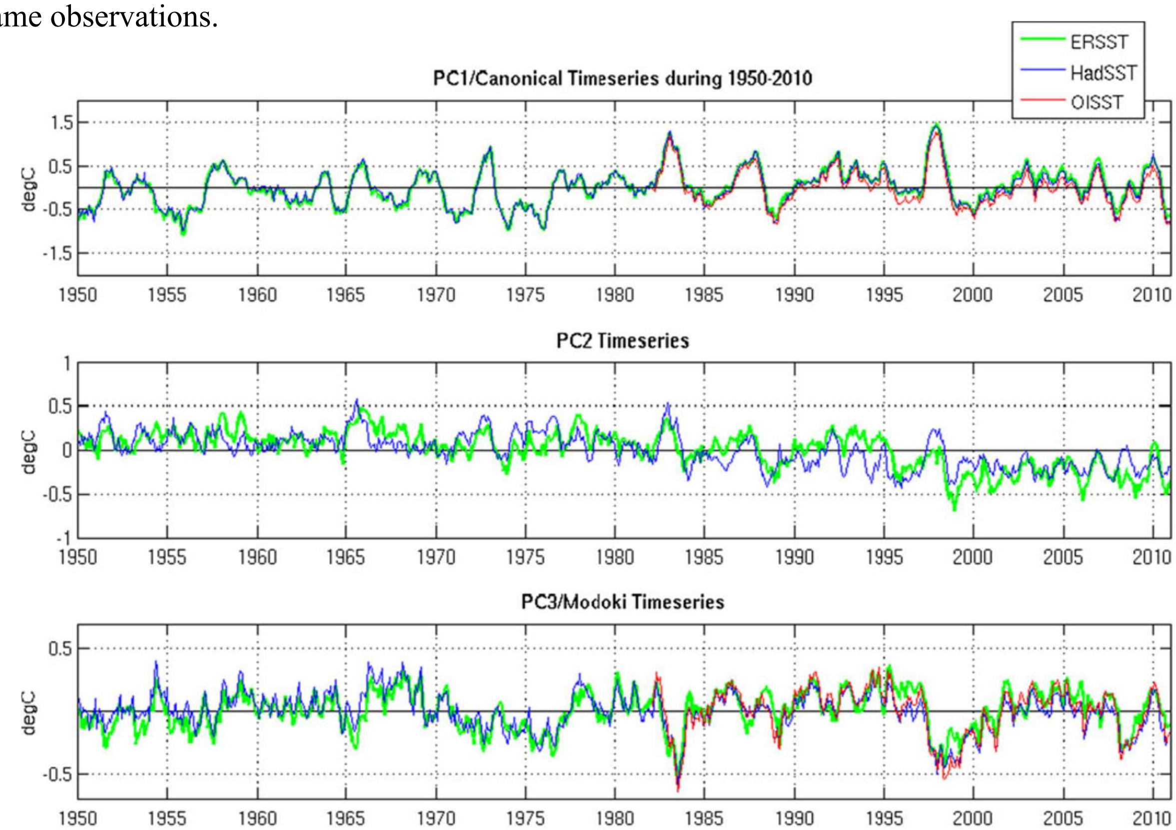

Figure 2.10 California linear regionalization based on Niño 3.4. (a) PC1 Time series compared for ERSST, HadSST and OISST (b) PC2 and (c) PC3 (L'Heureux et al., 2013).

For example, one dataset contains climate variables and another contains hydrological variables. Its goal is to find linear combinations of the variables in the first dataset and in the second dataset that are as highly correlated with each other. This makes it possible to identify which combination of variables in one dataset is most strongly linked to a particular combination of variables in the other, revealing cross-domain relationships that traditional PCA cannot detect.

Niranjan Kumar and Ouarda (2014) applied CCA to find the influence of global sea surface temperature (SST) patterns, particularly those in the equatorial Pacific, on winter precipitation variability over the United Arab Emirates (UAE) during 1981–2011. Their analysis revealed that the leading canonical mode captured a strong ENSO teleconnection (see Figure 2.11a,c), while a second mode in 2.11b,d linked precipitation variability to storm tracks over the eastern Arabian Peninsula. The authors recognized a changepoint around 1999 in the Pacific Decadal Oscillation (PDO) and ENSO, which coincided with a shift toward a prolonged below-normal rainfall regime in the UAE. This demonstrates a limitation of CCA, but its performance diminishes when the underlying relationships are nonstationary or nonlinear.

This case study illustrates the advantages of CCA, such as the extraction of physically interpretable coupled modes that were more directly linked to teleconnection mechanisms. These modes revealed meaningful cross-field linkages between oceanic variability and regional precipitation.

2.4.1.4. Rotated Principal Component Analysis (RPCA)

Another variant of PCA is the Rotated Principal Component Analysis (RPCA), which replaces the orthogonality of the components with a rotation applied after the initial extraction of the principal components. This rotation, using methods such as varimax or promax, is essentially a change of basis that redistributes the explained variance into fewer components, yielding more localized and physically interpretable spatial patterns. This approach produces modes that are easier to associate with physical processes compared to those from unrotated PCA.

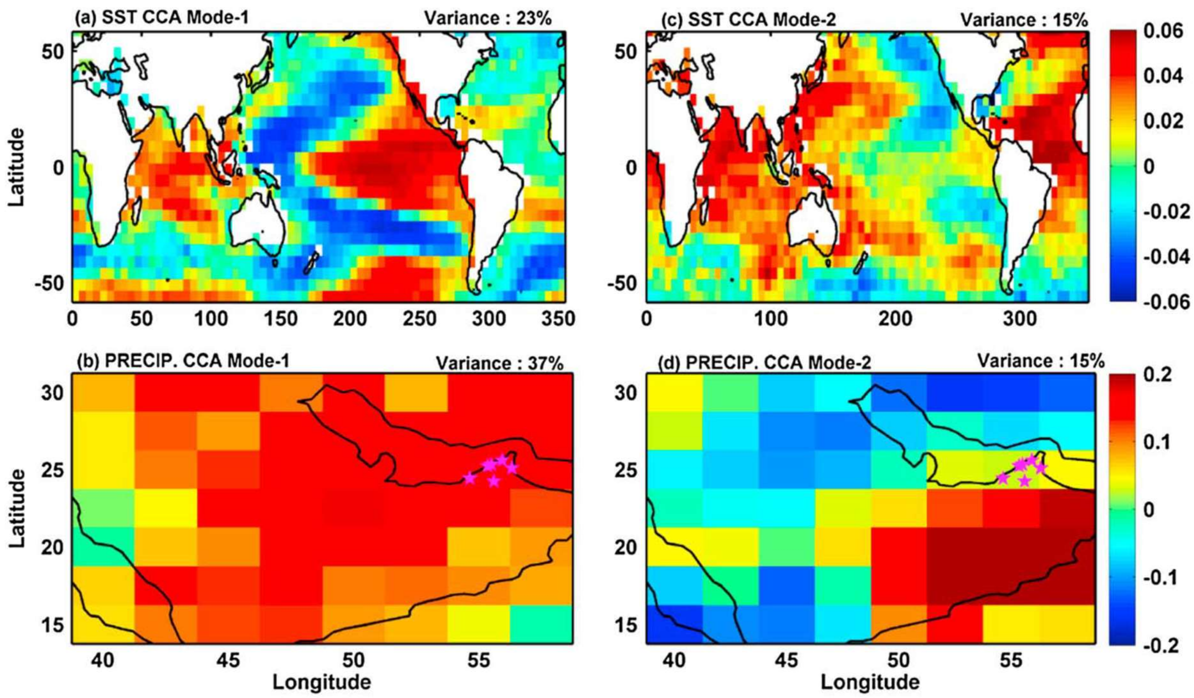

Figure 2.11 SST CCA decomposition for UAE. (a-b) Decomposition of SST CCA Mode 1 and 2, (c-d) Decomposition for Precipitation in the study area Mode 1 and 2 (Niranjan Kumar and Ouarda, 2014).

Table 2.6 Congruence coefficient between the RPCA loadings and the correlation vector that indexes the highest loading magnitude on that PC (Adapted Ibebuchi, 2023).

Region	Congruence Coefficient
R1	0.94
R2	0.9
R3	0.93
R4	0.96
R5	0.93
R6	0.9

Table 2.7 Correlation coefficients between regionalized rainfall time series (averaged over the classified homogeneous regions) and climatic modes (including average global sea surface temperature (Adapted Ibebuchi, 2023).

Region	Nino 3.4	IOD	SAM	SIOD	Global SST
R1	-0.32	-	0.33	0.25	0.25
R2	-	-	-		-0.44
R3		-	0.27	0.26	0.239
R4	-0.49	-	-	0.28	-
R5	-0.36	-	-	0.2	-0.26
R6	-	0.47	0.46	-	0.62

In this way, Ibebuchi et al. (2023) regionalized southern Africa for austral summer (November–March) precipitation anomalies. The analysis classified six homogeneous precipitation regions, each with intermittent precipitation variability. The results also revealed land–ocean correlations in different patterns, such as the Southern Annular Mode (SAM) and the El Niño–Southern Oscillation (ENSO). Above-average Niño 3.4 index values (El Niño) correlated negatively with precipitation over large parts of southern Africa. In contrast, the positive phase of SAM correlated positively with precipitation in subtropical and western equatorial regions. The robustness of these patterns was confirmed through comparison with ERA5 reanalysis and GPCP merged satellite–gauge datasets, which reproduced the main RPCA modes despite some spatial biases.

Although RPCA application in austral summer rainfall regionalization over southern Africa evidenced high congruence coefficients (see Table 2.6), the spatial coherence does not translate into a homogeneous climatic response to large-scale forcings (see Table 2.7). In several regions, correlations with modes such as ENSO, SAM, or global SST are weak or inconsistent. This suggests that while RPCA is strong at grouping series with similar patterns, it does not guarantee that the resulting regions maintain a uniform linkage with the climatic patterns modulating them.

This mismatch may be due to the emphasis on maximizing linear spatial coherence, without optimally capturing the nonlinear and nonstationary complexity of climate–precipitation teleconnections.

2.4.2. Nonlinear Approaches

Nonlinear methods can be broadly divided into two categories. The first includes adapted approaches such as Nonlinear Principal Component Analysis (NLPCA), a nonlinear extension of PCA that does not capture the nonstationarity inherent in time series. The second involves wavelet-based analysis, which is a signal-processing technique that breaks down a time series into the time–frequency domain. This allows for the simultaneous detection of variations in both time and scale.

2.4.2.1. Nonlinear PCA (NLPCA)

Standard Principal Component Analysis (PCA) assumes orthogonal linear projections to identify dominant modes of variability in time series relationships, as discussed in section 2.4.1.2. However, Nonlinear Principal Component Analysis (NLPCA) switch this approach by projecting the data onto curved surfaces, allowing it to detect more complex spatiotemporal patterns. This is achieved through a multi-layer neural network arranged in an auto-associative topology (Hsieh, 2001; Scholz, 2012). By training the network to reproduce the original signal, NLPCA learns nonlinear transformations that maximize variance while preserving the inherent geometry of the data. As a result, it can uncover patterns that linear PCA would miss, particularly when nonlinear dynamics govern the relationships. Nevertheless, despite this advantage, NLPCA assumes statistical stationarity, becoming sensitive to training parameters and overfitting factors. Hsieh (2001) compared PCA and NLPCA for monthly sea surface temperature data in the Pacific from 1950 to 1999, finding that NLPCA performed well for capturing nonlinear patterns. Yet, it is cautioned that NLPCA is less effective for short or noisy records.

An illustrative case is provided by Canchala et al. (2020), who employed NLPCA to delineate homogeneous regions of rainfall variability in Colombia. They identified teleconnection linkages with large-scale climate patterns using Pearson's correlation and Wavelet Transform analysis. As discussed in Section 2.4, there is no universally established methodology for teleconnection analysis, mainly due to the inherent complexity and nonlinearity of these relationships. In this case, the application of NLPCA by Canchala et al. (2020) identified two dominant modes of variability. The Andean region explained 75% of the variance, and the Pacific region 48%. These results demonstrate the method's strength in delineating distinct regions based on rainfall pattern behaviour. Its performance was notable given the analysis of 33 years of records with less than 10% missing data. However, because NLPCA does not explicitly account for nonstationarity, complementary methods such as wavelets were used for teleconnection analysis.

2.4.3. Wavelet-Based Analysis

Wavelet analysis decomposes a time series into the time–frequency domain, detecting variations in scale and time. Fourier transforms are a similar tool, but they assume fixed relationships and provide only a global frequency spectrum. In contrast, wavelets use functions that can be shifted and scaled, making them ideal for identifying nonstationary features. For teleconnection analysis, it can be helpful based on the timing, duration, and frequency ranges in which two variables share common variability. However, the effectiveness of this approach depends on the choice of a mother wavelet, the length and completeness of the record, and careful interpretation of time–frequency patterns.

Torrence and Compo (1998) established a methodology for applying the Continuous Wavelet Transform (CWT), applicable to Cross-Wavelet Transform (XWT) and Wavelet Transform Coherence (WTC), described as follows:

a) **Data preparation**: handling missing values and normalizing to avoid amplitude bias.
b) **Selection of the mother wavelet**: Morlet is most common in climatology for its balance between time and frequency resolution.
c) **Application of Transform**: convolving the time series with scaled and translated wavelet functions to obtain the time–frequency spectrum.
d) **Statistical significance testing**: comparing wavelet power to white/red noise and identifying the cone of influence (COI) to avoid edge effects.
e) **Interpretation**: linking high-energy regions to climatic or hydrological events.

Regarding the classification of wavelet-based teleconnection analysis methods, the Continuous Wavelet Transform (CWT) emerges as an initial method. It allows decomposing a time series in the time–frequency domain and revealing how its variability changes over time. However, this analysis is univariate, so its effectiveness is limited when comparing two time series. In this context, Cross Wavelet Transform (XWT) and Wavelet Transform Coherence (WTC) are bivariate options. The XWT indicates where common variability exists (Grinsted et al., 2004; Maraun and Kurths, 2004), while the WTC indicates how strong the relationship is (Torrence and Webster, 1999). Their joint application offers a complementary and more complete view of how teleconnections evolve over time and in different frequency bands.

2.4.3.1. Cross Wavelet Transform (XWT)

The Cross Wavelet Transform (XWT) is based on the Continuous Wavelet Transform (CWT) by applying it to two time series simultaneously. As stated by Torrence and Compo (1998), the procedure begins by computing the CWT for each series using a chosen mother wavelet. The Morlet function is suitable for detecting nonstationary behaviour across different scales, from months to years. Its complex form enables phase analysis and identification of lead–lag relationships. However, it may perform less effectively for abrupt events, with its spectral power being susceptible to normalization effects (Maraun and Kurths, 2004). The CWT of each series is obtained by convolving the original signal with scaled and shifted versions of the mother wavelet, producing two outputs for each time–scale location: the magnitude, which indicates the intensity or local variability in the data, and the phase, which signals the timing of oscillations. The XWT is then computed by multiplying the CWT of one series by the complex conjugate of the CWT of the other, yielding the cross-wavelet power and the relative phase between them. To confirm that the detected patterns are not due to random chance, the cross-power is compared with noise simulations, retaining only those values above the 95% confidence level. A key step involves the cone of influence (COI), used to mask edge effects caused by the finite length of the series that can distort the outcomes. The COI has been criticized as a weakness of wavelet analysis because it can exclude low-frequency events outside its boundaries, a concern especially relevant for shorter records. Torrence and Compo (1998) caution that beyond the COI, wavelet power may be artificially diminished due to zero-padding effects.

As an example, Ojara et al. (2022) applied the Cross Wavelet Transform (XWT) and Wavelet Transform Coherence (WTC) to investigate the relationship between ENSO and seasonal precipitation across East Africa. The study delineated homogeneous rainfall regions previously through EOFs, Pearson correlation and clustering described in Indeje et al. (2000) and Ongoma et al. (2018). Then, the XWT was computed between ENSO and the rainfall series for each subregion to detect the influence of different climatic patterns. The analyzed records from 1960 to 2017 used the Morlet wavelet, capturing high- and low-frequency variability. The results highlighted significant power concentrated in the 2–8 year band, consistent with ENSO-driven variability. However, beyond quantifying the time–frequency co-variability between ENSO and precipitation for each subregion, the XWT analysis does not inherently perform spatial regionalization or provide predictive capability; it simply relates the temporal oscillatory components of the paired series.

2.4.3.2. Wavelet Transform Coherence (WTC)

The Wavelet Transform Coherence (WTC) is a robust method for evaluating the intensity of covariance between two time series. Unlike the Cross-Wavelet Transform (XWT), which highlights regions where both series exhibit high simultaneous variability, WTC emphasizes the consistency of the phase relationship. This provides a more stable measure of the strength of association even when this shared variability is weak (Jevrejeva et al., 2003).

Yang et al. (2021) compared XWT and WTC to assess how climate indices influence precipitation anomalies in the Poyang Lake Basin (Figure 2.12). Panel (a) shows the observed precipitation anomalies, where alternating wet and dry phases highlight the variability every 2–4 years, consistent with the typical ENSO cycle. This recurrent behaviour of the precipitation anomaly signal provides a statistical basis for its analysis with wavelets, which are well-suited to handle nonstationary and nonlinear signals (Figure 2.12 b–c).

In both XWT and WTC, the resolution of long-period signals is limited by the record length. The vertical axis in Figure 2.12b–c shows cycle length in years. Short cycles, such as ENSO events of 2–4 years, repeat many times in the record. This makes their estimation reliable. Longer cycles, such as 8 or 16 years, occur only a few times. Most of these signals fall inside the shaded cone of influence (COI), where edge effects reduce statistical confidence (e.g., Figure 2.12c, 2010–2017). In XWT (Figure 2.12b), this appears as scattered or broken patches of high power. The signal is not consistently supported. In WTC, coherence may still look high in the same regions. However, this can be misleading because too few cycles exist to confirm persistence.

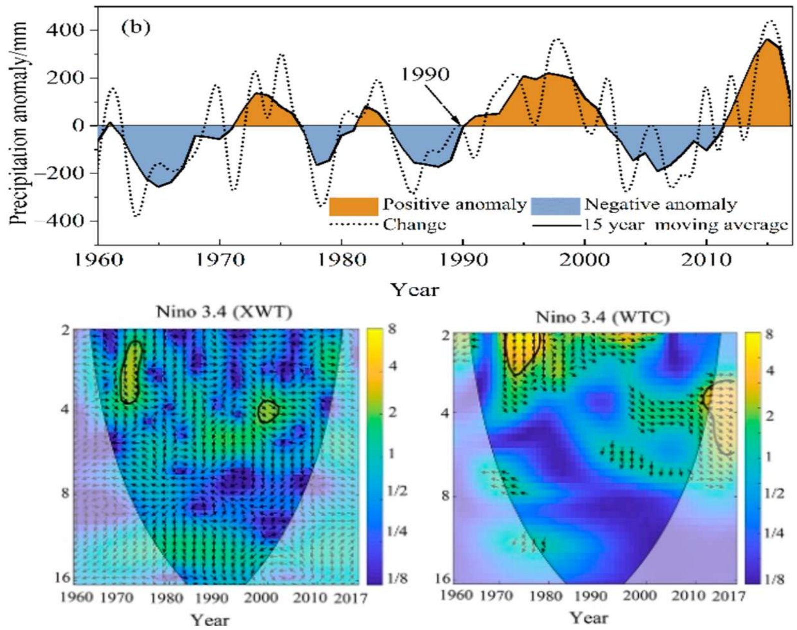

Figure 2.12 Wavelet-based analysis. (a) Precipitation anomaly time series (b) XWT frequency graph and (c) WTC frequency graph (Adapted Yang et al., 2021).

Although the comparative application of XWT and WTC demonstrates their value in uncovering time and frequency-domain associations between climate indices and hydroclimatic variables, it is important to recognize their inherent limitations. For instance, WTC has an advantage over XWT because it is designed to capture the consistency with which two variables move together. This allows it to identify persistent teleconnections even when shared variance is weak. However, both methods are an exploratory tool, revealing covariability but do not establish causality for the observed relationships. Therefore, their results should be regarded as preliminary indications of relationships between time series, constrained by limitations such as record length, interpretability, and the lack of forecasting capability.

2.5. Literature Review Summary

The literature reviewed shows that climate–hydrology teleconnections are highly complex. They are shaped by multiple climate modes, spatial heterogeneity, and nonstationary behaviour across scales. A wide range of analytical tools has been applied, from simple linear correlations and PCA to advanced methods such as XWT, WTC, and nonlinear dimensionality reduction (Table 2.8). Each methodology provides partial insights. Some identify regional patterns, while others quantify links with large-scale drivers. Yet, none overcomes the inherent limitations, leaving important gaps in fully capturing the nonlinear and nonstationary nature of teleconnections.

1. Teleconnections are natural climate phenomena with variable periodicity that modulate the distribution of precipitation and hydrological extremes at the global scale. The El Niño–Southern Oscillation (ENSO) is the most documented example due to its recurrent impacts on droughts and floods across multiple regions (Ropelewski and Halpert, 1987; IPCC, 2021).
2. Climate change and anthropogenic pressures on watersheds intensify the impacts of teleconnections. Events such as floods, prolonged droughts, and wildfires increasingly occur outside the range of historical variability (Blöschl et al., 2019; Hsiang et al., 2017).
3. Teleconnection analyses rely on multiple climatic variables, including sea surface temperature (SST), sea-level pressure (SLP), and regional atmospheric circulation patterns. Depending on temporal and spatial resolution, these processes are often summarized into climate indices defined by specific geographic domains (Trenberth, 1997).
4. The methodologies used to study teleconnections typically focus on four main dimensions: (i) defining the relevant variables, (ii) quantifying statistical associations, (iii) regionalizing areas with similar responses, and (iv) developing predictive models (Arias et al., 2021).

5. Analyses can be linear or nonlinear, and due to the complexity of the phenomena, it is common to combine multiple statistical and spectral tools to achieve more robust interpretations (Maraun and Kurths, 2004).
6. Linear methods remain the most widely applied, particularly simple correlations and Principal Component Analysis (PCA), which are used for both association and regionalization (Compagnucci and Richman, 2008). However, the assumption of linearity fails to adequately capture nonstationary or intermittent processes, limiting the robustness of long-term projections (Slater et al., 2021).
7. Nonlinear methods, such as the Wavelet Transform, provide greater ability to capture the inherent nonstationarity of teleconnections. Nevertheless, they are difficult to interpret and subject to constraints such as the cone of influence (COI), the record length, and the choice of the mother wavelet. Moreover, these approaches remain exploratory and associative, lacking direct capacity for regionalization or prediction (Torrence and Compo, 1998; Grinsted et al., 2004).

Table 2.8 Summary of Teleconnection frameworks in literature.

Category	Methodology	Strengths	Limitations
Linear approaches	Correlation (Pearson, Spearman)	Simple, widely used, captures direct linear links	Fails under nonstationarity, cannot detect nonlinearity.
	Principal Component Analysis (PCA) / EOFs	Reduces dimensionality, identifies dominant patterns	Linear decomposition only, may mix signals, stationary assumption.
Nonlinear approaches	Nonlinear PCA (NLPCA)	Detects nonlinear spatial structures	Complex interpretation, computationally demanding.
	Wavelet Transform (CWT, XWT, WTC)	Captures nonstationarity, multi-scale patterns	Sensitive to record length, edge effects, exploratory not causal.

Chapter 3 Methodology

The methodological limitations highlighted in the literature underscore the need for analytical frameworks capable of capturing the nonlinear and nonstationary nature of climate–hydrology teleconnections. Traditional linear approaches, such as correlation analysis or PCA, remain useful for identifying associations but are inherently limited in their ability to detect structural regime shifts. More advanced nonlinear tools, such as Wavelet Transform Coherence (WTC), offer improvements by accommodating time-varying relationships; however, they remain sensitive to choices such as the mother wavelet, edge effects, and record length, which can bias interpretation. These constraints reinforce the need for a robust methodological framework that not only detects teleconnection signals but also supports regionalization and predictive applications under changing climate conditions.

A fundamental challenge in teleconnection analysis lies in distinguishing genuine structural changes from simple statistical noise. Transient irregularities or isolated extreme events can mimic structural shifts when assessed using standard trend or correlation-based methods, particularly in short hydroclimatic records. In this dissertation, nonstationarity is defined as a persistent and coherent modification of the mean, variance, or slope regime, supported by consistent evidence across segments rather than by individual anomalous points. The Bayesian changepoint framework is particularly advantageous in this respect: it evaluates the posterior probability of alternative segmentations and assigns high probability to breakpoints only when they substantially improve model evidence. This probabilistic treatment naturally mitigates false detections arising from noise, a known challenge in hydroclimatic time-series analysis.

Within this context, changes in segment-specific trends, typically viewed as a limitation in traditional methods, become a meaningful source of structural information. Changepoints mark reorganizations in the underlying dynamics of a time series, reflecting shifts in mean behavior, variance regimes, or directional tendencies. Building on this principle, the methodology introduced in this dissertation proposes a new similarity measure, Point–Slope Similarity (PS), which integrates changepoint timing with the sign and magnitude of segment-specific slopes to quantify structural resemblance between time series. In doing so, the PS framework allows the detection of nonlinear and nonstationary teleconnection behaviors that remain hidden to classical linear tools.

This chapter is organized around three fundamental components:

1. A detailed description of the Bayesian changepoint detection methodology developed by Seidou and Ouarda (2007), which forms the foundation for identifying structural shifts in hydroclimatic series.
2. The introduction and definition of the proposed Point–Slope Similarity (PS) measure, outlining its scope and application for teleconnection analysis.
3. The evaluation of its potential to delineate homogeneous regions based on shared structural behaviors across stations or climate indices.

As illustrated in Figure 3.1, this methodology fits into a broader framework where the progression moves from the identification of symptoms (extremes or anomalies) through data analysis, detection of changepoints, and the identification of drivers. This then allows attribution of observed changes to large-scale climate modes and supports management strategies under nonstationary conditions.

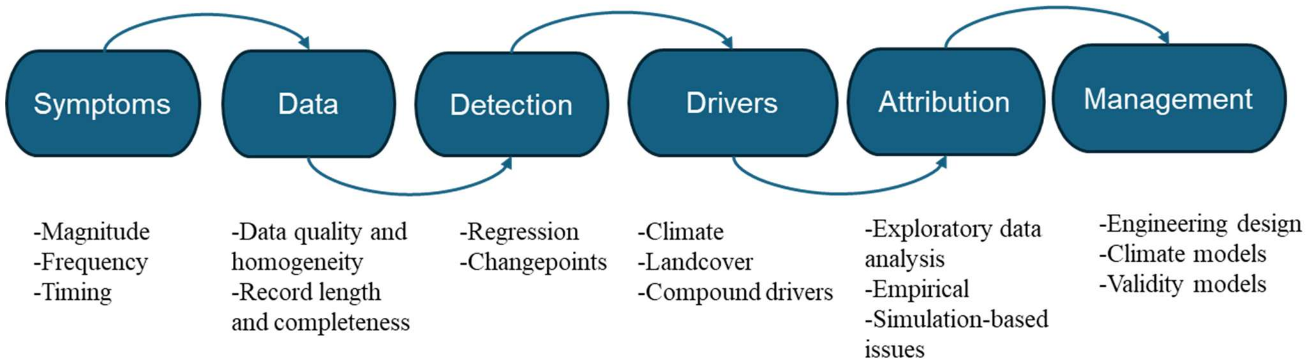

Figure 3.1 Flowchart followed by Changepoint Analysis (Adapted Slater et al., 2021).

3.1. Introduction to Changepoints

In hydrological and climatological studies, changepoints have often been treated as disturbances to be removed, for example when changes in instrumentation or station relocation introduced artificial discontinuities (Gallagher et al., 2013). However, recognizing nonstationarity through the detection of changepoints can reveal meaningful structural reorganizations in hydroclimatic processes, such as shifts in mean, variance, or slope, that provide valuable information for teleconnection analysis.

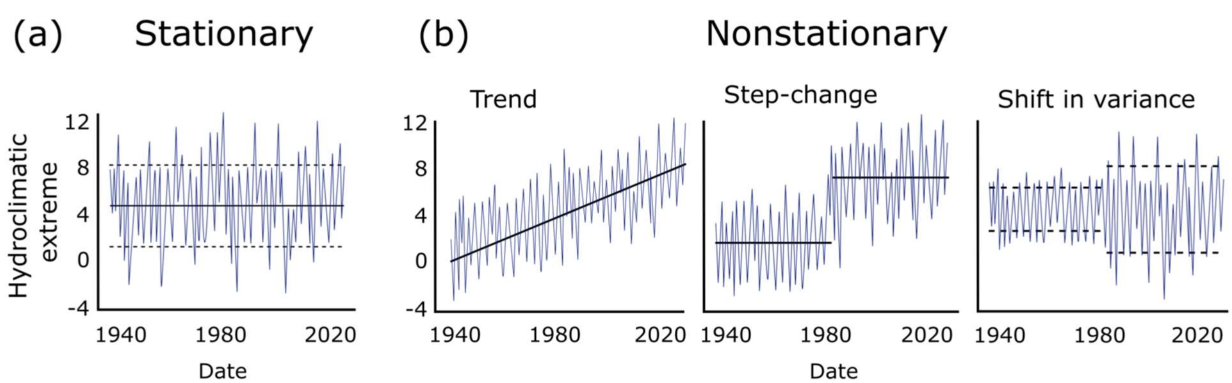

Figure 3.2 (a) Stationary and (b) Nonstationary trends in a typical Hydroclimate time series (Slater et al., 2021).

These structural changes may appear as gradual trends, abrupt regime shifts, or modifications in variance, reflecting hydroclimatic variability. Figure 3.2 illustrates a contrast between a stationary and a non-stationary time series, highlighting the differences among several types of changes. A stationary series with constant mean and variance fluctuates randomly around a stable threshold, as shown in Figure 3.2a. In contrast, panel (b) depicts nonstationary behavior in three forms: a long-term trend in the mean, an abrupt regime shift, and a variance change reflecting alterations in the amplitude of variability.

Capturing these patterns motivated the development of statistical tests for changepoint detection, such as Pettitt's test (Pettitt, 1979), the Buishand range test (Buishand, 1982), among others. These approaches aim to determine whether a change is statistically significant, but are limited to detecting a single changepoint and do not quantify the uncertainty associated with the estimation. Moreover, Easterling and Peterson (1995) emphasized that distinguishing discontinuities in time series requires assessing whether they stem from natural processes or from measurement system failures. Against this backdrop, Bayesian methodology emerged as a powerful alternative, allowing changepoints to be assigned probabilities rather than deterministic estimates. By segmenting a time series into homogeneous intervals, it becomes possible to characterize changes based on their statistical properties, integrate prior information, and obtain posterior distributions. Fearnhead (2006) proposed recursive algorithms based on the partition model of Barry and Hartigan (1992), enabling more efficient calculation of posterior probabilities and improving the performance of MCMC simulations, which are traditionally computationally expensive.

Nevertheless, although recursive methods represented a major step forward compared to standard MCMC, computational costs remained high for long records. To address this limitation, Seidou and Ouarda (2007) introduced three key contributions:

1. Technical improvement: they adopted Jeffreys' non-informative prior, ensuring that the analysis does not rely on subjective assumptions about the number or location of changes. Instead, changepoints are inferred directly from the information contained in the data.
2. Computational cost: while the method still requires MCMC simulations, its implementation allows for a more robust exploration of possible changepoint configurations, reducing the risk of biased solutions despite the elevated computational burden.
3. Physical reproducibility in hydrology: by avoiding strong assumptions in the priors, the detected changes are more likely to reflect genuine hydroclimatic processes rather than statistical artifacts or instrumental discontinuities.

These advances found immediate applications, ranging from the identification of changes in large-scale climate indices (Djibo et al., 2015; Naizghi et al., 2016) to linking ruptures in precipitation records with low-frequency oscillations such as ENSO (Ouarda et al., 2021). More recently, Morabbi et al. (2022) demonstrated the value of this approach for regionalization, comparing changepoint-based similarity with wavelet coherence.

Recent reflections highlight that changepoint analysis has become a cornerstone in the evolution of statistical hydrology, as it explicitly addresses nonstationarity and strengthens predictive frameworks (Volpi et al., 2024). In this sense, Bayesian approaches are particularly suitable, as they allow the incorporation of prior knowledge, probabilistic assessment, and adaptation to nonlinear and nonstationary datasets, where traditional methods often underperform (Scott and Berger, 2006; Rasmussen, 2001; Ruggieri, 2013).

3.1.1. Multiple Bayesian Changepoint Detection

Traditional changepoint algorithms such as AMOC, CUSUM, or PELT typically rely on fixed thresholds or penalized likelihood rules, which means they return a single optimal configuration of breakpoints. While these classic methods can be efficient, they do not explicitly measure the uncertainty in the number or exact placement of the changepoints. They can also be sensitive to noise, missing data, or if the data deviates from standard Gaussian assumptions (Fearnhead, 2006). In contrast, the Bayesian approach adopted here treats both the number and the position of the changepoints as random variables and computes their full posterior probability distribution. By utilizing specific product-partition models and dynamic-programming recursions, we can achieve exact or highly efficient Bayesian inference. This provides probabilistic evidence for many alternative segmentations of the data, rather than just a single, deterministic solution. This capability makes the method particularly attractive for hydroclimatic applications, where record length is often limited and nonstationarity can be subtle.

The methodology of Seidou and Ouarda (2007) expands Bayesian changepoint detection into a multiple regression framework, in which a time series is decomposed into homogeneous segments separated by changepoints. Within each segment, a fixed number of observations is assumed to share constant regression parameters, ensuring statistical homogeneity. This segmentation explicitly addresses nonstationarity, since regression parameters vary across each segment, and it accommodates nonlinearity, as the predictor-response relationship adopt different structural shapes over time. The starting point is the assumption that the dependent variable y_j at time j can be expressed as a linear function of d predictors x_{ij}, and a random error term:

$$y_j = \sum_{i=1}^{d} \theta_i \, x_{ij} + \varepsilon_j \qquad \varepsilon_j \sim \mathcal{N}(0, \sigma^2) \tag{3.1}$$

where θ_i denotes the regression coefficient associated with the i-th predictor in a segment, and σ^2 is the variance of the error term associated. A changepoint is defined as a time t at which either the regression coefficients or the variance shift to new values, indicating a structural change.

Detecting these shifts requires a probabilistic framework that can infer where and when such changes occur, rather than assuming them a priori. Within this perspective, Bayesian inference offers a coherent approach by combining observed data with prior assumptions. In a Bayesian framework, inference combines the likelihood and the prior. The likelihood indicates how probable the observed data are under specific values of the regression parameters, while the prior reflects the assumptions made before any data are observed. Their combination yields the posterior distribution, which represents the updated knowledge of the parameters once the information from the data has been incorporated. In this context, Fearnhead (2006) demonstrated that efficient computation can be achieved by recursively combining the likelihood of each segment with the prior, thereby enabling the evaluation of multiple possible segmentations. However, this recursive scheme is also sensitive to the choice of prior assumptions. To minimize the influence of external or subjective information, Seidou and Ouarda (2007) adopt Jeffreys' non-informative prior, which provides an invariant and assumption-free baseline, ensuring that inference is primarily driven by the data:

$$p(\theta, \sigma) \propto \sigma^{-d^*/2} \tag{3.2}$$

where d^* is the effective dimension for the parameter vector in each segment.

Jeffrey's priors provide an invariant, minimally informative baseline that does not favour specific parameter values or changepoint configurations, ensuring that inference is driven primarily by the information contained in the data. This choice is especially valuable in hydroclimatic applications, where deviations from normality, noise, and missing observations can otherwise bias classical likelihood-based changepoint procedures. While the present work does not modify or explore any aspects of prior selection or model configuration as proposed by Seidou and Ouarda, Chapter 7 discusses this avenue as a promising direction for methodological improvement and future refinement of the Bayesian changepoint component.

An important advantage of Bayesian inference is its ability to quantify uncertainty in both the number and the location of changepoints. Instead of providing deterministic estimates, the method assigns posterior probabilities to each candidate changepoint, which can be interpreted as confidence intervals. This probabilistic representation enhances interpretability by offering not only point estimates but also a measure of reliability associated with each detection. As discussed in Chapter 2, hydrological and climatic time series often suffer from limitations such as data gaps, intermittency, or short record lengths. Traditional methods tend to propagate these limitations into the results, whereas the Bayesian approach can still infer changepoints by computing the parameters from the available data and disregarding missing entries.

Nevertheless, short records reduce statistical evidence and may increase the risk of false detections. To mitigate this, Seidou and Ouarda (2007) introduce a minimum segment length constraint, which avoids attributing every minor fluctuation to a structural change and ensures that detected changepoints represent persistent and meaningful shifts. For each candidate segmentation, the algorithm evaluates the marginal likelihood of the data within each segment, and these likelihoods are then combined with the prior to generate posterior probabilities of alternative segmentations. The output of the algorithm is a set $E = \{S_k, k = 1, \ldots, M\}$ where each candidate segmentation S_k consists of a set of m_k changepoints $\{t_1^k, t_2^k, \ldots, t_{m_k}^k\}$. In Figure 3.3 is shown a changepoint detection using this methodology, where each candidate segmentation is associated with a posterior probability. Inference can proceed either by selecting the most likely segmentation or by identifying changepoints whose marginal posterior probability exceeds a predefined threshold α. The choice of α determines the balance between detecting more changes and avoiding false positives. The Algorithm 1 summarize the procedure of this methodology.

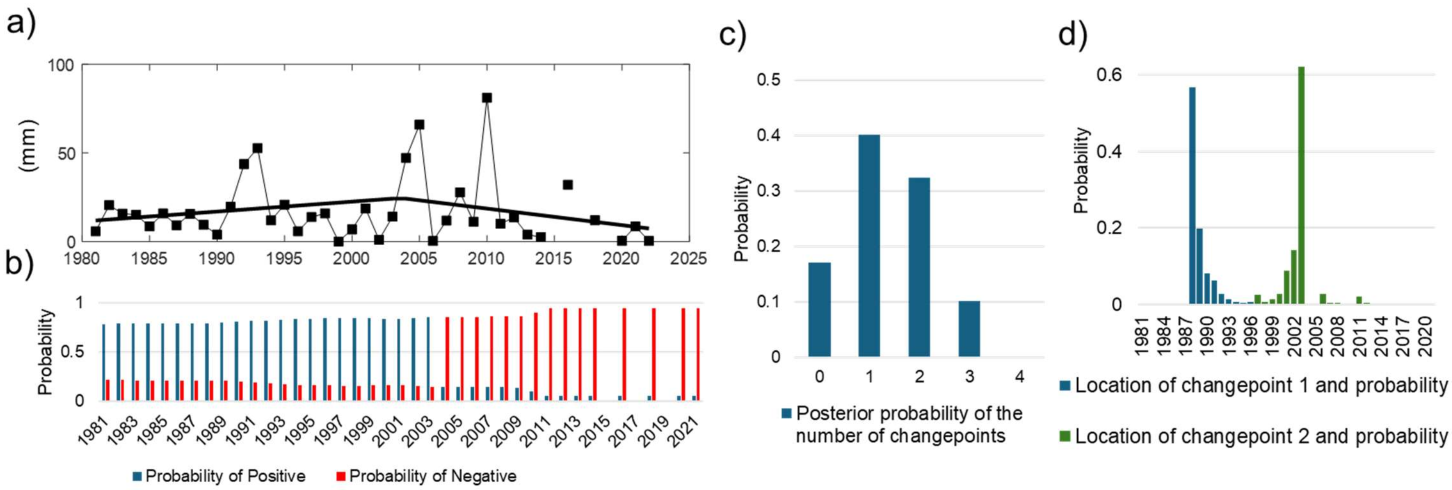

Figure 3.3 Results of Bayesian changepoint detection. (a) Time series with the black line showing the estimated trend and the most probable changepoint. (b) Sign of the most probable trend. (c) Posterior probability distribution of the number of detected changepoints.

Algorithm 1. Bayesian multiple changepoint detection (Seidou and Ouarda, 2007)

1. Define the regression model $y_j = \sum_{i=1}^{d} \theta_i \, x_{ij} + \varepsilon_j$.
2. Assign Jeffreys' non-informative prior $p(\theta, \sigma) \propto \sigma^{-d^*/2}$.
3. Specify a minimum segment length l_{min} to ensure stability.
4. Compute the marginal likelihood of each candidate segment.
5. Recursively evaluate posterior probabilities of possible segmentations using the Fearnhead (2006) dynamic scheme.
6. Construct the set $E = \{S_k\}$, where each S_k includes its changepoints and posterior probability.
7. Select the most probable segmentation or report changepoints with posterior probability exceeding α.

3.1.2. Slope Analysis

Changepoint detection identifies the timing of structural breaks, directly capturing nonstationary and nonlinear behavior. However, by incorporating slope analysis, each segment provides a physical interpretation, indicating whether the variable strengthens or weakens in response to external forcings across a set of inferences. In teleconnection studies, this distinction is crucial, as it allows a purely statistical detection process to be translated into the assumption of a direct climatic–hydrological impact (López-Parages and Rodríguez-Fonseca, 2012).

This additional layer of information has been highlighted in the literature as essential for understanding hydroclimatic variability. For example, during ENSO events, increases in sea surface temperature in the central Pacific during winter are associated with enhanced rainfall in Southern California (Ropelewski and Halpert, 1986; Dettinger et al., 1998) but reduced rainfall in Australia (Risbey et al., 2009). This illustrates that the goal is not only to detect the timing of regime shifts but also to evaluate how such regimes drive trends over time. Similarly, Hamed (2008) and Serinaldi and Kilsby (2015) emphasize that accounting for both the timing and the direction of change enhances the interpretation of nonstationary processes, particularly in systems influenced by climate variability and anthropogenic pressures. In this case, efter the identification of the changepoints $\{t_1^k, t_2^k, \dots, t_{m_k}^k\}$ using the Bayesian method, the time series t and the dependent variable y are segmented accordingly. Each segment k spans from one changepoint t_k to the next t_{k+1}. For every segment and each inference item in M, a linear regression model is applied to estimate the slope β_{1k} and the intercept β_{0k}. Following the algorithm of Slope analysis based on the changepoints detected is shown:

Algorithm 2. Slope analysis based on changepoints detected.

For each $m \in \{1,2,\dots,M\}$:

1. For $k = 1$ to $m_k + 1$

i. Define the dependent variable values for the k^{th} segment:

$$\mathbf{Y}_{\text{segment}_k} = \{y_j \mid t_{k-1} \leq j \leq t_k\}$$

where t_0 is the first point in the line and t_{m_k+1} is the last point in the line

ii. Set up the design matrix X_k, which includes the time points in the segment:

$$X_k = \begin{bmatrix} 1 & t_{k-1} \\ 1 & t_{k-1}+1 \\ \vdots & \vdots \\ 1 & t_{k-1}-1 \\ 1 & t_k \end{bmatrix}$$

iii. Estimate the coefficients $\boldsymbol{\beta}_k = [\beta_{0k}, \beta_{1k}]^T$, which represent the intercept and the slope of the linear trend, using the following formula:

$$\boldsymbol{\beta}_k = (X_k^T X_k)^{-1} X_k^T \mathbf{Y}_{\text{segment}_k}$$

Here, $\mathbf{Y}_{\text{segment}_k}$ represents the values of y in the segment between t_{k-1} and t_k. This method effectively partitions the data based on temporal changes, aiding in the analysis of trends and variations within each segment.

2. When no changepoint is detected $m_k = 0$:

i. The entire time series is treated as a single segment, i.e., t_0 is the first point, and t_{mk+1} is the last.

ii. The same regression procedure applies to estimate β_0 and β_1 for the entire dataset:

$$\boldsymbol{\beta} = (X^T X)^{-1} X^T \boldsymbol{Y}$$

where X is the design matrix for the full time series, and $\boldsymbol{Y}$ represents all the dependent variable values.

This approach is applied for every inference in M. However, since linear regression is applied between the points detected for each m, if no changepoint exists, the linear regression is fitted to the overall data of the time series. Figure 3.3b illustrates an example of slope analysis between changepoints, showing the probability of positive (blue bars) and negative (red bars) slopes over time. This visualization highlights the dynamic behavior of the data and the usefulness of this method in identifying and interpreting temporal shifts.

3.2. Construction of Point-Slope relationship

Various methods have been employed to identify behavior patterns and quantify similarities in time series, though high dimensionality and specific characteristics often limit their effectiveness. Ouarda et al. (2014) and Morabbi et al. (2022) utilized changepoints to explain behaviors in hydrological time series and assess the influence of climatic variables. Slope analysis complements this approach by uncovering underlying patterns within segments, further enhancing the ability to detect shifts in behavior. For normally distributed time series, linear regression is commonly applied to estimate trends, while parametric or non-parametric methods are used for non-normally distributed data (Killick et al., 2012; Wang et al., 2023). Methods combining simplified time series representations, segment slopes, and Euclidean distance, as described by Abebe et al. (2022) and Kamalzadeh et al. (2020), have proven effective for improving clustering and similarity analysis. This integrated methodology facilitates the development of similarity measures that account for both the physical form and structural patterns of time series data (Xiong et al., 2015; Galeano and Peña, 2007). The proposed similarity measure, summarized in Algorithm 3, compares changepoints within the same temporal framework and utilizes segment slopes to estimate relationships between variables, enabling a more comprehensive understanding of time series variability.

Two time series (here the predictor and predictand) are assumed to be similar if they have the same number and changepoints and the changepoints are located at the same position. To handle potential missing data, we identify years where both time series have valid values $Y = \{y_1, y_2, \dots, y_n\}$ and compute the change points for each series within this time frame. Let $P_{\text{predictor}}$

and $P_{\text{predictand}}$ denote the change point matrices of the predictor and predictand time series, respectively. For each row i in $P_{\text{predictor}}$ and each row j in $P_{\text{predictand}}$, we compute the proportion of matching change points as follows:

$$P_{\text{comparison}} = \frac{1}{mn}\sum_{i=1}^{m}\sum_{j=1}^{n}\frac{\sum_{t\in Y} I\left(P_{\text{predictor},i}(t) = 1 \wedge P_{\text{predictand},j}(t) = 1\right)}{\max\left(\sum_{t\in Y} P_{\text{predictor},i}\ (t), \sum_{t\in Y} P_{\text{predictand},j}\ (t)\right)} \tag{3.3}$$

This comparison score quantifies the temporal alignment of structural breaks between the two series. The indicator function I equals 1 when both have a changepoint at the same time t, and 0 otherwise. Normalization by the maximum number of changepoints ensures the metric is proportional, facilitating comparability. The final score, averaged across all row comparisons, ranges from 0 (no similarity) to 1 (perfect alignment).

The slopes of the segments between changepoints in Y are then compared. Let $S_{\text{predictor}}$ and $S_{\text{predictant}}$ denote the slope matrices. The slope comparison score is defined by matching the signs of the slopes:

$$S_{\text{comparison}} = \frac{1}{mn}\sum_{i=1}^{m}\sum_{j=1}^{n}\frac{\sum_{t\in Y} I\left(\text{sign}\left(S_{\text{predictor},i}(t)\right) = \text{sign}\left(S_{\text{predictant},j}(t)\right)\right)}{|Y|} \tag{3.4}$$

This score reflects the proportion of matching slope directions (positive or negative) between the two series. Averaging across all row comparisons ensures robustness and captures whether the variables tend to co-evolve in the same direction over time.

A combined components of the similarity measure PS is defined as follows:

$$PS = \frac{P_{\text{comparison}} + S_{\text{comparison}}}{2} \tag{3.5}$$

This composite measure integrates changepoint alignment (capturing nonstationary structural similarity) with slope orientation (capturing physical trend direction). The normalization keeps values within 0–1, ensuring interpretability and comparability across datasets. Equal weighting prevents either changepoints or slopes from dominating, providing a balanced metric.

From a teleconnection perspective, this approach gives a more complete view of the relationship between climate drivers and hydrological responses. Changepoint alignment highlights shared structural variability, while slope direction conveys whether a forcing leads to strengthening or weakening of a response. Thus, PS provides a robust metric for identifying meaningful hydroclimatic linkages.

Algorithm 3. Computation of PS Similarity Measure.

Input: Predictor series, Predictand series, common valid years, changepoint settings (l_{min}, α).

Output: $PS \in [0,1]$.

1. Detect changepoints in both time series:

   Apply Bayesian multiple changepoint detection to Predictor and Predictand restricted to t in years with the changepoint settings.

   Build binary changepoint matrices $P_{predictor}$ and $P_{predictand}$, each row encoding one credible segmentation.

2. Changepoint alignment score $P_{comparison}$:

   For each row i of $P_{predictor}$ and row j of $P_{predictand}$, count coincident changepoints at times t in common years and normalize by the larger count of changepoints in the pair.

   Average over all i, j pairs to obtain $P_{comparison} \in [0,1]$.

3. Estimate segment slopes in both series:

   For each credible segmentation, split the series into segments and fit OLS per segment to get a slope time series $S_{predictor}$ and $S_{predictand}$ piecewise constant over segments.

4. Slope alignment based on signs:

   For each pair i, j pair, compute the portion of times t in common years where sign of $S_{predictor}$ and $S_{predictand}$ are equal.

   Average over all i, j pairs to obtain $S_{comparison} \in [0,1]$.

5. Combine: $PS = \left(P_{comparison} + S_{comparison}\right)/2$.

3.3. Use of PS for Teleconnection Analysis

The similarity between two signals is understood as the degree of covariability or alignment in their behavior over time. This resemblance can be assessed in multiple ways such as understanding their magnitude, correlation, temporal alignment, or structural dynamics. Similarity measures provide a quantitative value that allows time series to be compared systematically. In hydroclimatic studies, these measures are particularly valuable because they enable the comparison of climatic drivers as predictors with hydrological responses. A similarity score can then be used as an input for clustering or mapping, leading to the delineation of homogeneous regions that respond coherently to external climatic forcings.

While the literature has described several methods to get similarity between signals, their limitations become evident when applied to nonlinear and nonstationary hydroclimatic data. For example, correlation-based measures capture linear associations but overlook regime shifts. Euclidean distance provides a simple metric of difference between two series but is highly sensitive to temporal misalignment and noise. Dynamic Time Warping (DTW) improves on this by allowing flexible temporal alignment, yet it may stress on local fluctuations at the expense of broader structural changes. In contrast, the strength of PS lies in its structural association, not relying on point-to-point alignment, focusing on identifying common changepoints and assessing the consistency of trends between them.

In this framework, changepoints reveal the timing of structural reorganizations, moments where the system shifts from one regime to another. On the other hand, slope analysis provides the physical meaning of these shifts. The slope of each segment indicates whether the variable is intensifying or weakening in response to external forcings, adding interpretability that pure changepoint alignment cannot achieve. Thus, PS captures not only when changes occur but also how the system evolves within each regime.

In line with this, Morabbi et al. (2022) showed that Bayesian changepoint detection following Seidou and Ouarda (2007) performed well for delineating homogeneous regions, paving the way for the development of new similarity measures. Building on these advances, the PS metric represents a natural evolution, explicitly linking the statistical detection of changepoints with the physical interpretation of slope, thereby offering a more comprehensive tool for teleconnection analysis. Recent studies have supported the importance of this analysis. Kamalzadeh et al. (2020) developed a slope-based similarity measure optimized with particle swarm algorithms, showing that slope information better captures structural patterns than raw values alone. Similarly, Abebe et al. (2022) demonstrated that slope comparisons improved the detection of common trends in hydrological time series. These works highlight that slopes provide a physically meaningful layer of information. By combining the timing of changepoints with the sign of segment slopes, PS transforms statistical breaks into physically interpretable signals of climate influence, providing a similarity score that can be directly applied to teleconnection analysis and regionalization. In the following chapters, the same methodology is illustrated conceptually to show how the PS metric operates in practice.

3.3.1. PS as a Similarity Measure

The Point–Slope (PS) similarity measure integrates the comparison of paired predictor–predictand time series into a single structurally based metric. Its practical scope lies in enabling classification, regionalization, and potentially prediction of hydroclimatic behaviours according to their structural dynamics. By simultaneously capturing the timing of changepoints and the direction of subsequent trends, PS provides not only a statistical value but also a physically interpretable signal of intensification or weakening. Unlike traditional approaches, this method does not require sequential steps such as first testing for nonlinearity and nonstationarity, then applying correlation methods, and later decomposing modes (e.g., PCA) to infer whether relationships are positive or negative (Dettinger et al., 2011; L'Heureux et al., 2013; González-Perez et al., 2022). Instead, PS condenses these processes into a unified framework. By detecting coincident changepoints and the associated slope directions within paired time series, PS produces a score between 0 and 1 that reflects the strength of structural alignment.

A key challenge, however, lies in classification: labelling similarity values as "low," "moderate," or "high" introduces arbitrary thresholds and the risk of bias. For this reason, the interpretation of PS values benefits from a statistical analysis complemented by visual inspection of the paired signals.

Figure 3.4 illustrates examples of predictor–predictand series with PS values ranging from 0.1 to 0.8. At low values (PS = 0.1–0.3), similarity is weak, since neither changepoints nor slopes align consistently, and co-fluctuations primarily reflect noise rather than structural correspondence. Importantly, PS evaluates long-term shifts and slope directions rather than interannual variability; thus, two series may fluctuate in parallel without being structurally aligned. At intermediate values (PS =0.5), partial alignment emerges, with some changepoints and slopes coinciding significantly, although not comprehensively. High values (PS = 0.7–0.8) indicate robust structural similarity, where changepoints and slope directions consistently match, revealing a strong though not necessarily perfect teleconnection signal.

Subsequent chapters will show that instead of relying on rigid thresholds, PS values can be classified through clustering techniques, such as k-means, fuzzy c-means, or empirically derived quantiles, allowing similarity classes to emerge from the data itself. This data-driven approach avoids arbitrary cutoffs and improves interpretability. Building on this, homogeneous regions or Regions of Influence (ROI) can be defined as areas where most stations exhibit high PS similarity with particular oceanic points or with each other, as demonstrated by Morabbi et al. (2022). Mendler et al. (2025) showed that clustering spatial objects into internally homogeneous and contiguous regions improves regional delineation compared to threshold-based methods. Mapping these structurally coherent zones is critical for understanding the spatial patterns of teleconnection impacts, which in turn supports improved long-term climate projections and water resources planning (Burn, 1997; Wilby and Wigley, 2000).

Spearman rank correlation is well suited to detect monotonic relationships, where an increase in the oceanic index consistently leads to an increase or decrease in the hydrological response. However, Spearman is blind to regime shifts and may average out episodes where the sign or strength of the teleconnection changes over time. The Point–Slope similarity measure was designed to address this limitation by focusing on structural features: the synchrony of changepoints and the alignment of segment-specific slopes. As a result, PS can capture nonmonotonic and episodic teleconnections-such as periods where a warming phase intensifies precipitation followed by periods where the same warming phase suppresses it-without assuming a globally monotonic relationship (Slater et al., 2021).

The proposed framework is highly flexible due to its mild structural assumptions, allowing time series to be piecewise linear with changepoints occurring arbitrarily without prescribing fixed windows or assumed stationarity. Furthermore, it offers transparency because every component of the model, including the number of changepoints, their locations, and the sign of the slopes, is directly interpretable in physical terms and can be mapped onto known climate processes. This contrasts sharply with many machine-learning approaches, which often lack a clear physical interpretation. Despite the advantages of PS as an alternative similarity measure between two signals, certain limitations remain. While these do not necessarily constitute disadvantages relative to other methodologies, it is important to acknowledge potential areas for improvement. Table 3.1 summarizes PS in comparison with other commonly used similarity measures. Furthermore, Section 5.2 presents direct comparisons between PS and these methods, highlighting the extent of their respective capabilities.

In summary, the methodology presented in this chapter serves as the foundation for the subsequent analyses. Chapter 4 introduces the construction of the PS metric within a climate–hydrology context, demonstrating its ability to capture structural similarities between signals. This represents the development of a new similarity measure, applied to define a Region of Influence (ROI) in the ocean and its connection with selected stations in California.

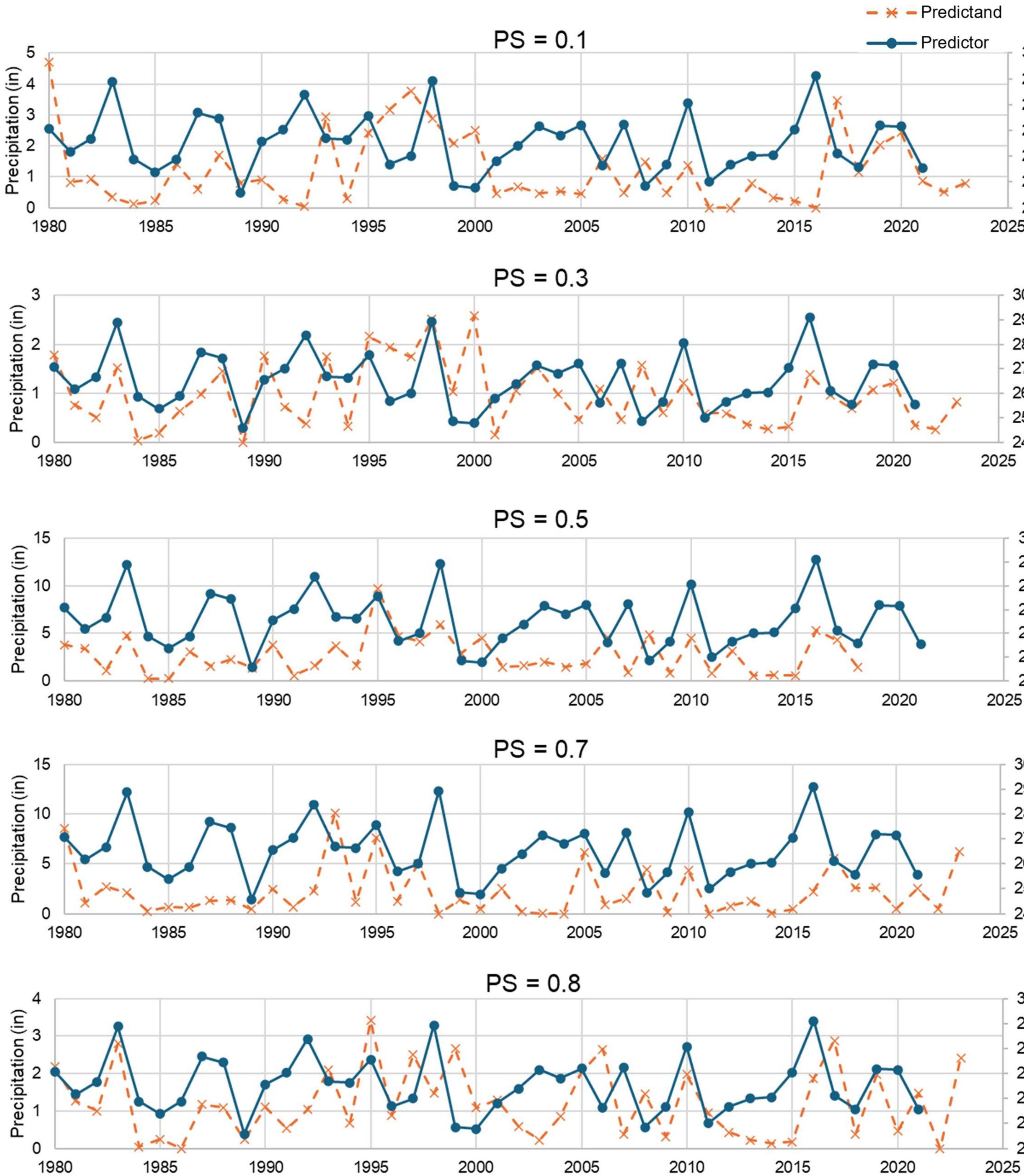

Figure 3.4 Examples of one predictor and five different predictand time series with a Point–Slope (PS) similarity scores captured by the methodology.

Building on this, Chapter 5 expands the framework to evaluate the degree of influence exerted across the entire state of California using a climate index, enabling the regionalization of hydrological responses. This chapter also provides a comparative evaluation of PS against other similarity measures. Finally, Chapter 6 extends the approach by implementing a double regionalization-delineating both oceanic and land-based regions-which facilitates the interpretation of large-scale climatic drivers and their localized hydrological repercussions.

Collectively, these chapters illustrate how the methodology advances teleconnection research, bridging the initial steps shown in Figure 3.1, toward a comprehensive assessment of climate influence and its regional impacts.

This framework was applied in California under the assumption that the region offers sufficient robustness for testing and comparison in future studies. However, the choice of this study area is not restrictive: the objective of the thesis is not to focus exclusively on California but to demonstrate the potential and applicability of the proposed methodology. Accordingly, the following chapters also present the rationale for selecting the study area, along with its geographic characteristics and the environmental and economic contexts in which teleconnections are particularly relevant.

Table 3.1 Comparison between Similarity Measures.

Similarity Measure	Structural Basis	Advantages	Limitations	Applicability in Teleconnections
PS	Changepoint alignment and slope direction	Captures nonlinearity and nonstationarity. Physically interpretable signals. Flexible to incorporate new conditions, such as delays.	Values require clustering or categorization. Computationally more demanding than simple metrics.	Ideal for detecting and interpreting evolving, nonstationary signals; supports classification and regionalization.
Correlation	Linear co-variability of paired values	Simple and most used. Measure strength and direction.	Captures only linear relationships. Fails under nonstationary conditions.	Useful for exploratory analysis; limited in complex teleconnection systems.
Euclidean Distance	Point-to-point difference in values	Intuitive for dissimilarity. No transformations are needed.	Sensitive to temporal misalignment and noise. Magnitude-driven; ignores shape similarity.	Rarely used alone; can complement clustering algorithms, but unsuitable for nonstationary teleconnections.
DTW	Flexible alignment of sequences in time	Handles temporal shifts and misalignments. Can match sequences with varying lengths.	Emphasizes local fluctuations, potentially masking broader structural changes. High computational cost for long records.	Useful when teleconnection signals are phase-shifted in time; less effective for structural regime analysis.

Chapter 4 Development of Station-Specific Regions of Influence for Teleconnection Analysis Using PS Similarity[1]

Carlos A. Rosas-Cabello[1], Mohammad H. Alobaidi[2], Fateh Chebana[3], Ousmane Seidou[1]

[1] Faculty of Engineering, University of Ottawa, Ottawa, ON, Canada

[2] Department of Civil Engineering, McGill University, Montréal, QC, Canada

[3] Centre Eau Terre Environnement, Institut National de la Recherche Scientifique, Québec, QC, Canada

Abstract

Understanding how hydrological variables drive climate fluctuations is essential for an array of models in modern hydrology. The improved modelling also facilitates more effective water resource management within watersheds, especially in inherently non-linear and non-stationary systems. In this regard, the linkage between time series, such as oceanic anomalies and regional hydrology, is an increasingly important topic. Prior efforts to study this dynamic relationship rely on feature analysis techniques such as Principal Component Analysis or Wavelet analysis. However, more work is needed to fully capture such dependencies. The present work introduces a novel framework that leverages the PS similarity value. PS is a newly developed metric designed to map and quantify the influence of Sea Surface Temperature Anomalies (SSTAs). The proposed method employs Bayesian changepoint detection and slope analysis to unravel the non-linear and non-stationary dependencies between SSTAs and localized precipitation trends. The generation of high-resolution influence maps is now possible, which reveal station-specific regions of impact. This

[1] A version of this chapter has been submitted to the Journal of Hydrology and is currently under revision at the time of the thesis submission.

approach is also capable of capturing how remote oceanic conditions affect regional weather variability. The method is demonstrated on precipitation patterns across meteorological stations in California from 1982 to 2021. Results successfully highlight the relationship between SSTA fluctuations and significant shifts in precipitation patterns. The strongest associations are observed during winter and autumn, though fluctuations remain evident across all seasons.

Keywords: PS similarity value, Oceanic anomalies, non-stationary systems, climate fluctuations.

4.1. Introduction

Water resource management and regional climate resilience face substantial challenges due to the increasing frequency of hydrometeorological extremes, driven by both climate change and land-use modifications in watersheds (Merz et al., 2014; Blöschl et al., 2019; Ragno et al., 2019; Alobaidi et al., 2022; Vidrio-Sahagún et al., 2024). These extreme events often stem from anomalies in regional and global atmospheric circulation, which in turn are intricately connected to ocean-atmosphere interactions (Kousky et al., 1984; Ouachani et al., 2013; Slater et al., 2021; Wang et al., 2022; Abdelkader and Yerdelen, 2022). Given that water systems are fundamental to economic development and societal well-being (Vörösmarty et al., 2015; Alcamo, 2019), understanding such anomalies and their hydrological consequences help design effective adaptation strategies and inform responsible policymaking (Milly et al., 2008; Lee et al., 2010; Xiao et al., 2017; Ouarda et al., 2019; Wongchuig et al., 2023).

A central topic in addressing these challenges is modeling the inherently dynamic and multi-scale nature of climate variations (Wallace and Guztler, 1981; Ropelewski et al., 1986; Liu et al., 2007; Taschetto et al., 2020; Zhang et al., 2024). Climate systems exhibit nonlinear behavior, meaning that shifts in one region can trigger cascading impacts in another, a phenomenon known as teleconnections (Chase et al., 2006; Chiew et al., 2002). These teleconnections are marked by further complex analysis (Tsonis and Roebber, 2004). To disentangle these interactions, the analysis framework often relies on feature mapping and decomposition techniques, where generally a decoupling of additive effects is attempted. The state-of-the-art has demonstrated a variety of tools to address these challenges (Torrence and Compo, 1998; Hurrell et al., 2003; Feldstein and Franzke, 2017; Arcodia et al., 2020; Canchala et al., 2020; Abdelkader and Yerdelen, 2022; Agarwal et al., 2022; González-Pérez et al., 2022). For example, simple approaches such as linear correlation (Djibo et al., 2015; Jong et al., 2016) have been used to detect relationships between climatic and hydrological variables. These studies typically rely on reanalysis data, which, while practical, may introduce biases or uncertainties due to their dependence on modeled rather than directly observed outputs. In contrast, L'Heureux et al. (2013) identified different modes of El Niño–Southern Oscillation (ENSO) by applying Principal Component Analysis (PCA) to sea surface temperature (SST) data from the tropical Pacific. The limitations of PCA are evident in L'Heureux et al. (2013), where removing linear trends from tropical Pacific SST data caused the second principal component (PC2), a cooling mode dependent on long-term trends, to disappear. This highlights PCA's heavy reliance on trend-dominated components and raises questions about its robustness in isolating physically independent climate modes. Similar critiques apply to non-traditional ENSO patterns like Modoki, which studies suggest may also be artifacts of trend contamination or decadal variability (Takahashi et al., 2011; Newman et al., 2011).

To overcome these limitations, researchers have turned to more sophisticated techniques, such as wavelet analysis, which offers a dynamic and multi-scale approach to examining climatic variability. Wavelet analysis is particularly effective for capturing nonlinear relationships and complex patterns that linear methods often fail to detect. For example, Canchala et al. (2020) employed wavelet transforms to explore monthly rainfall variability across different regions in Colombia. Their study combined multiple methodologies, including non-linear Principal Component Analysis (PCA) to extract modes of variability and regionalization, Pearson Correlation to identify teleconnections between inland regions and various climate indices, and Wavelet Coherence using the Morlet function to confirm these relationships. The results of their analysis were robust, revealing the influence of the La Niña phenomenon on regional rainfall patterns, a finding that had not been previously well-documented in the literature, especially in comparison to the more extensively studied El Niño phenomenon. Similarly, Naizghi and Ouarda (2016) investigated the long-term variability of wind speed in the United Arab Emirates (UAE) and its connections with global climate indices based on Pearson correlation, changepoint detection, and wavelet analysis. Yet even these advanced tools require careful application: understanding the results demands vigilant attention to methodological details such as the "cone of influence" in wavelet analysis and the selection of appropriate teleconnection indices (Torrence and Compo, 1998; Grinsted et al., 2004; Guo et al., 2022).

Recently, Lee and Ouarda (2012a) applied Empirical Mode Decomposition (EMD) combined with non-parametric techniques to predict the streamflow of the Romaine River in Quebec. Later, Lee and Ouarda (2019) extended this work to the Great Lakes, employing EMD for multivariate analysis and correlating climatic and hydrological variables using synthetic teleconnection indices. Although EMD is effective for decomposing complex time series into intrinsic components, their reliance on modeling separate variable combinations raises concerns in highly nonlinear systems. For example, interdependent processes like coupled ocean-atmosphere feedbacks may resist decoupling, potentially misrepresenting causality or extremes and reducing predictive skill during transitional climate states (e.g., ENSO-neutral or PDO phase shifts) (Mantua and Hare, 2002).

Despite the availability of advanced tools like wavelet analysis and EMD, capturing the full complexity of climate systems remains an ongoing challenge. While PCA is effective for dimensionality reduction, it operates as a static analysis tool and is inherently limited in addressing dynamic, time-specific problems (Hannachi et al., 2007). Conversely, wavelet analysis and EMD provide dynamic insights but remain source-agnostic, meaning they fail to account for hydrologic systems with nodes of unequal contribution (Sang et al., 2009). This can lead to critical misinterpretations, such as attributing non-stationarity to typical non-linearity (Priestley, 1988; Salas and Fernandez, 1993; Chen and Rao, 2003; Lins and Cohn, 2011). To address this ambiguity, Helsel and Hirsch (1992) developed a comprehensive method for detecting nonstationary behavior in time series. Specifically, two fundamental characteristics can determine non-stationarity in a time series: changepoints, defined as abrupt shifts in variable distributions, and trends, which are gradual distributional changes. These challenges are further compounded by data limitations, exacerbating the difficulty of accurately representing teleconnection effects on regional hydrology using such techniques (Coulibaly and Burn, 2004).

As an alternative to conventional methods, station-specific Regions of Influence (ROIs) enable analysis to independently assess each station's unique climate response. This individualized approach circumvents the dilution of critical local signals, a pervasive issue when regions are delineated solely by geographic proximity or when methods overlook meteorological and hydrological nuances (Burn, 1990; Coulibaly and Burn, 2004).

ROI-based frameworks are particularly adept at resolving scale-dependent teleconnections, such as the El Niño–Southern Oscillation (ENSO) and the Pacific Decadal Oscillation (PDO), which exert disproportionate and often opposing impacts on neighboring locations. For instance, ENSO may drive flooding in coastal stations while exacerbating drought in nearby inland basins—a spatial dichotomy masked by PCA's aggregated modes or wavelet's source-agnostic coherence (McCabe and Dettinger, 1999; González-Pérez et al., 2022). By isolating station-specific drivers, ROIs provide the spatial granularity needed to map these localized responses.

Nevertheless, delineating meaningful ROIs remains intricate due to the inherent non-linearity and non-stationarity of both climatic and hydrological processes. These complexities obscure causal relationships and hinder the identification of coherent spatiotemporal patterns. To address these challenges, changepoint detection has emerged as a pivotal tool for isolating abrupt transitions in climate regimes, such as those driven by anthropogenic forcing or alterations in oceanic circulation (Reeves et al., 2007). However, relying solely on changepoint detection is insufficient to fully unravel the complexities of climate-ocean-atmosphere interactions. A robust analytical framework must integrate changepoint analysis with methodologies that contextualize detected shifts within broader trends or oscillatory behaviors (Volpi et al., 2024).

For instance, abrupt regime shifts identified through changepoint analysis may coincide with or obscure underlying multidecadal variability, necessitating approaches to disentangle overlapping signals (Seidou and Ouarda, 2007). Recent work attempts to devise the desired integrated approach, offering tools that handle shorter time series and adapt to non-stationary signals (Morabbi et al., 2022).

Building upon these methodological advancements, the present study introduces a novel approach for analyzing teleconnections. We propose a PS similarity value integrating changepoint detection and trend direction analysis. This method delineates station-specific ROIs to identify impactful oceanic drivers for individual meteorological stations. By capturing both non-linear behavior and sudden or gradual changes in teleconnection patterns, this approach aspires to provide more nuanced insights than traditional linear models alone. To demonstrate its utility, the proposed approach is applied on a case study in California. This region is considered due to its diverse climate zones, significant vulnerability to hydrometeorological extremes, and reliance on effective water resource management. High-resolution oceanic mapping will help stakeholders develop targeted adaptation strategies, supporting climate resilience and sustainable water management.

The remainder of this paper is structured as follows: **Section 4.2** describes the extended methodology of changepoint detection, including the development of the PS similarity value and its application to seasonal precipitation records. **Section 4.3** describes the case of study.

In **Section 4.4**, presents the key findings, illustrating how station-specific ROIs capture diverse teleconnection effects. Finally, **Section 4.5** discusses the broader implications of these findings and outlines future directions for research and policy. By situating station-specific ROIs within a robust analytical framework, this study aims to advance our understanding of climate-ocean-atmosphere interactions and enhance predictive accuracy for hydrometeorological extremes in California and beyond.

4.2. Methodology

4.2.1. Bayesian Multiple Changepoint Detection

A core element of this study involves detecting abrupt changes in climate and hydrological variables over time. To achieve this, we extend the Bayesian procedure first described by Seidou and Ouarda (2007), which offers a flexible and probabilistic framework for identifying both the number and locations of changepoints. Unlike classical methods that often assume a fixed number of breakpoints, the Bayesian approach incorporates prior information and updates it with observed data, resulting in robust posterior probability distributions for the location and number of changepoints. This section provides an overview of the original approach and details the proposed framework in this study.

4.2.1.1. Model Formulation

This method detects changepoints in either (1) the relationship between independent variables and a response variable or (2) the distribution of the response variable itself when predictors are absent. To formalize this, consider a dataset with n observations and d independent variables. The dependent variable y_j (where $j = 1, \dots, n$) is modeled as a linear combination of predictors x_{kj} (where $k = 1, \dots, d$ and $j = 1, \dots, n$) represented by the j-th value of the k-th independent variable. The multiple linear relationship can then be expressed as:

$$y_j = \sum_{k=1}^{d} \theta_k \, x_{kj} + \varepsilon_j \tag{4.1}$$

where θ_k are the regression coefficients for the independent variables, and ε_j is the error term.

The Bayesian multiple changepoint identifies time points where the relationship between x_{kj} and y_j changes significantly. The achieve this, the algorithm by Fearnhead (2006) constructs a set $E = \{S_1, S_2, S_3, \dots, S_M\}$ of M possible scatter schemes. Each element k^{th} in E is a set of m_k changepoints $S_k = \{t_1^{\sim k}, t_2^{\sim k}, \dots, t_{m_k}^{\sim k}\}$. This Bayesian framework detects structural breaks, in raw data or predictor-predictand relationships, to advance understanding of climate-ocean-atmosphere dynamics. Its ability to identify abrupt hydrological or climatic shifts is especially critical in regions where such changes cascade into environmental and societal risks (see Table 4.1).

4.2.1.2. Slope Analysis

Following the identification of the changepoints $\{t_1^{\sim k}, t_2^{\sim k}, \dots, t_{m_k}^{\sim k}\}$ using the Bayesian method, we include t_0^k as the first point in the entire time series and the $t_{m_{k+1}}^k$ as the last point. Consequently, the time series $\{t\text{-}\}$ and the dependent variable $\{y\text{-}\}$ are divided into $m_k + 1$ segments. For each segment ℓ spanning all data indices between $t_{\ell-1}^k$ and t_ℓ^k and for each inference model $m \in \{1,2,\dots,M\}$ it is fitted a linear regression to estimate the slope $\beta_{1,\ell}$ and the intercept $\beta_{0,\ell}$.

4.2.1.3. Implications

Bayesian changepoint detection estimates posterior distributions for changepoint numbers and locations, avoiding single point estimates. This quantifies uncertainty in when and how shifts occur. Each potential breakpoint is assigned a probability (via Bayesian inference) reflecting its likelihood as a true change and the precision of its timing. The method adapts to multi-phase climate systems by letting data determine the number of breaks. For example, it identifies periods where a teleconnection index strongly influences a predictand before weakening or reversing. In each segment, slopes quantify the teleconnection's effect magnitude and direction. When breakpoints align between predictor and predictand, the method isolates intervals where their relationship shifts. Beyond detecting abrupt climate transitions, it provides confidence measures for each shift, clarifying how teleconnections evolve.

4.2.2. Similarity Measure

Researchers have employed diverse methods to identify patterns and quantify similarities in time series, though challenges like high dimensionality and data-specific traits constrain technique selection. A similarity measure, in this context, refers to a mathematical tool that quantifies how closely two time series align in terms of structural features, such as trends or abrupt shifts (Lhermitte et al., 2011). Changepoint analysis, as applied by Ouarda et al. (2014) and Morabbi et al. (2022), helps decode hydrological behaviors and climatic drivers by segmenting time series into homogeneous intervals. Integrating slope analysis further uncovers underlying trends: linear regression estimates trends for normally distributed data, while parametric/non-parametric methods adapt to non-Gaussian cases (Kamalzadeh et al., 2020; Abebe et al., 2022)

Table 4.1 Algorithm for Slope analysis with/without Changepoints.

Case	Step	Action/Formula
With Changepoints	1. For $m \in \{1,2,\ldots,M\}$:	Iterate over candidate numbers of changepoints.
$(m \geq 1)$	2. For $\ell = 1$ to $(m_k + 1)$:	Loop through each segment defined by changepoints $t_1^{\sim k}, t_2^{\sim k}, \ldots, t_{m_k}^{\sim k}$.
	3. Define segment data:	Extract dependent variable values for the ℓ^{th} segment: $\boldsymbol{Y}_{\text{segment}_\ell} = \{ y_j \mid t_{\ell-1}^k \leq j \leq t_\ell^k \}$
	4. Construct design matrix:	Build X_ℓ for the ℓ^{th} segment, including time points: $X_k = \begin{bmatrix} 1 & t_{\ell-1}^k \\ 1 & t_{\ell-1}^k + 1 \\ \vdots & \vdots \\ 1 & t_\ell^k - 1 \\ 1 & t_\ell^k \end{bmatrix}$
	5. Estimate coefficients:	Compute intercept $(\beta_{0\ell})$ and slope $(\beta_{1\ell})$: $\beta_\ell = (X_\ell^T X_\ell)^{-1} X_\ell^T \boldsymbol{Y}_{\text{segment}_\ell}$
No Changepoints	1. If $(m_k = 0)$:	Treat the entire series as a single segment.
$(m = 0)$	2. Define full dataset:	$\boldsymbol{Y}_{\text{segment}_\ell} = \{ y_j \mid j = 1, \ldots, n \}$
	3. Construct design matrix:	$X_k = \begin{bmatrix} 1 & t_1 \\ 1 & t_2 \\ \vdots & \vdots \\ 1 & t_{n-1} \\ 1 & t_n \end{bmatrix}$
	4. Estimate coefficients:	Compute global intercept (β_0) and slope (β_1): $\beta = (X_\ell^T X_\ell)^{-1} X_\ell^T \boldsymbol{Y}_{\text{segment}_\ell}$

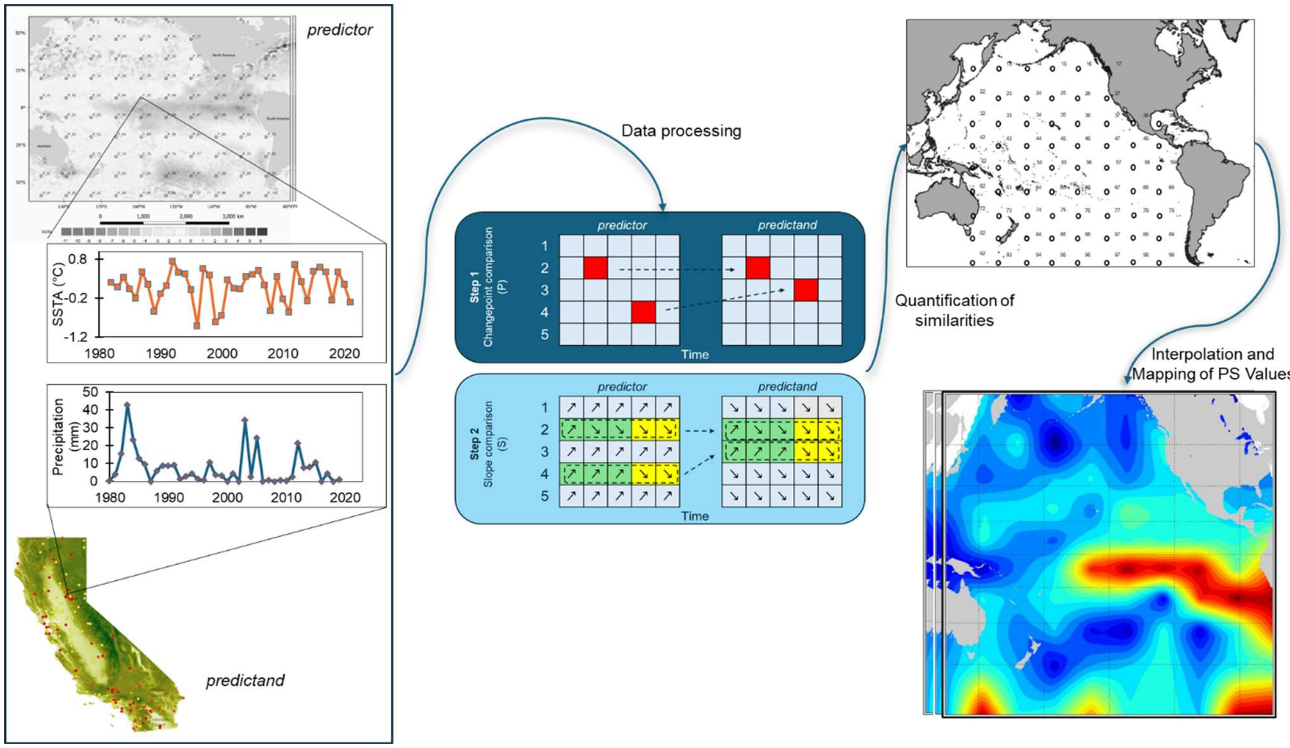

Figure 4.1 Framework for Analyzing Regional Precipitation and Teleconnections.

These approaches combine simplified time-series representations, segment slopes, and distance metrics to enhance clustering and similarity quantification. For instance, slopes quantify trend magnitudes (e.g., increasing or decreasing precipitation), while distance metrics compare structural forms (e.g., abrupt shifts). The proposed similarity measure (Figure 4.1) integrates these elements by (1) aligning changepoints within shared temporal windows to synchronize phase differences and (2) comparing segment-specific slopes to assess variable relationships. This dual focus balances physical similarity (magnitude/direction of trends) and structural similarity (temporal alignment of changepoints or cycles), offering a robust framework for analyzing complex hydroclimatic interactions. In Sections 4.2.1 and 4.2.2, we introduced how to measure the similarity between changepoints and slopes, while Section 4.2.3 details the PS value as follows:

4.2.2.1. Similarity based on changepoint positions

Two time series (here the predictor and predictand) are assumed to be similar if they have the same number and changepoints and the changepoints are located at the same position. To handle potential missing data, we identify years where both time series have valid values $Y = \{y_1, y_2, \dots, y_n\}$ and compute the change points for each series within this time frame. Let $P_{\text{predictor}}$ and $P_{\text{predictand}}$ denote the change point matrices of the predictor and predictand time series, respectively. For each row i in $P_{\text{predictor}}$ and each row j in $P_{\text{predictant}}$, we compute the proportion of matching change points:

$$P_{\text{comparison}} = \frac{1}{mn}\sum_{i=1}^{m}\sum_{j=1}^{n}\frac{\sum_{t\in Y} I\left(P_{\text{predictor},i}(t) = 1 \wedge P_{\text{predictant},j}(t) = 1\right)}{\max\left(\sum_{t\in Y} P_{\text{predictor},i}\,(t), \sum_{t\in Y} P_{\text{predictant},j}\,(t)\right)} \tag{4.2}$$

The changepoint comparison score is designed to quantify the similarity of changepoints between two time series, referred to as the predictor and the predictand. To achieve this, the score is calculated by comparing each row in the changepoint matrix of the predictor with each row in the changepoint matrix of the predictand. Let m be the number of rows in the predictor matrix and n be the number of rows in the predictant matrix. The process involves summing up the instances where both the predictor and the predictant have a change point at the same time t within the set of common years Y. This count is facilitated by an indicator function I that returns 1 when both time series have a changepoint at the same time, and 0 otherwise. This count is then normalized by the maximum number of change points found in either the predictor or the predictand for the given time period, ensuring the result is a proportion rather than an absolute number. This proportion is averaged over all possible row comparisons, providing a final score that represents the overall similarity of changepoints between the two time series. This method helps in capturing the alignment of significant changes in both time series, giving insights into their structural similarities. The values obtained from the P comparison score range from 0 to 1, where 0 indicates no similarity in changepoints and 1 indicates a perfect match in changepoints between the predictor and the predictand.

4.2.2.2. Similarity based on slopes

The slopes of the segments between changepoints in Y are compared. The slope matrices $S_{\text{predictor}}$ and $S_{\text{predictant}}$ are used to calculate the slope comparison score by matching the signs of the slopes:

$$S_{\text{comparison}} = \frac{1}{mn}\sum_{i=1}^{m}\sum_{j=1}^{n}\frac{\sum_{t\in Y} I\left(\text{sign}\left(S_{\text{predictor},i}(t)\right) = \text{sign}\left(S_{\text{predictant},j}(t)\right)\right)}{|Y|} \tag{4.3}$$

The score $S_{\text{comparison}}$ is determined by comparing the signs of the slopes in the segments between changepoints. Here, m represents the number of rows in the predictor slope matrix and n represents the number of rows in the predictant slope matrix. For each row i in the predictor matrix and each row j in the predictant matrix, the comparison involves summing the instances where the signs of the slopes match at the same time t within the set of common years Y. The indicator function $I(\cdot)$ returns 1 if the signs match and 0 otherwise. This count is then normalized by the total number of comparisons, resulting in a proportion rather than an absolute number. The average of all possible row comparisons gives a final score, representing the overall similarity of slopes between the two time series.

4.2.2.3. Combined Similarity Measures

The combined components of the similarity measure PS is defined as follows:

$$PS = \frac{P_{\text{comparison}} + S_{\text{comparison}}}{2} \tag{4.4}$$

This measure combines changepoint and slope analyses to provide a comprehensive similarity metric that captures the underlying patterns and trends in the time series. By dividing the sum of the two scores by 2, the combined similarity measure is normalized, ensuring it remains within the range of 0 to 1. This normalization facilitates easier interpretation and comparison of similarity scores across various datasets and applications. Equal weighting of both changepoint and slope comparisons ensures that neither aspect dominates the analysis, offering a balanced perspective. This approach provides a holistic view of structural similarities between the time series. Additionally, by integrating both changepoints and slopes into a single measure, multiple dimensions of time series behaviour are captured, enhancing the robustness and reliability of the similarity metric. This method enables a more nuanced understanding of relationships between time series, making it an effective tool for analysis and clustering.

4.3 Case of study

4.3.1. Study Area

California has recently endured unprecedented hydrometeorological extremes. These events highlight the state's acute vulnerability to climate change and exacerbate regional water management challenges (Huang and Swain, 2022; Patricola et al., 2022). Its varied geography increases the impact of distant ocean climate patterns, causing different responses in its ecosystems. For example, the southern Mojave and Colorado Deserts face high summer temperatures and low rainfall due to subtropical high-pressure systems (Hereford et al., 2004). In contrast, the Sierra Nevada's elevations, covered in snow by heavy storms during the cooler seasons, provide essential water for agriculture, cities, and ecosystems (Das et al., 2009; Cayan et al., 2010; Dettinger et al., 2011). Coastal areas have Mediterranean climates with temperatures cooled by fog and seasonal rainfall (Chiew et al., 2002; Chase et al., 2006; Johnstone and Dawson, 2010).

These climatic dynamics impact significant socio-economic factors. As a leading agricultural state with rapidly growing urban areas, California's water resources are vital to its economy (Hanak et al., 2011). However, these water systems are under increasing stress from external factors that cause direct damage. For example, the megadrought from 2012 to 2016, driven by a persistent Pacific high-pressure system, reduced the Sierra Nevada snowpack to levels seen only once in 500 years (Lund et al., 2018; Jong et al., 2016). This reduction led to water shortages, ecological instability, and increased wildfire risks (Swain et al., 2014; Belmecheri et al., 2016; Williams et al., 2020).

In that sense, wildfire seasons, once confined to certain times of the year, now extend into winter due to delayed rains and longer dry periods. Even wetter areas, like the Sierra Nevada, face higher fire risks. This trend is linked to changes in precipitation patterns and atmospheric interactions (Goss et al., 2020; Abatzoglou et al., 2021). For example, wildfires such as the catastrophic in 2020 consumed over 4 million acres (Williams et al., 2019; Goss et al., 2020), significantly impacting agriculture, forestry, wildlife habitats, and public health (Keeley and Syphard, 2021). Recently, La Niña conditions in 2024, predicted by the U.S. Climate Predictor Center (CPC, 2024) with 65% certainty, caused record dryness. This led to unprecedented wildfires in Southern California by early 2025 (Swain et al., 2025).

On the other hand, atmospheric rivers, influenced by the interactions of several large-scale climate phenomena, including the El Niño-Southern Oscillation (ENSO), the Pacific-North American (PNA) pattern, and the North Atlantic Oscillation (NAO), bring 30–50% more of the state's annual rainfall in short periods (Hurrell, 1995; Wang et al., 2022). These intense rains can overwhelm flood infrastructure (Dettinger et al., 2011; Du et al., 2020). In 2023, El Niño conditions led to exceptionally heavy rains and resulted in severe floods across California, causing widespread damage (Purohit, 2025). Consequently, addressing both drying trends and extreme rainfall events, understanding the impact of remote factors, is crucial for California's resilience. This requires the development of resilient infrastructure, adaptive governance, and sustainable allocation of water resources (McPhaden et al., 2006).

4.3.2. Rainfall Dataset

To examine the effects of climate variability on precipitation, this study employs monthly rainfall data from the Western Regional Climate Center (WRCC, 2023) for the period 1980–2022. A total of 178 stations are selected based on data completeness (no more than 10% missing values), and all 178 stations are thoroughly analyzed. Seasonal precipitation totals are derived for winter (December–February), spring (March–May), summer (June–August), and autumn (September–November), in addition to annual aggregates.

Rather than representing every station across the state in the final results, the study focuses on six strategically chosen stations located along California's borders, capturing a wide range of climatic regions. This approach allows for a manageable analysis while avoiding redundancy. These border stations provide a representative overview of the diverse climate zones across California, from coastal to desert to mountainous areas, ensuring that the key patterns of regional climate variability are adequately captured. By selecting stations from different climate zones rather than focusing on the heart of the state, the study captures the breadth of California's climatic diversity in a practical manner.

From the comprehensive dataset, the representative stations are illustrated in Figure 4.2 with red circles, while the remaining stations are shown in white. Table 4.2 summarizes these stations, each located in a distinct climate region:

a. **Southern Desert Region** (Station 043855): Characterized by arid conditions and minimal annual rainfall, primarily influenced by subtropical high-pressure systems (Dettinger et al., 2011). The Mojave and Colorado Deserts in this region exhibit extremely elevated temperatures and limited moisture availability.

b. **Sierra Nevada Mountain Range** (Stations 048758, 043603): Known for significant snowfall that sustains urban, agricultural, and ecological water needs (Cayan et al., 2008). Precipitation in the Sierra Nevada is sensitive to climate variability, with snowpack levels exerting a major influence on water availability statewide.

c. **Coastal Region** (Stations 047772, 048014): Heavily influenced by Pacific Ocean dynamics, the region's Mediterranean climate features wet winters and dry summers (Johnstone and Dawson, 2010). Fog and moderate temperatures are common, contributing to diverse microclimates along the coast.

d. **Northern Region** (Station 049866): Receives high precipitation due to orographic lifting and frequent storm tracks (Das et al., 2011). The abundant rainfall in this region is crucial for keeping California's overall water balance.

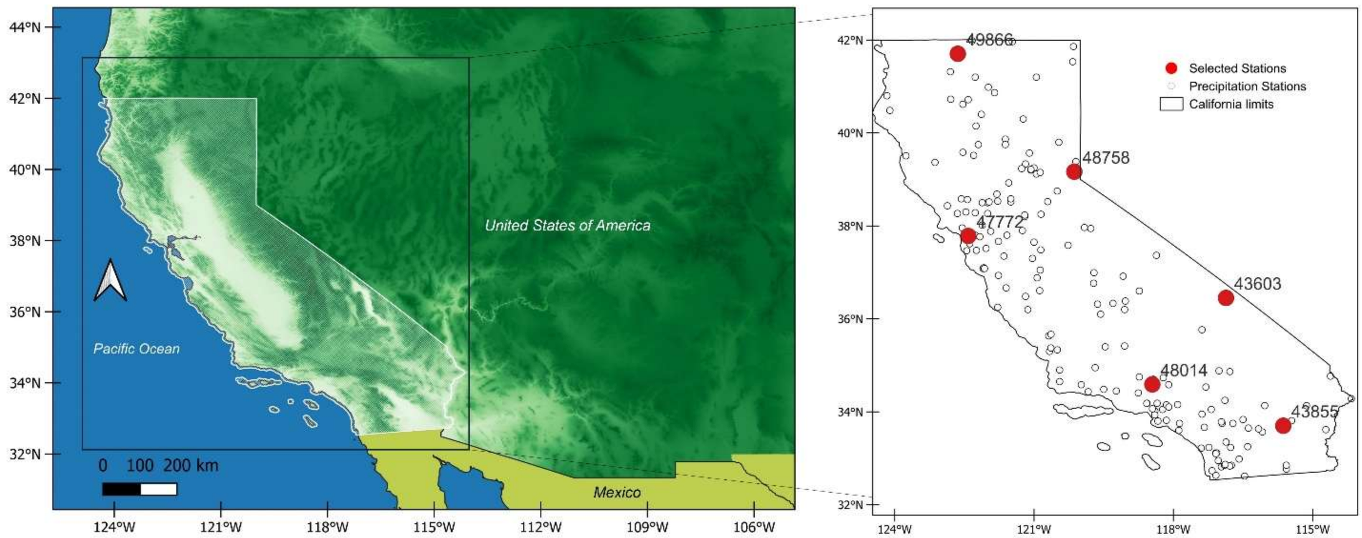

Figure 4.2 Map of Precipitation Stations Across California: The map displays the locations of rainfall stations (white circles) and selected example stations (red circles).

Over recent decades, California's precipitation patterns have shifted unevenly across its diverse regions, reflecting both natural climate variability and anthropogenic warming. In Yreka (Northern California), winter precipitation has increased by 10–15% since the 1980s, amplifying Sierra Nevada snowpack accumulation but raising flood risks during early melt events (Mote et al., 2018). Conversely, Death Valley National Park has seen a 20% reduction in annual rainfall since the 1990s, intensifying aridification and ecosystem stress (Williams et al., 2020). Central California stations like San Francisco Downtown and exhibit heightened interannual variability, with atmospheric rivers punctuated by multiyear droughts (Dettinger et al., 2011). Tahoe City has experienced a 15% decline in winter snowfall since 1950, shortening the snow season and threatening water supply reliability (Hatchett et al., 2017). Meanwhile, Hayfield (Southern California) shows a trend toward concentrated extreme rainfall events amid overall drying, aligning with projected "precipitation whiplash" under warming (Swain et al., 2018).

These spatial disparities, mapped in Figure 3, highlight how regional topography and Pacific climate modes (e.g., ENSO, PDO) modulate local precipitation responses. Figure 4.3 plots seasonal mean precipitation for the six stations across the December-January-February (DJF) and September-October-November (SON) periods, revealing stark contrasts even in averaged conditions. For instance, ENSO's warm phases enhance rainfall in Southern California (Hayfield) during DJF, while suppressing Sierra Nevada snowfall (Tahoe City) due to warmer winter temperatures patterns that align with the divergent trends described earlier. Similarly, Death Valley's arid SON means contrast sharply with Saugus PWR's variable autumn rainfall, reflecting the interplay of rain-shadow effects and atmospheric river variability. The persistent differences in DJF and SON precipitation between coastal (San Francisco Downtown), mountainous (Yreka), and desert (Death Valley) stations further underscore how topography amplifies or dampens Pacific climate signals.

This study analyzes Sea Surface Temperature (SST) anomalies from the NOAA/NESDIS/NCEI Daily Optimum Interpolation Sea Surface Temperature (DOISST v2.1) dataset. Spanning 1982–2022, the dataset provides daily SST anomalies at 0.25° resolution. It integrates satellite and in situ measurements to minimize bias. Daily anomalies were aggregated into monthly means, retaining months with ≥90% valid daily data. Monthly SST anomalies were then averaged into 3-month seasonal means (DJF, MAM, JJA, SON) for each calendar year.

Table 4.2 Table with Information on Stations by Region in California.

Number	Station	Latitude (N)	Longitude (W)	Period record	Years	Missing (%)
49866	Yreka	41° 42' 13"	122° 38' 27"	1914-2022	108	6.28
47772	San Francisco Downtown	37° 46' 60"	122° 25'	1850-2022	172	4.65
48758	Tahoe City	39° 10'	120° 7' 60"	1910-2022	112	5.37
43603	Death Valley National Park	36° 27'	116° 52'	1912-2022	110	8.18
48014	Saugus PWR	34° 35' 25"	118° 27' 13"	1919-2022	103	9.7
43855	Hayfield	33° 42'	115° 37' 60"	1933-2022	89	8.98

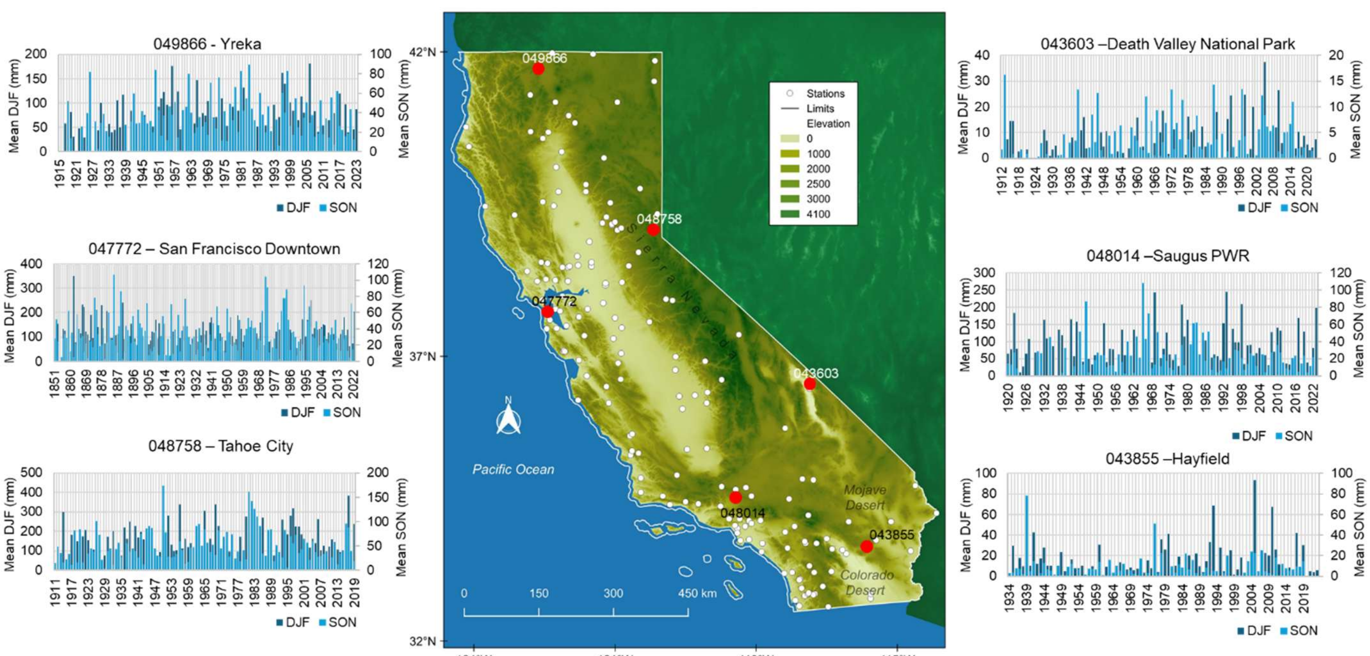

Figure 4.3 Mean Winter and Autumn Precipitation Across Selected Stations in California.

4.3.3. Climate Data

Seasonal SST anomalies were computed for the Pacific Ocean (135°E–75°W, 60°N–60°S) using a uniform 100-point grid. This ensures consistent spatial coverage to assess SST variability and its influence on regional climate patterns, such as California's weather. The seasonal averaging reduces intra-seasonal noise and aligns with the timescales of ocean-atmosphere interactions. By harmonizing SST and precipitation data into matching seasonal resolutions, comparisons between the two variables avoid biases introduced by mismatched temporal scales. This ensures that relationships reflect true climate linkages rather than artifacts of differing data granularity.

4.4. Results and Discussion

4.4.1. Changepoint detection and slope analysis

Determining the Regions of Influence for each station begins with identifying the changepoints and slopes associated with segments in the time series data. This analysis involves performing $M = 2{,}500$ iterations and setting a minimum segment length of $l_{min} = 7$ for each time series of precipitation and Sea Surface Temperature Anomalies (SSTA). Given that the length of the time series varies between stations and SSTA, we establish a common data period from 1981 to 2022 to standardize the analysis. After processing the data using our proposed methodology, we calculate the PS values.

Tables 4.3 to 4.6 summarize the changepoints detected at the six stations for each season. In Table 4.2, which covers winter (December–February, DJF), only three stations show probable changepoints with probabilities below 0.5. This indicates a lack of strong evidence for significant changes occurring during this season at most stations. Additionally, both positive and negative slopes are observed, suggesting mixed trends in precipitation during winter. Notably, station 43603 exhibits up to three sign changes in its slopes with detected changepoints, indicating considerable variability in trend direction over time.

In spring (March–May, MAM), as presented in Table 4.4, there is a lower incidence of changepoints among the stations. However, station 043855 stands out by exhibiting a high probability (0.84) of a sign change. This suggests a significant shift in precipitation trends during this season at that particular location. During summer (June–August), detailed in Table 4.5, a greater number of changepoints are detected across the stations. Various changes are observed, some involve a reversal in the sign of the trend, while others reflect changes in the intensity of the trend without altering its direction. This means that some stations experience a switch from positive to negative trends or vice versa, while others maintain the same trend direction but see it intensify or diminish. For example, certain stations continue with a positive trend, but the slope becomes steeper or flatter over time. Regarding autumn (September–November, SON), Table 4.6 shows that fewer changepoints are detected overall. The most notable case was at station 047772, which has a high probability (0.78) of a changepoint occurring. This indicates a significant alteration in precipitation trends during autumn at this station.

These findings highlight the temporal and spatial variability of precipitation trends across different seasons and stations. The identification of changepoints and the analysis of the slopes between them are crucial for understanding the dynamics of regional precipitation patterns. By examining these aspects, we can establish relationships with the changepoints and slopes in the Sea Surface Temperature Anomalies (SSTA) time series.

Table 4.3 Summary of Changepoints and Trends for Winter.

Number	No. Changepoints	No. Changepoint probability	Location	Probability of Location	Trend
49866	0	0.7824	-	-	pos
47772	0	0.4956	-	-	neg
48758	1	0.3988	2016	0.4782	neg/neg
43603	1	0.4744	1995/2011	0.7348	pos/pos/neg
48014	0	0.474	-	-	neg
43855	1	0.4436	1978	0.6211	pos/neg

Table 4.4 Summary of Changepoints and Trends for Spring.

Number	No. Changepoints	No. Changepoint probability	Location	Probability of Location	Trend
48966	0	0.7804	-	-	pos
47772	0	0.9372	-	-	neg
48758	0	0.8352	-	-	pos
43603	1	0.3752	1992	0.5571	neg/neg
48014	0	0.9224	-	-	neg
43855	1	0.8424	1985	0.2739	pos/neg

Table 4.5 Summary of Changepoints and Trends for Summer.

Number	No. Changepoints	No. Changepoint probability	Location	Probability of Location	Trend
49866	1	0.378	1999	0.2519	pos/neg
47772	2	0.4956	2004/2012	0.3393/0.7464	pos/pos/neg
48758	0	0.4836	-	-	neg
43603	0	0.574	-	-	pos
48014	1	0.5536	1995	0.146	neg/pos
43855	2	0.4424	1984/2002	0.6835/0.6925	pos/neg/pos

Table 4.6 Summary of Changepoints and Trends for Autumn.

Station	No. Changepoints	No. Changepoint probability	Location	Probability of Location	Trend
49866	0	0.808	-	-	pos
47772	1	0.7896	1997	0.2781	neg/neg
48758	1	0.1954	1989	0.4782	neg/neg
43603	0	0.7708	-	-	pos
48014	0	0.5844	-	-	neg
43855	0	0.5076	-	-	pos

Building upon this approach, analyzing station 043855 (Hayfield) during the summer months (June–August) offers a detailed perspective on the relationship between local precipitation trends and SSTA. The precipitation data at Hayfield exhibits significant fluctuations and notable shifts in trends over the examined period. In contrast, the SSTA at point P55 between 1981 and 2021 shows a smoothly increased trend after 2002. This case study exemplifies how the identification of changepoints and slopes, along with the calculation of PS ratio values, can reveal insights into how local precipitation patterns relate with broader climatic factors like Sea Surface Temperature Anomalies (See Figure 4.4).

Illustrating the probability of trend changes, we utilize bar charts where red and blue bars represent negative and positive trends, respectively. As shown in Figure 4.5, the sea surface temperature anomalies (SSTA) at point P55 exhibit predominantly positive trends from 1981 to 2001. However, starting in 2002, there is a noticeable decrease in the probability of positive trends. This shift aligns with a changepoint detected in 2002.

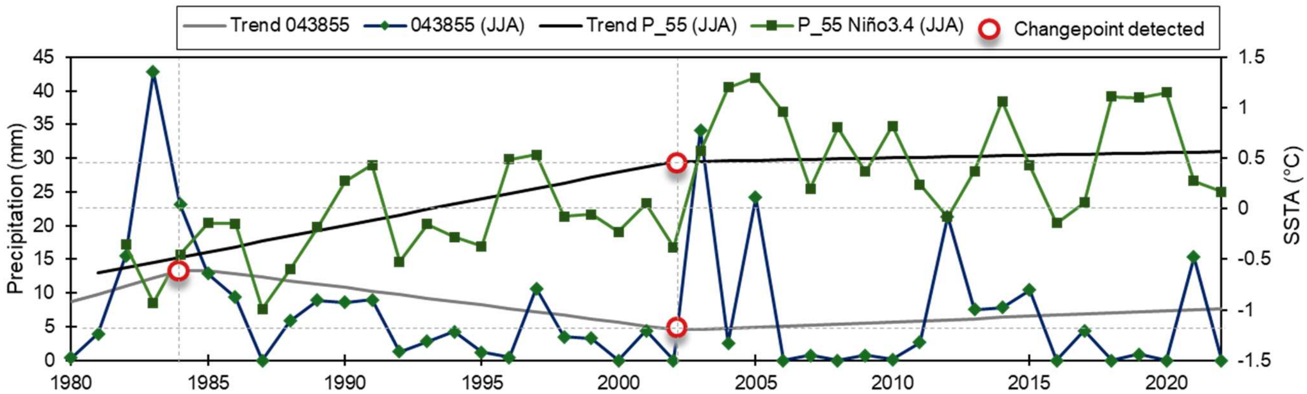

Figure 4.4 Precipitation (043855) and SSTA (P55) time series for Summer (JJA).

From that point onward, higher values of red bars are observed, signaling an increased likelihood of negative trends. When compared with Figure 4.4, it becomes apparent that the overall trend in the second segment remains slightly positive but is less pronounced than in the first segment. This suggests that during our iterations, there are values contributing to a weakening of the positive trend or even introducing negative trend components. This allows us to infer that the behavior of the SSTA trends has changed since 2002, showing a clear variation of the Sea Surface Temperaures at point P55.

Conversely, the precipitation trends at Hayfield station display a distinct pattern compared to the SSTA at point P55. During the early 1980, specifically in 1981, 1982, and 1983, the precipitation data shows a higher probability of positive trends, indicated by prominent blue bars in our bar charts. However, starting in 1984, this pattern reverses. There is a noticeable decrease in the probability of positive trends and an increase in negative trends, marked by the emergence of red bars. Following 1984, the likelihood of positive slopes continues to decline, indicating a sustained period of negative or less positive precipitation trends. Notably, around 2002, there is a resurgence in positive trend probabilities, suggesting a potential changepoint in the precipitation data.

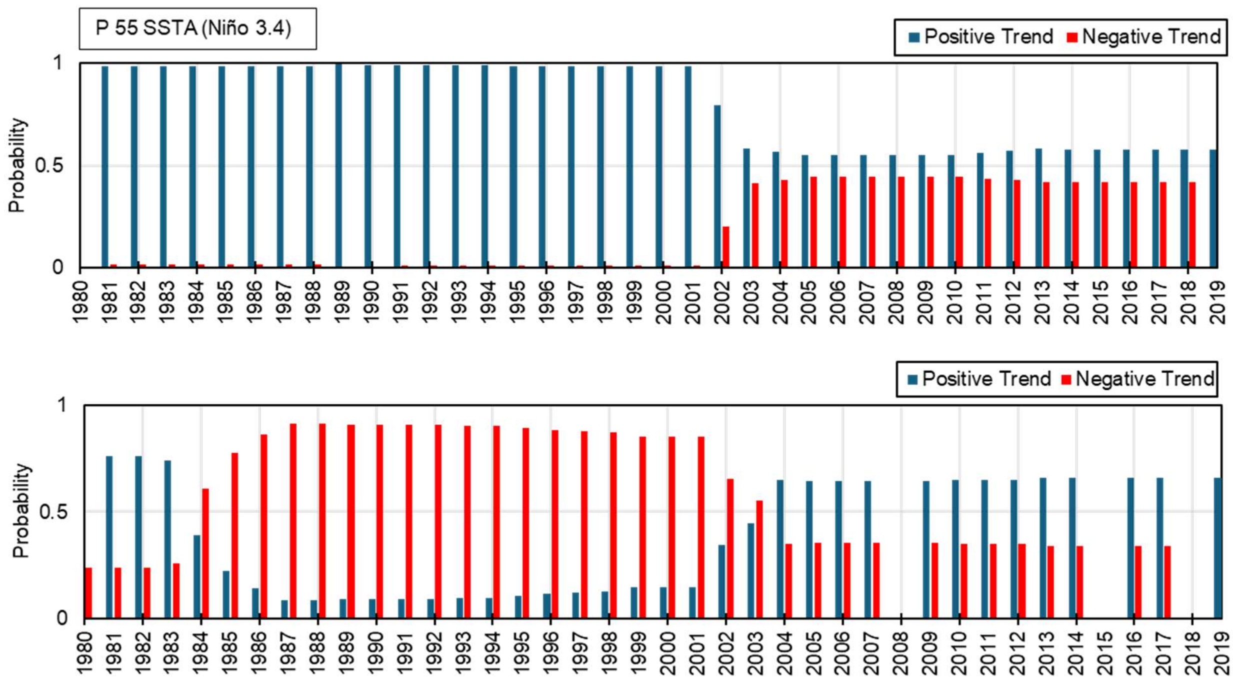

Figure 4.5 Slope probability for P55 and Precipitation (043855).

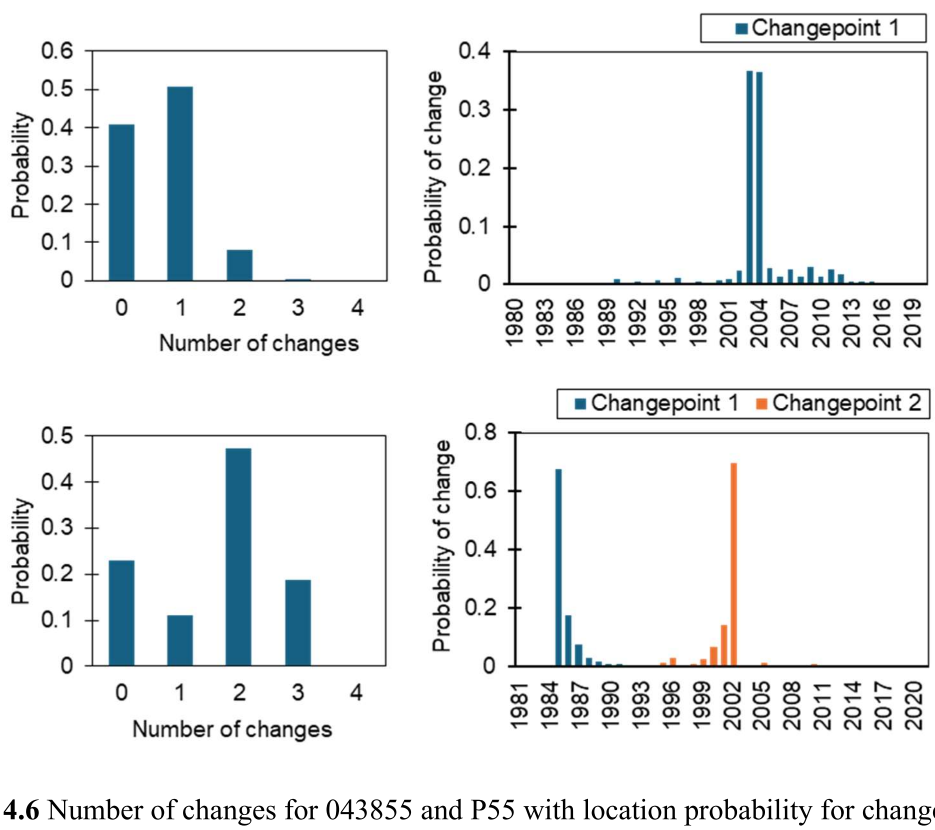

Figure 4.6 Number of changes for 043855 and P55 with location probability for changepoints.

Our analysis confirms this by identifying a 48% probability of two changepoints occurring between 1984 and 2002 in the precipitation data, as depicted in Figure 4.6. This indicates significant shifts in the precipitation trends during this period, aligning with the changes observed in the SSTA data.

When applying the similarity criterion between the precipitation at Hayfield and the SSTA at point P55, it becomes crucial to compare both the probabilities of changepoints and the signs of the trends for each corresponding segment. By aligning the segments where changepoints occur and assessing whether the trend signs (positive or negative) coincide, we derive a single similarity value, denoted as PS, assigned to this specific station and SSTA point combination. This comparative analysis allows us to quantify the degree of relation between local precipitation patterns and Sea Surface Temperature Anomalies.

4.4.2. Region of Influence Map

Figures 4.7–4.12 present the ROI analysis, revealing the dynamic and non-stationary nature of teleconnection patterns across seasons. Table 4.7 summarizes key statistics, including maximum (Max PS) and minimum (Min PS) similarity values, associated grid points (e.g., P_69), and standard deviations (SD) for each station. Coastal stations such as 047772 (San Francisco Downtown) and 048014 (Saugus PWR) exhibit consistently high Max PS values (0.94565 and 0.9028, respectively) at oceanic grid point P_69, indicating robust and stable teleconnections with Central Pacific SST anomalies (Figures 4.7a, 4.9a, 4.10a). These findings align with the established dominance of ENSO in driving winter precipitation variability along the California coast (Ropelewski and Halpert, 1986; Dettinger et al., 1998). In contrast, inland stations like 043855 (Hayfield) show lower and more variable PS values (e.g., Max PS = 0.6123, SD = 0.15), reflecting weaker or intermittent teleconnection influences, a pattern consistent with the spatially heterogeneous impacts of ENSO documented by González-Pérez et al. (2022).

Temporal variability is evident in seasonal shifts of dominant teleconnection regions. For instance, 049866 (Yreka) transitions from grid maximum value at point P_66 (winter) to P_34 (spring), accompanied by increased variability (SD = 0.20707; Figure 4.7b). This phase shift mirrors the sub seasonal evolution of ENSO teleconnections, where Central Pacific SST anomalies exert delayed or modified impacts on Northern California precipitation (Gershunov and Barnett, 1998; González-Pérez et al., 2022). Coastal stations like 047772 maintain strong teleconnections but shift their dominant regions seasonally (e.g., P_69 in winter to P_45 in spring), underscoring the dynamic interplay between oceanic anomalies and local hydroclimatic responses.

Seasonal weakening of teleconnections is observed across all stations, with Max PS values declining sharply (e.g., 049866 drops to 0.426887 at P_12 in summer). During these periods, regions of influence shift toward the Central Pacific (Figures 4.9, 4.10), suggesting the emergence of secondary drivers like the (PMM) or intra-seasonal Madden-Julian Oscillation (MJO) activity (Zhang et al., 2018). These patterns align with studies showing reduced ENSO coherence in summer due to diminished ocean-atmosphere coupling (Hu et al., 2019).

Table 5.7 Summary of Maximum and Minimum PS Values.

Station	Season	Max PS	Max Loc	Min PS	Min Loc	SD
49866	Winter	0.82985	P_66	0.08142	P_36	0.1877
49866	Spring	0.85211	P_34	0.09468	P_46	0.20707
49866	Summer	0.42689	P_12	0.19958	P_95	0.06296
49866	Autumn	0.84673	P_66	0.0913	P_4	0.20646
47772	Winter	0.94565	P_69	0.0963	P_14	0.20552
47772	Spring	0.83962	P_98	0.04462	P_36	0.15635
47772	Summer	0.42666	P_67	0.13322	P_95	0.04847
47772	Autumn	0.95152	P_66	0.05614	P_4	0.24682
48758	Winter	0.53465	P_34	0.14655	P_36	0.10444
48758	Spring	0.84052	P_34	0.10889	P_46	0.19764
48758	Summer	0.64942	P_12	0.23768	P_35	0.12155
48758	Autumn	0.34018	P_55	0.18303	P_23	0.05112
43603	Winter	0.50162	P_66	0.13358	P_36	0.09449
43603	Spring	0.47815	P_34	0.25307	P_47	0.06893
43603	Summer	0.69962	P_12	0.18043	P_70	0.14782
43603	Autumn	0.90061	P_66	0.0794	P_4	0.22849
48014	Winter	0.9028	P_69	0.10133	P_14	0.19321
48014	Spring	0.78973	P_98	0.04625	P_36	0.14705
48014	Summer	0.43618	P_31	0.10721	P_70	0.08829
48014	Autumn	0.28285	P_59	0.16986	P_33	0.03175
43855	Winter	0.56647	P_69	0.15751	P_14	0.09708
43855	Spring	0.45336	P_98	0.09071	P_35	0.07934
43855	Summer	0.38397	P_98	0.10647	P_22	0.06541
43855	Autumn	0.63697	P_66	0.17634	P_4	0.12362

A resurgence in teleconnection strength occurs in autumn, particularly for coastal stations like 047772 (Max PS = 0.951515) and 043603 (Death Valley) (Max PS = 0.90061), coinciding with the re-intensification of ENSO-driven SST anomalies (Figure 4.10). These results corroborate the biennial rhythm of ENSO impacts in California, where autumn/winter phases amplify teleconnection signals (Leathers et al., 1991; Jong et al., 2016).

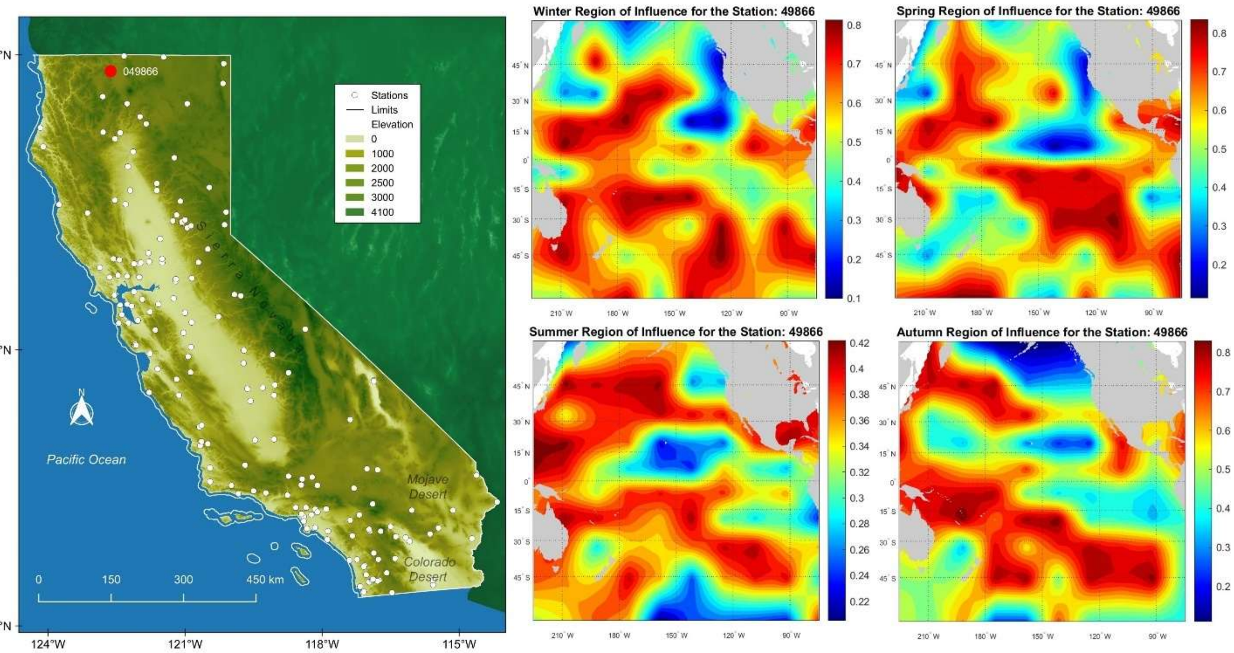

Figure 4.7 Region of Influence for Station 049866.

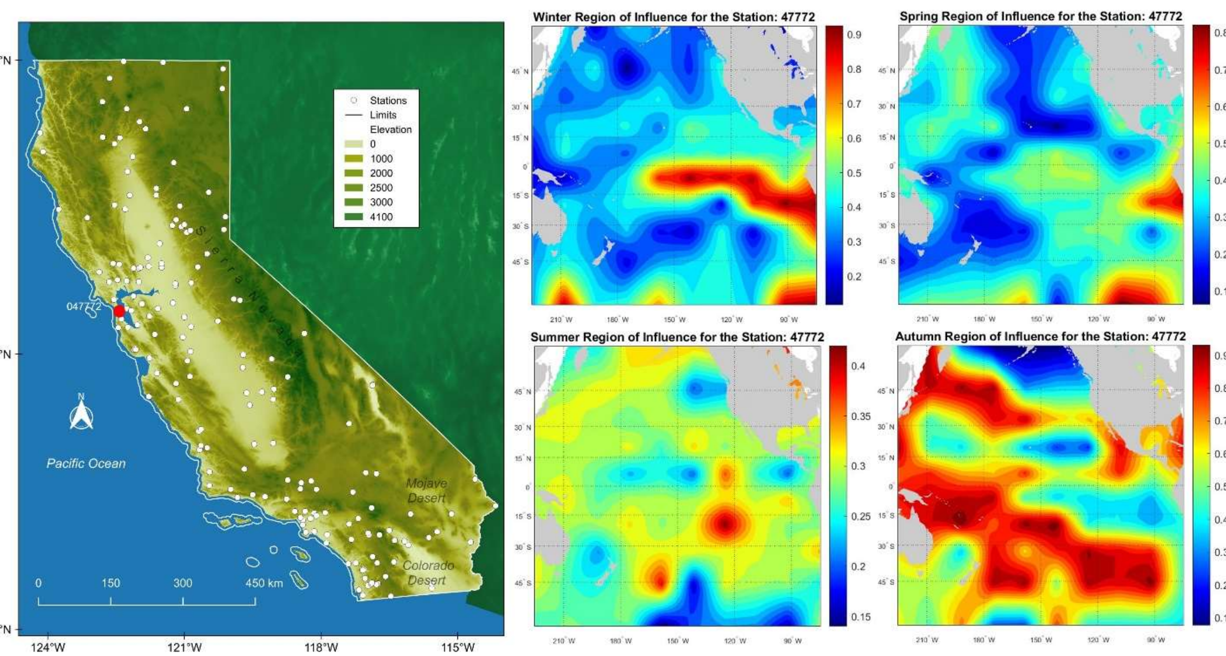

Figure 4.8 Region of Influence for Station 047772.

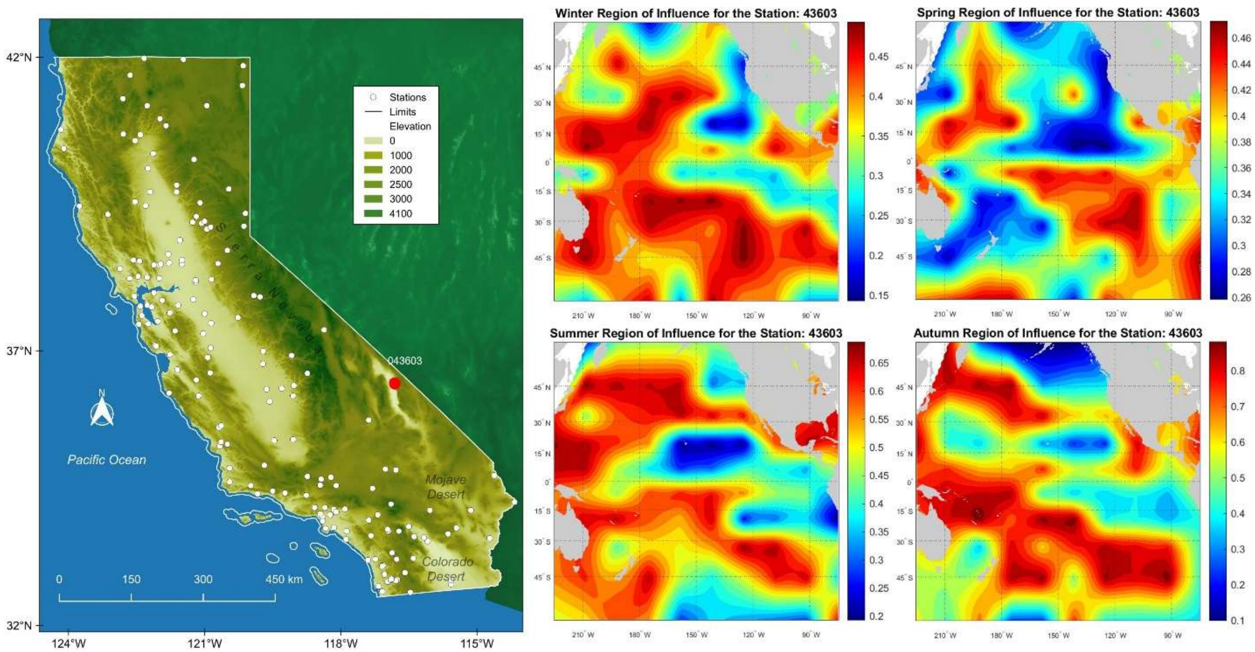

Figure 4.9 Region of Influence for Station 043603.

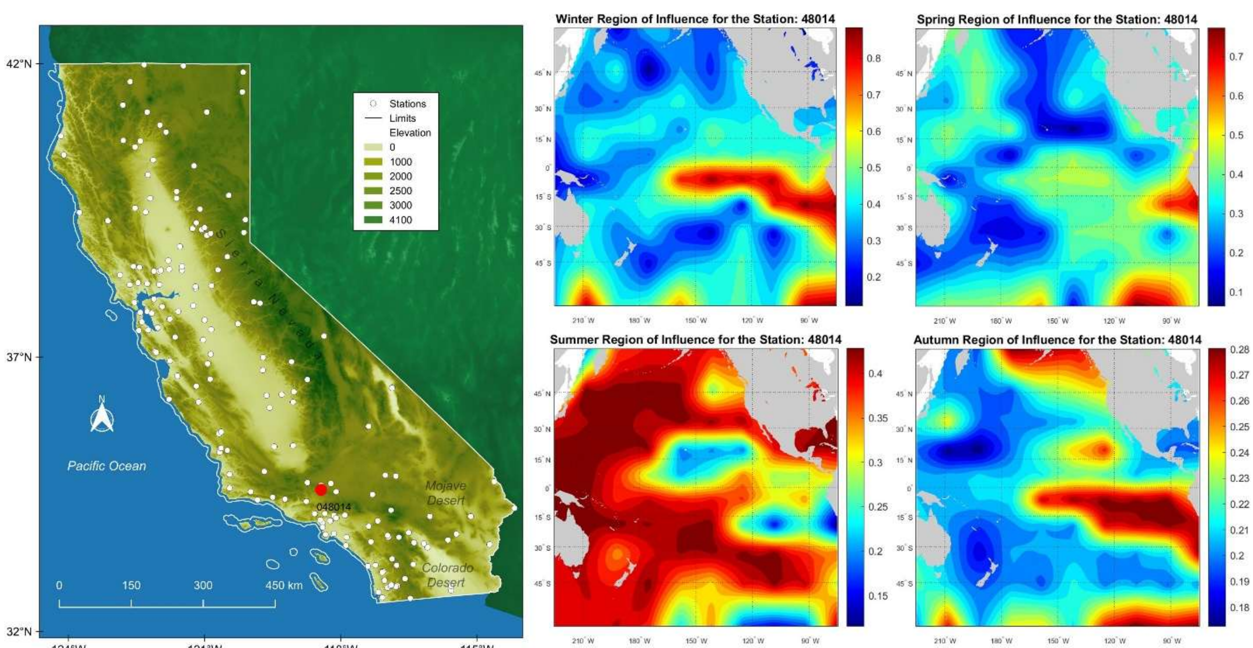

Figure 4.10 Region of Influence for Station 048014.

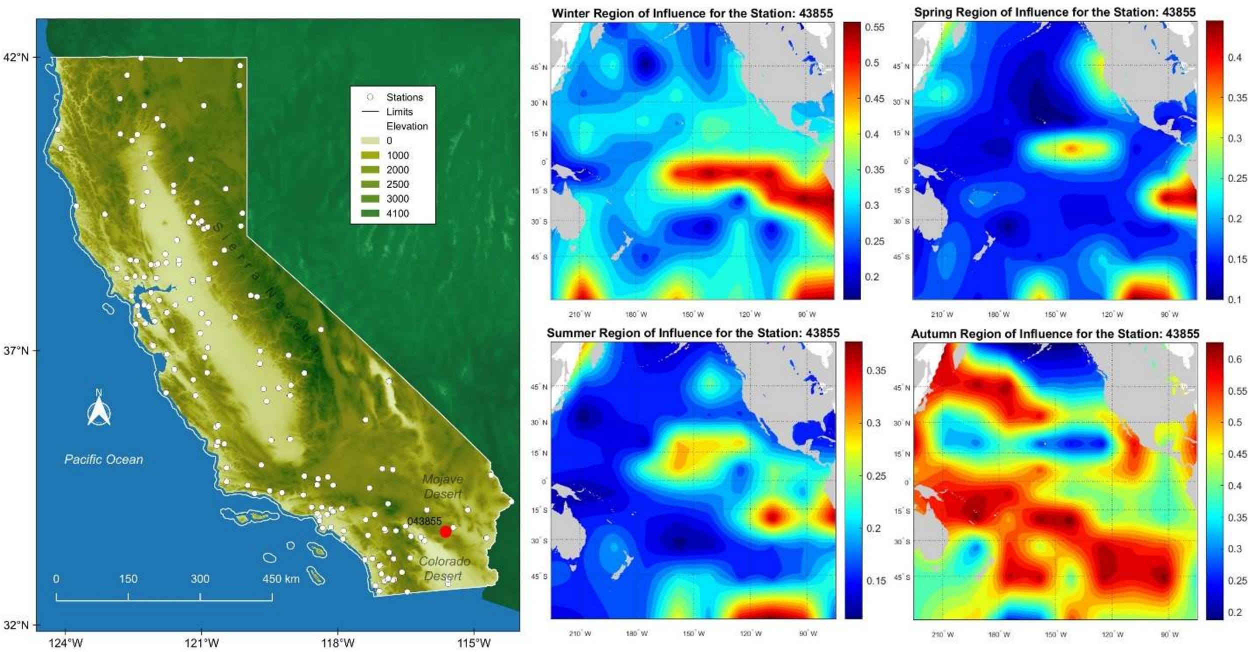

Figure 4.11 Region of Influence for Station 043855.

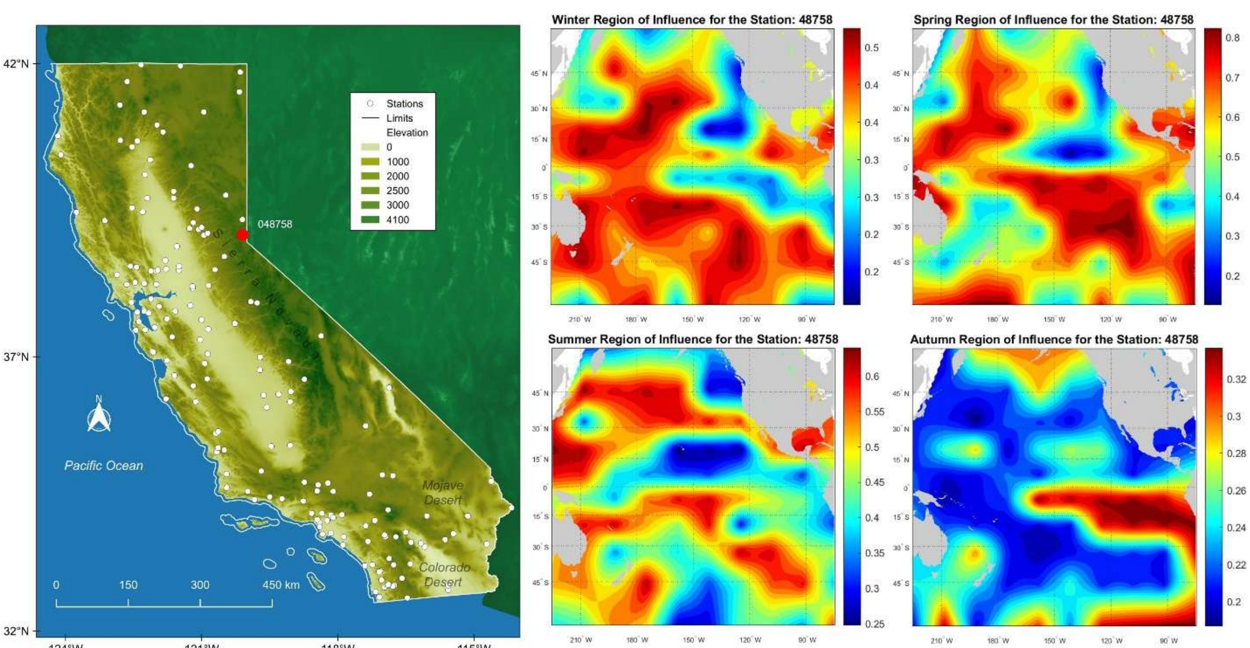

Figure 4.12 Region of Influence for Station 048758.

4.4.3. Discussion

This study advances conventional frameworks by defining station-specific ROIs through the PS similarity measure, a novel metric derived from changepoint analysis that captures nonlinear and non-stationary relationships between precipitation and oceanic drivers. Unlike prior approaches that aggregate stations into broad regions (Dettinger et al., 1998; Ropelewski and Halpert, 1986), our method isolates localized drivers, revealing stark contrasts even between neighboring stations. For example, 049866 (Yreka) exhibits heightened sensitivity to Central Pacific SST anomalies (ROI: P_66) in winter/spring, while 043603 (Death Valley) responds strongly to resurgent ENSO signals (ROI: P_34) in autumn, patterns obscured in regionalized models (González-Pérez et al., 2022).

The PS measure improves upon traditional linear correlation methods, which fail to resolve nonlinear teleconnections. It also surpasses wavelet analysis by providing time-specific quantification of relationships while retaining linear interpretability (e.g., PS = 0.9 implies 90% alignment in number of changepoints detected and trend direction between station and oceanic grid point). This innovation is critical in California, where complex topography amplifies localized responses to Pacific SST anomalies (Neelin et al., 2013; Ralph et al., 2019). Crucially, our approach assigns unique ROIs to each station, enabling tailored predictors for hydrological modeling. Traditional methods prescribe fixed oceanic regions, such as Niño 3.4 for all stations (Dettinger et al., 1998), ignoring subregional variability. For example, Death Valley (043603) and Tahoe City (048758) share proximity but exhibit distinct autumn ROIs (P_45 vs. P_12), highlighting how localized SST gradients drive disparate precipitation outcomes. This customization is particularly valuable during ENSO-neutral or PDO-transition phases, where non-stationary teleconnections dominate (Mantua and Hare, 2002; Wang et al., 2022). The observed heterogeneity aligns with studies of ENSO teleconnections, where topographic barriers and land-atmosphere feedbacks modulate precipitation (Neelin et al., 2013). Temporal shifts in ROI dominance (e.g., Yreka's transition from P_66 to P_34) further reflect the Pacific Decadal Oscillation's (PDO) modulation of ENSO's SST gradients (Maher et al., 2021). The PS measure's integration of changepoint detection allows these non-stationary interactions to be isolated, addressing a key limitation of static methods like PCA or fixed regionalization (Milly et al., 2008).By prioritizing localized rather than broad-scale regional analyses, we illuminate how a single ENSO event can yield markedly different precipitation outcomes even in close geographical proximity. For instance, station 047772 sees a pronounced intensification of precipitation, whereas station 043855 simultaneously experiences a reduction, contrasting effects that remain invisible under linear and aggregated models (Dettinger et al., 1998; Milly et al., 2008).

4.5. Conclusions

This study provides a comprehensive analysis of the dynamic and spatially variable nature of teleconnections, emphasizing their influence on precipitation patterns across multiple stations in California. By introducing a changepoint-based similarity measure (PS), we capture nonlinear and non-stationary relationships between oceanic and terrestrial time series—a key advancement over purely linear correlation methods. Using PS, we delineate station-specific Regions of Influence (ROIs), ensuring each station is associated with the areas of the Pacific Ocean most relevant to its precipitation drivers. This customized approach stands in contrast to traditional methods, which often rely on a fixed oceanic region for all stations or broad-scale wavelet analyses that may overlook critical temporal shifts.

Applying PS to analyze teleconnections between California precipitation and the Pacific Ocean reveals important seasonal dynamics. Coastal stations like San Francisco Downtown (047772) and Saugus PWR (048014) experience consistently strong teleconnection influences, especially during winter and autumn, aligning with dominant ENSO-driven processes. Conversely, inland stations such as Death Valley National Park (043603) and Yreka (049866) exhibit more localized or weaker teleconnections, reflecting heavier reliance on local climatic factors. These seasonal variations highlight the evolving nature of large-scale climate drivers, with winter and autumn emerging as periods of heightened teleconnection impact, while summer exhibits reduced and fragmented regions of influence. Notably, some stations exhibit similar patterns of teleconnection influence, suggesting shared climatic drivers or geographic proximity. While station-level precision is a core strength of this framework, these observed similarities may merit clustering analyses to refine our understanding of subregional teleconnection groupings. Such clustering could preserve unique station identities while enabling more robust insights into collective teleconnection behaviours, ultimately enhancing forecasting accuracy and improving regional climate models.

Overall, this novel, station-specific ROI approach demonstrates clear benefits for precipitation forecasting, water resource management, and adaptive strategies to mitigate climate variability and change. Future work could integrate additional climatic indices (e.g., NAO, PDO phases) and extend the method to diverse climatic regions, further validating the utility of changepoint-based similarity measures in capturing complex, non-stationary ocean–land interactions.

Chapter 5 Clustering Hydroclimatic Regions in California Using Point–Slope Similarity and Partial Correlation[2]

Carlos A. Rosas-Cabello[1], Mohammad H. Alobaidi[2], Fateh Chebana[3], Ousmane Seidou[1]

[1] Faculty of Engineering, University of Ottawa, Ottawa, ON, Canada

[2] Department of Civil Engineering, McGill University, Montréal, QC, Canada

[3] Centre Eau Terre Environnement, Institut National de la Recherche Scientifique, Québec, QC, Canada

Abstract

Accurate delineation of hydrologically homogeneous regions is essential for climate-informed water-resource planning. This study clusters California precipitation stations into regions based on their response to the Niño 3.4 index using two methods: a linear partial-Spearman (LPS) approach and a nonlinear Point–Slope (NPS) similarity framework. Using the 1981-2021 monthly data from 178 gauges (1981–2021), each method was used to identify groups of stations that respond similarly to the interannual El-Niño-Southern Oscillation (ENSO) variability. The LPS model isolates the correlation between each station and Niño 3.4, whereas the NPS method captures nonstationary behaviour by detecting synchronous changepoints and consistent trends in each precipitation series relative to the index. We then feed these structural similarities into a spatially constrained k-means algorithm. Both methods delineate hydrological regions, but the PS approach produces more internally consistent clusters that align with known physiographic transitions. Two dominant groups emerge in peak winter (January and February), and three appear in the transitional

[2] A version of this chapter has been submitted to the Journal of Hydrology: Regional Studies and is currently under revision at the time of the thesis submission.

months (March, July and September). Elevation seems to modulate teleconnection strength but does not control it, as several high-elevation sites fall within the strongly ENSO-sensitive cluster. NPS-derived composites show a pronounced amplification of winter rainfall, exceeding the increases observed in other seasons and maintaining a stronger structural similarity to Niño 3.4 than the LPS-derived composites. These results confirm that the NPS framework better captures nonlinearity and structural variability, providing a more adaptive basis for teleconnection-informed regionalization.

Keywords Teleconnections, Sea Surface Temperature Anomalies, Precipitation, California, Niño Regions, Bayesian Changepoint Detection, Climate Variability

5.1.Introduction

Detecting spatiotemporal trends in precipitation and streamflow for forecasting purposes remains one of the most persistent challenges in hydrology (Blöschl et al., 2019). Climate variability and land-use changes frequently mask or distort the underlying signal. Misattributing these drivers can skew hydrological projections and undermine adaptation planning measures (Milly et al., 2008; Zhang et al., 2014; Iliopoulou and Koutsoyiannis, 2020).

Regionalization, which clusters stations that respond similarly to shared climate controls, provides a practical way to disentangle these intertwined influences and reduce uncertainty (Hrachowitz et al., 2013; Rosas-Cabello et al., 2025). Yet static regional boundaries fail when precipitation regimes shift (Kundzewicz and Robson, 2004). Existing regionalization methods fall into three categories—physiographic, geostatistical, and statistical—each suited to specific contexts. Physiographic grouping transfers knowledge across similar landforms but breaks down in complex terrain where microclimates dominate (Saharia et al., 2021; Bárdossy and Pegram, 2011). Simple geostatistical tools such as Thiessen polygons and inverse-distance weighting are efficient yet miss fine-scale variability (Koutsoyiannis and Langousis, 2011). Data-driven statistical clustering is flexible, but performance deteriorates under nonstationary forcing and short records (Goovaerts, 2000).

Regionalization is especially valuable when external climate modes impose coherent spatial signals. In California, El Niño–Southern Oscillation (ENSO) is known to modulate storm-track latitude and the frequency of atmospheric rivers, creating sharp north–south and elevational gradients in winter precipitation (Dettinger et al., 2011; Ralph and Dettinger, 2012). Defining regions around this teleconnection rather than around topography alone can therefore provide more meaningful domains for water-resource management.

Capturing the ENSO imprint, however, is methodologically demanding. ENSO's intensity, phase, and longitudinal position vary from event to event, introducing nonlinearity and nonstationarity into ocean–atmosphere–land links (Capotondi et al., 2015). Linear tools such as simple correlations or Empirical Orthogonal Functions (EOFs) highlight the canonical signal but fail to capture regime shifts and seasonal lags.

Principal Component Analysis (PCA) is widely used to reduce dimensionality before clustering. It preserves dominant precipitation patterns while minimizing redundancy (El Alaoui El Fels et al., 2020). González-Pérez et al. (2022) coupled partial Spearman correlation with PCA to delineate four ENSO-related regions in California, yet their framework did not address nonstationarity. Morabbi et al. (2022) introduced changepoint-based regionalization, but changepoints alone can be weak discriminants (Volpi et al., 2024).

Metrics that combine changepoint detection with trend information offer a way to diagnose both abrupt and gradual responses within a single framework.

This study addresses two key questions: (1) Can a changepoint-aware similarity measure delineate ENSO-sensitive precipitation regions more consistently than a linear correlation controlling for the confounding effect of time (i.e., partial Spearman correlation)? (2) Does elevation retain explanatory power once nonstationarity is considered? Addressing these questions will clarify how to translate oceanic signals into actionable regional boundaries that inform reservoir operations, flood-control rules, and drought-risk assessments across California’s diverse hydroclimates.

Building on earlier work, including the changepoint-based regionalization of Morabbi et al. (2022) and the nonstationary analyses of Seidou and Ouarda (2007), we incorporate trend information into a Nonlinear Point–Slope (NPS) similarity metric and benchmark it against partial Spearman correlation for 178 California stations (1981–2021). The NPS metric quantifies the concordance between changepoint timing and trend direction, and we identify clusters with a spatially constrained k-means algorithm optimized via the elbow method. The following sections present the NPS formulation, the clustering framework, and its evaluation relative to the linear benchmark.

5.2.Methodology

We employ two modeling strategies in this study. The first is a nonlinear, nonstationary approach based on changepoint and slope analysis (the NPS method). The second is a traditional linear, stationary framework that uses partial Spearman correlation to uncover spatial teleconnection modes (LPS). Figure 5.1 summarizes the methodological workflow.

5.2.1. The NPS-Based regionalization

5.2.1.1. Changepoint Detection and Trend Analysis

Changepoint detection methods have become essential tools for identifying nonstationarities in climate and hydrological time series. These techniques enable the delineation of homogeneous regions by precisely characterizing abrupt shifts in trends, means, or variances (Reeves et al., 2007; Rodionov, 2004; Killick et al., 2012; Volpi et al., 2024). By challenging the traditional assumption of temporal homogeneity in regional variables (Hosking and Wallis, 1997), they reduce the risk of aggregating subregions with divergent trend dynamics, an issue that can obscure structural differences and compromise regional analyses (Villarini et al., 2009; Ehsanzadeh et al., 2016). Integrating changepoint detection helps partition regions based on consistent statistical properties, thereby improving the reliability of flood-frequency estimation and water-resource planning under nonstationary conditions (Merz et al., 2014; Slater et al., 2021). We adopt the Bayesian changepoint detection framework proposed by Seidou and Ouarda (2007), which identifies abrupt changes in hydrological time series by combining prior knowledge with observed data.

The method infers posterior probabilities for both the number and locations of changepoints. Unlike traditional techniques that assume a fixed number of shifts, this Bayesian approach flexibly captures structural changes either in the variables themselves or in the relationships between predictors and responses. It assumes normally distributed residuals and incorporates a carefully chosen prior to enhance the detection of subtle signals. Although the method does not include prewhitening or block bootstrapping to address autocorrelation (Hamed and Rao, 1998; Yue et al., 2002), its robust structure has been shown to identify the most probable changepoints reliably, as confirmed by several studies (e.g., Vincent, 1998; Ouarda et al., 2014; Naizghi et al., 2016; Morabbi et al., 2022; Rosas-Cabello et al., 2025). We employ a trend-sign analysis to assess the consistency and direction of changes across segments.

This provides valuable insights into the temporal structure of hydrological data, which is critical for understanding evolving climatic conditions and supporting adaptive management strategies (Mudelsee, 2019). Let n be the number of observations and d the number of independent variables. The dependent variable y_j (where $j = 1, \dots, n$) is modeled as a linear function of predictors x_{kj} (where $k = 1, \dots, d$ and $j = 1, \dots, n$) and the residuals represented by ε_j , as follows:

$$y_j = \sum_{k=1}^{d} \theta_k \, x_{kj} + \varepsilon_j \tag{5.1}$$

where θ_k are the regression coefficients for the independent variables.

In multiple changepoint detection, the goal is to identify time points at which the relationship between x_j and y_j changes significantly. The algorithm generates a set of possible partitioning schemes; each composed of different combinations of changepoints $\{t_1^{\sim k}, t_2^{\sim k}, \dots, t_{m_k}^{\sim k}\}$. From this set, the method estimates the posterior probabilities of the number and locations of changepoints.

Once a set of changepoints $\{t_1^k, t_2^k, \dots, t_{m_k}^k\}$ is identified, we divide the full time series is divided into $m_k + 1$ segments by including the initial time t_0^k and the series endpoint $t_{m_{k+1}}^k$. For each segment ℓ, defined between $t_{\ell-1}^k$ and t_ℓ^k, we fit a simple linear regression to estimate the intercept $\beta_{0\ell}$ and slope $\beta_{1\ell}$ (see Figure 5.2). This procedure captures gradual trends within each segment, complementing the abrupt shifts identified by the Bayesian approach and offering a more comprehensive perspective of nonstationary behaviors in climate-hydrology time series.

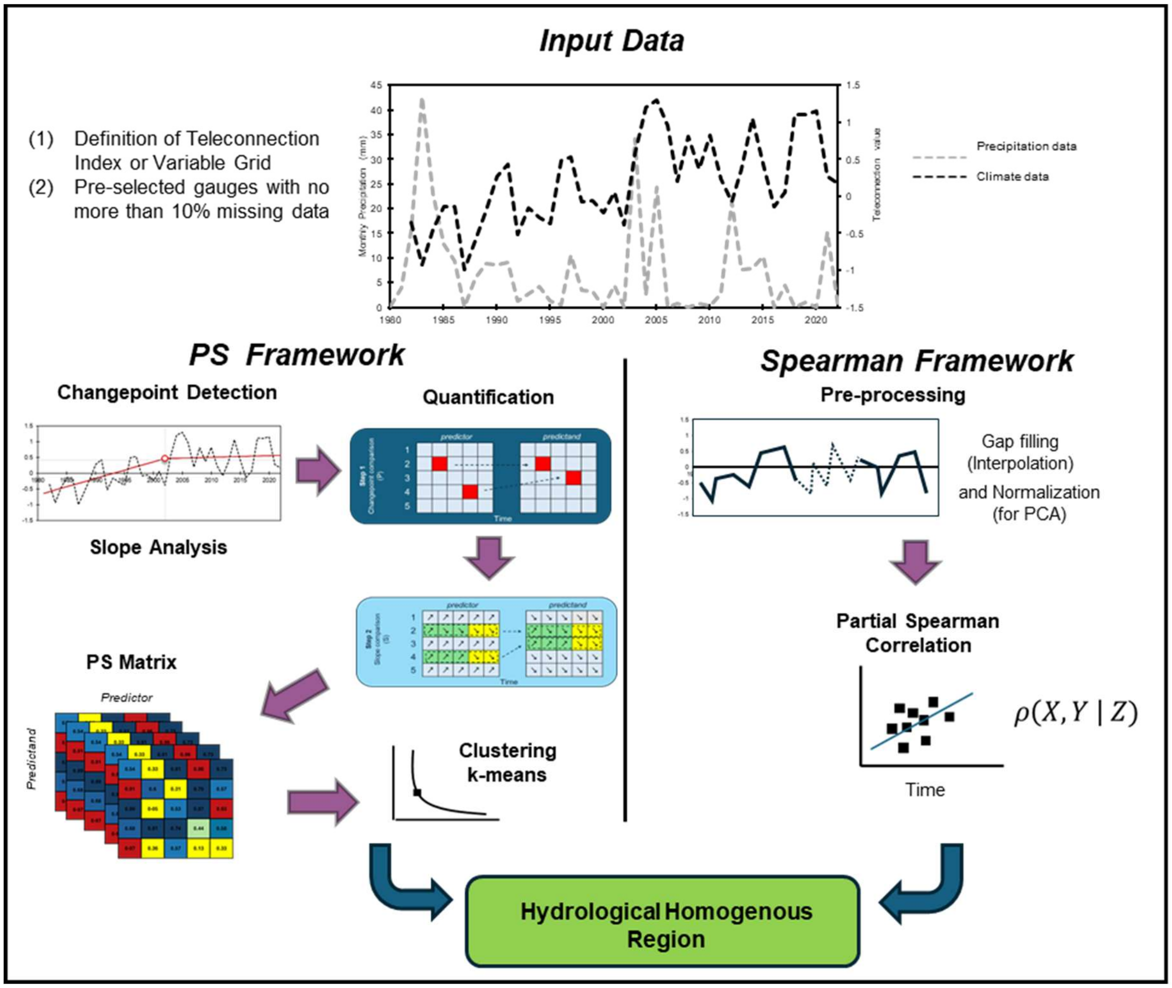

Figure 5.1 Workflow for Regionalization Using Partial Correlation and PS Similarity.

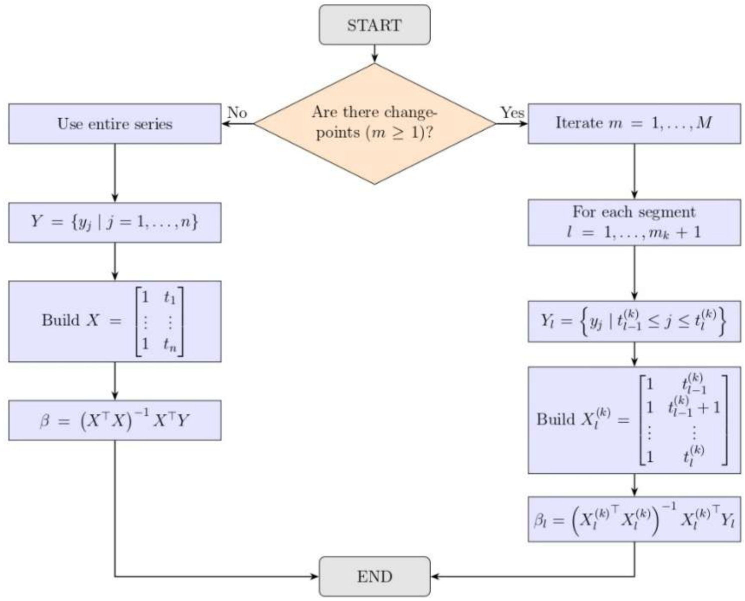

Figure 5.2 Flowchart of Segmented Regression Based on Changepoint Detection.

5.2.1.2. The NPS Similarity Measure

The Point-Slope (PS) similarity measure, proposed by Rosas-Cabello et al. (2025), combines abrupt changepoints and segment trends to quantify the structural similarity between pairs of time series. For each pair, changepoints are identified, and trends are estimated within segments. For row i in $P_{\text{predictor}}$ and row j in $P_{\text{predictant}}$, the proportion of matching changepoints is given by:

$$\mathrm{P} = \frac{1}{mn} \sum_{i=1}^{m} \sum_{j=1}^{n} \frac{\sum_{t \in Y} I\left(P_{\text{predictor},i}(t) = 1 \wedge P_{\text{predictand},j}(t) = 1\right)}{\max\left(\sum_{t \in Y} P_{\text{predictor},i}\,(t), \sum_{t \in Y} P_{\text{predictand},j}\,(t)\right)} \tag{5.2}$$

where $I(\cdot)$ is the indicator function. This expression evaluates the alignment of breakpoints across the two series, yielding a score in [0,1], with 1 signifying perfect changepoint agreement.Next, we compare the slope matrices$S_{\text{predictor}}$ and $S_{\text{predictand}}$ focusing on the sign of the slope. For row i in $S_{\text{predictor}}$ and row j in $S_{\text{predictant}}$, the proportion of matching slope sign is:

$$S = \frac{1}{mn}\sum_{i=1}^{m}\sum_{j=1}^{n}\frac{\sum_{t\in Y} I\left(\text{sign}\left(S_{\text{predictor},i}(t)\right) = \text{sign}\left(S_{\text{predictand},j}(t)\right)\right)}{|Y|} \tag{5.3}$$

The PS score ($0 \leq PS \leq 1$) combines two components: changepoint alignment (P) and slope direction concordance (S) as follows:

$$PS = \frac{(P+S)}{2} \tag{5.4}$$

This unified index captures both abrupt and gradual changes, allowing for flexible comparison between precipitation and climate index series under nonstationary conditions. The spatial distribution of PS values across all station–index pairs is visualized to detect regions of coherent hydroclimatic behaviour. For each pair of time series, they first identify the most probable changepoints, positions and numbers of abrupt shifts across the entire inference set. The data are then segmented to estimate linear trends within each segment. Higher PS values indicate stronger alignment of changepoints and trends in both series. In practical terms, this measure supports more meaningful clustering and regionalization, enhancing interpretations of how climatic and hydrological processes co-vary over time. Each PS value represents the relationship between a single pair of datasets. For instance, if two meteorological stations are compared, the resulting PS applies only to that station pair. Similarly, comparing a teleconnection signal with a precipitation time series yields one PS value exclusive to those two data sets. Consequently, the total number of PS values corresponds directly to the number of pairs analyzed.

5.2.1.3. NPS-based clustering

We performed clustering for a population of stations based on the NPS values calculated between monthly precipitation records and climate indices. The cluster with the highest PS value represents stations most strongly influenced by oceanic signals. This continuous clustering approach captures subtle spatial coherence in PS similarity and enhances the resolution of hydroclimatic regionalization. We chose k-means for its computational efficiency, straightforward interpretation, and compatibility with methods such as the elbow method for selecting an optimal number of clusters. To further assess cluster coherence, we calculated silhouette scores to evaluate internal consistency and separation between groups. However, hierarchical or other clustering algorithms can be easily adapted to this framework. Each station i is represented by a feature vector x_i . The clustering process seeks to minimize the within-group sum of squared distances:

$$\min_{\{\mu_1, \ldots, \mu_k\}} \sum_{i=1}^{N} \min_{1 \leq j \leq k} \left\| x_i - \mu_j \right\|^2 \tag{5.5}$$

To optimize this clustering, we apply the elbow method, which plots the sum of squared distances or variance against the number of clusters or threshold values. Formally, for a set of k clusters,

$$W_k = \sum_{i=1}^{k} \sum_{x \in C_i} \left\| x - \mu_i \right\|^2 \tag{5.6}$$

Where C_i denotes a cluster i and μ_i its centroid. Plotting W_k against k helps identify the "elbow" point, indicating the optimal k (or threshold) beyond which further clustering yields diminishing returns. This balances accuracy with computational efficiency.

5.2.2. LPS-based regionalization

5.2.2.1. Time-controlled Partial Spearman Correlation

To identify the canonical ENSO signal in California precipitation with a second methodology, we computed partial Spearman correlations between each station's monthly precipitation series and the Niño 3.4 index while controlling for time. This approach isolates the statistical relationship between precipitation and the Niño 3.4 signal and removes potential bias from shared long-term trends (González-Pérez et al., 2022). Before the correlation analysis, we filled missing values in both the precipitation and climate-index series with simple linear interpolation to ensure continuity. Let X denote the precipitation time series at a given station Y the Niño 3.4 index, and Z a linear time vector from 1981 to 2021. The partial Spearman correlation coefficient $\rho_{XY.Z}$ was computed as:

$$\rho_{XY.Z} = \frac{\rho_{XY} - \rho_{XZ}\rho_{YZ}}{\sqrt{(1-\rho^2{}_{XZ})(1-\rho^2{}_{YZ})}} \tag{5.7}$$

Where ρ_{XY} is the Spearman rank correlation between precipitation and Niño 3.4, and ρ_{XZ}, ρ_{YZ} are their respective correlations with time. Stations with statistically significant partial correlations $(p < 0.05)$ were identified as ENSO-sensitive.

To isolate the true teleconnection signal between oceanic indices and precipitation, we calculated partial Spearman correlation while controlling for time. The variable Z is a linear time vector covering the entire study period (1981–2021). This control removes shared background trends, such as long-term warming, drought progression, and large-scale anthropogenic changes, that could bias the correlation. By removing the temporal component, the resulting $\rho_{XY.Z}$ coefficient captures the stationary, monotonic relationship between the climate variable and precipitation, independent of any co-evolution over time.

5.2.1.3. Region delineation

To delineate ENSO-sensitive regions using the partial Spearman correlation model, we adopted a confidence level of 95% ($p < 0.05$) as the threshold for statistical significance. This criterion ensures that only robust and non-spurious station–index relationships are included in the regionalization, filtering out weaker signals that could obscure the canonical ENSO teleconnection. Because this procedure directly reproduces the approach of González-Pérez et al. (2022), it provides a consistent benchmark against which our proposed PS-based methodology can be compared. In this way, the resulting regions can be interpreted not only as a validation exercise but also as a reference framework to evaluate the additional explanatory power provided by changepoint similarity.

5.3. Case Study

5.3.1. Study Area

The complex topography of California plays a critical role in how remote oceanic anomalies influence regional climate patterns (Stagge et al., 2019). Coastal zones, mountain ranges, and desert basins interact in distinct ways with large-scale atmospheric signals. In some areas, orographic uplift enhances precipitation linked to Pacific anomalies, whereas desert regions receive a muted signal. Empirical evidence from Dettinger et al. (2011) shows that topographic variability filters the intensity of remote climate signals such as those related to El Niño–Southern Oscillation (ENSO).

This filtering also shapes their spatial distribution, producing contrasting climate responses across the state. In southern California, the Mojave and Colorado Deserts experience high summer temperatures and low rainfall under persistent subtropical high-pressure systems (Hereford et al., 2004). Farther inland, winter snow accumulation in the Sierra Nevada sustains water resources for urban areas, agriculture, and ecosystems (Cayan et al., 2010;

Dettinger et al., 2011). Along the Pacific coast, a Mediterranean climate dominates wet winters and dry summers, with marine fog and moderate temperatures fostering unique microclimates (Johnstone and Dawson, 2010). In the northern highlands, frequent storms and orographic uplift generate high precipitation essential for reservoir recharge and regional water security (Das et al., 2009).

This climatic diversity increases exposure to variability in large-scale circulation and underscores the need for detailed regionalization. Although many studies examine California climate, localized microclimatic differences remain underrepresented, and the topographic controls on water availability and disaster risk are not fully explored. The 2012–2016 drought, intensified by a persistent Pacific ridge, sharply reduced Sierra Nevada snowpack, while atmospheric-river events have delivered rainfall intense enough to overwhelm flood-control systems (Griffin and Anchukaitis, 2014; Swain et al., 2014; Dettinger, 2011). Because oceanic and atmospheric processes, especially ENSO, interact with topography, integrating regional characteristics into climate models is essential. A clearer understanding of teleconnection-driven variability will improve extreme-event forecasting and water-management strategies, enhancing predictive capacity and policy responses across California.

5.3.2. Precipitation Data

We used monthly rainfall records (millimeters) from the Western Regional Climate Center (https://wrcc.dri.edu/) for 1981–2021. We selected 178 stations that met a strict completeness threshold (≤ 10 % missing values), ensuring robust statewide coverage. Monthly-average plots (Figure 5.3) show marked differences: northern stations receive notably higher precipitation volumes from December through March than southern stations.

5.3.3. Climate Index

Climate variability across the western United States, particularly in California, is largely driven by ocean–atmosphere interactions in the tropical Pacific. Among these, the El Niño–Southern Oscillation (ENSO) exerts a dominant influence by modulating large-scale circulation and moisture transport. Warm-phase events (El Niño) typically enhance California winter precipitation by weakening the trade winds and intensifying storm activity, whereas cold-phase events (La Niña) are often associated with drier conditions and prolonged droughts (Ropelewski and Halpert, 1986; Trenberth et al., 1998; Hoell et al., 2015; Patricola et al., 2019).

We characterize ENSO activity with the Niño 3.4 region (5° S–5° N, 170° W–120° W), which captures the core dynamics of equatorial Pacific variability and serves as the benchmark for defining El Niño and La Niña events (Trenberth and Stepaniak, 2001; NOAA CPC, 2023). Sea-surface-temperature anomalies (SSTAs) in this area are widely recognized as reliable indicators of ENSO phases and their teleconnected impacts on mid-latitude precipitation. The Niño 3.4 index used here was obtained from the NOAA Climate Prediction Center (https://www.cpc.ncep.noaa.gov/data/indices/sstoi.indices). The SSTA values originate from the NOAA/NESDIS/NCEI Daily Optimum Interpolation SST dataset (DOISST v2.1; L'Heureux et al., 2013; Huang et al., 2021) and were aggregated to monthly means to match the temporal resolution of precipitation records from the 178 California stations.

5.4. Results

5.4.1. Changepoint detection and slope analysis

To ensure robustness in changepoint detection, we ran the Bayesian multiple changepoint framework for 2 500 iterations, capturing uncertainty in both the number and timing of shifts across all series. We imposed a 7-year minimum segment length ($l_{min} = 7$) to avoid over-fitting and to ensure that detected breaks represent long-term shifts rather than short-lived ENSO pulses. A sensitivity test (Table 5.1) applied the same algorithm with shorter thresholds (2, 3, and 5 years) and shows that, once the threshold reaches 5 years, both the mean number of changepoints and the probability of detecting at least one break stabilize. The Jensen–Shannon distance (JSD; Stosic et al., 2017; Lv et al., 2023) confirms this: distributions for segment lengths of 5 and 7 years differ only minimally, whereas shorter lengths diverge substantially.

Adopting a long segment length does not erase the imprint of shorter-lived phenomena. Events such as El Niño Modoki (L'Heureux et al., 2013) or any 1–3-year perturbation fall below the 7-year threshold and, therefore, are not counted as explicit changepoints. Because the Point–Slope (PS) metric assigns equal weight to changepoint coincidence and segment-slope concordance, any transient event that tilts the local slope is fully reflected in the similarity score. The Point component, which compares the full posterior distribution of changepoint locations, filters out spurious year-to-year jumps via the 7-year segment criterion, whereas the Slope component captures trend changes caused by subdecadal episodes. Together these elements ensure that both long-term regime shifts and shorter events are represented in the PS similarity. Because record length varies among stations and indices, we conducted all analyses on a common 1981–2021 window to maintain temporal consistency.

During the early months (January–April; Figure 5.4), most northern-coast stations are colored yellow, indicating zero most-probable breaks and thus relatively stable precipitation behavior. Importantly, the map shows only the mode of the posterior; the absence of darker symbols does not imply a lack of breaks, merely a lower detection frequency. Because the clustering procedure ingests the entire posterior distribution of changepoint probabilities and slope estimates, even low-probability breaks contribute to PS scores and can influence the final regional classifications.

In contrast, southwestern California shows a notable concentration of stations with more detected changepoints, represented by darker circles, particularly during June, October, and November.

This spatial clustering suggests significant precipitation variability associated with seasonal transition periods, namely, the shift from spring to summer (June) and from summer to fall (October). Such variability aligns with well-documented teleconnection patterns, including ENSO-related oscillations. Additionally, in May and June the coastal zone displays a homogeneous pattern of changepoints, which contrasts sharply with the adjacent southwestern interior, where at least one significant changepoint is frequently observed.

As summer progresses into July and August, the spatial distribution reveals persistent changepoints across much of the coastal and central regions, reflecting continued homogeneous trends from late spring. However, sporadic darker circles appear in the Sierra Nevada foothills and eastern desert regions, suggesting localized regime shifts potentially linked to monsoonal moisture influxes or convective precipitation during the summer peak (Adams and Comrie, 1997). By September, a transitional pattern emerges, scattered stations in central California show moderate changepoint probabilities, bridging the stable summer conditions and approaching autumn variability. In December, northern California stations again appear yellow, indicating stabilized precipitation trends as winter rainfall patterns dominate.

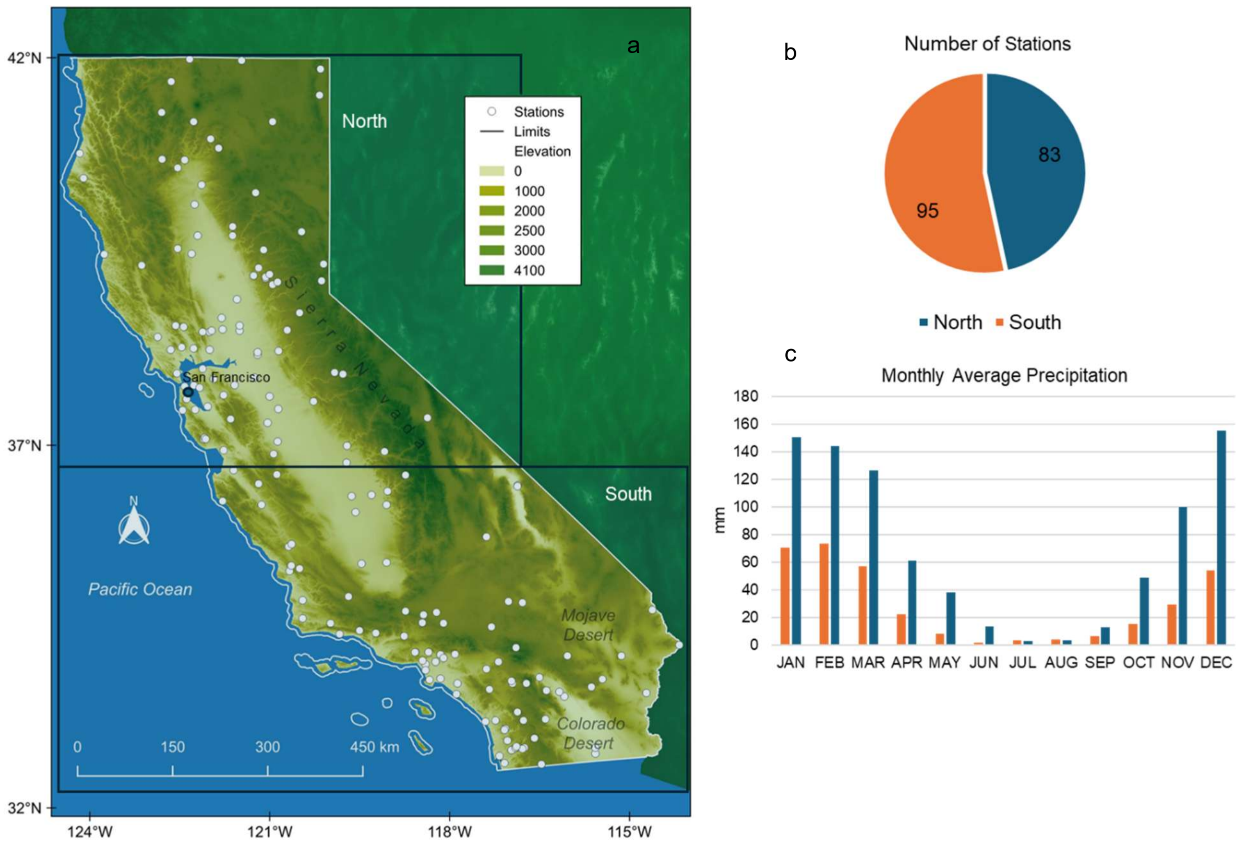

Figure 5.3 Precipitation Data: (a) Spatial Distribution of Meteorological Stations; (b) Number of Stations in the North and South; (c) Monthly Average Precipitation in Each Area.

Table 5.1 Sensitivity of Niño 3.4 changepoints (CP) detection to segment length.

l_{min}	**Mean No. of changepoints $\mathbb{E}$ [CP]**	**Probability ($\geq$ 1 CP)**	**JSD** vs **7 years**
2	1.02	0.54	0.31
3	0.68	0.37	0.18
5	0.44	0.3	0.06
7	0.17	0.12	-

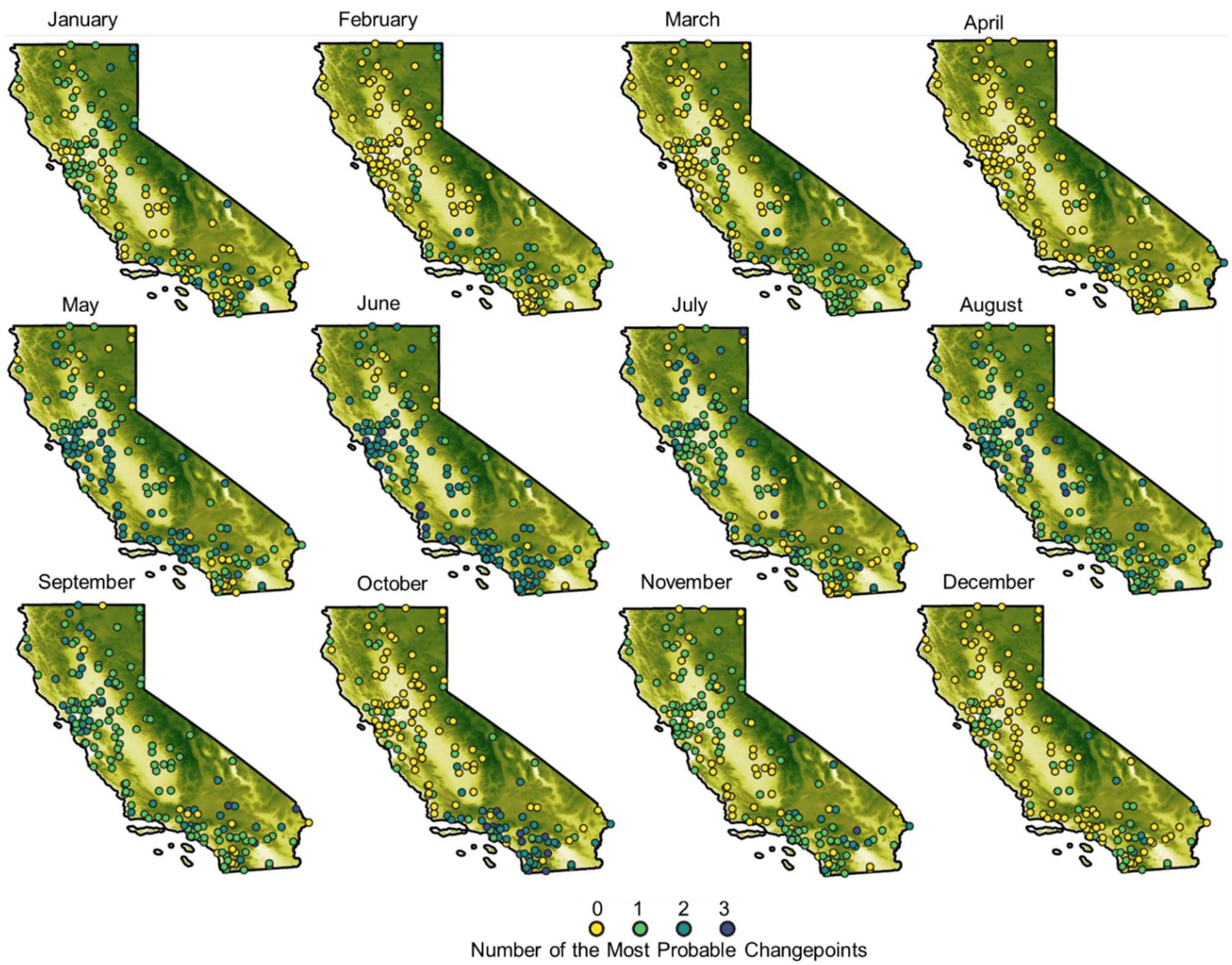

Figure 5.4 Monthly Most Probable Number of Changepoint spatial distribution.

In contrast, southern coastal and inland desert regions display intermittent darker circles, pointing to residual variability possibly influenced by early-season atmospheric-river events or delayed ENSO responses (Ralph and Dettinger, 2012).

Complementing the changepoint assessment, Figure 5.5 presents the dominant monthly slope direction for precipitation series across California. This adds a trend-focused dimension by classifying each station according to the most frequent slope direction detected within segments. Stations with at least 60 % of seasonal segments showing positive slopes are dark blue, those with a majority of negative slopes are white, and stations without a dominant direction are light blue.

From January through March, northern California shows stable positive trends, whereas the southeastern regions, including desert and lower-elevation areas, exhibit a more heterogeneous slope pattern, often marked by light-blue and white markers that indicate neutral or slightly negative trends. Despite the wet season, this part of the state appears to experience weaker precipitation accumulation and greater interannual variability. Notably, these regions also show a higher incidence of changepoints during early-year months (Figure 5.4), reinforcing the interpretation of less stable precipitation regimes. The combined presence of inconsistent trend direction and frequent structural breaks highlights the southeastern interior as a zone of greater temporal variability within an otherwise stable seasonal context.

In late spring and throughout summer (May to August), the coastal and central regions are dominated by dark-blue and light-blue markers, reflecting predominantly positive trends or neutral conditions, consistent with the low changepoint activity observed during these months (Figure 5.4). This combination suggests relatively stable precipitation regimes, with persistent accumulation patterns or neutral variability during the dry-to-wet seasonal transition. In contrast, the southwestern region, which shows frequent changepoints in June, October, and November, also exhibits stronger slope signals, both positive and negative (Figure 5.5). This overlapping pattern of high slope magnitude and high changepoint probability may mark zones of dynamic hydroclimatic behavior, where abrupt changes and gradual trends coexist, potentially under ENSO influence. Likewise, areas such as the Sierra Nevada foothills and eastern desert regions display a mixed pattern of light-blue and white markers, indicating localized negative trends or weakly defined slope direction. This heterogeneity coincides with sporadic changepoints in Figure 4, suggesting nonlinear or monsoon-related variability in these subregions during the peak of summer convective activity.

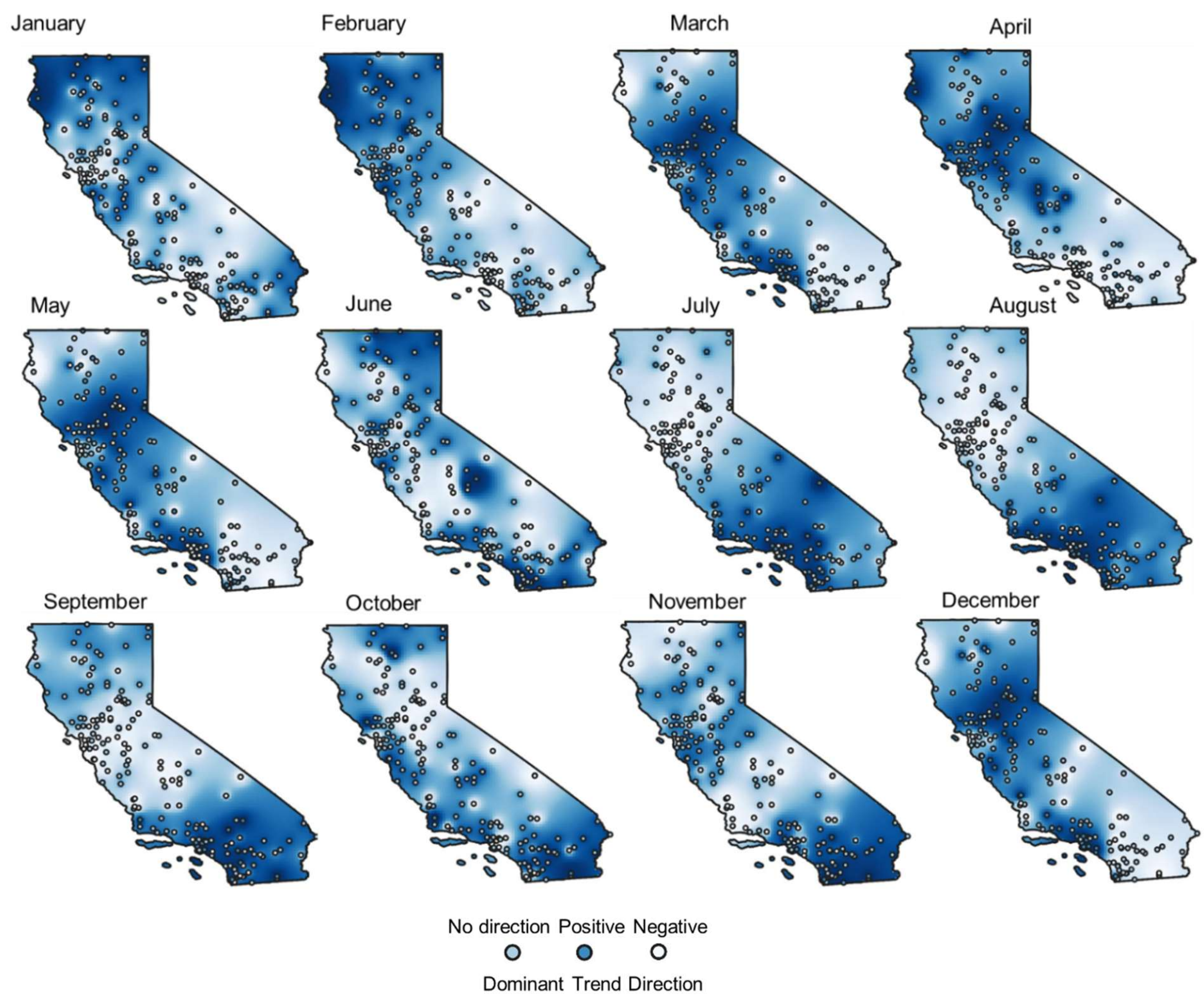

Figure 5.5 Monthly Dominant Slope Direction. Stations with ≥60% of years showing positive slopes are shown in dark blue, negative in white, and no direction (<60% in either direction) in light blue.

By September, a transitional slope pattern emerges in central California, bridging the relatively stable summer with the more dynamic autumn. The southern interior continues to show localized slope variability through October and November, matching the spatially variable changepoint structure and possibly linked to delayed oceanic influences or regional topographic modulation. In December, northern California again displays stable slope signals (mostly dark-blue or light-blue) with few changepoints, consistent with the dominance of winter frontal systems and stabilized moisture influx. Conversely, the southern interior and coastal areas maintain intermittent slope variability, echoing the localized changepoint activity that may result from early-season atmospheric disturbances or lagged ENSO signals.

5.4.2. Regionalization

This section presents the spatial distribution of meteorological stations influenced by the Niño 3.4 index using two distinct approaches: Point–Slope (PS) similarity with k-means clustering and partial Spearman correlation with statistical-significance filtering ($p < 0.05$). Note that the analysis is limited to the Niño 3.4 region, which represents a monthly average of sea-surface-temperature anomalies (SSTAs) over a defined area of the equatorial Pacific (5° N–5° S, 170° W–120° W) rather than a single point in the ocean. Consequently, the regionalization presented here reflects the relationship between precipitation and a spatially aggregated oceanic signal.

5.4.2.1. NPS + k-means

Figure 5.6 shows the classification of precipitation stations based on PS similarity with the Niño 3.4 index. Stations were grouped using k-means clustering without fixed thresholds; instead, cluster assignment reflects inherent structure in the multidimensional PS-similarity space captured by the algorithm. Each color represents a distinct cluster: red indicates stations with strong structural similarity to Niño 3.4, blue denotes intermediate responses, and white highlights stations with weak or inconsistent similarity.

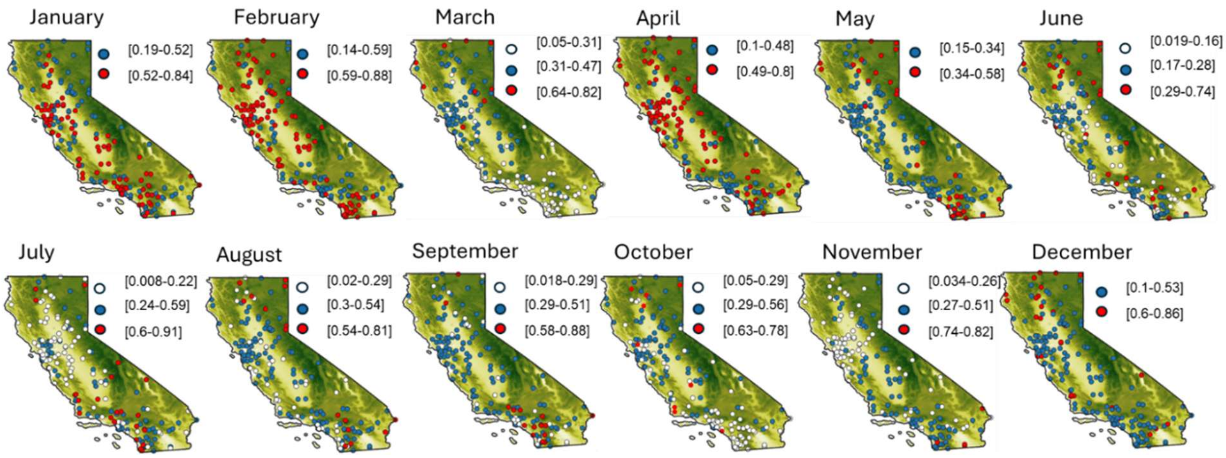

Figure 5.6 Meteorological stations clustered based on PS relationship between rainfall and Niño3.4

The optimal number of clusters was selected monthly with the elbow method (Figure 5.7), which identifies inflection points in the within-cluster sum of squares. Most months favoured a simple structure with k = 2 or 3, capturing the dominant spatial modes of ENSO-related influence. January and February displayed compact, coherent clustering with two well-defined groups. This aligns with high silhouette coefficients (Figure 5.9), confirming that stations respond synchronously to Niño 3.4 during peak ENSO months. In these months, clusters were also clearly separated in the PS–elevation space (Figure 5.8): stations with high similarity scores (red) were located mainly below 500 m, especially along the southern coast and in the central valleys. These results support previous findings that ENSO exerts stronger influence on lowland precipitation through enhanced moisture transport and circulation anomalies (Dettinger et al., 2011).

In contrast, transitional months such as July and September required k = 3 to capture the more diverse station behavior. A third cluster emerged, typically composed of high-elevation stations with low PS values, reflecting limited ENSO influence and stronger modulation by localized orographic processes. These extra groups refine the regional response pattern by reducing within-cluster dispersion and clarifying intermediate levels of similarity.

Notably, even at higher elevations some exceptions appear. In February and September, a few mountain stations still show strong PS similarity, indicating that altitude alone does not determine ENSO sensitivity; geographic setting and local dynamics also matter. Average silhouette values for January and February were 0.62 and 0.64, confirming well-separated, coherent groups during peak ENSO months. July and September achieved similarly high scores of 0.71 and 0.63, indicating that a three-cluster solution improves internal consistency by isolating weak and intermediate responses.

These results support k = 2 in winter, when ENSO influence is spatially concentrated, and k = 3 in transitional months to resolve finer structural differences in station behavior (Figure 5.9).

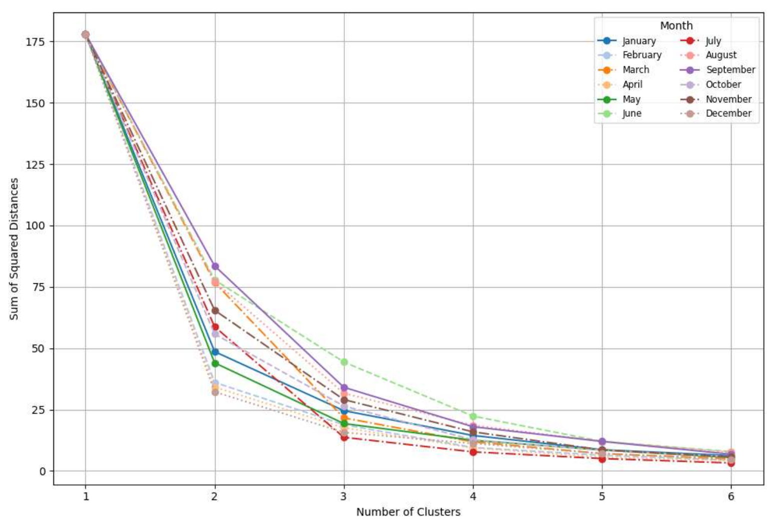

Figure 5.7 Optimal Number of Clusters per Month Based on the Elbow Method for PS and index Niño 3.4.

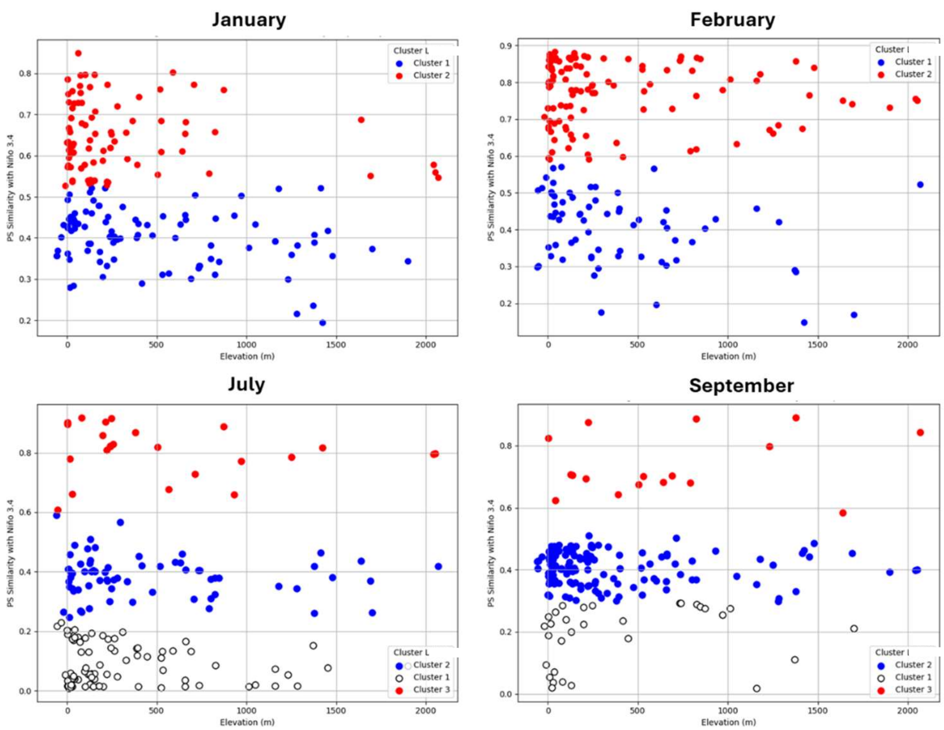

Figure 5.8 Elevation - Clusters per Month for PS with index Niño 3.4.

5.4.2.2. Partial Correlation

On the other hand, Figure 10 displays the spatial distribution of stations with statistically significant relationships ($p < 0.05$) between precipitation and the Niño 3.4 index, identified with partial Spearman correlation following González-Pérez et al. (2022). Blue markers denote stations where this monotonic association is significant; white markers denote nonsignificant sites. Significant stations are few overall, with notable concentrations in January and February along the southern coast and parts of central California. During spring and autumn, they become increasingly sparse, and by the summer months, virtually no significant relationships are detected.

To examine whether elevation influences these associations, Figure 11 plots elevation against p-value for selected months. In January and February, significant stations span a wide elevation range, though most lie below 500 m. A few outliers above 1,000 m appear early in the year, but no clear elevation-dependent pattern emerges. Thus, altitude alone does not determine the statistical link to Niño 3.4 in this test; other geographic or climatic factors must modulate this sensitivity. Comparing Figure 5.6 with Figure 5.10 shows that, while both methods highlight southern California in January and February, PS-based clustering also identifies coherent groups in the northern interior and Sierra Nevada foothills-regions not captured by the partial-Spearman approach.

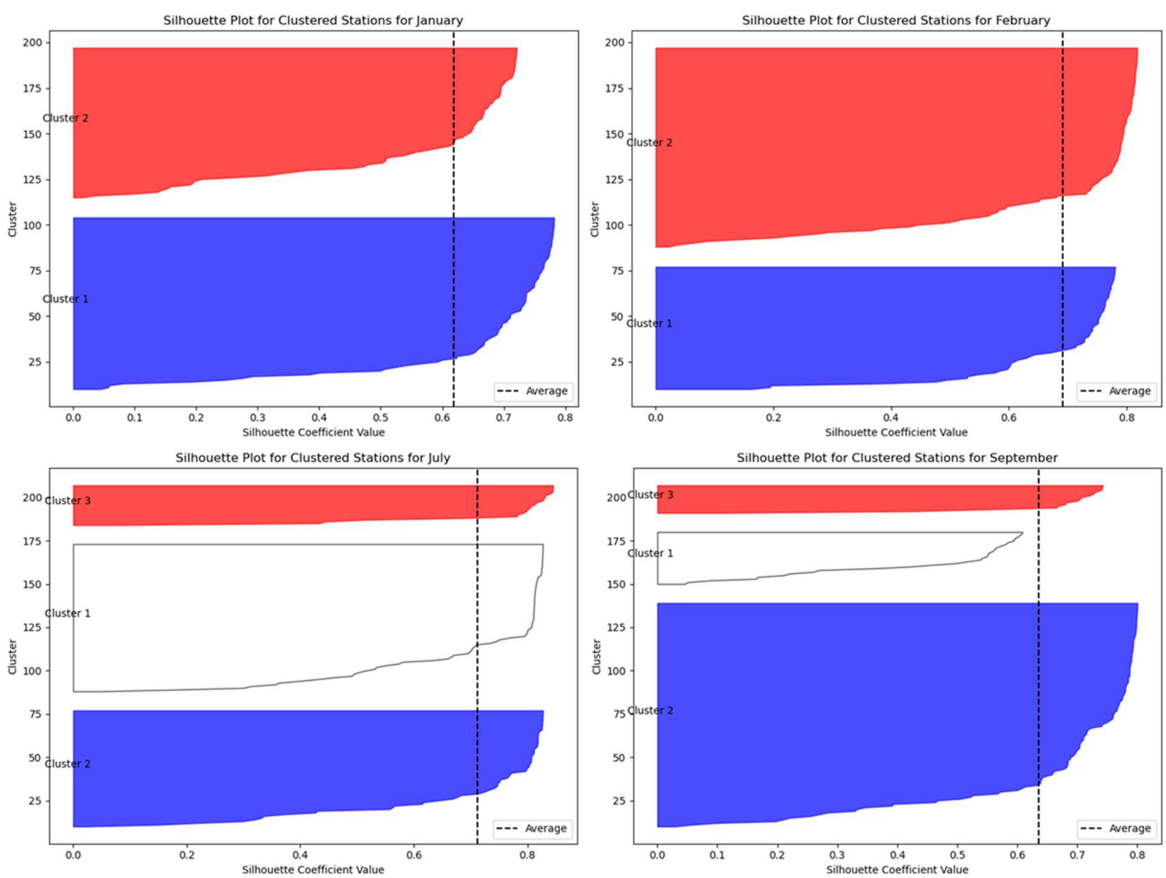

Figure 5.9 Silhouette plots of k-means clustering applied to PS similarity between California precipitation stations and the Niño 3.4 index, for January (0.62), February (0.64), July (0.71), and September (0.63). The dashed vertical line indicates the average silhouette coefficient for each month.

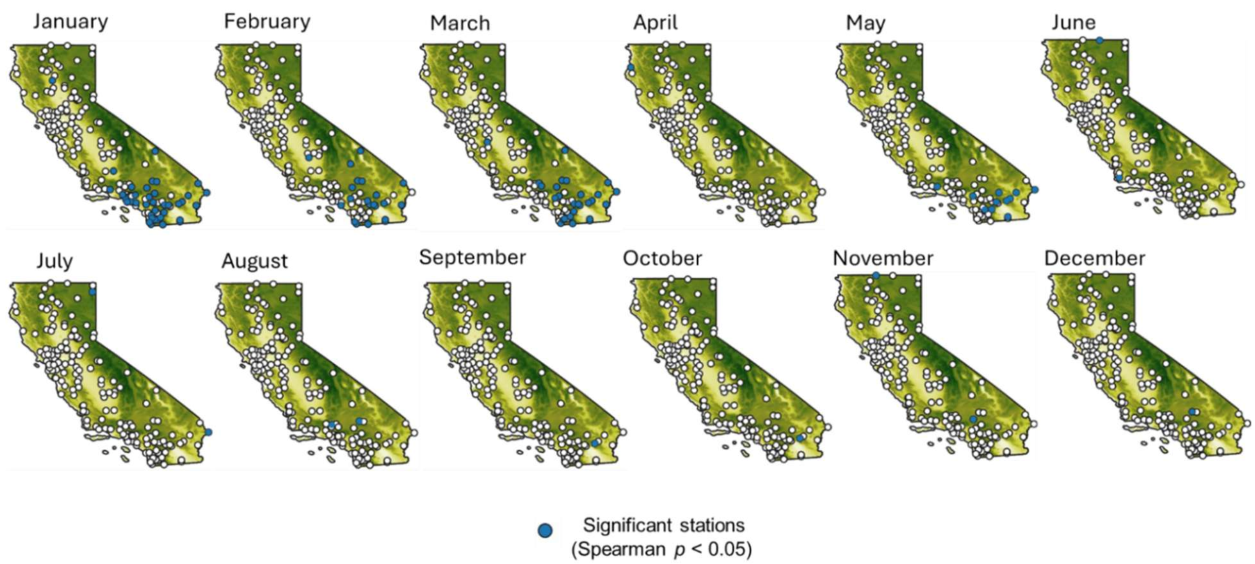

Figure 5.10 Significant Meteorological stations for ρ < 0.05 to Niño 3.4 index.

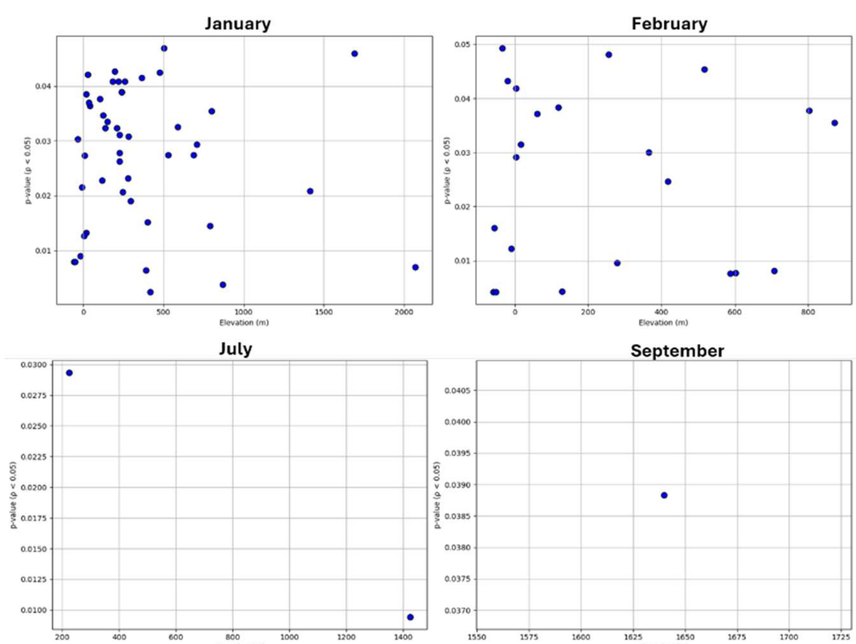

Figure 5.11 Significant Meteorological stations for ρ < 0.05 to Niño 3.4 index.

5.4.2.3. Validation

Figures 5.12–5.15 compare the Niño 3.4 index with the mean precipitation of stations most responsive to ENSO. For the Point–Slope (PS) method with k-means, the mean is calculated across all stations in the cluster with the highest PS scores. For the partial-Spearman approach, only stations whose correlation with Niño 3.4 is significant ($p < 0.05$), whether positive or negative, are included.

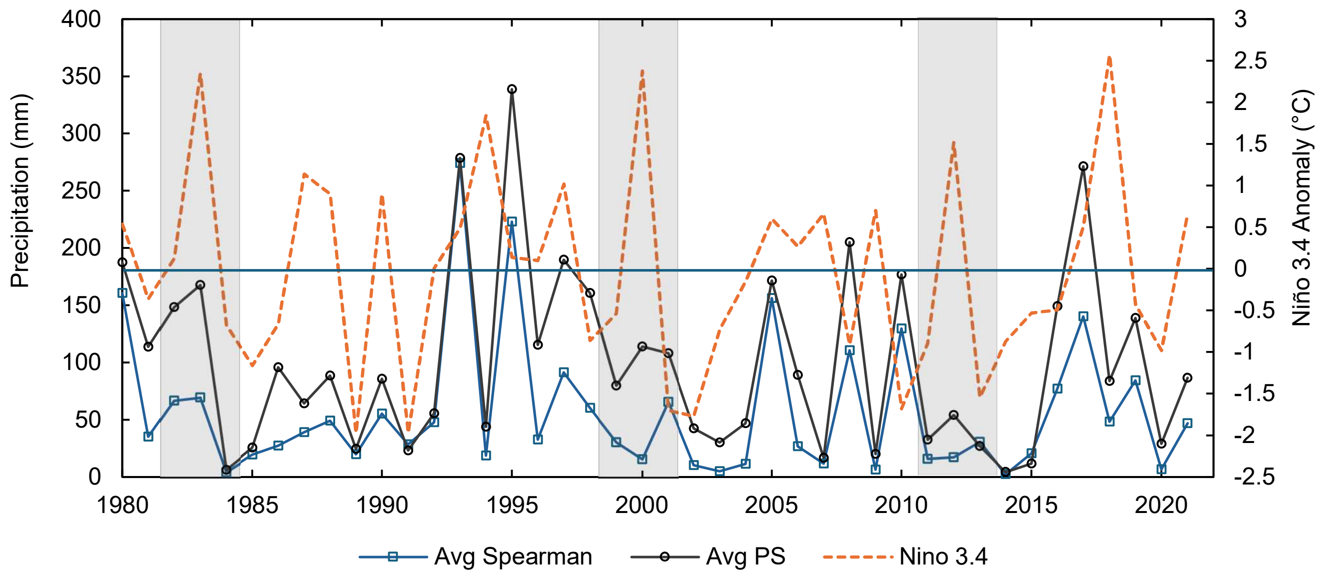

Figure 5.12 Average Signal of partial Spearman and PS groups with Niño 3.4 in January.

The light-green bands highlight periods when the PS composite tracks Niño 3.4 in both amplitude and slope, whereas the Spearman composite remains flat or diverges. These intervals show that the structural information captured by PS adds explanatory power beyond a traditional linear metric. During the strongest El Niño winters identified by Patricola et al. (2019), 1982, 1997, and 2015, the January PS curve rises above 150 mm month^{-1} in phase with the positive SST anomalies, while the Spearman curve reaches only about half that value. A similar contrast appears during the 1999-2000 La Niña: the PS composite falls with the negative Niño 3.4 anomaly, indicating reduced rainfall at ENSO-sensitive stations, whereas the Spearman series stays near its long-term mean.

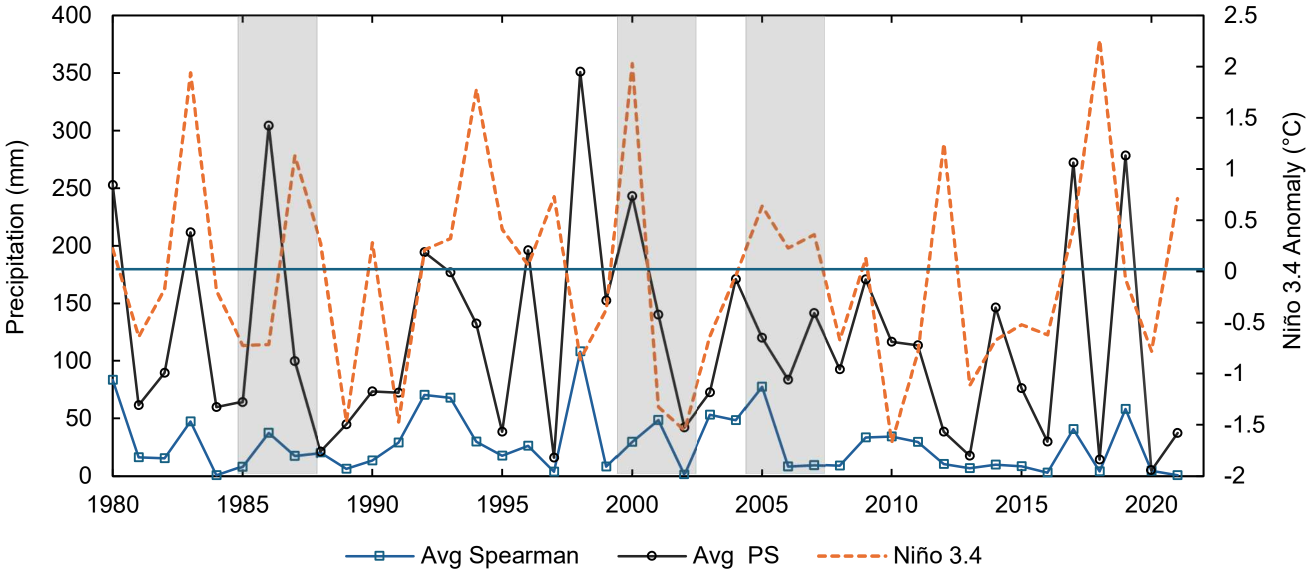

Figure 5.13 Average Signal of partial Spearman and PS groups with Niño 3.4 in February.

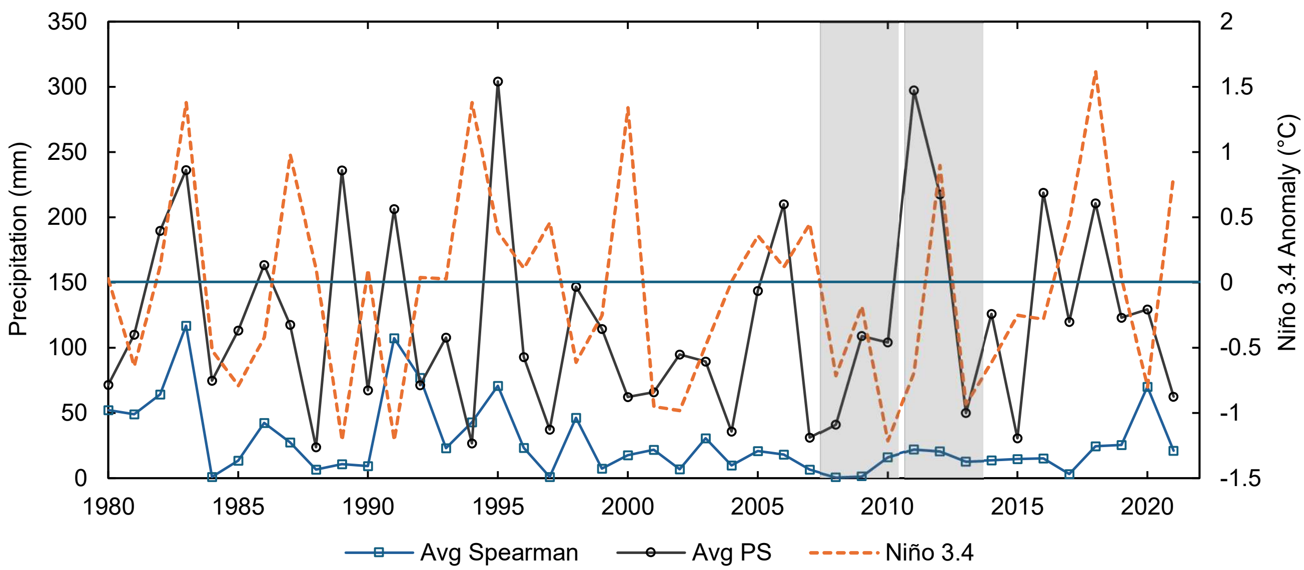

Figure 5.14 Average Signal of partial Spearman and PS groups with Niño 3.4 in March.

Figure 5.13 shows an even larger dynamic range. During the wettest ENSO winters (1983, 1998, 2017), the PS composite exceeds twice the long-term February average; in 1999 it drops to almost zero. The Spearman composite, by contrast, stays within a narrow 0–80 mm month^{-1} band, muting both extreme wet and dry events. The same pattern continues in March

(Figure 5.14). Although Niño 3.4 displays fewer pronounced anomalies, the PS composite still mirrors its interannual variability, particularly during 2009–2017, whereas the Spearman series remains comparatively muted. In September (Figure 5.15) no Spearman composite is available because significant correlations are lacking, yet the PS curve continues to track ENSO behavior, falling sharply in 1999 and peaking near strong El Niño years. Even with lower seasonal totals, the PS signal retains coherent ENSO features.

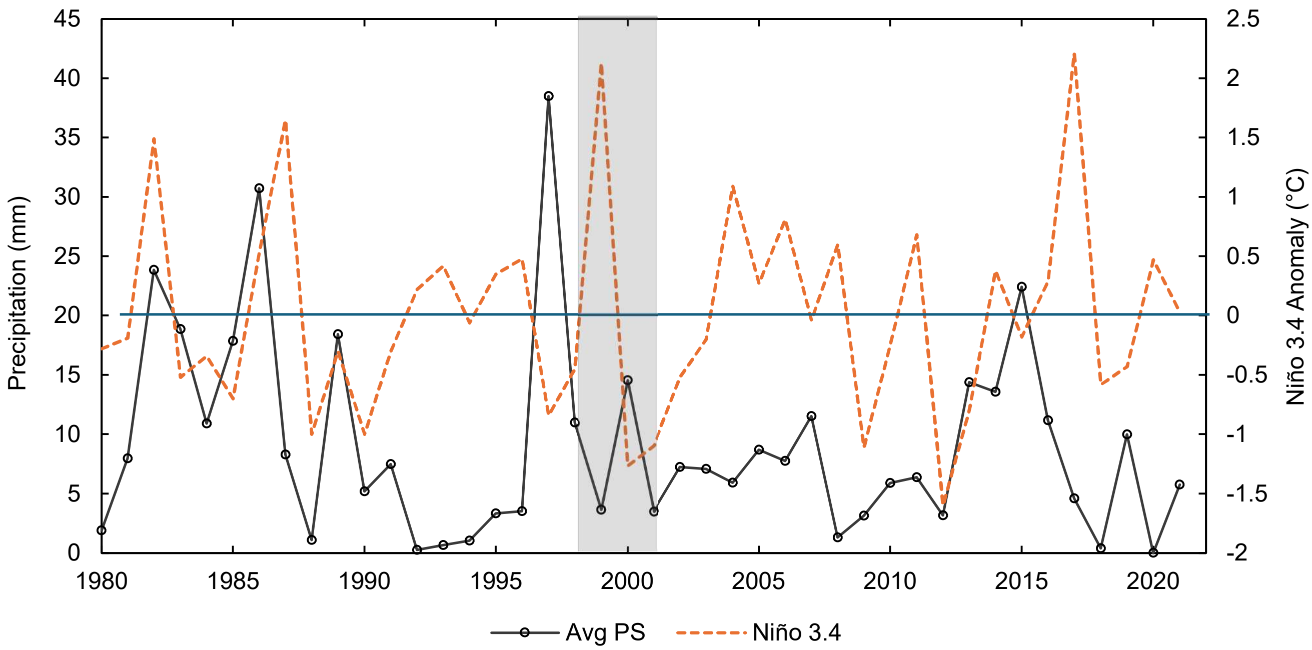

Figure 5.15 Average Signal of PS groups with Niño 3.4 in September.

Tables 5.2–5.4 quantify these visual results using different metrics performed between the signals. Pearson captures only linear links, Spearman any monotonic trend, while distance correlation and DTW detect broader structure and timing. In January–February, the PS composite shows stronger Niño 3.4 coupling (distance correlation = 0.335/0.259 vs 0.286/0.203 for Spearman). Higher DTW values for PS (817.5/951.0) reflect its wider amplitude and closer phase match, whereas lower Spearman DTW values mirror its muted response.

Table 5.2 Metrics between Niño 3.4 and PS.

Measure	January	February	March	September
Spearman	0.283	0.074	-0.043	-0.071
Pearson	0.219	0.099	-0.003	-0.075
DTW	817.495	950.973	916.327	70.9909
Distance Correlation	0.33494	0.25867	0.21253	0.23433

Table 5.3 Metrics between Niño 3.4 and partial Spearman.

Measure	January	February	March
Spearman	0.198	0.086	0.121
Pearson	0.121	0.034	0.097
DTW	525.2	234.934	248.914
Distance Correlation	0.28657	0.20301	0.21437

Table 5.4 Metrics between PS and partial Spearman.

Measure	January	February	March
Spearman	0.871	0.755	0.422
Pearson	0.898	0.734	0.412
DTW	299.5949	576.7846	500.2096
Distance Correlation	0.894116	0.719534	0.402776

Similarity between PS and Spearman peaks in January (Spearman = 0.871, Pearson = 0.898, distance correlation = 0.894, DTW lowest). Agreement weakens in February and collapses by March ($\rho \sim 0.42$, distance correlation ~ 0.40, DTW ~ 500). After the ENSO peak, the PS composite still follows nonlinear, non-stationary rainfall variations, whereas the Spearman series reverts toward its mean, highlighting the added value of PS.

5.5. Discussion

Our results show that imposing a seven-year minimum segment length stabilizes the Bayesian changepoint detector, preventing short ENSO pulses from being misclassified as regime shifts while still allowing the slope term of the Point–Slope (PS) metric to register subdecadal perturbations. This dual sensitivity explains the north-south contrast seen in Figures 5.4 and 5.5. Northern stations exhibit few breaks with steady positive slopes, whereas southern and interior sites display both abrupt changepoints and alternating slope signs in transition months. These patterns align with the influence of atmospheric rivers and monsoonal incursions documented by Adams and Comrie (1997) and Ralph and Dettinger (2012). Mapping the series into PS-similarity space and clustering with k-means isolates coherent ENSO responses that a partial-Spearman filter misses (Jong et al., 2016). In peak months two clusters suffice to separate strongly from weakly influenced stations, whereas July and September require a third cluster to capture intermediate orographic behavior. Scatterplots of PS similarity versus elevation (Figure 5.8) show that altitude is not a primary control; clusters overlap throughout the 0–2000 m range, and several high-elevation sites still belong to the strongly ENSO-sensitive group. Elevation therefore modulates but does not dictate teleconnection strength (Stagge et al., 2023).

Composite rainfall curves reinforce this interpretation. During major El Niño winters the PS composite rises above 150 mm month^{-1} in January and doubles the February climatology, whereas the Spearman composite rarely exceeds 80 mm. Distance correlation between Niño 3.4 and the PS composite peaks at 0.335 in January and remains higher than the Spearman value through February. After March, the two rainfall composites diverge rapidly. These patterns underscore the benefit of a changepoint-aware, slope-sensitive metric: it captures nonlinear and forms hydroclimatically meaningful clusters without arbitrary thresholds and preserves structure throughout the seasonal cycle.

5.6. Conclusions

We introduced a changepoint-aware Point–Slope (PS) framework for diagnosing ENSO–precipitation teleconnections in California via the Niño 3.4 index. The main contributions are: (i) adapting Bayesian multiple-changepoint detection to hydrological teleconnection analysis, (ii) integrating slope-based trend information into a unified similarity metric sensitive to subdecadal ENSO pulses, (iii) developing a k-means clustering application in PS space that delineates coherent station groups without arbitrary thresholds, and (iv) demonstrating that PS-derived composites outperform partial Spearman correlation in tracking Niño 3.4 variability, particularly during peak winter months. The analysis further shows that elevation modulates but does not govern teleconnection strength, as high-altitude sites can exhibit strong PS similarity when synoptic moisture pathways align.

This work should encourage broader use of changepoint-informed, structure-based similarity measures in hydro-climate research and operational water-resource planning. Future efforts should explore multiscale temporal windows to capture weekly extremes and decadal modulations, extend the PS framework to gridded sea-surface-temperature fields and additional climate modes such as the Pacific Decadal Oscillation (PDO) and Pacific–North American pattern (PNA), and test alternative clustering algorithms that can accommodate irregular or nested response patterns. Coupling PS-based regionalization with dynamical or statistical seasonal forecasts also offers a promising avenue for improving real-time drought and flood prediction in a changing climate.

Chapter 6 Tracing Pacific Ocean Influence on California's Precipitation: A Comparison of Point–Slope Similarity and EOF-Based Correlation Patterns[3]

Carlos A. Rosas-Cabello[1], Mohammad H. Alobaidi[2], Fateh Chebana[3], Ousmane Seidou[1]

[1] Faculty of Engineering, University of Ottawa, Ottawa, ON, Canada

[2] Department of Civil Engineering, McGill University, Montréal, QC, Canada

[3] Centre Eau Terre Environnement, Institut National de la Recherche Scientifique, Québec, QC, Canada

Abstract

Recent work shows that hydrologic regionalization gains predictive power when it is based on large-scale ocean-atmosphere teleconnections. However, traditional approaches often rely on fixed key boxes, such as the canonical Niño regions, which capture only parts of that variability. Furthermore, linear and stationary tools, like Empirical Orthogonal Functions (EOFs), struggle to detect phase shifts in the teleconnection pattern. Consequently, fully capturing the evolving influence of Sea Surface Temperature Anomalies (SSTAs) requires methods that account for nonlinearity and temporal variability. In this study, we applied a structural similarity metric called Point–Slope (PS). The metric synchronizes paired series based on the alignment of their changepoints and trend directions. Our analysis moved from predefined indices to a region of influence perspective. We related monthly SSTA records from 1981 to 2022, sampled at every 1.5° node, to rainfall at 178 gauges in California using PS. We then compared the resulting map with EOFs derived from partial Spearman correlations. PS revealed a coherent warm-pool corridor extended from 160° W to 90° W,

[3] A version of this chapter has been submitted to the Stochastic Environmental Research and Risk Assessment (SERRA) and is currently under revision at the time of the thesis submission.

whereas EOF variance clustered near Niño 3.4 and faded eastward. To highlight the strongest teleconnections, we extracted the upper 5% values separately in each method that is, PS similarity scores above their 95th percentile, and EOF loadings above the 95th percentile of their spatial distribution. At these extremes, the metric rose linearly and added many grid points to the high PS zone. EOFs could not hold this extra variance in their leading mode and instead moved it to secondary patterns, which widened the diagnostic gap between the two approaches. This behaviour showed that PS captured the full, non-stationary footprint of Pacific forcing, while EOFs fragmented it across modes. Mapping these high-percentile tails allows PS to reveal potential hotspots of hydrologic sensitivity that conventional linear methods leave unaddressed.

Keywords ENSO; Point-Slope similarity; Empirical Orthogonal Functions; California; Regionalization; SSTA

6.1 Introduction

Water security in the western United States partly depends on how accurately Sea Surface Temperature Anomalies (SSTAs) can be translated into precipitation forecasts over land (Seager et al., 2015; McKinnon and Deser, 2018; Sengupta et al., 2025). In California, this ocean–land link drives swings from prolonged drought to damaging floods, exemplified by the late-December 2022 to January 2023 atmospheric-river sequence, which forced reservoir operators to balance flood-control releases with rapid increases in storage volumes (DeFlorio et al., 2024). Much of this volatility comes from the El Niño–Southern Oscillation (ENSO), which ranges from classic eastern-Pacific events to central-Pacific (Modoki) cases and mixtures of both (Ashok et al., 2007; Capotondi et al., 2015). Each type steers storms differently, and the warm-pool centre shifts east– west as an event unfolds (Capotondi et al., 2020). ENSO also links with slower modes like the Pacific Decadal Oscillation (Newman et al., 2016) and can change within a season. Simple region indices such as Niño 3.4 therefore miss parts of this moving target and weaken forecasts of extreme rain or drought used in reservoir and flood control planning (Nigam et al., 2021). Empirical Orthogonal Functions (EOFs) are still the common tool for mapping ocean–atmosphere links, but their linear, fixed-pattern design can blur signals during fast ENSO shifts (Barnston and Livezey, 1987; Alexander et al., 2002). L'Heureux et al. (2013) showed that removing the long- term SST trend drops a cooling mode EOF and lifts a Modoki pattern, proving that trends can hide key variations. Stuecker et al. (2013) found that the eastward-moving warm pool spreads across several EOFs, showing how fixed patterns miss seasonal ENSO changes. Together these studies expose a core limit of standard EOFs: signals that drift or mix with slow trends get pushed into higher-order modes or chopped into separate pieces, hiding their real effect on rainfall. To confront this gap, we propose the recently developed Point–Slope (PS) similarity metric (Rosas-Cabello et al., 2025), an extension of the non-parametric changepoint framework of Seidou and Ouarda (2007). PS gauges synchrony through coincident changepoints marking regime shifts and concordant segment slopes that track shared evolution. By doing so, it enables tracing of Pacific influence via synchronized regime shifts and trend co-evolution across ocean– land systems. Unlike methods that isolate a single dynamical attribute, for example, wavelet coherence that targets periodic variance, PS jointly evaluates discontinuities and directional trends, offering a comprehensive lens for teleconnections (Hu and Si, 2021). The present study uses PS to reassess where Pacific

SSTAs influence California precipitation. Rather than averaging within predefined Niño boxes, we analyze every 1.5° grid node in the Pacific and relate each anomaly in the 1981-2022 period record to 178 rain gauges. The present study utilizes PS to reassess the areas where Pacific SSTAs influence California precipitation. Rather than averaging within predefined Niño boxes, we analyze every 1.5° grid node in the Pacific and relate each anomaly in the 1981-2022 period record to 178 rain gauges. The PS teleconnection field is compared against Principal Component EOF modes derived from partial Spearman correlations, providing a comparison between a linear stationary method and a nonlinear non stationary method. The paper is organized as follows: Section 6.2 describes the datasets; Section 6.3 presents the methodology; Section 6.4 shows results on teleconnection mapping, regionalization and discussion about the results. In Section 6.5 we outline directions for future research on nonstationary climate linkages using PS.nonstationary climate linkages using PS.

6.2 Datasets

6.2.1. Sea Surface Temperature Anomaly Grid

The Daily Optimum Interpolation Sea Surface Temperature dataset, version 2.1 (DOISST v2.1; Reynolds et al., 2007; Huang et al., 2021), was employed for this study. One of this source's benefits is its blend of in-situ and satellite observations on a 0.25° × 0.25° grid, providing both absolute SST and pre-computed anomalies. For the analysis, the anomaly field was directly utilized. Daily anomalies were first monthly averaged and then conservatively re-gridded to a 1.5° × 1.5° resolution in latitude and longitude. This approximately 150 km mesh helps suppress mesoscale noise, which is irrelevant for basin-scale teleconnections, while retaining the zonal gradients that characterize ENSO. As Table

6.1 illustrates, a 1° to 2° resolution is standard in recent ENSO-diagnostic studies (e.g., Alexander et al., 2002; Newman et al., 2016; Nigam et al., 2021), and the chosen 1.5° resolution fits comfortably within this range. This intermediate resolution decision aimed to capture as much influence as possible, reduce noise, and optimize computational cost. The resulting Sea Surface Temperature Anomaly (SSTA) field thus spans from 140° E to 60° W and 50° N to 40° S, yielding approximately 6,000 oceanic grid cells. These cells were extracted from the NetCDF anomaly files and used as independent predictors in the Point–Slope analysis.

6.2.2. Precipitation

Monthly precipitation totals from 178 California stations formed the land data set from the Western Regional Climate Center (https://wrcc.dri.edu/). Station selection followed the screening criteria in Rosas-Cabello et al. (2025) and required at least 90 % completeness over 1981–2022. Daily observations were aggregated to calendar months and passed through the same range and neighbour checks described in that study. For the linear comparison, partial-Spearman correlations and EOFs, any remaining gaps (≤ 10 % of months in a series) were filled by simple linear interpolation along the time axis, followed by a forward–backward fill to eliminate residual gaps and produce continuous vectors. In Point–Slope (PS) analysis, gaps were not completed. The recursive changepoint framework of Seidou and Ouarda (2007) computes the test statistic using only the available observations. The specific handling adopted here is detailed in Sect. 6.3.1. Although every month was processed, the discussion centres on January, February and March, the period when ENSO exerts its strongest influence on California precipitation (González-Pérez et al., 2022).

Table 6.1 Datasets employed for ENSO characterization.

Reference	SST Dataset	Working resolution	Analysis
Alexander et al. (2002)	ERSST (2° × 2°, monthly)	2° × 2°	Leading EOF modes linking global SST and SLP.
L'Heureux et al. (2013)	ERSST.v3b (2° × 2°)	2° × 2°	Trend-dominated vs. Modoki ENSO patterns via PCA.
Stuecker et al. (2013)	HadISST (1° × 1°)	1° × 1°	Eastward-propagating warm-pool "combination modes".
Newman et al. (2016)	ERSST.v4 (2° × 2°)	2° × 2°	Re-evaluation of PDO structure and its ENSO link.
Nigam et al. (2021)	ERSST.v5 (1° × 1°)	1° × 1°	ENSO-PDO controls on North American precipitation.
Current study	NOAA OISST v2.1 (0.25° × 0.25°, daily)	1.5° × 1.5° monthly (re-gridded)	Grid-point Point–Slope teleconnection mapping, 1981–2022.

6.3. Methodology

6.3.1. Point–Slope (PS) Similarity

The Point–Slope (PS) metric quantifies structural similarity between two time series by assessing (1) synchronization of changepoints and (2) concordance in post-shift trend directions. Changepoints were identified using the Bayesian procedure of Seidou and Ouarda (2007), which modeled the response as a piecewise multiple linear regression and estimates both the number and location of breakpoints by combining normal priors on regression parameters with a recursive calculation of posterior probabilities. This formulation allows for flexible detection of structural shifts in predictor–predictand relationships without fixing the number of changepoints a priori. To avoid spurious detection, a minimum segment length of seven years was enforced, following the rationale in Rosas-Cabello et al. (2025). For each k series, once the optimal set of changepoints $\{t_1^k, t_2^k, \ldots, t_{m_k}^k\}$ was determined, the record was partitioned into $m_k + 1$ segments. Then, a least-squares line was fitted to each segment, producing two time-indexed vectors:

- $P_k(t) = 1$ if year t is a changepoint, 0 otherwise.
- $S_k(t) = sgn(slope)$ for the segment containing t, constant within each segment.

The PS similarity between series 1 and 2 was computed as:

$$\mathrm{PS} = \frac{1}{2}\left[\underbrace{\frac{\sum_t I\,(P_1(t) = 1 \wedge P_2(t) = 1)}{\max\left(\sum_t P_1\,(t), \sum_t P_2\,(t)\right)}}_{\textit{Changepoint Alignment}} + \underbrace{\frac{\sum_t I\left(\mathrm{sign}\left(S_1(t)\right) = \mathrm{sign}\left(S_2(t)\right)\right)}{N_t}}_{\textit{Trend-sign concordance}}\right], \quad 0 \leq PS \leq 1 \quad (6.1)$$

Where $I(\cdot)$ is the indicator function, N_t is the number of years common in both series. A value of PS= 1 indicates perfect alignment in both changepoint timing and directional trends.

6.3.1.1. Missing Data Handling

Years with missing data were excluded during Bayesian likelihood computation. Monte Carlo tests in Seidou and Ouarda (2007) confirm that changepoint location accuracy deteriorates by < 2 % of record length while gaps stay below 15 %. All gauges here exceeded 90 % of completeness, so no fill was needed for PS. Whereas linear interpolation was applied only to supply continuous vectors for the partial Spearman correlation and EOF benchmark (Sect. 6.3.2).

6.3.1.2. Land-Ocean Regionalization

This study constructed a land–ocean regionalization using the Point–Slope (PS) similarity framework as it can be seen in Figure 6.1. A matrix $M = N\ X\ G$ was assembled, where $N =$

178 was the number of California rain-gauge stations and $G = 6000$ the number of Pacific SSTA grid nodes. Each element PS_{ng} quantified the structural affinity between station n and node g by combining Bayesian changepoint synchrony and post-break trend concordance.

Each station was thus associated with a G -dimensional vector x_n capturing its pattern of oceanic influence (Bevington et al., 2019), here referred to as its Region of Influence (ROI). These station-specific ROIs were clustered using k-means clustering (Coe et al., 2021), with the number of clusters k_L chosen by the elbow criterion. The resulting clusters $\{C_1, \dots, C_{kL}\}$ partitioned California into hydroclimatic domains whose rain gauges exhibited similar PS-based teleconnection structures.

To map each terrestrial domain back onto the Pacific, we analyzed the subset of the matrix M corresponding to the stations in cluster C. By extracting only, the columns of M associated with those stations, we retained the PS values for each node g that reflected its structural relationship with the grouped stations. These values defined the Region of Influence (ROI) for cluster C, as they preserved the direct PS link between oceanic nodes and the terrestrial domain without aggregation.

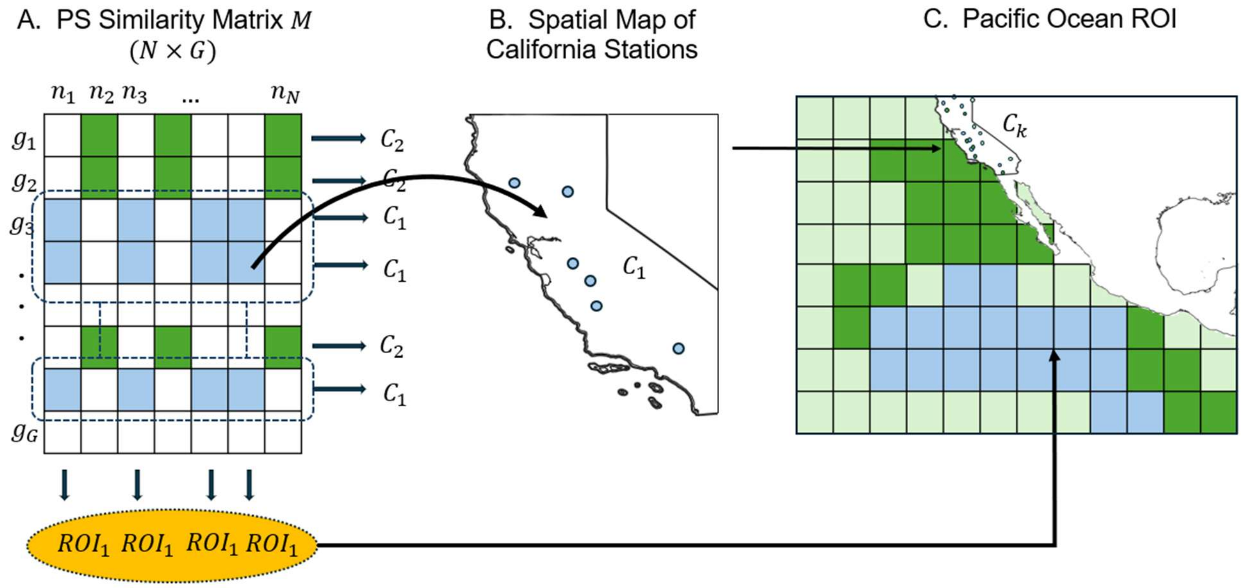

Figure 6.1 Scheme of the land–ocean regionalization process. A) The PS similarity matrix (stations × ocean grid nodes). B) Clustering of stations based on PS vectors. C) Identification of the Region of Influence (ROI) for clusters by extracting relevant oceanic nodes from the matrix.

6.3.2. Partial-Correlation EOF field

6.3.2.1. Partial Spearman Correlation

A parallel methodology was implemented to evaluate stationary teleconnections via partial Spearman correlations. This approach served to verify the structural regionalization derived from the Point–Slope (PS) similarity. We computed partial Spearman correlations between each of the 6,000 Pacific SSTA grid nodes and the 178 California precipitation stations, controlling for temporal trends. To satisfy the continuity requirements of correlation methods, missing values (fewer than 10%) were linearly interpolated, contrasting with the gap-tolerant nature of the PS framework. This procedure yielded a 6000 × 178 matrix R, where each entry quantified the strength of a stationary, monotonic association between ocean variability and land-based precipitation.

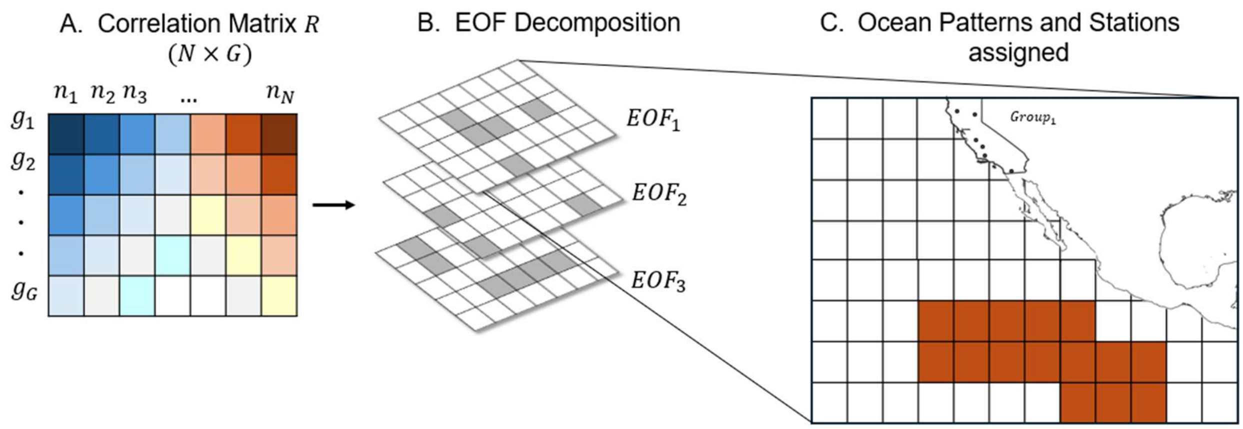

Figure 6.2 Schematic workflow of the partial Spearman correlation and EOF-based teleconnection analysis. A) A matrix R of partial Spearman. B) Principal Component Analysis (PCA) is applied to the correlation matrix. C) Each station is assigned to a dominant EOF mode based on maximal projection.

6.3.2.2. Principal Component Analysis of the Correlation Matrix

Principal Component Analysis (PCA) was applied to the matrix R as shown in Figure 6.2. This matrix captured stationary, normalized associations ranging from –1 to 1, with each row corresponded to an ocean location and each column to a rain gauge. Unlike the standard approach, where PCA is performed on the covariance matrix of the raw observations, in this study it was appropriate to apply PCA to the correlation matrix for several reasons. First, all variables (stations) were already standardized and dimensionless, ensuring equal contribution to the total variance. Second, using a covariance matrix would introduced unit-scale inconsistencies and undermined interpretability in this cross-domain context. The reason is because the analysis was based on correlation coefficients, not original data in physical units like millimeters or Celsius.

In this framework, the Empirical Orthogonal Functions (EOFs) represented coherent spatial modes of ocean–land teleconnection, while the associated Principal Components (PCs) described the temporal evolution of each mode (von Storch and Zwiers, 1999). In this study, PCs were not analyzed for their temporal structure. Instead, each precipitation station is assigned to the EOF mode with the largest absolute projection coefficient. In our case, over 85% of the stations were associated with the first three modes, and more than 95% fell within the first ten. Only a small fraction was linked to higher-order modes. This classification yielded a set of proxy teleconnection domains in which grouped stations exhibited similar sensitivity to dominant SSTA patterns. This classification yielded a set of proxy teleconnection domains in which grouped stations exhibited similar sensitivity to dominant SSTA patterns. Thus, this analysis provided a linear reference framework for comparison with the PS-based regionalization.

6.3.3. Comparison Between EOF and PS-Based Regionalization

The Point–Slope (PS) similarity metric and Empirical Orthogonal Functions (EOFs) approached teleconnection regionalization from distinct perspectives. PS emphasized the time-series structure and mapped stations via a well-defined, single-valued mapping, whereas EOF condensed the ocean–land correlation field into orthogonal spatial patterns. The resulting maps displayed the stations most strongly correlated with each mode.

To compare the two methods, a common selection criterion was required. In this study, EOF analysis retained only the first three modes, whose eigenvalues exceeded the sampling-error envelope. Because the study period covered just 40 years, the effective degrees of freedom were limited. Under the criterion of North et al. (1982), only modes with eigenvalues clearly separated from noise were considered physically meaningful. Thus, using more than the first five EOFs risked spurious interpretations, as higher modes often fitted structures dominated by random variability (von Storch and Zwiers, 1999; Monahan et al., 2009).

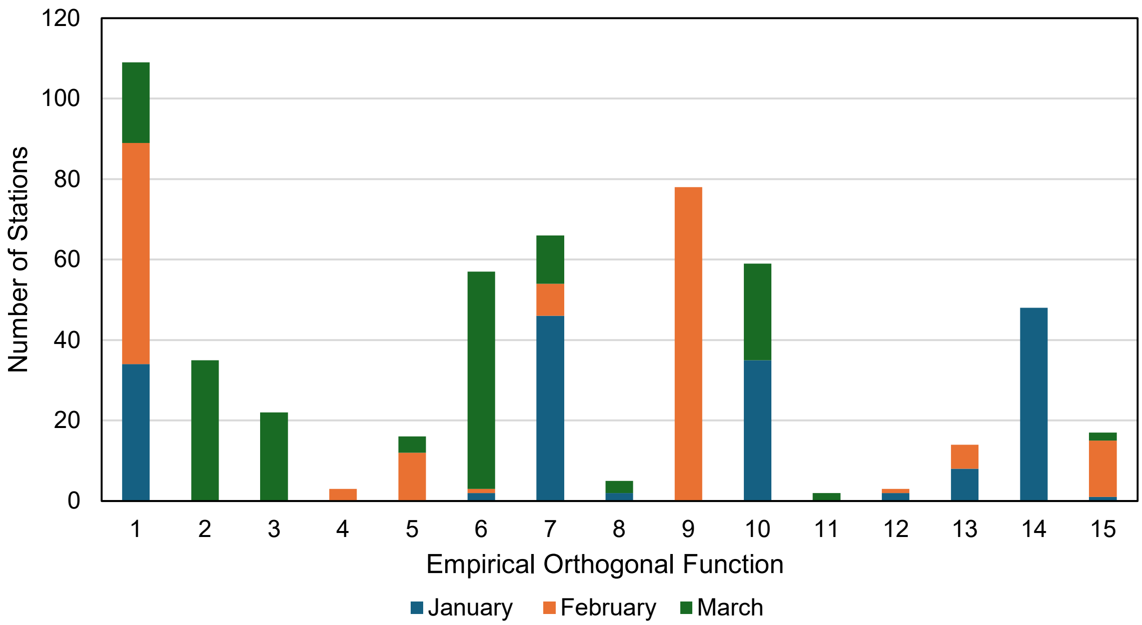

Figure 6.3 Number of stations associated with each EOF mode.

For example, in January, the largest absolute correlations emerged in EOF 7 and EOF 14, whereas modes 2 and 3 yielded noticeably weaker signals (see Figure 6.3). Yet Figure 6.4 reveals that EOF 7 and EOF 14 captured only a small fraction of the total SSTA variance when compared with the leading modes. This mismatch, high local correlations but low variance contribution, suggested that the apparent strength of modes 7 and 14 stemmed from localized noise amplification rather than a physically coherent teleconnection.

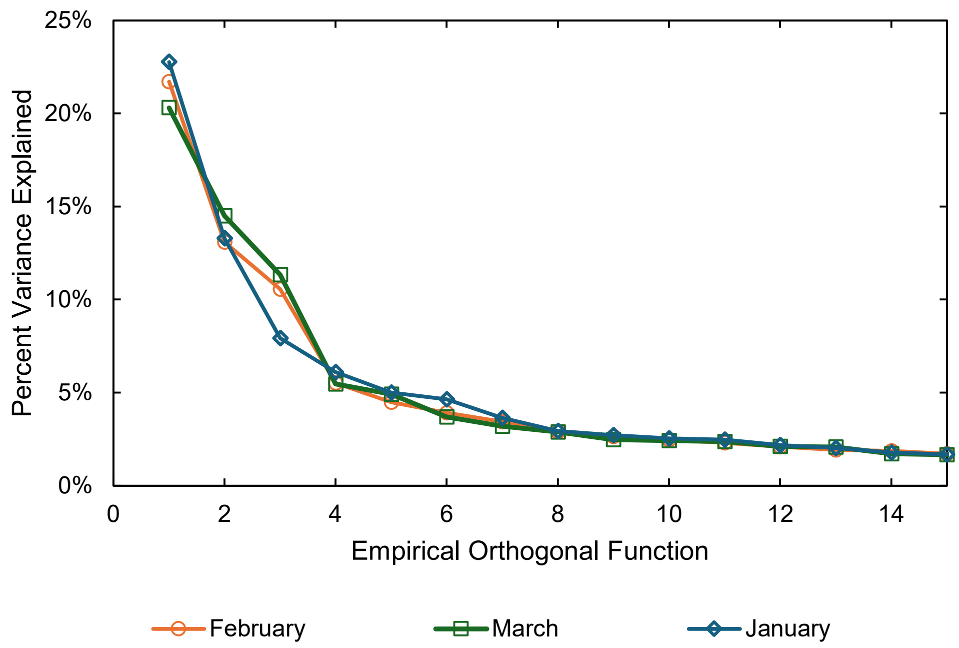

Figure 6.4 Percent variance explained by EOF mode (January – March).

Accordingly, the 95th percentile of PS values was taken for each month, and the same percentile was applied to the first three EOF modes after standardization. For the EOFs, absolute values were taken because the partial Spearman correlation yielded monotonic positive and negative signals. Comparing the top 5 % of values from PS and the three EOFs therefore offered a practical view of the magnitude of the SSTA impact on precipitation, while intentionally disregarding phase differences.

6.3.4. Correlation Maps between Ocean-Land based on EOFs

To compare with the PS framework, we decomposed each monthly Sea Surface Temperature Anomaly (SSTA)–precipitation correlation matrix into Empirical Orthogonal Functions (EOFs), keeping the three leading modes. For every mode, we then computed the field of standardized regression coefficients $\beta = L\sqrt{\lambda}$ (Bretherton et al., 1992), where L is the loading vector and λ is its eigenvalue. Using these units sharpened the spatial contrast between oceanic anomalies and their terrestrial responses, giving the resulting maps greater interpretative impact. Next, we assigned each rain gauge to the EOF whose principal component (PC) had the highest absolute Spearman partial correlation $|\rho|$. Stations linked to these top three were then projected onto a California map and colored by their original ρ to differentiate between positive and negative impacts.

6.4. Results and Discussion

6.4.1. Regionalization using PS-based Pacific influence

The Point–Slope (PS) similarity matrix M, containing values for every ocean–land pair ($N \times G$), was partitioned using the k-means algorithm with k=5, consistent with Rosas-Cabello et al. (2025). This partitioning aimed to isolate sub-regional teleconnection regimes and enhance the differentiation of PS values.

In January, Figure 6.5 (top row) shows the strongest ocean-land coupling centered on the Niño 3 and Niño 3.4 regions. On land, the results reveal two distinct bands of high-PS stations in California: one in the northwestern and another in the southern coastal region. Figure 6.6 displays the five resulting clusters, ordered by station count, and their internal PS spread via box-and-whisker plots. Figure 6.7 reports the monthly station counts for each cluster, allowing for a simultaneous assessment of their size and cohesion throughout the boreal winter. In that sense, Cluster 1 comprised 45 gauges and attained the highest median PS (0.7). Clusters 2 and 3 also exceeded 0.5, bringing the total to 64 stations that exhibited strong coupling. By contrast, Cluster 5 grouped 98 gauges with a median near 0.2, revealing pronounced spatial gradients in winter teleconnection strength. Linear methodologies, such as those of Jong et al. (2016) and González-Pérez et al. (2022), identified far fewer influenced stations in mid-winter, only a few in the north and south. This limitation arises partly because linear approaches are more sensitive to data gaps and regime shifts. PS, on the other hand, detected stronger structural similarity across both zones, demonstrating greater spatial dispersion while maintaining a clear affinity with the oceanic hotspot.

Moving into February (Figure 6.5, middle row), the core of maximum coherence shifted toward the northwestern Pacific, with the warm oceanic patch extending south of the Equator. On land, Cluster 1 became dominant, comprising 98 gauges and showing a median PS of 0.78. Cluster 2, though consisting of only two gauges, also exhibited strong coupling with a median of 0.67. Together, these were the sole clusters exceeding the 0.5 PS threshold, accounting for 100 strongly coupled stations. The clustering dynamics between January and February clearly demonstrate how shifts in sea-surface temperature anomalies reorganize continental impacts from one month to the next (Jin and Neelin, 1993).

For March (Figure 6.5, bottom row), the oceanic maximum shifts back toward Niño 3 and advances toward the South American coast. Cluster 1 contracts to 82 stations but still maintains a median PS of 0.78. Including clusters 2 and 3 (22 + 14 gauges) brings the total to 118 strongly coupled stations. The land pattern becomes more diffuse, suggesting that oceanic influence controls but is distributed over a less cohesive rainfall base as winter transitions to spring (Patricola et al. 2019). The persistent weakness of clusters east of the Sierra Nevada during this month reflects the orographic barrier that diminishes Pacific influences. In contrast, the robustness of coastal clusters corresponds to the preferred landfall corridors of atmospheric rivers and frontal systems along windward slopes and low-elevation coastal basins (Guan and Waliser, 2015; Rutz et al., 2019).

6.4.2. Correlation Maps between Ocean-Land based on EOFs

The number of stations assigned monthly varied progressively (Figure 6.8), increasing from 35 in January to 55 in February and 78 in March. This rise reflects an intensifying ocean-land coupling from mid-winter to early spring. It has been driven by the evolution of warm Niño 3.4 anomalies and the redistribution of variance within the EOFs (Figure 6.4). Physically, the ENSO teleconnection to California intensifies as winter advances. Warmer equatorial SSTs and a more coherent convective center amplify the Pacific–North America wave train and shift the subtropical jet landward (Mo and Higgins, 1998; Seager et al., 2015; Jong et al., 2016). Statistically, the variance that in January was dispersed among higher-order, noise-like EOFs is gradually absorbed by the first three modes. Once their eigenvalues separate from the noise threshold (North et al., 1982), these leading patterns gain signal to noise ratio, expand their terrestrial coverage, and dominate a large number of stations.

An EOF study of California winter rainfall by Hu et al. (2021) showed a similar structure. EOF1 explained 70 % of the seasonal variance, while EOF2 and EOF3 added a further 12 to 15 %. Consequently, the portion of stations whose maximum $|\rho|$ lies in the three leading EOFs climbs from 35 in January to 78 in March, even without imposing a correlation threshold. This behaviour illustrates how a maturing oceanic driver and the variance-ordering property of EOF analysis converge as winter turns to spring. A comparable, but seasonally offset, pattern emerges in the PS framework, where the number of strongly influenced stations rises from January to February and declines in March, reflecting the retreat of the warm SST pool and the end of the rainy season.

In January, the stations most affected by EOF1 clustered in southern California, showing both positive and negative signals, while only a few appeared in the northwest (see Figure 6.9). These spatial patterns closely resembled the PS clusters and the maps of González-Pérez et al. (2022).

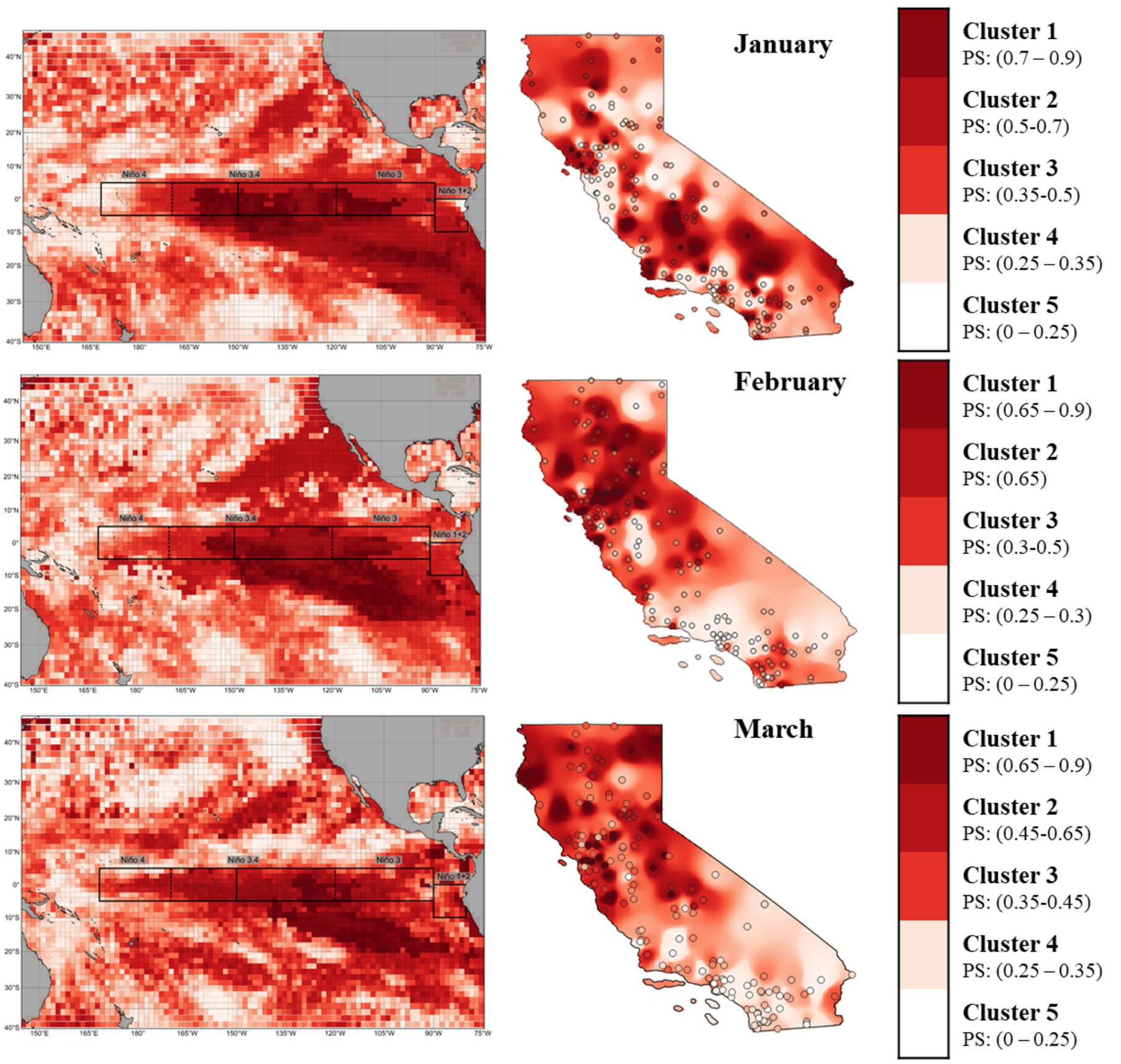

Figure 6.5 Pacific Regions of Influence (ROI) and California Stations Clusters for January, February and March. Left panels: PS-based similarity maps showing Pacific SSTA most strongly affect California precipitation. Right panels: California PS clusters using the using the corresponding color code.

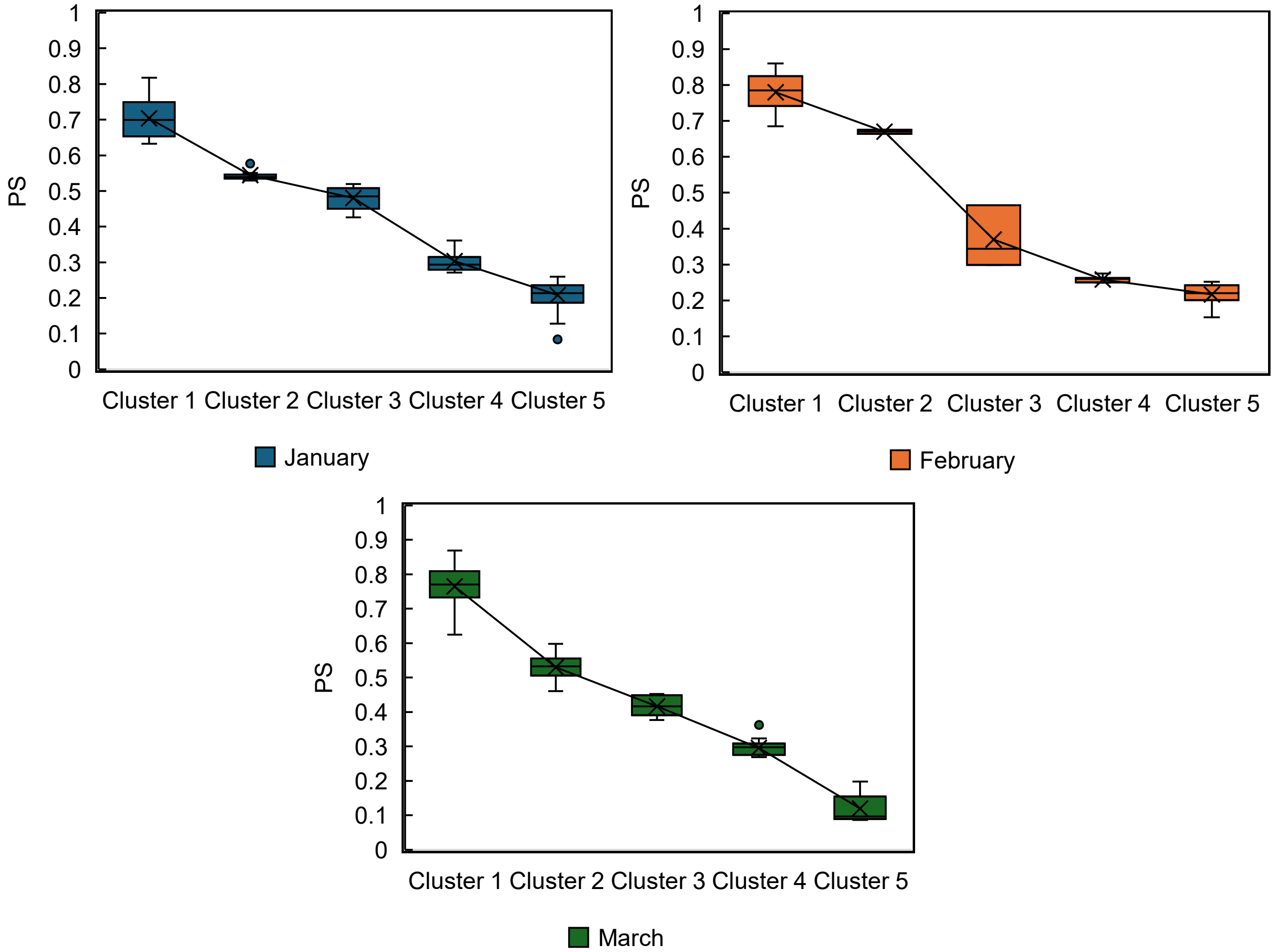

Figure 6.6 Distribution of Point–Slope (PS) similarity values by cluster for January, February, and March. Boxplots represent the internal PS coherence within each cluster derived from the k-means algorithm.

Unlike PS, however, Spearman's partial correlation requires a linear, time-dependent signal. As a result, PS linked more stations (45) than Spearman (35), underscoring its capacity to capture broader structural similarities. Figure 6.10 depicts the canonical EOF1 El Niño warming in the central–eastern equatorial Pacific, while EOF2 displays an equatorial dipole and EOF3 captures subtropical variability northeast of Hawaii. Taken together, these modes demonstrate how partial Spearman correlation partitions variability across distinct spatial patterns, whereas PS condenses the information into a single similarity map. A systematic comparison between the two methodologies will be presented in the following section. In February, 55 rain gauges located across the coastal ranges and Sierra Nevada foothills recorded their maximum |ρ| values.

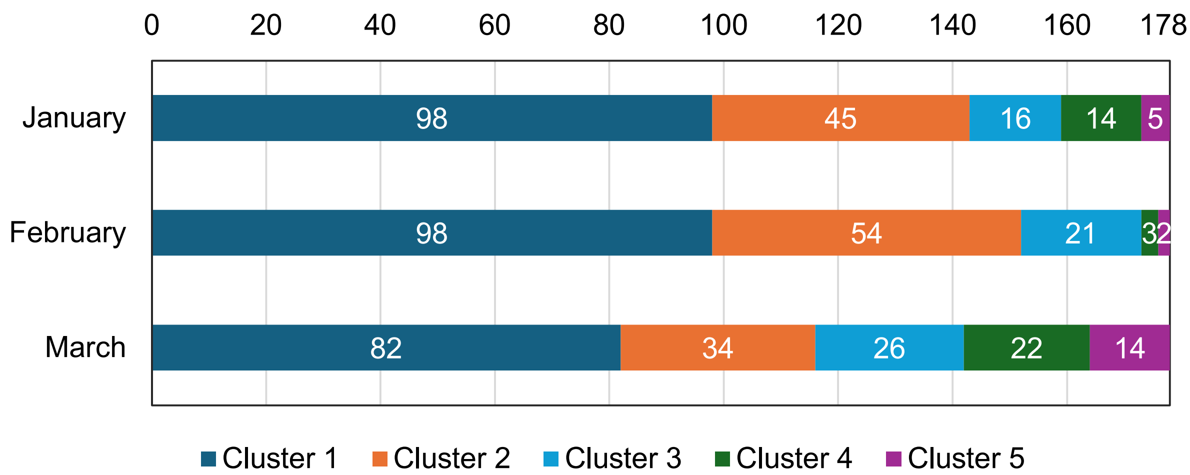

Figure 6.7 Monthly number of stations per PS cluster (January–March).

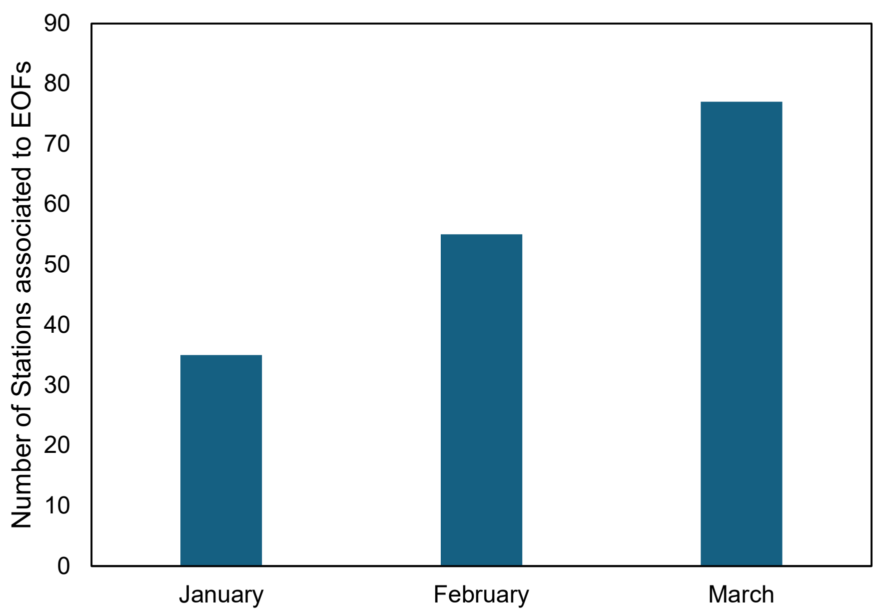

Figure 6.8 Monthly number of stations associated to first three EOFs (January–March).

A westward-intensified equatorial plume enhanced the spatial coherence of EOF1, while EOF2 evolved into a meridional oscillation that incorporated several inland gauges; EOF3 remained secondary (Figure 6.10). The total number of stations assigned was similar to PS (54), but their spatial allocation diverged: PS emphasized Northern California and the Mojave Desert, whereas Spearman concentrated on southern regions, consistent with González-Pérez et al. (2022). By March, the SSTA maximum shifted into the Niño 3 and Niño 4 sector, with EOF1 strengthening accordingly. EOF2 assumed a horseshoe-shaped pattern across the subtropical eastern Pacific and emerged as the dominant mode for several high-elevation gauges in the northern Sierra Nevada, while EOF3 remained secondary. Collectively, the three leading EOFs accounted for 78 stations, with only a few located in far-northern California, a sharp contrast to the PS framework, which concentrated its strongest signal in this region. Despite these differences, both the Spearman–EOF and PS analyses captured the same east–west displacement of oceanic forcing. This convergence underscores that a single fixed index, such as Niño 3.4, is insufficient to represent ENSO's evolving seasonal influence, as also emphasized by Nigam et al. (2021).

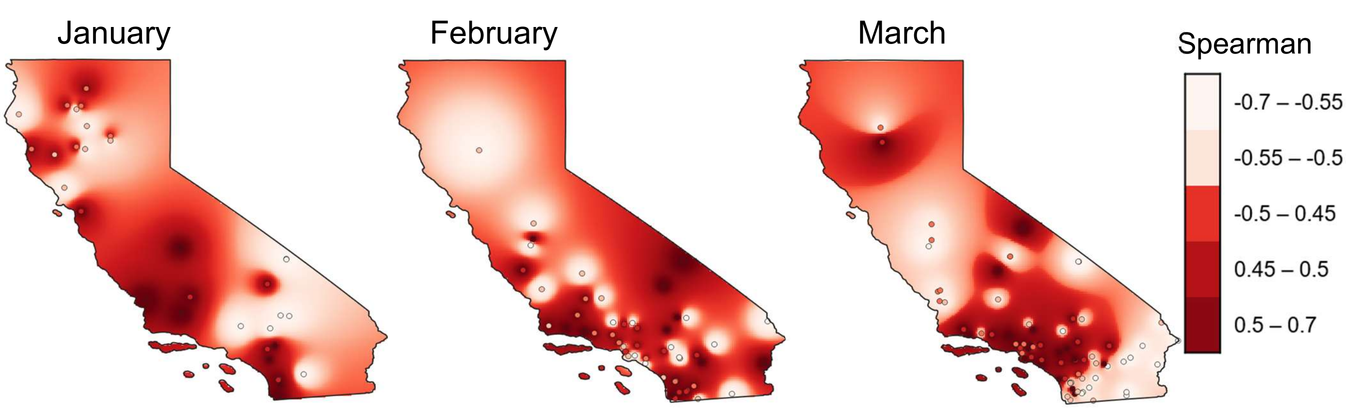

Figure 6.9 Stations most strongly associated with the first three leading EOF modes in January, February and March. Colours show partial Spearman rank correlation ρ between gauge precipitation and the corresponding EOF.

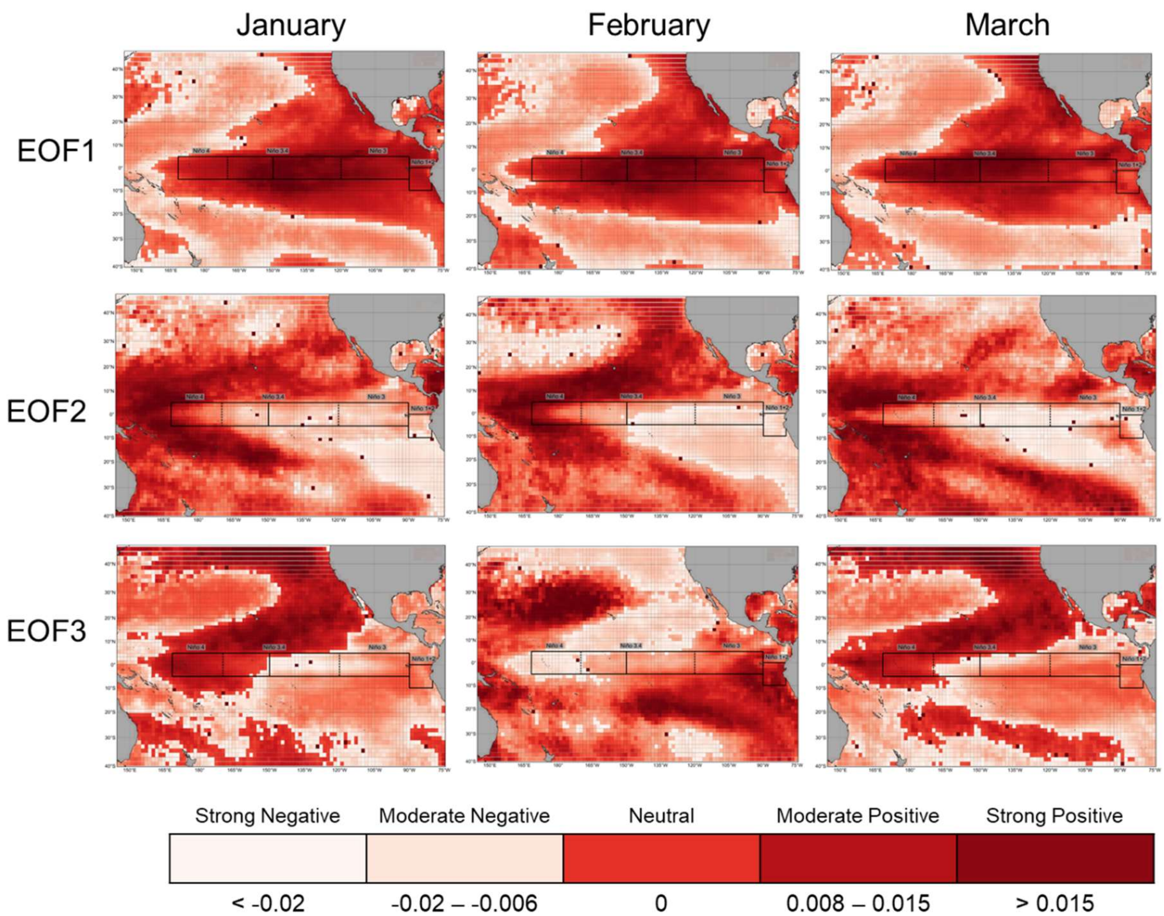

Figure 6.10 Spatial patterns of the first EOF modes for January, February, and March. Colours show standardized regression coefficients β relating Pacific SSTA to California precipitation.

6.4.3. Comparative Analysis of Oceanic Influence Zones

Figure 6.11 compares the standardized values of the Point–Slope (PS) metric with the standardized loadings of the three leading Empirical Orthogonal Functions (EOFs). Only points exceeding the 95th percentile of each method's distribution (top 5 %) are retained, regardless of whether their locations coincide. This criterion isolates oceanic hotspots according to each method independently, allowing us to examine how sensitive one method is to the extremes detected by the other. Because both variables are expressed in standardized units (mean = 0, standard deviation = 1), each scatter plot represents a point-by-point statistical comparison, assessing whether a grid cell flagged as extreme by PS also falls in the extreme range for the corresponding EOF. Figure 6.12, in contrast, applies the same 95th-percentile threshold but only to grid cells sharing the same latitude and longitude in both methods, thus focusing on spatially coincident extremes.

The January scatter plots show a clear separation between EOF extremes (blue) and PS extremes (orange). For EOF1, two distinct clusters are visible: one compact between x = 2 and x = 3, and another closer to zero on the positive side. PS points are primarily grouped within the positive EOF1 range, with a few scattered between 0 and -1, indicating that Niño 3–3.4 is the dominant forcing region (see Figure 6.12). However, the presence of PS points below the main EOF1 cluster reveals that PS also detects localized ruptures in areas where EOF1 exhibits minimal explained variance. This contrast reflects EOF1's tendency to emphasize a single dominant mode, while PS identifies additional irregularities within the same domain. In comparison, EOF2 produces a diffuse cloud near zero, while PS forms a compact cluster at the other extreme. This indicates that EOF2 contributes minimally to the variance in January, whereas PS highlights extremes independently, linked to subtropical signals. EOF3 exhibits a similarly narrow band of concentrated values, while PS extends into a broader distribution of both positive and negative extremes. This divergence underscores how EOF3 isolates only a limited subset of anomalies, whereas PS assigns greater influence to marginal areas such as the eastern Pacific boundary. The partial alignment of EOF1 and PS extremes nonetheless reflects the canonical ENSO regime described by Gershunov and Barnett (1998).

In February, EOF1 forms a broader horizontal distribution with intermediate values, while PS condenses into a dense band shifted toward the positive side of the plot. Overlap is weaker than in January, with fewer coincident points in the mid-range. Nevertheless, PS consistently reaches stronger extremes, emphasizing the intensification and westward extension of Niño 3–3.4 anomalies that EOF1 distributes across multiple cells due to orthogonality constraints. EOF2 appears as an elongated cloud along the horizontal axis, with PS points grouped more narrowly at one end, suggesting only weak correspondence between the two methods. EOF3 shows a diffuse pattern scattered around the origin, with limited overlap with PS. This partial agreement indicates that EOF3 captures only a small fraction of the variability that PS isolates within a distinct cluster, complementing the broader variance allocation of EOF1. The presence of two bands in EOF1, observed in both January and February, arises from its distribution of variance into separate groups of cells: one capturing the most extreme ENSO-related anomalies and another representing moderate values. This separation reflects the inherent constraint of EOF analysis, where a single mode cannot fully represent the dominant pattern, in contrast to PS, which concentrates the signal more coherently within a single framework.

In March, EOF1 separates into two groups. The first is compact and concentrated near intermediate values around zero, extending into the negative range, while a second group is more dispersed around x = 2–3, where it partially overlaps with PS. In this region, PS aligns within a vertical band centred on positive loadings and clustering near x = 3. This pattern indicates that EOF1 distributes anomalies across the Niño 3–4 sector, whereas PS highlights fewer shared cells but with greater weight. Since the first EOF mode explains a significant fraction of the variance, a comparison across the three months shows that overlap between

EOF1 and PS declines gradually, while EOF1 shifts part of its variability toward negative values. This reflects the behaviour of partial Spearman correlation, which captures both positive and negative monotonic signals, distinguishing transitions between warm and cold ENSO phases. Warm anomalies are mainly expressed in EOF1, while the cold phase appears in EOF2. As winter transitions into spring, the standardized variability in EOF1 changes, reducing its correspondence with PS. EOF2 forms a horizontally extended distribution centred near zero, while PS remains compact, concentrated in regions not represented by EOF2. EOF3 produces a more diffuse spread, covering a wider amplitude range and diverging from PS. PS, in turn, forms a cluster shifted toward positive values, with limited overlap. These values correspond to subtropical lobes near Hawaii and Central America (Dettinger et al, 2011; Rutz et al., 2019), which PS identifies as influential due to their association with storm activity in California.

Across the three months, the sequence shows a transition in the distribution of the 95th-percentile points of both methods. Cohesion is highest in January and decreases toward March. Across modes, variance among points grows as they depart from EOF1, while PS maintains a relatively stable clustering. This suggests that PS captures variability consistently across months, without being constrained by orthogonality, thereby detecting structural changes that EOFs distribute among multiple modes.

Figure 6.12 applies the same 95th-percentile threshold but restricts the comparison to grid cells sharing the same latitude and longitude in both methods, emphasizing spatially coincident extremes. Blue points represent cells above the 95th percentile for EOF1, while orange points indicate those for PS. In January, EOF1 shows a strong concentration in the central and eastern equatorial Pacific, consistent with the canonical El Niño pattern. PS, by contrast, exhibits a wider distribution, with several high-value cells outside this core region, reflecting its sensitivity to nonlinear and nonstationary behaviour across the Pacific. In February, EOF1 detections remain cohesive and clustered, whereas PS extremes shift eastward and extend beyond the central Pacific, underscoring the role of seasonality and the importance of accounting for temporal variations in agreement between the two metrics.

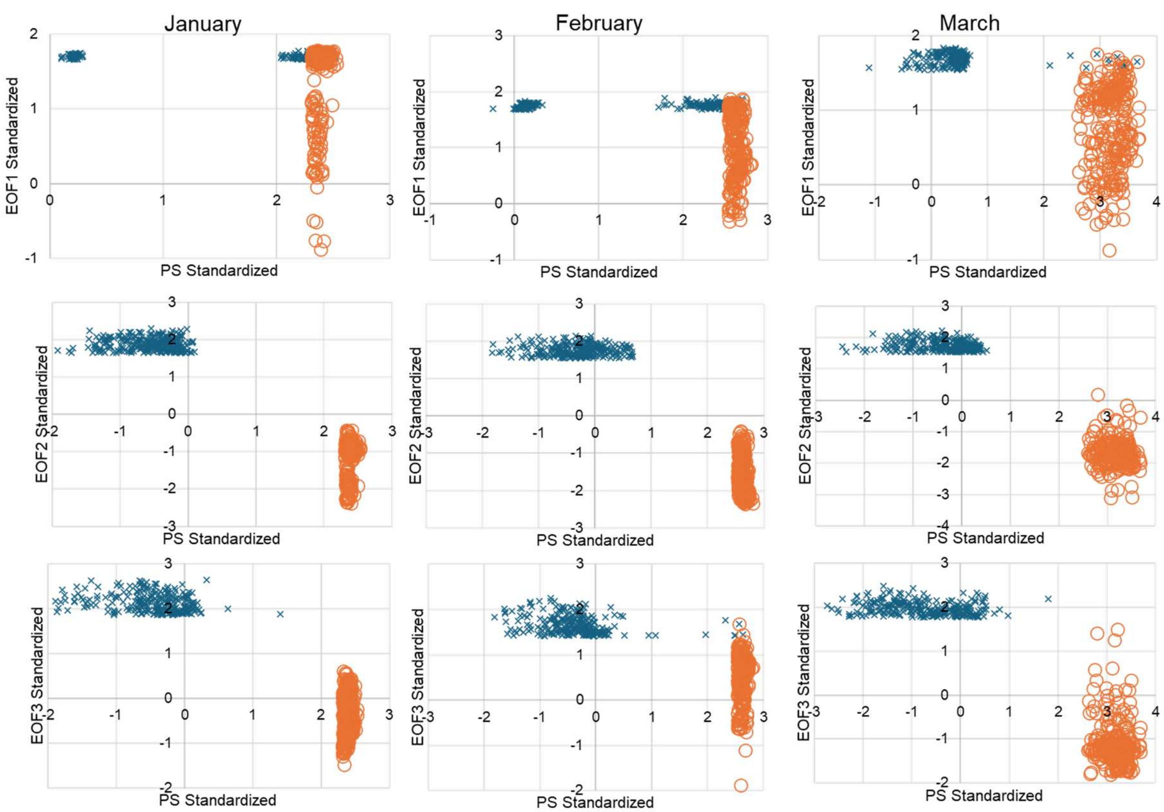

Figure 6.11 Comparison between standardized Point–Slope similarity values and EOF spatial loadings across oceanic grid points in the 95th percentile.

By March, both blue and orange points appear more scattered and less dense. While coincidences persist in the equatorial Pacific, the pattern weakens and shifts relative to January and February. EOF1 is highlighted here because it represents the dominant spatial mode of SST variability, capturing the largest share of explained variance and providing a consistent reference for large-scale teleconnection analysis. Comparing PS with EOF1 ensures that overlaps are evaluated against the primary mode of climate variability. Even so, the methods diverge in the magnitude assigned to the warmest cells, particularly late in winter when trend changepoints become more pronounced.

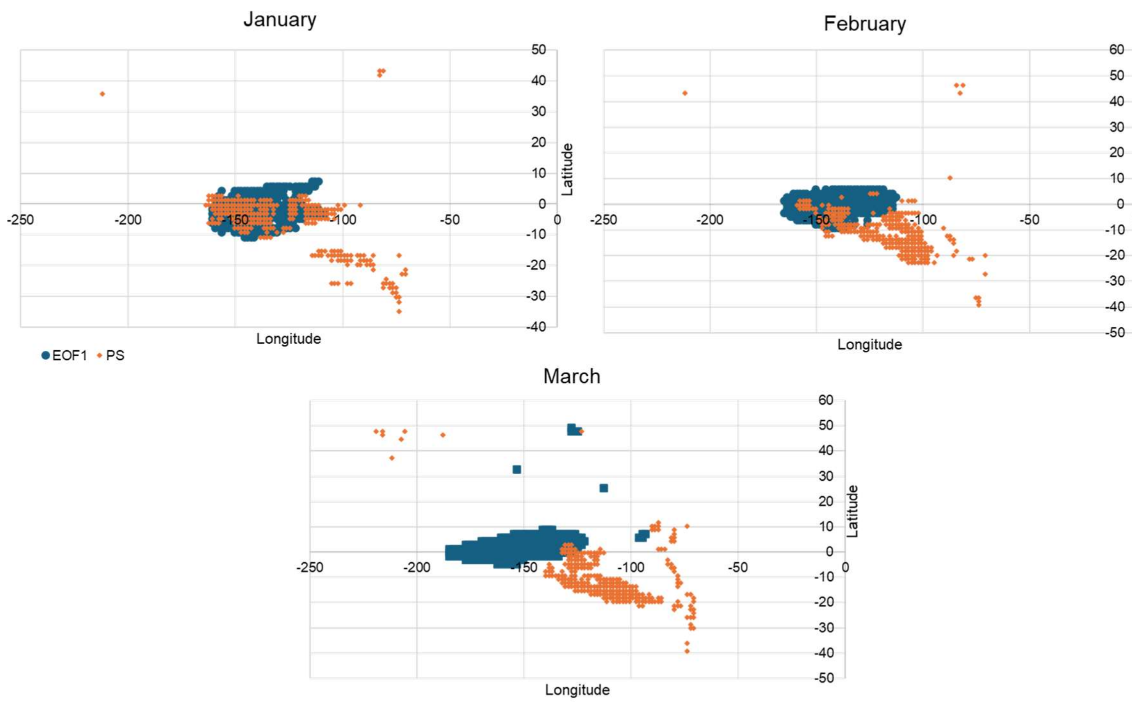

Figure 6.12 Spatial distribution of 95th-percentile extremes detected by EOF1 (blue) and Point–Slope (PS, orange).

Evidently, Figures 6.11 and 6.12 are intrinsically related, as they depict the same points; visualizing them shifts the statistical comparison into a physical context that clarifies the differences between the two methods. Agreement in the Niño 3–3.4 sector confirms the physical robustness of the ENSO signal, whereas divergences at the extremes, illustrated in Figure 6.11, demonstrate PS's ability to isolate nonstationary hot spots that linear EOFs diffuse across multiple modes. This differentiation, enabled by the 1.5° × 1.5° grid, provides scale-appropriate insights into subtle teleconnection dynamics that could be masked at coarser resolutions.

6.5. Conclusions

This study explored how ENSO influences winter precipitation in California from 1981 to 2022 by contrasting two diagnostic frameworks: (i) the nonlinear, non-stationary Point–Slope (PS) similarity metric coupled with spatial clustering, and (ii) a traditional linear approach combining partial Spearman correlations with Empirical Orthogonal Functions (EOF). Our analyses covered January, February, March; months known for significant ENSO impact in California. Furthermore, it was evaluated every 1.5°X 1.5° Sea Surface Temperature Anomaly (SSTA) grid point across the Pacific, creating oceanic Regions of Influence (ROI). Our findings highlight several key advancements and insights:

1. By aligning changepoints and equally directed trends, PS detected coherent clusters of rain gauges that responded in joint magnitude to Pacific forcing, being largely visible during January and February. Unlike other studies, this analysis made it possible to establish land regions influenced by varied oceanic zones, thereby modifying the idea of established or averaged indices like the Niño 3.4 corridor.
2. The leading EOF mode captured the main linear variability near Niño-3.4, but higher-order modes redistributed variance and produced fragmented station patterns, missing key teleconnection links in northern and interior California.
3. Examination of individual SSTA nodes revealed several high-impact, non-exclusive centers. While a significant portion of SSTA concentrated impacts around Niño 3.4, a movement outside the canonical Niño 3.4 box was observed as winter ended

(March). The importance of these centers became evident in the upper 5% of the PS distribution, where similarity continued to increase almost linearly.

4. Both methods broadly described the Pacific influence; however, the structural similarity method (PS) uniquely represented its full spatial reach and structural complexity, highlighting increased hydroclimatic sensitivity in Southern and Central California. This precise differentiation, made possible by the 1.5° oceanic grid, provided valuable, scale-appropriate information on subtle teleconnection dynamics that might otherwise be obscured at lower resolutions.
5. The PS-clustering framework offers a robust, scale-adaptive tool for improving seasonal forecasts and water-management strategies. Its ability to locate detailed ROIs, despite nonlinearity and data gaps, opens avenues for more accurate predictive models that extend beyond traditional correlation techniques.

Chapter 7 Conclusions and Recommendations

7.1. General Conclusions

This dissertation aimed to strengthen the study of climate-hydrology teleconnections within a nonlinear and nonstationary framework, overcoming the limitations of traditional approaches. While linear and stationary methods have advanced the understanding of climate variability and its hydrological impacts, they provide only a partial view of a phenomenon that is inherently complex. In response, this research proposed the Point–Slope (PS) similarity metric, which segments time series into homogeneous intervals and integrates both the timing of changepoints and the sign of trends. This approach not only captures structural similarities between signals but also translates them into physically interpretable indicators of intensification or weakening. The PS metric proved useful as a regionalization tool, enabling the delineation of influence regions across both oceanic and terrestrial domains under a biunivocal framework. Nevertheless, the study also highlighted that the reliance on predefined climate indices introduces constraints, as these linear “boxes” fail to represent natural irregularities adequately. Overall, the results demonstrate that this methodological framework provides a robust and flexible basis for characterizing oceanic influence on regional hydrology, opening new opportunities for both the study and practical application of teleconnections.

Although teleconnections have received increasing attention in recent research, many studies remain primarily focused on ocean–atmosphere interactions, often without fully quantifying their impacts on land. At the same time, the concept of teleconnections is vast in scope. For this reason, the methodology in this dissertation concentrated specifically on ENSO, justified by two main factors: (a) ENSO is the most widely recognized and studied teleconnection, with well-documented adverse effects across the globe, and (b) its pervasive impacts make it an appropriate case study. However, the framework developed here is not exclusive to ENSO. On the contrary, it was designed with the flexibility to be applied globally and can be reproduced at finer regional scales in future work. Similarly, California was chosen as a prototype study region—not as the central objective of the thesis. While California has been extensively documented for its hydroclimatic vulnerabilities, its extreme climatic variability and contrasting hydrological conditions provide an ideal testbed. This choice also opens the door to applying the proposed methodology in other regions facing acute climatic challenges, such as the Sahel or the Amazon Basin.

Another important point, as discussed in **Chapter 2**, is that teleconnections offer compelling evidence of climate change. However, the results here also underscore that climate variability itself is being amplified by climate change, and in turn, this amplified variability negatively affects watershed conditions. Consequently, it is essential to continue studying and characterizing these phenomena in order to anticipate future interactions and support adaptation strategies, with a clear emphasis on protecting economies and societies at large.

Building on these conditions, the development of a teleconnection analysis to link meteorological stations with their regions of influence (**Chapter 4**) demonstrated the initial capability of the Point–Slope (PS) similarity measure. From a methodological perspective, this represented the formal introduction of PS as an alternative for aligning nonlinear and nonstationary signals distributed across California. The main contribution of this approach was to show that two distant time series can be connected through segmentation and their similarity quantified by the coincidence of changepoints and the direction of slopes.

The resulting maps provide a novel conceptualization of teleconnections. Unlike previous studies, this work introduces a compact and consistent framework for their representation, without requiring additional transformations or the combined use of multiple statistical tools. At the same time, the results demonstrate the feasibility of identifying which oceanic climate regions may exert a direct influence on land-based precipitation, thereby offering an interpretive bridge between oceanic dynamics and regional hydrological response.

Once the phenomenon was examined through the application of PS, the next step was to determine the actual effects of the teleconnection. To this end, a canonical climate index, Niño 3.4, was related to the full spectrum of precipitation stations across California. The delineation of regions based on this widely used index aimed to test the ability of PS to capture signals of climatic influence robustly and to benchmark its performance against established approaches. This analysis carries strong methodological relevance, as it enables a comparative evaluation between a traditional framework, the partial Spearman correlation, and the newly proposed PS metric, explicitly designed to incorporate nonlinearity and nonstationarity.

In addition, the study incorporated a comparison with alternative metrics such as Dynamic Time Warping (DTW), which, although not intended to capture structural alignment between signals, highlight temporal dissimilarities and remain a widely used reference in time series analysis.

Consequently, **Chapter 5** provides an explicit evaluation of PS in relation to these well-established methodologies, offering a critical comparison with the tools that dominate most current teleconnection studies. This exercise not only underscores the advantages of PS in detecting structural similarity but also positions it within the broader methodological landscape of hydroclimatic research, highlighting its potential as an alternative framework for future applications.

Finally, **Chapter 6** confirms the capacity of PS by breaking with the paradigm of previous teleconnection analyses. Unlike traditional approaches constrained by fixed climate indices, which act as spatial "boxes" that condense only part of the phenomenon, this chapter demonstrates that regionalization can be performed in both directions, from ocean to land and vice versa. This innovation shows that the irregular and heterogeneous nature of ocean–atmosphere interactions can, under optimal conditions, lead to more realistic delineations of regions of influence. Moreover, when these regions are defined under explicit assumptions of nonlinearity and nonstationarity, the resulting framework more accurately reflects the complexity of hydroclimatic variability.

Several elements across Chapters **4**, **5**, and **6** indicate that the PS framework is not dominated by noise. In Chapter 4, changepoints with high posterior probability tend to occur at similar dates across stations and predictors, suggesting that they reflect genuine structural changes rather than random fluctuations. In Chapters 4 and 6, the resulting Regions of Influence exhibit strong spatial coherence and reproduce well-documented Pacific teleconnection patterns, which would be unlikely to arise from stochastic variability alone. Chapter 5 provides further support through cross-method validation: PS patterns show consistent agreement with partial correlations, PCA modes, and DTW-based diagnostics, indicating that the dominant signals captured by PS are also detected by independent frameworks. Additionally, the sign and distribution of dominant slopes remain stable across months, predictors, and clustering configurations, providing indirect evidence of robustness to moderate perturbations in model configuration. Uncertainty is quantified through posterior distributions of changepoint locations and slope parameters, which can be visualized as probability fields of structural change. The spatial agreement between these posterior maps and independent diagnostics provides further confidence in the reliability of PS-based regions of influence.

A key contribution of this work is that the physical manifestation of teleconnection patterns can now be visualized directly through clear and interpretable maps, without the need for post-processing steps. This advantage is particularly relevant for decision-makers, who require precise information on where, how, and when climatic variations impact hydrological systems. Ultimately, an indirect objective of this framework is to make teleconnection analysis both simpler and more robust, bridging the gap between methodological sophistication and practical applicability.

From a practical perspective, PS-based Regions of Influence provide spatially explicit information on where and when large-scale oceanic anomalies are most strongly coupled to local hydroclimatic conditions. This knowledge can be exploited in climate-change adaptation strategies by identifying basins whose hydrology is particularly sensitive to specific SSTA patterns and by designing early-warning systems and reservoir operation rules that account for evolving teleconnections under global warming. As the frequency and intensity of extreme ENSO events and other modes of variability are projected to change in a warming climate, teleconnection-informed planning is likely to become increasingly important for robust water-resources management and flood–drought risk mitigation.

7.2. Limitations

While the ability of PS to capture signals with dynamic characteristics has been clearly demonstrated, further refinements are still necessary to optimize its implementation and efficiency for large-scale or operational applications.

One of the main limitations of this framework lies in its computational cost, primarily due to the statistical inference inherent to the Bayesian process. Although the computational performance did not show a decisive impact on the analyses presented here, it did influence the feasibility of applying the method to another study area and dataset. From a technical standpoint, further exploration of more efficient implementations of the MCMC algorithm, as originally employed by Seidou and Ouarda (2007), could significantly improve the scalability of changepoint detection, especially for larger datasets or higher-resolution applications.

Another aspect that was not explored in depth is the performance of the method at smaller spatial or temporal scales. While in theory this should not pose a major limitation, delays or lags in the climate–hydrology response system may become relevant at finer resolutions, and incorporating these explicitly could strengthen the robustness of the approach.

Additionally, while PCA was used as the primary comparison benchmark, it would have been useful to contrast the PS-based regionalization with alternative frameworks, such as nonlinear principal component analysis (NLPCA) combined with wavelet transforms. These hybrid approaches, while conceptually different from PCA, are widely recognized for their ability to capture nonlinearity and multiscale variability. Demonstrating how PS compares with such methods would not only reinforce its validity but also highlight its added value as a parsimonious yet physically interpretable similarity measure.

7.3. Future works

This research demonstrated the potential of the Point–Slope (PS) similarity framework as an alternative tool for analyzing hydroclimatic teleconnections, but several avenues remain open for further exploration.

1. Computational efficiency: One limitation of the current framework is the computational cost associated with Bayesian inference, particularly the reliance on Markov Chain Monte Carlo (MCMC) for changepoint detection (Seidou and Ouarda, 2007). Future work should investigate more efficient inference strategies, such as Sequential Monte Carlo (SMC), Variational Bayes, or Hamiltonian Monte Carlo, which could accelerate convergence and make PS more scalable for large datasets.
2. Incorporation of delay effects: Teleconnections often exhibit delayed impacts. For example, oceanic anomalies may influence precipitation with a lag of several weeks or months. The current PS framework does not explicitly account for such delays. Extending PS to integrate lagged similarities, by allowing changepoint and slope alignment under shifted time windows, would provide a more realistic representation of climate–hydrology linkages.
3. Comparison with advanced nonlinear frameworks: While PCA was used as a benchmark in this study, other nonlinear or hybrid approaches, such as Nonlinear PCA (NLPCA), Empirical Mode Decomposition (EMD), or wavelet-based frameworks, are recognized for their ability to capture nonstationary and multiscale signals. Comparing PS against these methods would strengthen its methodological positioning and highlight its advantages.

4. Application to diverse climatic regions: California served as a prototype case due to its climatic variability and ENSO sensitivity. Future studies should extend the application of PS to regions with different hydroclimatic regimes, such as the Sahel, the Amazon Basin, or South Asia. This would test its robustness across contexts and demonstrate its universality as a teleconnection analysis tool.
5. Integration with machine learning: Another promising direction is the combination of PS-based similarity metrics with machine learning methods (e.g., clustering, classification, or neural networks). Such integration could enhance regionalization tasks, automate the detection of influence zones, and potentially support predictive models of precipitation or streamflow based on teleconnection signals.
6. Uncertainty quantification and robustness testing: Although PS incorporates uncertainty through Bayesian changepoint detection, further work is needed to assess its robustness under data limitations systematically. For instance, hydroclimatic records often contain gaps, measurement errors, or varying lengths across stations. Future research should evaluate how sensitive PS outcomes are to missing data, short records, and observational noise.
7. Decision-making and adaptation strategies: Finally, future research should explore how PS-derived influence zones can be incorporated into water resources planning and climate adaptation frameworks. By linking statistical similarity to actionable insights (e.g., flood forecasting, drought risk assessment), PS can bridge the gap between methodological innovation and societal impact.

References

1. Abatzoglou, J. T., Kunkel, K. E., and Stevens, M. (2021). Examining the potential effects of climate change on teleconnection patterns. Climatic Change, 159(1), 23–41. https://doi.org/10.1007/s10584-020-02838-6
2. Abdelkader, M., and Yerdelen, C. (2022). Hydrological drought variability and its teleconnections with climate indices. Journal of Hydrology, 605, 127290. https://doi.org/10.1016/j.jhydrol.2021.127290
3. Abebe, S. A., Qin, T., Zhang, X., and Yan, D. (2022). Wavelet transform-based trend analysis of streamflow and precipitation in upper Blue Nile River basin. Journal of Hydrology: Regional Studies, 44, 101251. https://doi.org/10.1016/j.ejrh.2022.101251
4. Adams, D. K., and Comrie, A. C. (1997). The North American monsoon. Bulletin of the American Meteorological Society, 78(10), 2197–2213. https://doi.org/10.1175/1520-0477(1997)078<2197:TNAM>2.0.CO;2
5. Agarwal, A., Yuan, N., Cheung, K. K. W., and Shukla, R. (2022). Emerging hydro-climatic patterns, teleconnections, and extreme events in a changing world at different timescales. Atmosphere, 13(1), 56. https://doi.org/10.3390/atmos13010056
6. AghaKouchak, A., Chiang, F., Huning, L. S., Love, C. A., Mallakpour, I., Mazdiyasni, O., Moftakhari, H., Papalexiou4, S.M., Ragno, E., and Sadegh, M. (2020). Climate extremes and compound events in a warming world. Annual Review of Earth and Planetary Sciences, 48, 519–548. https://doi.org/10.1146/annurev-earth-071719-055228

7. Alcamo, J. (2019). Water quality and its interlinkages with the Sustainable Development Goals. Current Opinion in Environmental Sustainability, 36, 126–140. https://doi.org/10.1016/j.cosust.2018.11.005
8. Alexander, M. A., Blade, I., Newman, M., Lanzante, J. R., Lau, N.-C., and Scott, J. D. (2002). The atmospheric bridge: The influence of ENSO teleconnections on air-sea interaction over the global oceans. Journal of Climate, 15(16), 2205-2231. https://doi.org/10.1175/1520-0442(2002)015<2205:TABTIO>2.0.CO;2
9. Alobaidi, M. H., Meguid, M. A., and Chebana, F. (2020). Varying-parameter modeling within ensemble architecture: Application to extended streamflow forecasting. Journal of Hydrology, 582, 124511. https://doi.org/10.1016/j.jhydrol.2019.124511
10. An, S.-I., Wang, C., and Mechoso, C. R. (2020). Teleconnections in the atmosphere. In Interacting Climates of Ocean Basins: Observations, Mechanisms, Predictability, and Impacts (pp. 54–88). Cambridge University Press. https://doi.org/10.1017/9781108610995.003
11. Arcodia, M. C., Kirtman B. P., and Siqueira L.S.P. (2020). How MJO teleconnections and ENSO interference impacts U.S. precipitation. Journal of Climate, 33(11), 4621–4640. https://doi.org/10.1175/JCLI-D-19-0448.1
12. Arias, P. A., Bellouin, N., Coppola, E., Jones, R. G., Krinner, G., Marotzke, J., ... and Zickfeld, K. (2021). Technical Summary. En: Masson-Delmotte, V., Zhai, P., Pirani, A., Connors, S. L., Péan, C., Berger, S., ... and Zhou, B. (Eds.), Climate Change 2021: The Physical Science Basis. Contribution of Working Group I to the Sixth

Assessment Report of the Intergovernmental Panel on Climate Change (pp. 33–144). Cambridge University Press. https://doi.org/10.1017/9781009157896.002

13. Ashok, K., Behera, S. K., Rao, S. A., Weng, H., and Yamagata, T. (2007). El Niño Modoki and its teleconnection. Journal of Geophysical Research: Oceans, 112, C11007. https://doi.org/10.1029/2006JC003798
14. Ashok, K., Guan, Z., and Yamagata, T. (2004). Individual and combined influences of ENSO and the Indian Ocean Dipole on the Indian summer monsoon. Journal of Climate, 17(16), 3141–3155. https://doi.org/10.1175/1520-0442(2004)017<3141:IACIOE>2.0.CO;2
15. Bárdossy, A. and Pegram, G. (2011) Downscaling Precipitation Using Regional Climate Models and Circulation Patterns toward Hydrology. Water Resources Research, 47, 1-18.http://dx.doi.org/10.1029/2010WR009689
16. Barnes, E. A., Barnes, R. J., Martin, Z. K., and Rader, J. K. (2022). This Looks Like That There: Interpretable Neural Networks for Image Tasks When Location Matters. Artificial Intelligence for the Earth Systems, 1(3), 1–34. https://doi.org/10.1175/AIES-D-22-0001.1
17. Barnston, A. G., and Livezey, R. E. (1987). Classification, seasonality, and persistence of low-frequency atmospheric circulation patterns. Monthly Weather Review, 115(6), 1083-1126. https://doi.org/10.1175/1520-0493(1987)115<1083:CSAPOL>2.0.CO;2
18. Barry, R. G., and Hartigan, J. (1992,). Climatological studies of Arctic Oscillation indices. Polar Geography, 16, 133–145.

19. Belmecheri, S., Cook, B. I., and Shuman, B. (2016). The teleconnections of climate variability and regional hydrology in the U.S. Journal of Hydrology, 543, 212-227. https://doi.org/10.1016/j.jhydrol.2016.01.040
20. Bevington, A. R., Gleason, H. E., Foord, V. N., Floyd, W. C., and Griesbauer, H. P. (2019). Regional influence of ocean–atmosphere teleconnections on the timing and duration of MODIS-derived snow cover in British Columbia, Canada. The Cryosphere, 13(10), 2693–2712. https://doi.org/10.5194/tc-13-2693-2019
21. Blöschl, G., Hall, J., and Viglione, A. (2019). An analysis of teleconnection patterns in hydrology. Water Resources Research, 55(5), 3640–3657. https://doi.org/10.1029/2018WR024445
22. Blöschl, G., Hall, J., Viglione, A., Perdigão, R. A. P., Parajka, J., Merz, B., Arheimer, B., Aronica, G. T., Bilibashi, A., Bonacci, O., Borga, M., Čanjevac, I., Castellarin, A., Chirico, G. B., Claps, P., Fiala, K., Frolova, N., Gorbachova, L., Gül, A., … Živković, N. (2019). Changing climate both increases and decreases European river floods. Nature, 573(7772), 108–111. https://doi.org/10.1038/s41586-019-1495-6
23. Bretherton, C. S., Smith, C., and Wallace, J. M. (1992). An intercomparison of methods for finding coupled patterns in climate data. Journal of Climate, 5(6), 541-560. https://doi.org/10.1175/1520-0442(1992)005<0541:AIOMFF>2.0.CO;2
24. Brönnimann, S. (2007). Impact of El Niño–Southern Oscillation on European climate. Reviews of Geophysics, 45(2), RG3003. https://doi.org/10.1029/2006RG000199

25. Buishand, T. A. (1982). Tests for detecting a shift in the mean of hydrological time series. Journal of Hydrology, 61(1–2), 71–85. https://doi.org/10.1016/0022-1694(82)90066-X

26. Burn, D. H. (1990). Evaluation of regional flood frequency analysis with a region of influence approach. Water Resources Research, 26(10), 2257–2265.

27. Burn, D. H. (1997). Catchment similarity for regional flood frequency analysis. Journal of Hydrology, 202(1–4), 212–230.

28. Cai, W., Borlace, S., Lengaigne, M., van Rensch, P., Collins, M., Vecchi, G., ... Jin, F.-F. (2014). Increasing frequency of extreme El Niño events due to greenhouse warming. Nature Climate Change, 4, 111–116. https://doi.org/10.1038/nclimate2100

29. Canchala, T., Alfonso-Morales, W., Loaiza Cerón, W., Carvajal-Escobar, Y., and Caicedo-Bravo, E. (2020). Teleconnections between monthly rainfall variability and large-scale climate indices in Southwestern Colombia. Water, 12(7), Article 1863. https://doi.org/10.3390/w12071863

30. Capotondi, A., and Sardeshmukh, P. (2020). ENSO: The past, present, and future (pp. 75-102). American Geophysical Union. https://doi.org/10.1002/9781119548164.ch4.

31. Capotondi, A., Wittenberg, A. T., Newman, M., et al. (2015). Understanding ENSO diversity. Bulletin of the American Meteorological Society, 96(6), 921-938. https://doi.org/10.1175/BAMS-D-13-00117.1.

32. Castro-Melgar, I., Falaras, T., Basiou, E., and Parcharidis, I. (2025). Assessment of the October 2024 Cut-Off Low Event Floods Impact in Valencia (Spain) with Satellite and Geospatial Data. Remote Sensing, 17(13), 2145. https://doi.org/10.3390/rs17132145

33. Cayan, D. R., Luers, A. L., and Barlow, M. (2010). Future dryness in the southwest U.S. and the hydrology of the early 21st century drought. Proceedings of the National Academy of Sciences, 107(50), 21271–21276. https://doi.org/10.1073/pnas.0912391107

34. Cayan, D. R., Redmond, K. T., and Riddle, L. G. (1999). ENSO and hydrologic extremes in the western United States. Journal of Climate, 12(9), 2881–2893. https://doi.org/10.1175/1520-0442(1999)012<2881:EAHEIT>2.0.CO;2

35. Cayan, D. R., Tyree, M., Dettinger, M. D., Hidalgo, H. G., Das, T., Maurer, E. P., and Flick, R. (2008). Climate change scenarios and sea level rise estimates for the California 2008 climate change scenarios assessment. California Climate Change Center.

36. Cazelles, B., Chavez, M., Berteaux, D., Ménard, F., Vik, J. O., Jenouvrier, S., and Stenseth, N. C. (2008). Wavelet analysis of ecological time series. Oecologia, 156(2), 287–304. https://doi.org/10.1007/s00442-008-0993-2

37. Chase, T. N., Pielke Sr., R. A., and Avissar, R. (2006). Teleconnections in the Earth System. En M. G. Anderson (Ed.), Encyclopedia of Hydrological Sciences (Vol. 15, pp. 2849–2862). John Wiley and Sons. https://doi.org/10.1002/0470848944.hsa190

38. Chen, H.-L., and Rao, A. R. (2003). Linearity analysis on stationary segments of hydrologic time series. Journal of Hydrology, 275(1-2), 43–54. https://doi.org/10.1016/S0022-1694(03)00086-6

39. Chiang, J. C. H., Kushnir, Y., and Giannini, A. (2002). Deconstructing Atlantic intertropical convergence zone variability: Influence of the local cross-equatorial sea surface temperature gradient and remote forcing from the eastern equatorial Pacific.

Journal of Geophysical Research: Atmospheres, 107(D1), 4004. https://doi.org/10.1029/2000JD000307

40. Chiew, F. H. S., and McMahon, T. A. (2002). Global ENSO–streamflow teleconnection, streamflow forecasting and interannual variability. Hydrological Sciences Journal, 47(3), 505–522. https://doi.org/10.1080/02626660209492950
41. Choi, K. S., and Moon, I. J. (2012). Influence of the Western Pacific teleconnection pattern on Western North Pacific tropical cyclone activity. Dynamics of Atmospheres and Oceans, 57, 1–16. https://doi.org/10.1016/j.dynatmoce.2012.04.002
42. Coe, D., Barlow, M., Agel, L., Colby, F., Skinner, C., and Qian, J.-H. (2021). Clustering analysis of autumn weather regimes in the Northeast United States. Journal of Climate, 34(18), 7587–7605. https://doi.org/10.1175/JCLI-D-20-0243.1
43. Compagnucci, R. H., and Richman, M. B. (2008). Can principal component analysis provide atmospheric circulation or teleconnection patterns? International Journal of Climatology, 28(6), 703–726. https://doi.org/10.1002/joc.1574
44. Corringham, T. W., Ralph, F. M., Gershunov, A., Cayan, D. R., and Talbot, C. A. (2019). Atmospheric rivers drive flood damages in the western United States. Science Advances, 5(12), eaax4631. https://doi.org/10.1126/sciadv.aax4631
45. Coulibaly, P. (2006). Spatial and temporal variability of Canadian seasonal precipitation (1900–2000). Advances in Water Resources, 29(12), 1846–1865. https://doi.org/10.1016/j.advwatres.2005.12.013
46. Coulibaly, P., and Burn, D. H. (2004). Wavelet analysis of variability in annual Canadian streamflows. Water Resources Research, 40(3). https://doi.org/10.1029/2003WR002667

47. CPC. (2024). Climate Prediction Center . Retrieved September 9, 2024, https://www.cpc.ncep.noaa.gov/

48. Dai, Y., and Tan, B. (2019). On the role of the eastern Pacific teleconnection in ENSO impacts on wintertime weather over East Asia and North America. Journal of Climate, 32(4), 1217–1234. https://doi.org/10.1175/JCLI-D-17-0789.1

49. Das, T., Dettinger, M. D., Cayan, D. R., and Hidalgo, H. G. (2011). Potential increase in floods in California's Sierra Nevada under future climate projections. Climatic Change, 109(1), 71-94.

50. DeFlorio, M. J., Ralph, F. M., Luna-Niño, R., and Gershunov, A. (2024). Atmospheric rivers as disruptors of canonical ENSO precipitation anomalies in the southwestern United States. Climate Dynamics. Advance online publication. https://doi.org/10.1007/s00382-024-07111-9.

51. Destouches, C., Diedhiou, A., Anquetin, S., Hingray, B., Pierre, A., Boisson, D., and Joseph, A. (2025). Changes in extreme precipitation patterns over the Greater Antilles and teleconnection with large-scale sea surface temperature. Earth System Dynamics, 16, 497–512. https://doi.org/10.5194/esd-16-497-2025

52. Dettinger, M. (2011). Climate change, atmospheric rivers, and floods in California—a multimodel analysis of storm frequency and magnitude changes. JAWRA Journal of the American Water Resources Association, 47(3), 514–523. https://doi.org/10.1111/j.1752-1688.2011.00546.x

53. Dettinger, M. (2013). Atmospheric rivers as drought busters on the U.S. West Coast. Journal of Hydrometeorology, 14(6), 1721–1732. https://doi.org/10.1175/JHM-D-13-02.1

54. Dettinger, M. D., and Diaz, H. F. (2000). Global characteristics of streamflow seasonality and variability. Journal of Hydrometeorology, 1(4), 289–310. https://doi.org/10.1175/1525-7541(2000)001<0289:GCOSFS>2.0.CO;2

55. Dettinger, M. D., and Redmond, K. T. (1998). Workshop assesses the 1997–1998 El Niño-Pacific climate perspectives PACLIM 1998 summary. Eos, Transactions of the American Geophysical Union, 79(36), 430–431.

56. Dettinger, M. D., Cayan, D. R., Diaz, H. F., and Meko, D. M. (1998). North–South precipitation patterns in western North America on interannual-to-decadal timescales. Journal of Climate, 11(12), 3095–3111. https://doi.org/10.1175/1520-0442(1998)011\<3095:NSPPIW>2.0.CO;2

57. Dettinger, M., Ralph, F. M., Das, T., Neiman, P. J., and Cayan, D. R. (2011). Atmospheric rivers, floods, and the water resources of California. Water, 3(2), 445-478.

58. Djibo, A. G., Rajagopalan, B., Prairie, J., and Moradkhani, H. (2015). Space-time variability of climate variables in the Upper Niger River Basin. Journal of Hydrology, 528, 632–645. https://doi.org/10.1016/j.jhydrol.2015.06.061

59. Djibo, S. A., Ouarda, T. B. M. J., and Boubacar, H. (2015). Statistical seasonal streamflow forecasting using a probabilistic approach over the West African Sahel. Natural Hazards, 80(1), 301–319. https://doi.org/10.1007/s11069-015-1866-8

60. Du, X., Hendy, I., Hinnov, L., Brown, E., Schimmelmann, A., and Pak, D. (2020). Interannual southern California precipitation variability during the common era and the ENSO teleconnection. Geophysical Research Letters, 47(1), e2019GL085891. https://doi.org/10.1029/2019GL085891

61. Duan, A. (2024). Quantifying the 2022 extreme drought in the Yangtze River Basin using GRACE-FO. International Journal of Remote Sensing, 45(24), 10197–10211. https://doi.org/10.1080/01431161.2024.2427915

62. Easterling, D. R., and Peterson, T. C. (1995). A new method for detecting and adjusting for undocumented discontinuities in climatological time series. International Journal of Climatology, 15(4), 369–377. https://doi.org/10.1002/joc.3370150403

63. EFE. (2024, noviembre 5). Gobierno y Generalitat estiman en 2.600 millones el coste de restaurar infraestructuras. EFE. Recuperado el 28 de abril de 2025, de https://efe.com/economia/2024-11-05/gobierno-y-generalitat-estiman-en-2-600-millones-el-coste-de-restaurar-infraestructuras/

64. Ehsanzadeh, E., van der Kamp, G., and Spence, C. (2016). On the changes in long-term streamflow regimes in the North American Prairies. Progress in Physical Geography, 40(2), 64–78. https://doi.org/10.1080/02626667.2014.967249

65. El Alaoui El Fels, A., Saidi, M.E.M., Bouiji, A., Benrhanem, M. (2020). Rainfall regionalization and variability of extreme precipitation using artificial neural networks: a case study from western central Morocco. Journal of Water and Climate Change. https://doi.org/10.2166/wcc.2020.217.

66. El Alaoui El Fels, R., El Alami El Filali, A., and El Hassani, H. (2020). Impacts of climate change on hydrological variability in arid regions. Journal of Arid Environments, 173, 1–13. https://doi.org/10.1016/j.jaridenv.2019.104019

67. EL PAÍS. (2024, diciembre 29). Paiporta, dos meses después de la DANA: Cronología de la tragedia que acabó con la vida de 46 de sus vecinos. El País.

Recuperado el 12 de marzo de 2025, de https://elpais.com/expres/2024-12-29/paiporta-dos-meses-despues-de-la-dana-cronologia-de-la-tragediaque-acabo-con-la-vida-de-46-de-sus-vecinos.html

68. Favre, A., B. Hewitson, M. Tadross, C. Lennard, and R. Cerezo-Mota, 2012: Relationships between cut-off lows and the semiannual and southern oscillations. Climate Dyn., 38, 1473–1487, https://doi.org/10.1007/s00382-011-1030-4.
69. Fearnhead, P. (2005). Exact and efficient bayesian inference for multiple changepoint problems. Journal of Statistics and Computing, 16, 203–213. https://doi.org/10.1007/s11222-006-8450- 8
70. Fearnhead, P. (2006). On Bayesian methods for multiple changepoint problems. Biometrika, 93(3), 583-597.
71. Fedorov, A., and Zhao, B. (2021, abril 19–30). The seesaw response of the Intertropical and South Pacific convergence zones to hemispherically asymmetric thermal forcing (EGU21-1428). EGU General Assembly 2021. https://doi.org/10.5194/egusphere-egu21-1428.
72. Feldstein, S. B., and Franzke, C. L. E. (2017). Atmospheric teleconnection patterns. In The climate system: A new perspective (pp. 90-112). Cambridge University Press. https://doi.org/10.1017/9781316339251.004
73. Fuenzalida, H. A., R. Sánchez, and R. D. Garreaud, 2005: A climatology of cutoff lows in the Southern Hemisphere. J. Geophys.Res., 110, D18101, https://doi.org/10.1029/2005JD005934.

74. Galeano, P., and Peña, D. (2007). Covariance changes detection in multivariate time series. Journal of Statistical Planning and Inference, 137(1), 194–211. https://doi.org/10.1016/j.jspi.2005.09.003

75. Gallagher, C., Lund, R., and Robbins, M. (2013). Changepoint Detection in Climate Time Series with Long-Term Trends. Journal of Climate, 26(15), 5618–5633.

76. Gershunov, A., and Barnett, T. P. (1998). Interdecadal modulation of ENSO teleconnections. Bulletin of the American Meteorological Society, 79(12), 2715–2726. https://doi.org/10.1175/1520-0477(1998)079\<2715:IMOET>2.0.CO;2

77. Gershunov, A., and Barnett, T. P. (1998). ENSO influence on intraseasonal extreme rainfall and temperature in the contiguous United States: Observations and model results. Journal of Climate, 11(7), 1575-1586. https://doi.org/10.1175/1520-0442(1998)011<1575:EIOIER>2.0.CO;2

78. González-Pérez, A., Álvarez-Esteban, R., Penas, A., and del Río, S. (2022). Analysis of recent rainfall trends and links to teleconnection patterns in California (U.S.). Journal of Hydrology, 612, 128211. https://doi.org/10.1016/j.jhydrol.2022.128211

79. Goovaerts, P. (2000). Geostatistical approaches for incorporating elevation into the spatial interpolation of rainfall. Journal of Hydrology, 228(1–2), 113–129. https://doi.org/10.1016/S0022-1694(00)00144-Xgu

80. Goss, M., Swain, D. L., Abatzoglou, J. T., Sarhadi, A., Kolden, C., Williams, A. P., and Diffenbaugh, N. S. (2020). Climate change is increasing the likelihood of extreme autumn wildfire conditions across California. Environmental Research Letters, 15(9), 094016.

81. Grinsted, A., Moore, J. C., and Jevrejeva, S. (2004). Application of the cross wavelet transform and wavelet coherence to geophysical time series. Nonlinear Processes in Geophysics, 11(5–6), 561–566. https://doi.org/10.5194/npg-11-561-2004

82. Guan, B., and Waliser, D. E. (2015). Detection of atmospheric rivers: Evaluation and application of an algorithm for global studies. Journal of Geophysical Research: Atmospheres, 120(24), 12514–12535. https://doi.org/10.1002/2015JD024257

83. Ham, Y.-G., Kim, J.-H., and Luo, J.-J. (2019). Deep learning for multi-year ENSO forecasts. Nature, 573(7775), 568–572

84. Hamed, K. H. (2008). Trend detection in hydrologic data: The Mann–Kendall trend test under the scaling hypothesis. Journal of Hydrology, 349(3–4), 350–363. https://doi.org/10.1016/j.jhydrol.2007.11.009

85. Hamed, K. H., and Rao, A. R. (1998). A modified Mann–Kendall trend test for autocorrelated data. Journal of Hydrology, 204(1–4), 182–196. https://doi.org/10.1016/S0022-1694(97)00125-X

86. Hanak, E., Lund, J., Mount, J., Howitt, R., Moyle, P., and Thompson, B. (2011). Managing California's Water: From Conflict to Reconciliation. Public Policy Institute of California

87. Hao, Z., Zheng, J., Liu, Y., and Ge, Q. (2023). Hydroclimate variations in the past 1000 years over Eastern China. International Journal of Climatology, 43(14), 6590–6602. https://doi.org/10.1002/joc.8221

88. Hatchett, B. J., Burak, S., Rutz, J. J., Oakley, N. S., Bair, E. H., and Kaplan, M. L. (2017). Avalanche Fatalities during Atmospheric River Events in the Western United States. Journal of Hydrometeorology, 18(5), 1359–1374.

89. Helsel, D. R., and Hirsch, R. M. (1992). Statistical Methods in Water Resources (Vol. 49). Elsevier.

90. Hereford, J., Hansen, T. F., and Houle, D. (2004). Comparing strengths of directional selection: how strong is strong? Evolution, 58(10), 2133–2143.

91. Higgins, R. W., Shi, W., and Guttman, N. B. (1999). Interannual variability of the North American warm season–precipitation regime. Journal of Climate, 12(3), 653–680. https://doi.org/10.1175/1520-0442(1999)012<0653:IVOTNA>2.0.CO;2

92. Hildebrandsson, H. H. (1897). Quelques recherches sur les centres d'action de l'atmosphère. Kongl. Svenska Vetenskapsakademiens Handlingar, 29(3).

93. Hlinka, J., Hartman, D., Vejmelka, M., Novotná, D., and Paluš, M. (2012). Non-linear dependence and teleconnections in climate data: Sources, relevance, nonstationarity. Climate Dynamics, 38(7-8), 1493–1501. https://doi.org/10.1007/s00382-011-1137-2

94. Hosking, J.R.M and Wallis, J.R. (1997) Regional Frequency Analysis: An Approach Based on L-moments. Cambridge University Press, UK. http://dx.doi.org/10.1017/cbo9780511529443

95. Hrachowitz, M., Savenije, H. H. G., Blöschl, G., McDonnell, J. J., Sivapalan, M., Pomeroy, J. W., Arheimer, B., Blume, T., Clark, M. P., Ehret, U., Fenicia, F., Freer, J. E., Gelfan, A., Gupta, H. V., Hughes, D. A., Hut, R. W., Montanari, A., Pande, S., Tetzlaff, D., Troch, P. A., Uhlenbrook, S., Wagener, T., Winsemius, H. C., Woods, R. A., Zehe, E., and Cudennec, C. (2013). A decade of Predictions in Ungauged Basins (PUB)—a review. Hydrological Sciences Journal, 58(6), 1198–1255. https://doi.org/10.1080/02626667.2013.803183

96. Hsiang, S., Kopp, R., Jina, A., Rising, J., Delgado, M., Mohan, S., ... Houser, T. (2017). Estimating economic damage from climate change in the United States. Science, 356(6345), 1362–1369. https://doi.org/10.1126/science.aal4369

97. Hsieh, W. W. (2001). Nonlinear principal component analysis by neural networks. Tellus A: Dynamic Meteorology and Oceanography, 53A, 599–615. https://doi.org/10.3402/tellusa.v53i5.12230

98. Hsieh,W.W. (2004) Nonlinear multivariate and time series analysis by neural network methods. Reviews of Geophysics, 42, RG1003, doi:10.1029/2002RG000112.

99. Hu W, Si B. 2021. Technical note: improved partial wavelet coherency for understanding scale-specific and localized bivariate relationships in geosciences. Hydrology and Earth System Sciences, 25(1): 321–331, https://doi-org/10.5194/hess-25-321-2021.

100. Hu, Q., and Feng, S. (2001). Variations of teleconnection of ENSO and interannual variation in summer rainfall in the central United States. Journal of Climate, 14(11), 2469–2480. https://doi.org/10.1175/1520-0442(2001)014,2469:VOTOEA.2.0.CO;2.

101. Hu, Q., and Feng, S. (2012). AMO- and ENSO-driven summertime circulation and precipitation variations in North America. Journal of Climate, 25(18), 6477–6495.

102. Hu, S., Zhou, T., Peng, D., Jiang, W., Lu, B., Wu, B., Chen, X., Zhang, L., Chen, X., Zhang, W., and Zhang, W. (2024). Extreme dry advection dominates the record-breaking Yangtze River heatwave in midsummer of 2022. Climate Dynamics, 62(6), 5049–5060. https://doi.org/10.1007/s00382-024-07150-0

103. Hu, Z.-Z., Kumar, A., Zhu, J., Peng, P., and Huang, B. (2019). On the challenge for ENSO cycle prediction: An example from NCEP Climate Forecast System, version 2. Journal of Climate, 32(1), 183–194. https://doi.org/10.1175/JCLI-D-18-0285.1

104. Huang, B., Liu, C., Banzon, V., Freeman, E., Graham, G., Hankins, B., Smith, T., and Zhang, H.-M. (2021). Improvements of the Daily Optimum Interpolation Sea Surface Temperature (DOISST) Version 2.1. Journal of Climate, 34(9), 2923–2939. https://doi.org/10.1175/JCLI-D-19-0909.1

105. Huang, B., Thorne, P. W., Banzon, V. F., Boyer, T., Chepurin G., Lawrimore, J.H., Menne, M.J., Smith, T.M., Vose, R.S., Zhang, H. (2021). Extended reconstructed sea-surface temperature, version 5 (ERSSTv5): Upgrades, validations, and intercomparisons. Journal of Climate, 34(10), 3413-3439. https://doi.org/10.1175/JCLI-D-20-0395.1

106. Huang, X., and Swain, D. L. (2022). Climate change is increasing the risk of a California Mega flood. Science Advances, 8(32), eabq0995.

107. Hurrell, J. W. (1995). Decadal Trends in the North Atlantic Oscillation: Regional Temperatures and Precipitation. Science, 269(5224), 676–679.

108. Hurrell, J. W., and Deser, C. (2010). North Atlantic climate variability: The role of the NAO and North Atlantic ocean. Journal of Marine Systems, 79(3–4), 231–244. https://doi.org/10.1016/j.jmarsys.2009.11.002

109. Hurrell, J. W., and Trenberth, K. E. (1999). Global sea surface temperature analyses: Multiple problems and their implications for climate analysis, modeling, and reanalysis. Bulletin of the American Meteorological Society, 80(12), 2661–2678.

110. Hurrell, J. W., Kushnir, Y., Ottersen, G., and Visbeck, M. (2003). An overview of the North Atlantic Oscillation. In The North Atlantic Oscillation: Climatic Significance and Environmental Impact (pp. 1–35). https://doi.org/10.1029/134GM01

111. Ibebuchi, C. C., and Abu, I. (2023). Rainfall variability patterns in Nigeria during the rainy season. Scientific Reports, 13, 7888. https://doi.org/10.1038/s41598-023-34970-7

112. Indeje, M., Semazzi, F. H. M., and Ogallo, L. J. (2000). ENSO signals in East African rainfall seasons. International Journal of Climatology, 20(1), 19–46. https://doi.org/10.1002/(SICI)1097-0088(200001)20:1<19::AID-JOC449>3.0.CO;2-0

113. Intergovernmental Panel on Climate Change. (2021). Climate Change 2021: The Physical Science Basis. Cambridge University Press. https://doi.org/10.1017/9781009157896

114. International Research Institute for Climate and Society (IRI). (2023). Seasonal climate forecasts and ENSO forecast products. International Research Institute for Climate and Society, Columbia University. Retrieved [August 21 2025], from https://iri.columbia.edu/our-expertise/climate/forecasts/

115. Jackson, J. E. (2005). A User's Guide to Principal Components (2nd ed.). Hoboken, NJ: Wiley-Interscience. https://doi.org/10.1002/0471725331

116. Jevrejeva, S., Moore, J. C., and Grinsted, A. (2003). Influence of the Arctic Oscillation and El Niño–Southern Oscillation (ENSO) on ice conditions in the Baltic Sea: The wavelet approach. Journal of Geophysical Research: Atmospheres, 108(D21), Article 4677. https://doi.org/10.1029/2003JD003417

117. Jin, F.-F., and Neelin, J. D. (1993). Modes of interannual tropical ocean–atmosphere interaction—a unified view. Part I: Numerical results. Journal of the Atmospheric

Sciences, 50(22), 3477-3503. https://doi.org/10.1175/1520-0469(1993)050<3477:MOITOI>2.0.CO;2

118. Johnstone, J. A., and Dawson, T. E. (2010). Climatic context and ecological implications of summer fog decline in the coast redwood region. Proceedings of the National Academy of Sciences, 107(10), 4533-4538.

119. Jolliffe, I. T., and Cadima, J. (2016). Principal component analysis: A review and recent developments. Philosophical Transactions of the Royal Society A, 374(2065), 20150202. https://doi.org/10.1098/rsta.2015.0202

120. Jong, B.-T., Ting, M., and Seager, R. (2016). El Niño's impact on California precipitation: Seasonality, regionality, and El Niño intensity. Environmental Research Letters, 11(5), 054021. https://doi.org/10.1088/1748-9326/11/5/054021

121. Kamalzadeh, H., Ahmadi, A., and Mansour, S. (2020). Clustering time-series by a novel slope- based similarity measure considering particle swarm optimization. Applied Soft Computing, 96, 106701. https://doi.org/10.1016/j.asoc.2020.106701

122. Keeley, J. E., and Syphard, A. D. (2021). Climate change and California wildfire. Fire Ecology, 17(3), 1–15.

123. Killick, R., Fearnhead, P., and Eckley, I. A. (2012). Optimal detection of changepoints with a linear computational cost. Journal of the American Statistical Association, 107(500), 1590-1598.

124. Klotzbach, P. J., Bowen, S. G., Pielke, R., and Bell, M. (2018). Continental U.S. Hurricane Landfall Frequency and Associated Damage: Observations and Future Risks. Bulletin of the American Meteorological Society, 99(1), 135–146. https://doi.org/10.1175/BAMS-D-17-0184.1

125. Kousky, V., Kagano, M., and Cavalcanti, I. (1984). A review of the Southern Oscillation: Oceanic-atmospheric circulation changes and related rainfall anomalies. Tellus, 36A(5), 490–504.

126. Koutsoyiannis, D., and Langousis, A. (2011). Precipitation. En P. Wilderer and S. Uhlenbrook (Eds.), Treatise on Water Science (Vol. 2, pp. 27–78). Academic Press. https://doi.org/10.1016/B978-0-444-53199-5.00027-0

127. Kumar, K. N., and Ouarda, T. B. M. J. (2014). Precipitation variability over UAE and global SST teleconnections. Journal of Geophysical Research: Atmospheres, 119(17), 10,313–10,322. https://doi.org/10.1002/2014JD021724

128. Kundzewicz, Z. W., and Robson, A. J. (2004). Change detection in hydrological records—a review of the methodology. Hydrological Sciences Journal, 49(1), 7–19. https://doi.org/10.1623/hysj.49.1.7.53993

129. Kwon, H.-H., Brown, C., Xu, K., and Lall, U. (2009). Seasonal and annual maximum streamflow forecasting using climate information: Application to the Three Gorges Dam in the Yangtze River basin, China. Hydrological Sciences Journal, 54(3), 582–595. https://doi.org/10.1623/HYSJ.54.3.582

130. L'Heureux, M. L., Collins, D. C., and Hu, Z.-Z. (2013). Linear trends in sea surface temperature of the tropical Pacific Ocean and implications for the El Niño-Southern Oscillation. Climate Dynamics, 40(5–6), 1223–1236. https://doi.org/10.1007/s00382-012-1331-2

131. Lana, X., Fernández Mills, G., and Burgueño, A. (1995). Daily precipitation maxima in Catalonia (north-east Spain): Expected values and their spatial distribution.

International Journal of Climatology, 15(3), 341–354. https://doi.org/10.1002/joc.3370150309

132. Leathers, D. J., Yarnal, B., and Palecki, M. A. (1991). The Pacific/North American teleconnection pattern and United States climate. Part I: Regional temperature and precipitation associations. Journal of Climate, 4(5), 517–528. https://doi.org/10.1175/1520-0442(1991)004<0517:TPATPA>2.0.CO;2

133. Lee, T. S., and Ouarda, T. B. M. J. (2012a). Stochastic simulation of nonstationary oscillation hydroclimatic processes using empirical mode decomposition. Water Resources Research, 48(2).

134. Lee, T., and Ouarda, T. B. M. J. (2019). Multivariate nonstationary oscillation simulation of climate indices with empirical mode decomposition. Water Resources Research, 55(6), 4765–4787.

135. Lhermitte, S., Verbesselt, J., Verstraeten, W. W., and Coppin, P. (2011). A comparison of time series similarity measures for classification and change detection of ecosystem dynamics. Remote Sensing of Environment, 115(12), 3129–3152. https://doi.org/10.1016/j.rse.2011.06.004

136. L'Heureux, M. L., Collins, D. C., and Hu, Z.-Z. (2013). Linear trends in sea surface temperature of the tropical Pacific Ocean and implications for the El Niño-Southern Oscillation. Climate Dynamics, 40(5–6), 1223–1236. https://doi.org/10.1007/s00382-012-1331-2

137. Li, G., Feng, J., Du, Y., Wang, B., Li, T., and Yuan, J. (2024). Two distinct interannual modes of the North Pacific Oscillation: Role of ocean–atmosphere coupling and

transient eddies. Climate Dynamics, Article 10. https://doi.org/10.1007/s00382-024-07524-4

138. Lindzen, R. S., and Holton, J. R. (1968). A theory of the quasi-biennial oscillation of the tropical stratosphere. Journal of the Atmospheric Sciences, 25(6), 1095–1107. https://doi.org/10.1175/1520-0469(1968)025<1095:ATOTQO>2.0.CO;2

139. Lins, H. F., and Cohn, T. A. (2011). Stationarity: Wanted Dead or Alive? Journal of the American Water Resources Association, 47(3), 475–480.

140. Liu, Z., and Alexander, M. (2007). Atmospheric bridge, oceanic tunnel, and global climatic teleconnections. Reviews of Geophysics, 45(4), RG4009. https://doi.org/10.1029/2005RG000172

141. Llasat, M. C., Ceperuelo, M., and Rigo, T. (2007). Rainfall regionalization on the basis of the precipitation convective features using a rain-gauge network and weather radar observations. Atmospheric Research, 83(3–4), 415–426. https://doi.org/10.1016/j.atmosres.2005.08.014

142. Llasat-Botija, M., Llasat, M. C., and López, L. (2007). Natural Hazards and the press in the western Mediterranean region. Advances in Geosciences, 12, 81–85. https://doi.org/10.5194/adgeo-12-81-2007

143. López-Parages, J., and Rodríguez-Fonseca, B. (2012). Multidecadal modulation of El Niño influence on the Euro-Mediterranean rainfall. Geophysical Research Letters, 39, L02704. https://doi.org/10.1029/2011GL050049

144. Lund, J., Medellin-Azuara, J., Durand, J., and Stone, K. (2018). Lessons from California's 2012–2016 drought. Journal of Water Resources Planning and

Management, 144(10), 04018067. https://doi.org/10.1061/(ASCE)WR.1943-5452.0000984

145. Ma, M., Qu, Y., Lyu, J., Zhang, X., Su, Z., Gao, H., Yang, X., Chen, X., Jiang, T., Zhang, J., Shen, M., and Wang, Z. (2022). The 2022 extreme drought in the Yangtze River Basin: Characteristics, causes and response strategies. River, 1(2), 162–171. https://doi.org/10.1002/rvr2.23

146. Magnini, A., Pavan, V., and Castellarin, A. (2024). Informativeness of teleconnections in local and regional frequency analysis of rainfall extremes. EGUsphere [preprint]. https://doi.org/10.5194/egusphere-2024-3261

147. Maher, N., Kay, J. E., and Capotondi, A. (2021). Modulation of ENSO teleconnections over North America by the Pacific decadal oscillation. Environmental Research Letters, 16(7), 074043. https://doi.org/10.1088/1748-9326/ac9327

148. Mantua, N. J., and Hare, S. R. (2002). The Pacific Decadal Oscillation. Journal of Oceanography, 58(1), 35–44. https://doi.org/10.1023/A:1015820616384

149. Maraun, D., and Kurths, J. (2004). Cross wavelet analysis: Significance testing and pitfalls. Nonlinear Processes in Geophysics, 11(4), 505–514. https://doi.org/10.5194/npg-11-505-2004

150. Marengo, J. A., Tomasella, J., Alves, L. M., Soares, W. R., and Rodriguez, D. A. (2011). The drought of 2010 in the context of historical droughts in the Amazon region. Geophysical Research Letters, 38, L12703. https://doi.org/10.1029/2011GL047436

151. Mariotti, A., Zeng, N., and Lau, K.-M. (2002). Euro-Mediterranean rainfall and ENSO — a seasonally varying relationship. Geophysical Research Letters, 29(8), 32-1–32-4. https://doi.org/10.1029/2001GL014248

152. McAfee, S. A. (2014). Consistency and the lack thereof in Pacific Decadal Oscillation impacts on North American winter climate. Journal of Climate, 27(18), 7410–7431. https://doi.org/10.1175/JCLI-D-14-00143.1

153. McCabe, G. J., and Dettinger, M. D. (1999). Decadal variations in the strength of ENSO teleconnections with precipitation in the western United States. International Journal of Climatology, 19(13), 1399–1410.

154. McKinnon, K. A., and Deser, C. (2018). Internal variability and regional climate trends in an observational large ensemble. Journal of Climate, 31(17), 6783-6802. https://doi.org/10.1175/JCLI-D-17-0901.1

155. McPhaden, M. J., Santoso, A., and Cai, W. (Eds.). (2020). El Niño Southern Oscillation in a Changing Climate. American Geophysical Union, Wiley. https://doi.org/10.1002/9781119548164

156. McPhaden, M. J., Zebiak, S. E., and Glantz, M. H. (2006). ENSO as an integrating concept in Earth science. Science, 314(5806), 1740–1745. https://doi.org/10.1126/science.1132588

157. Mendler, F., Koch, B., Meißner, B., Voglstätter, C., and Smolinka, T. (2025). Evaluation of spatial clustering methods for regionalisation of hydrogen ecosystems. Energy Strategy Reviews, 57, 101627. https://doi.org/10.1016/j.esr.2024.101627

158. Milly, P. C. D., Betancourt, J., Falkenmark, M., Hirsch, R. M., Kundzewicz, Z. W., Lettenmaier, D. P., and Stouffer, R. J. (2008). Stationarity is dead: Whither water management? Science, 319(5863), 573–574. https://doi.org/10.1126/science.1151915

159. Mo, K. C., and Higgins, R. W. (1998). The Pacific–South American modes and tropical convection during the Southern Hemisphere winter. Monthly Weather Review,

126(6), 1581-1599. https://doi.org/10.1175/1520-0493(1998)126<1581:TPSAAT>2.0.CO;2

160. Monahan, A. H., Fyfe, J. C., Ambaum, M. H. P., Stephenson, D. B., and North, G. R. (2009). Empirical orthogonal functions: The medium is the message. Journal of Climate, 22(24), 6501-6514. https://doi.org/10.1175/2009JCLI2856.1

161. Morabbi, A., Bouziane, A., Seidou, O., Habitou, N., Ouazar, D., Ouarda, T., Charron, C., Hasnaoui, M., Benrhanem, M., and Sittichok, K. (2022). A multiple changepoint approach to hydrological regions delineation. Journal of Hydrology, 604, 127118.

162. Mote, P. W., Hamlet, A. F., Clark, M. P., and Lettenmaier, D. P. (2005). Declining mountain snowpack in western North America. Bulletin of the American Meteorological Society, 86(1), 39-49.

163. Mote, P. W., Li, S., Lettenmaier, D. P., Xiao, M., and Engel, R. (2018). Dramatic declines in snowpack in the western US. npj Climate and Atmospheric Science, 1(1), Article 2. https://doi.org/10.1038/s41612-018-0012-1

164. Mudelsee, M. (2019). Trend analysis of climate time series: A review of methods. Earth-Science Reviews, 190, 310–322. https://doi.org/10.1016/j.earscirev.2018.12.005

165. Muñoz, C., Schultz, D. M., and Vaughan, G. (2020). A midlatitude climatology and interannual variability of 200- and 500-hPa cut-off lows. Journal of Climate, 33(3), 2201–2222. https://doi.org/10.1175/JCLI-D-19-0497.1

166. Naizghi, M. S., and Ouarda, T. B. M. J. (2017). Teleconnections and analysis of long-term wind speed variability in the UAE. International Journal of Climatology, 37(2), 230–248. https://doi.org/10.1002/joc.4700

167. Naizghi, M. S., and Ouarda, T. B. M. J. (2016). Teleconnections and analysis of long-term wind speed variability in the UAE. International Journal of Climatology, 37(2), 964–979. https://doi.org/10.1002/joc.4700

168. National Oceanic and Atmospheric Administration (NOAA). (2017). ENSO Diagnostic Discussion (Annual Compendium). https://www.noaa.gov/

169. Neelin, J. D., Langenbrunner, B., Meyerson, J. E., Hall, A., and Berg, N. (2013). California winter precipitation change under global warming in the Coupled Model Intercomparison Project Phase 5 ensemble. Journal of Climate, 26(17), 6238–6256. https://doi.org/10.1175/JCLI-D-12-00514.1

170. Newman, M., Alexander, M. A., Ault, T. R., et al. (2016). The Pacific Decadal Oscillation, revisited. Journal of Climate, 29(12), 4399-4427. https://doi.org/10.1175/JCLI-D-15-0508.1.

171. Newman, M., Shin, S. I., and Alexander, M. A. (2011). Natural variation in ENSO flavors. Geophysical Research Letters, 38(14), L14705. https://doi.org/10.1029/2011GL047658

172. Nicholson, S. E., and Kim, J. (1997). The relationship of the El Niño–Southern Oscillation to African rainfall. International Journal of Climatology, 17(2), 117–135. https://doi.org/10.1002/(SICI)1097-0088(199702)17:2<117::AID-JOC84>3.0.CO;2-O

173. Nieto Ferreira, R. N. (2021). Cut-Off Lows and Extreme Precipitation in Eastern Spain: Current and Future Climate. Atmosphere, 12(7), 835. https://doi.org/10.3390/atmos12070835

174. Nigam, S. (2003). Teleconnections. En J. R. Holton, J. A. Pyle, and J. A. Curry (Eds.), Encyclopedia of Atmospheric Sciences (pp. 2243–2269). Academic Press. https://doi.org/10.1016/B978-0-12-382225-3.00400-X

175. Nigam, S., and Baxter, S. (2015). Teleconnections. In G. R. North, J. Pyle, and F. Zhang (Eds.), Encyclopedia of Atmospheric Sciences (2nd ed., pp. 228–239). Academic Press. https://doi.org/10.1016/B978-0-12-382225-3.00348-1

176. Nigam, S., and Sengupta, A. (2021). The full extent of El Niño's precipitation influence on the United States and the Americas: The suboptimality of the Niño 3.4 SST index. Geophysical Research Letters, 48(3), e2020GL091447. https://doi.org/10.1029/2020GL091447

177. Nigam, S., Sengupta, A., and Ghosh, R. (2021). The full extent of El Niño's precipitation influence on the United States and the Americas: The suboptimality of the Niño-3.4 SST index. Geophysical Research Letters, 48(5), e2020GL091447. https://doi.org/10.1029/2020GL091447.

178. Nobre, P., and Shukla, J. (1996). Variations of sea surface temperature, wind stress, and rainfall over the tropical Atlantic and South America. Journal of Climate, 9(10), 2464–2479. https://doi.org/10.1175/1520-0442(1996)009<2464:VOSSTW>2.0.CO;2

179. North, G. R., Bell, T. L., Cahalan, R. F., and Moeng, F. J. (1982). Sampling errors in the estimation of empirical orthogonal functions. Monthly Weather Review, 110(7), 699-706. https://doi.org/10.1175/1520-0493(1982)110<0699:SEITEO>2.0.CO;2

180. Ojara, M. A., Yunsheng, L., Uddin, M. J., Babaousmail, H., and Ayugi, B. O. (2022). Statistical evaluation of changes and periodicity in rainfall over East Africa during the

period 1960–2017. Pure and Applied Geophysics, 179, 2969–2992. https://doi.org/10.1007/s00024-022-03101-0

181. Okumura, Y. M. (2019). ENSO diversity from an atmospheric perspective. Current Climate Change Reports, 5(3), 245–257. https://doi.org/10.1007/s40641-019-00138-7

182. Ongoma, V., Chen, H., and Gao, C. (2018). Projected change in mean rainfall and temperature over East Africa based on CMIP5 models. International Journal of Climatology, 38(3), 1375–1392. https://doi.org/10.1002/joc.5252

183. Ouachani, R., Bargaoui, Z., and Ouarda, T. B. M. J. (2013). Power of teleconnection patterns on precipitation and streamflow variability of upper Medjerda Basin. International Journal of Climatology, 33(1), 58–76. https://doi.org/10.1002/joc.3407

184. Ouarda, T. B. M. J., and Charron, C. (2019). Non-stationary intensity-duration-frequency curves integrating information concerning teleconnections and climate change. International Journal of Climatology, 39(4), 2306–2323. https://doi.org/10.1002/joc.5953

185. Ouarda, T. B. M. J., Charron, C., and St-Hilaire, A. (2019). A network approach for delineating homogeneous regions in regional flood frequency analysis. Water Resources Research, 55(10), 8279–8297. https://doi.org/10.1029/2019WR025910

186. Ouarda, T., Charron, C., Kumar, K. N., Marpu, P., Ghedira, H., Molini, A., and Khayal, I. (2014). Evolution of the rainfall regime in the United Arab Emirates. Journal of Hydrology, 514, 258–270. https://doi.org/10.1016/j.jhydrol.2014.04.032

187. Patricola, C. M., O'Brien, J. P., Risser, M. D., Rhoades, A. M., O'Brien, T. A., Ullrich, P. A., Stone, D. A., and Collins, W. D. (2019). Maximizing ENSO as a source of western

us hydroclimate predictability. Climate Dynamics, 54(1–2), 351–372. https://doi.org/10.1007/s00382- 019- 05004-8

188. Pettitt, A. N. (1979). A non-parametric approach to the change-point problem. Journal of the Royal Statistical Society, Series C (Applied Statistics), 28(2), 126–135. https://doi.org/10.2307/2346729

189. Philip, S. Y., Kew, S. F., van Oldenborgh, G. J., Anslow, F. S., Seneviratne, S. I., Vautard, R., Coumou, D., Ebi, K. L., Arrighi, J., Singh, R., van Aalst, M., Pereira Marghidan, C., Wehner, M., Yang, W., Li, S., Schumacher, D. L., Hauser, M., Bonnet, R., Luu, L. N., Lehner, F., Gillett, N., Tradowsky, J. S., Vecchi, G. A., Rodell, C., Stull, R. B., Howard, R., and Otto, F. E. L. (2022). Rapid attribution analysis of the extraordinary heat wave on the Pacific coast of the US and Canada in June 2021. Earth System Dynamics, 13(4), 1689–1713. https://doi.org/10.5194/esd-13-1689-2022

190. Power, S., Casey, T., Folland, C., Colman, A., and Mehta, V. (1999). Inter-decadal modulation of the impact of ENSO on Australia. Climate Dynamics, 15, 319–324. https://doi.org/10.1007/s003820050284

191. Priestley, M. B. (1988). Non-linear and non-stationary time series analysis. Academic Press.

192. Purohit, S. (2025). Rainfall in California: Special Reference to 2023 Rains That Caused Floods. Annals of the American Association of Geographers, 1–13. https://doi.org/10.1080/24694452.2024.2400078

193. Ragno, E., AghaKouchak, A., Love, C. A., Cheng, L., and Lima, C. H. R. (2019). A generalized framework for process-informed nonstationary extreme value analysis.

Advances in Water Resources, 130, 270–282. https://doi.org/10.1016/j.advwatres.2019.06.007

194. Ralph, F. M., and Dettinger, M. D. (2012). Historical and national perspectives on extreme West Coast precipitation associated with atmospheric rivers during December 2010. Bulletin of the American Meteorological Society, 93(6), 783–790. https://doi.org/10.1175/BAMS-D-11-00188.1

195. Ralph, F. M., Rutz, J. J., Cordeira, J. M., Dettinger, M., Anderson, M., Reynolds, D., Schick, L. J., and Smallcomb, C. (2019). A scale to characterize the strength and impacts of atmospheric rivers. Bulletin of the American Meteorological Society, 100(2), 269–289. https://doi.org/10.1175/BAMS-D-18-0023.1

196. Rasmussen, P. (2001). Bayesian estimation of change points using the general linear model. Water Resources Research, 37(11), 2723–2731.

197. Reeves, J., Chen, J., Wang, X. L., Lund, R., and Lu, Q. Q. (2007). A review and comparison of changepoint detection techniques for climate data. Journal of Applied Meteorology and Climatology, 46(6), 900–915. https://doi.org/10.1175/JAM2493.1

198. Reichstein, M., Camps-Valls, G., Stevens, B., Jung, M., Denzler, J., Carvalhais, N., and Prabhat (2019). Deep learning and process understanding for data-driven Earth system science. Nature, 566(7743), 195–204. https://doi.org/10.1038/s41586-019-0912-1

199. Reuters. (2022, August 23). China battles forest fires as fears linger over harvest. Reuters. Retrieved from https://www.reuters.com/world/china/chinas-southwest-battles-forest-fires-end-heatwave-approaches-2022-08-23/

200. Reuters. (2022, August). China’s Yangtze drought coverage (series). Reuters. https://www.reuters.com/

201. Reynolds, R. W., Rayner, N. A., Smith, T. M., Stokes, D. C., and Wang, W. (2002). An improved in-situ and satellite SST analysis for climate. Journal of Climate, 15(13), 1609-1625. https://doi.org/10.1175/1520-0442(2002)015<1609:AIISAS>2.0.CO;2

202. Risbey, J. S., Pook, M. J., McIntosh, P. C., Wheeler, M. C., and Hendon, H. H. (2009). On the remote drivers of rainfall variability in Australia. Monthly Weather Review, 137(10), 3233–3253. https://doi.org/10.1175/2009MWR2861.1

203. Rodionov, S. N. (2004). A sequential algorithm for testing climate regime shifts. Geophysical Research Letters, 31(9), L09204. https://doi.org/10.1029/2004GL019448

204. Ropelewski, C. F., and Halpert, M. S. (1987). Global and regional precipitation patterns associated with the El Niño/Southern Oscillation. Monthly Weather Review, 115(8), 1606–1626. https://doi.org/10.1175/1520-0493(1987)115<1606:GARPPA>2.0.CO;2

205. Ropelewski, C. F., and Halpert, M. S. (1986). North American precipitation and temperature patterns associated with the El Niño/Southern Oscillation (ENSO). Monthly Weather Review, 114(12), 2352–2362. https://doi.org/10.1175/1520-0493(1986)114<2352:NAPATP>2.0.CO;2

206. Rosas-Cabello, C.A., Alobaidi, M.H., Chebana F., Seidou, O. (2025). Development of Station-Specific Regions of Influence for Teleconnection Analysis Using PS Similarity. Manuscript submitted for publication to Journal of Hydrology. (Submitted)

207. Ruggieri, E. (2013). A Bayesian approach to detecting change points in climatic records. International Journal of Climatology, 33(2), 520–528

208. Rutz, J. J., Shields, C. A., Lora, J. M., Payne, A. E., Guan, B., Ullrich, P., … Viale, M. (2019). The Atmospheric River Tracking Method Intercomparison Project (ARTMIP): Quantifying uncertainties in atmospheric river climatology. Journal of Geophysical Research: Atmospheres, 124(24), 13777–13802. https://doi.org/10.1029/2019JD030936

209. Saharia, M., Kirstetter, P.-E., Vergara, H., Gourley, J. J., Emmanuel, I., and Andrieu, H. (2021). On the impact of rainfall spatial variability, geomorphology, and climatology on flash floods. Water Resources Research, 57(9), e2020WR029124. https://doi.org/10.1029/2020WR029124

210. Salas, J.D. and Fernandez, B., 1993. Models for data generation in hydrology: univariate techniques. Stochastic Hydrology and Its Use in Water Resources Systems Simulation and Optimization, 47–73.

211. Schaeffer, R., Schipper, E. L. F., Ospina, D., Mirazo, P., Alencar, A., Anvari, M., Artaxo, P., Biresselioglu, M. E., Blome, T., Boeckmann, M., Brink, E., Broadgate, W., Bustamante, M., Cai, W., Canadell, J. G., Cardinale, R., Chidichimo, M. P., Ditlevsen, P., Eicker, U., … Ziervogel, G. (2025). Ten new insights in climate science 2024. One Earth, 8(6), Article 101285. https://doi.org/10.1016/j.oneear.2025.101285

212. Scholz, M. Validation of nonlinear PCA. Neural Process. Lett. 2012, 36, 21–30.

213. Scott, S. L., and Berger, J. O. (2006). An exploration of aspects of Bayesian multiple testing. Journal of Statistical Planning and Inference, 136(7), 2144-2162.

214. Seager, R., and Hoerling, M. P. (2014). Atmosphere and ocean origins of North American droughts. Journal of Climate, 27(12), 4581-4606. https://doi.org/10.1175/JCLI-D-13-00329.1.

215. Seidou, O., and Ouarda, T. B. M. J. (2007). Recursion-based multiple changepoint detection in multiple linear regression and application to river streamflows. Water Resources Research, 43(7). https://doi.org/10.1029/2006WR005021

216. Sengupta, A., Waliser, D. E., DeFlorio, M. J., Guan, B., Delle Monache, L., and Ralph, F. M. (2025). Role of evolving sea surface temperature modes of variability in improving seasonal precipitation forecasts. Communications Earth and Environment, 6, 256. https://doi.org/10.1038/s43247-025-02235-y (Peer review)

217. Serinaldi, F., and Kilsby, C. G. (2015). Stationarity is undead: Uncertainty dominates the distribution of extremes. Advances in Water Resources, 77, 17–36. https://doi.org/10.1016/j.advwatres.2014.12.013

218. Shi, N., Wang, Y., Wang, X., and Tian, P. (2019). Interdecadal variations in the frequency of persistent hot events in boreal summer over midlatitude Eurasia. Journal of Climate, 32(16), 5161–5177. https://doi.org/10.1175/JCLI-D-18-0706.1

219. Shin, C.-S., Dirmeyer, P. A., and Huang, B. (2023). A joint approach combining correlation and mutual information to study land and ocean drivers of U.S. droughts: Methodology. Journal of Climate, 36(9), 2795–2814. https://doi.org/10.1175/JCLI-D-22-0429.1

220. Shin, N. Y. (2022). More frequent central Pacific El Niño and stronger eastern Pacific El Niño in a warmer climate. npj Climate and Atmospheric Science, 5, Article 24. https://doi.org/10.1038/s41612-022-00324-9

221. Slater, L. J., Villarini, G., Archfield, S., Faulkner, D., Lamb, R., Khouakhi, A., and Yin, J. (2021). Global changes in hydrological extremes. Nature Reviews Earth and Environment, 2(5), 383–399. https://doi.org/10.1038/s43017-021-00124-7

222. Slater, L. J., Wilby, R. L., and Murphy, C. (2021). Nonstationary weather and water extremes: a review of methods for their detection, attribution, and management. Hydrology and Earth System Sciences, 25(7), 3897–3935. https://doi.org/10.5194/hess-25-3897-2021

223. Stagge, J. H., Rosenberg, D. E., Abdallah, A. M., Akbar, H., Attallah, N. A., and James, R. (2019). Assessing data availability and research reproducibility in hydrology and water resources. Scientific Data, 6, 190030. https://doi.org/10.1038/sdata.2019.30

224. Stagge, J. H., Torbenson, M. C. A., Sung, K., Phillips, B., and Kingston, D. G. (2023). Orographic amplification of El Niño teleconnections on winter precipitation across the Intermountain West of North America. Nature Water, 1, 1016–1026. https://doi.org/10.1038/s44221-023-00163-9

225. Stanway, D. (2022, August 17). China races to alleviate drought, power cuts amid record heatwave. Reuters. Retrieved from https://www.reuters.com/world/china/china-takes-action-alleviate-drought-record-heatwave-continues-2022-08-17/

226. Stuecker, M. F., Timmermann, A., Jin, F.-F., McGregor, S., and Ren, H.-L. (2013). A combination mode of the annual cycle and the El Niño/Southern Oscillation. Nature Geoscience, 6, 540-544. https://doi.org/10.1038/ngeo1826

227. Swain, D. L., Langenbrunner, B., Neelin, J. D., and Hall, A. (2018). Increasing precipitation volatility in twenty-first-century California. Nature Climate Change, 8(5), 427–433.

228. Swain, D. L., Tsiang, M., Haugen, M., Singh, D., Charland, A., Rajaratnam, B., and Diffenbaugh, N. S. (2014). The extraordinary California drought of 2013/2014:

Character, context, and the role of climate change. Bulletin of the American Meteorological Society, 95(9), S3–S7.

229. Takahashi, K., and Martínez, A. G. (2019). The very strong coastal El Niño in 1925 in the far-eastern Pacific. Climate Dynamics, 52, 7389–7415. https://doi.org/10.1007/s00382-017-3702-1

230. Takahashi, K., Montecinos, A., Goubanova, K., and Dewitte, B. (2011). ENSO regimes: Reinterpreting the canonical and Modoki El Niño. Geophysical Research Letters, 38(10), L10704. https://doi.org/10.1029/2011GL047364

231. Taschetto, A. S., Ummenhofer, C. C., Stuecker, M. F., Dommenget, D., Ashok, K., Rodrigues, R. R., and Yeh, S.-W. (2020). ENSO Atmospheric Teleconnections. In M. J. McPhaden, A. Santoso, and W. Cai (Eds.), El Niño Southern Oscillation in a Changing Climate (pp. 309–335). American Geophysical Union. https://doi.org/10.1002/9781119548164.ch14

232. Thompson, D. W. J., and Wallace, J. M. (2000). Annular modes in the extratropical circulation. Part I: Month-to-month variability. Journal of Climate, 13(5), 1000–1016. https://doi.org/10.1175/1520-0442(2000)013<1000:AMITEC>2.0.CO;2

233. Torrence, C., and Webster, P. J. (1999). Interdecadal changes in the ENSO–monsoon system. Journal of Climate, 12(8), 2679–2690. https://doi.org/10.1175/1520-0442(1999)012<2679:ICITEM>2.0.CO;2

234. Torrence, C., and Compo, G. P. (1998). A practical guide to wavelet analysis. Bulletin of the American Meteorological Society, 79(1), 61–78.

235. Trenberth K (1997) The definition of El Nino. Bulletin of the American Meteorological Society 78(12):2771– 2777

236. Trenberth, K. E., and Stepaniak, D. P. (2001). Indices of El Niño evolution. Journal of Climate, 14(8), 1697–1701. https://doi.org/10.1175/1520-0442(2001)014<1697:LIOENO>2.0.CO;2

237. Trenberth, K. E., Branstator, G. W., Karoly, D., Kumar, A., Lau, N.-C., and Ropelewski, C. (1998). Progress during TOGA in understanding and modeling global teleconnections associated with tropical sea surface temperatures. Journal of Geophysical Research: Oceans, 103(C7), 14291–14324. https://doi.org/10.1029/97JC01444

238. Tsonis, A. A., and Roebber, P. J. (2004). The architecture of the climate network. Physica A: Statistical Mechanics and its Applications, 333, 497–504. https://doi.org/10.1016/j.physa.2003.10.045

239. United Nations Office for Disaster Risk Reduction (UNDRR). (2019). Global Assessment Report on Disaster Risk Reduction 2019. UNDRR.

240. United Nations Office for Disaster Risk Reduction (UNDRR). (2023). Global Assessment Report 2023. UNDRR.

241. Van Loon, A. F., and Laaha, G. (2015). Hydrological drought explained. Wiley Interdisciplinary Reviews: Water, 2(4), 359–392. https://doi.org/10.1002/wat2.1085

242. Villarini, G., Smith, J. A., Serinaldi, F., Bales, J., Bates, P. D., and Krajewski, W. F. (2009). Flood frequency analysis for nonstationary annual peak records in an urban drainage basin. Advances in Water Resources, 32(8), 1255–1266. https://doi.org/10.1016/j.advwatres.2009.05.003

243. Volpi, E., Grimaldi, S., Aghakouchak, A., Castellarin, A., Chebana, F., Papalexiou, S. M., Aksoy, H., Bárdossy, A., Cancelliere, A., Chen, Y., Deidda, R., Haberlandt, U., Eris,

E., Fischer, S., Francés, F., Kavetski, D., Rodding Kjeldsen, T., Kochanek, K., Langousis, A., Mediero Orduña, L., Montanari, A., Nerantzaki, S. D., Ouarda, T. B. M. J., Prosdocimi, I., Ragno, E., Rajulapati, C. R., Requena, A. I., Ridolfi, E., Sadegh, M., Schumann, A., and Sharma, A. (2024). The legacy of STAHY: Milestones, achievements, challenges, and open problems in statistical hydrology. Hydrological Sciences Journal, 69(14), 1913–1949. https://doi.org/10.1080/02626667.2024.2385686

244. von Storch, H., and Zwiers, F. W. (1999). Statistical analysis in climate research. Cambridge University Press.

245. Walker, G. T., and Bliss, E. W. (1932). World Weather V. Memoirs of the Royal Meteorological Society, 4(36), 53–84.

246. Wallace, J. M., and Gutzler, D. S. (1981). Teleconnections in the geopotential height field during the Northern Hemisphere winter. Monthly Weather Review, 109(4), 784–812. https://doi.org/10.1175/1520-0493(1981)109<0784:TITGHF>2.0.CO;2

247. Wang, B., Luo, X., Yang, Y.-M., Sun, W., Cane, M. A., Cai, W., Yeh, S.-W., and Liu, J. (2019). Historical change of El Niño properties sheds light on future changes of extreme El Niño. Proceedings of the National Academy of Sciences, 116(45), 22512–22517. https://doi.org/10.1073/pnas.1911130116

248. Wang, D., Dong, Z., Jiang, F., Zhu, S., Ling, Z., and Ma, J. (2022). Spatiotemporal variability of drought/flood and its teleconnection with large-scale climate indices based on standard precipitation index: A case study of Taihu Basin, China. Environmental Science and Pollution Research, 29(33), 50117–50134. https://doi.org/10.1007/s11356-022-19329-1

249. Wang, S., Huang, J., He, Y., and Guan, Y. (2014). Combined effects of the Pacific Decadal Oscillation and El Niño–Southern Oscillation on global land dry–wet changes. Scientific Reports, 4, Article 6651. https://doi.org/10.1038/srep06651

250. Wang, S., Meng, J., and Fan, J. (2023). Exploring the intensity, distribution and evolution of teleconnections using climate network analysis. Chaos, 33(10), Article 103127. https://doi.org/10.1063/5.0153677

251. Ward, P. J., Jongman, B., Kummu, M., Dettinger, M. D., Sperna Weiland, F. C., and Winsemius, H. C. (2014). Strong influence of El Niño–Southern Oscillation on flood risk around the world. Proceedings of the National Academy of Sciences, 111(44), 15659–15664. https://doi.org/10.1073/pnas.1409822111

252. Wilby, R. L., and Wigley, T. M. L. (2000). Precipitation predictors for downscaling: Observed and general circulation model relationships. International Journal of Climatology, 20(6), 641–661. https://doi.org/10.1002/(SICI)1097-0088(200005)20:6<641::AID-JOC501>3.0.CO;2-1

253. Williams, A. P., Abatzoglou, J. T., Gershunov, A., Guzman-Morales, J., Bishop, D. A., Balch, J. K., and Lettenmaier, D. P. (2019). Observed impacts of anthropogenic climate change on wildfire in California. Earth's Future, 7, 892–910. https://doi.org/10.1029/2019EF001210

254. Williams, A. P., Cook, E. R., Smerdon, J. E., Cook, B. I., Abatzoglou, J. T., Bolles, K., Baek, S. H., Badger, A. M., and Livneh, B. (2020). Large contribution from anthropogenic warming to an emerging North American megadrought. Science, 368(6488), 314–318. https://doi.org/10.1126/science.aaz9600

255. Wongchuig, S., Kitambo, B., Papa, F., Paris, A., Fleischmann, A. S., et al. (2023). Improved modeling of Congo's hydrology for floods and droughts analysis and ENSO teleconnections. Journal of Hydrology: Regional Studies, 50, 101563. https://doi.org/10.1016/j.ejrh.2023.101563

256. World Meteorological Organization. (2021). State of the Global Climate 2021. WMO. https://library.wmo.int/

257. World Meteorological Organization. (2021). WMO Atlas of Mortality and Economic Losses from Weather, Climate and Water Extremes (1970–2019). WMO. https://library.wmo.int/

258. WRCC. (2023). Western regional climate center. Retrieved November 30, 2023, from http://wrcc. dri.edu/.

259. Xiao, M., Zhang, Q., and Singh, V. P. (2017). Spatiotemporal variations of extreme precipitation regimes during 1961–2010 and possible teleconnections with climate indices across China. International Journal of Climatology, 37(1), 468–480. https://doi.org/10.1002/joc.4719

260. Xiong, L., Jiang, C., Xu, C.-Y., Yu, K.-X., and Guo, S. (2015). A framework of change-point detection for multivariate hydrological series. Water Resources Research, 51(10), 8198–8217. https://doi.org/10.1002/2015WR017677

261. Yang, X., Li, Y., Chen, Z., and Zhang, J. (2021). Changes of extreme precipitation and possible influence of ENSO events in a humid basin in China. Atmosphere, 12(11), Article 1522. https://doi.org/10.3390/atmos12111522

262. Yue, S., Pilon, P., Phinney, B., and Cavadias, G. (2002). The influence of autocorrelation on the ability to detect trend in hydrological series. Hydrological Processes, 16(9), 1807–1829. https://doi.org/10.1002/hyp.1095

263. Zhang, L., Zhou, T., Zhang, X., Zhang, W., Li, L., and Li, L. (2024). Attribution of the extreme 2022 summer drought along the Yangtze River Valley in China based on detection and attribution system of Chinese Academy of Sciences. Bulletin of the American Meteorological Society, 105(7), E1062–E1067. https://doi.org/10.1175/BAMS-D-23-0258.1

264. Zhang, T., Zhang, W., Jiang, F., and Jin, F.-F. (2024). La Niña's teleconnection to the Indian Ocean Dipole controlled by its longitudinal position. Geophysical Research Letters, 51, e2023GL107119. https://doi /10.1029/2023GL107119.

265. Zhang, W., Villarini, G., Vecchi, G. A., and Murakami, H. (2018). Impacts of the Pacific Meridional Mode on North Atlantic tropical cyclones making U.S. landfall. Climate Dynamics, 51(11–12), 5397–5411. https://doi.org/10.1007/s00382-017-3656-3

266. Zhang, X., Tang, Q., Pan, M., and Tang, Y. (2014). A long-term land surface hydrologic fluxes and states dataset for China. Journal of Hydrometeorology, 15(5), 2067–2084. https://doi.org/10.1175/JHM-D-13-0170.1